ABSTRACT

Title of Document: MODELING OF FALLING-PARTICLE SOLAR RECEIVERS FOR HYDROGEN PRODUCTION AND THERMOCHEMICAL ENERGY STORAGE.

Andrew S. Oles, Doctor of Philosophy, 2014

Directed By: Associate Professor Gregory S. Jackson, Department of Mechanical Engineering

One of the most important components in a solar-thermal power plant is the central receiver where concentrated solar energy is absorbed in a medium for storage and eventual use in power generation or fuel production. Current state-of-the-art receivers are not appropriate for future power-plant designs due to limited operating temperatures. The solid-particle receiver (SPR) has been proposed as an alternative architecture that can achieve very high temperatures (above 1500 °C) with high efficiency, while avoiding many of the thermal stress issues that plague alternative architectures. The SPR works by having a flow of solid particles free-fall through a cavity receiver while directly illuminated to absorb the solar energy. Because of the high operating temperatures that can be achieved, along with the ability to continuously flow a stream of solid reactant, the SPR has the potential for use as a reactor for either chemical storage of solar energy or fuel production as part of a solar water-splitting cycle. While the operation of the SPR is relatively simple, analysis is complicated by the many physical phenomena in the

receiver, including radiation-dominated heat transfer, couple gas-particle flow, and inter-phase species transport via reaction.

This work aims to demonstrate a set modeling tools for characterizing the operation of a solid particle receiver, as well as an analysis of the key operating parameters. A inert receiver model is developed using a semi-empirical gas-phase model and the surface-to-surface radiation model modified to account for interaction with the particle curtain. A detailed thermo-kinetic model is developed for undoped-ceria, a popular material for research into solar fuel production. The inert-receiver model is extended to integrate this kinetic model, and further used to evaluate the potential of perovskite materials to enhance the storage capability of the receiver. A modified undoped ceria model is derived and implemented via custom user functions in the context of a computational fluid dynamics simulation of the receiver using the discrete-ordinates method for radiation transfer. These modeling efforts provide a basis for in-depth analysis of the key operating parameters that influence the performance of the solid-particle receiver.

MODELING OF FALLING-PARTICLE SOLAR RECEIVERS FOR HYDROGEN PRODUCTION AND THERMOCHEMICAL ENERGY STORAGE

By

Andrew S. Oles

Dissertation submitted to the Faculty of the Graduate School of the
University of Maryland, College Park, in partial fulfillment
of the requirements for the degree of
Doctor of Philosophy
2014

Advisory Committee:
Professor Gregory Jackson, Chair
Professor Ken Kiger
Professor Amir Riaz
Professor Peter Sunderland
Professor Michael Zachariah

Dedication

For Amanda, my dad, and family.

Acknowledgements

The author would like to acknowledge the many collaborators and supporters who assisted with this work:

Foremost, I would like to personally thank Dr. Greg Jackson for his support and direction throughout this research project. Even from across the country, his weekly guidance was invaluable in furthering this work, keeping me on track, and challenging me to achieve higher.

My sincerest thanks to Warren Citrin for his support through the Warren Citrin Graduate Fellowship for Entrepreneurial Students at the University of Maryland. This financial support made this research possible.

Many thanks to Dr. Chandrasekhar Thamire for help and support while starting this research into solar thermal receivers.

A special thanks to my dissertation committee members for their time and attention evaluating this work to uphold the highest standards: Dr. Ken Kiger, Dr. Amir Riaz, Dr. Peter Sunderland, and Dr. Michael Zachariah.

Many thanks to Dr. Clifford Ho from Sandia National Labs for his guidance and collaboration regarding full-scale receiver design and simulation methods.

Much appreciation for members of my research group for their help, companionship, and many great discussions: Esteban Echeverria, Babak Eslami, Danica Gordon, William Gibbons, Lei Wang, Josh Pearlman, Jennie Moton, and Rick Stroman.

Many thanks to Chad Stern for keeping me in-touch with the world through our weekly dinners.

Deepest gratitude to Cindy, my sister, and Brian and Shawn, my brothers for their unquestioning support and understanding my sometimes absence. You all were vital supports during the long research process.

My deepest gratitude to my mom and dad for their love and support. I never could have done this work without all you have done to teach and care for me.

To my girlfriend, Amanda, my greatest thanks for all of her love, time, and support. Even from another country, you helped me stay motivated and focused while also making sure I found time for fun and enjoyment. This work would not have been possible without your help.

Table of Contents

List of Tables

List of Figures

Chapter 1: Introduction – The Potential for Solar Thermal Particle Receivers and Reactors

1.1 Introduction to Concentrated Solar Thermal Technologies

Concentrated solar thermal power (CSP) is emerging as a high-value energy technology that can fulfill baseload generation requirements through long-term storage with minimal emissions or environmental impacts. CSP plants use mirrored surfaces to concentrate terrestrial solar energy onto a receiver to achieve high temperatures (ranging from 400 °C to more than 1000 °C, depending on the technology) to drive a power-cycle. The highest temperature CSP technologies also have the potential to drive chemical reactions to provide industrial process-heat or to create fuel.

There are three kinds of concentrated solar thermal technologies, each with their own benefits and applications: line-concentrating systems, dish concentrating systems, and central tower systems. These technologies are primarily separated by their scale and operating temperatures.

Line-concentrating technologies, which include parabolic troughs and linear Fresnel systems, track the sun along 1-axis and concentrate radiation along long tubes through which a heat-transfer fluid flows, before being sent to storage or a power-cycle. Line-concentrating technologies can concentrate sunlight 30-100 times (Kodama and Gokon, 2007), have operating temperatures up to 400 °C, and are used in plants sized from 25-200 MW (González-Aguillar et al., 2007). While line-concentrating technologies are the most developed due to their simplicity and integrated storage, they have less long-term potential due to the limited temperatures.

Dish concentrating systems are modular systems featuring large parabolic dishes that track the sun in two-directions concentrating sunlight at the focal point of the dish where a small receiver is mounted. Dish concentrating systems can achieve concentration ratios as high as 1000-5000, have operating temperatures up to 1500 °C or more, and, due to their modularity, are used in plants ranging from 10 kW to hundreds of MW (Kodama and Gokon, 2007). However, dish concentrating systems have challenges associated with maintaining a mounted receiver while achieving accurate tracking, which can incur high costs. Further, dish concentration is difficult to integrate with storage in most applications; therefore, dish concentration is usually used in remote areas where conventional power cannot be supplied (Tester et al., 2012). Due to the relatively small size and high-temperatures, dish concentrators are often used as test-beds for thermochemical reaction cycles.

Central tower systems feature a large tower with a central receiver at the top onto which reflectors, called heliostats, track the sun in two directions and concentrate the sunlight onto the receiver. The central receiver transfers the concentrated solar energy to a working fluid or reactant stream, before being sent to storage or a power-cycle. Tower systems, in theory, can achieve concentration ratios as high as 1500, have operating temperatures up to 1500 °C or more (Kodama and Gokon, 2007), and are used in plant sizes up to 500 MW (González-Aguillar et al., 2007). The stationary receiver and high operating temperatures make central tower systems ideal for long-term development for both large-scale power and fuel production facilities. Further, central tower systems are expected to have the lowest levelized cost for electricity of the three CSP technologies long- term.

1.2 Common Receiver Designs

For a central tower CSP plant, the receiver absorbs the concentrated solar energy and transfers it directly to a heat-transfer fluid. Receiver technology has been investigated at a variety of temperatures for many different power cycles and applications, hence many different receiver architectures have been proposed. Selecting the proper receiver architecture requires careful consideration of the application and desired working fluid. The various receiver architectures can be classified into three categories based on how radiation is absorbed and transferred to the working fluid: tube absorption receivers, volumetric receivers, and particle receivers.

Tube absorption receivers feature dark tubes that absorb solar energy and transfer that heat via convection to a working fluid inside. Due to their simplicity, tube absorption receivers are used in currently deployed commercial plants which operate ~500 °C. However, tube absorption receivers are impractical for higher-temperature designs which have larger thermal stresses and require expensive Ni-alloy materials (Amsbeck et al., 2008). Tube absorption receivers are able to use materials such as molten salts directly as their working fluid, allowing for simple integrated storage (Lata et al, 2008).

Volumetric receivers use dark, porous supports into which radiation penetrates and is absorbed. The most common working fluid for a volumetric receiver is air, which is pressurized in most configurations and thus requires a window (Ávila-Marín, 2011). Volumetric receivers can operate at temperatures over 1000 °C, and developers have demonstrated large concrete blocks as a means of short-term sensible storage (Medrano et al., 2010). However, volumetric receivers face the challenge of either maintaining a window under high temperatures and pressures, or overcoming the poor conductivity of

air at atmospheric pressure. Further, volumetric receivers generally use rigid ceramic supports, which can face thermal stress issues in long-term operation.

Particle receivers use dark particles to directly absorb sunlight before being sent to storage. Due to its simple design and open structure, particle receivers are appropriate for operating temperatures above 1000 °C without facing significant thermal stress constraints. Further, many materials can be made conveniently into particles, which may then be used for solid-state chemistry (Tan and Chen, 2010). Since these particles are able to maintain continuous- flow operation, particle receivers can obtain high throughput and greater efficiencies. The combination of high temperatures, integrated storage, and flexibility make particle receivers an attractive technology for further development.

1.3 Challenges in Central Receiver Designs

Due to very high solar fluxes (concentration ratios over 1000, i.e. 1 MW/m^2) and temperatures, solar thermal central receiver designs face a variety of challenges which require careful consideration to overcome. The ability to make on-demand energy through integrated storage allows CSP plants to fill a need that other intermittent renewable energy sources (such as wind and photovoltaics) cannot. As such, it is critical that receiver designs be coupled closely with efficient storage technology with adequate energy densities to keep operating costs low. The receiver working fluid must integrate with the storage technology, preferably by using few, cost-effective heat exchangers in the design. The receiver must operate with reliable outlet temperatures for down-stream processes; this is complicated by variability in solar insolation during the day and in response to transients such as passing clouds. With inherent variability in the high

operating temperatures and solar fluxes, thermal stress issues can arise and compromise material durability for long-term operation. In addition, achieving the maximum efficiency within the receiver is critical for minimizing costs. Higher temperatures can enhance down-stream cycle efficiencies or throughput, but can also drive increases in radiation losses from receivers (Medrano et al., 2010). This presents interesting system-level tradeoffs.

In this study, the issues related with the receiver are investigated with the greatest detail. Particle receivers were chosen because they exhibit great potential to achieve low-cost storage that can be integrated into a variety of down-stream processes with relative ease. By using particles as the "working-fluid" and storage medium, the need and expense for additional heat-transfer devices are eliminated. By using high heat-capacity particles and/or reactive particles, high storage densities can be achieved that exhibit sufficient storage for long periods. Directly irradiated particle receivers also use the particles for radiation collection, so they can achieve consistent outlet conditions during a wide-range on solar inlet conditions through simple operational adjustments. This can potentially decrease startup and shutdown time and improve response times to transient conditions. Using a simple, open design, the solid-particle receiver is able to avoid many of the thermal stress and survival issues that other architectures face. This study hopes to provide effective design tools and knowledge necessary for proper integration into a down-stream process. The performance of particle receivers is explored under a wide variety of operation conditions. Integration of various reactant particles is investigated in order to evaluate their potential to improve efficiencies, storage capability, and even enable fuel production.

1.4 Concentrated Solar-Driven Fuel Production and Storage

This study investigates the impacts of incorporating reacting particles into a falling particle receiver to promote either fuel production or high- energy density storage. Due to the high temperatures and thermal stability, particle receivers are attractive for many of the proposed high-temperature cycles for production of hydrogen or carbon monoxide. Most of these cycles use an oxide material that undergoes an endothermic reduction process at high-temperatures (> 1200 K) to expel oxygen while being heated with solar energy. In a second, non-solar dependent step, the reduced material is exothermically re-oxidized at a lower temperature (<1200 K) with either steam or carbon dioxide to produce hydrogen or carbon monoxide, respectively.

$$MO_x + \text{heat} \rightarrow MO_{x-1} + 0.5 \cdot O_2 \qquad \text{[R. 1-1]}$$

$$MO_{x-1} + H_2O \rightarrow MO_x + H_2 + \text{heat} \qquad \text{[R. 1-2]}$$

$$MO_{x-1} + CO_2 \rightarrow MO_x + CO + \text{heat} \qquad \text{[R. 1-3]}$$

The process illustrated in R. 1-1 is driven thermodynamically by shifts in temperature and gaseous O_2 partial pressure. The temperature dependence can be readily seen in Eq. 1-1, where the reaction will proceed in the forward direction as long as $\Delta\mu_{rxn} < 0$. As Δh_{rxn} and Δs_{rxn} are approximately constant with temperature and positive for this reaction, driving the ceria species to higher temperatures promotes greater reduction.

$$\Delta\mu_{rxn} = \Delta h_{rxn} - T\Delta s_{rxn} \qquad \text{[Eq. 1-1]}$$

Many different materials and fuel-production cycles have been investigated for their potential to create fuel using solar thermal energy as an input. Many studies have sought to characterize thermochemical cycles in order to identify attractive candidates for further development (Perret et al., 2005; Kodama and Gokon, 2007; Roeb et al., 2012; Charvin et al., 2008; Steinfeld, 2005; Ghandehariun et al., 2010; Chueh and Haile, 2010; Lapp et al., 2012). Perret et al. (2005) evaluated over 200 thermochemical cycles, based on metrics such as number of steps, operating temperatures, physical state of reaction products, thermodynamic driving force, and projected efficiency. Some of the most promising cycles have been reviewed more thoroughly by Kodoma and Gokon (2007) and Roeb et al. (2012). The water and CO_2-splitting cycles most often developed are the volatile metal-oxide cycles (including Zn/ZnO, Sn/SnO, and Cd/CdO), nonvolatile metal oxide cycles (ferrites, ceria, and perovskites), and multi-step cycles with maximum operating temperatures below 1200 K (Sulfur and Cu/Cl) (Perret et al., 2005). Other authors have investigated other chemical processes, such as ammonia splitting (Lovegrove et al., 2004), high-temperature metal-hydrides (Felderhoff and Bogdanović, 2009), and $CaCO_3$ splitting with production of lime (Meier et al., 2004).

One of the more promising cycles based on the ceria redox , uses CeO_2 partial reduction to $CeO_{2-\delta}$, which can be readily reoxidize with H_2O or CO_2 to produce H_2 and CO for fuel production. $CeO_{2-\delta}$ maintains its cubic fluorite structure to relatively high values of δ (Zinkevich et al., 2006) unlike many other materials that undergo significant structural and phase transformations during reduction. This gives ceria long-term

stability. Further, with high oxide-ion conductivity at elevated temperatures (Giordano et al., 2000), ceria can sustain relatively high reduction and reoxidation rates with relatively large particle sizes. These properties make it an attractive material for solar fuel-production processes.

One drawback of undoped ceria is the very high temperatures required to drive large reductions. In order to get a reduction of only $\delta = 0.01$ at an oxygen pressure of 10^{-5} atm, a temperature of 1573 K is required (Mogensen et al., 2000). Many different researchers have examined doping strategies in order to reduce the temperature needed for reduction (Gibbons et al., 2014; Chueh and Haile, 2010; Le Gal et al., 2011; Scheffe et al., 2012; Meng et al, 2011; Yang et al, 2008; Mutthukkumaran et al, 2007). Most of these doping strategies seek to replace some of the ceria in CeO_2 with alternative chemicals such as Zr, Hf, Ca, Sr, Gd, Y, and Cr, among others (Scheffe et al. 2012). However, these approaches have been faced with difficulties. Many of the most popular dopants are able to successfully decrease the energy required to reduce the doped species, but also reduce the low-temperature kinetics of the slower reoxidation process (Scheffe et al., 2012). Gibbons et al. (2014) attempted to overcome this kinetic limitation, by exploring structural approaches to obtaining a very high surface area. While met with some success, such approaches are often hampered by sintering during the high-temperature reduction step.

Beyond solar applications, ceria (often in doped forms) is a useful material in catalytic converters and solid-oxide fuel cells; there is a wealth of physical and electrochemical data available, much of which has been compiled by Mogensen et al.

(2000). As such, ceria is an excellent trial material to use in numerical models so that physically meaningful results can be reasonably obtained.

There are a variety of reactors that have been developed to handle the high-temperature thermochemical processes in a Central Receiver System (CRS). Roeb et al. (2012) review many of the reactors that have been developed for water-splitting cycles, highlighting key operational and material challenges, and loosely separating them into two categories: reactors based on reactive particle streams and reactors based on fixed solid supports. Particle stream reactors include: a multi-tube, aerosol-flow solar cavity receiver (Perret et al., 2005; Martinek, 2012; Dersch et al, 2006), a fluidized-bed reactor based on beam-down optics (Kodama and Gokon, 2007), and a screw-conveyor reactor based on beam-down optics (Siegel et al., 2010). In general, particle reactors have the advantage of allowing continuous operation and lower thermal stresses, but face greater issues related to intra-particle sintering and loss of activity. Solid-support reactors include: stationary monolithic supports coated in reactive material (Kodama and Gokon, 2007; Roeb et al., 2012; Dersch et al., 2006; Agrafiotis et al., 2005), stationary foams heated directly (Kodama and Gokon, 2007; Roeb et al., 2012; Villafán-Vidales et al., 2011) stationary foams heated indirectly (Singh et al., 2011), rotary cylinder coated in reactive ceramics (Kodama and Gokon, 2007), and a counter-rotating ring structure (Miller et al., 2008). Ceramic-supported reactors can limit sintering in two directions, but face challenges with thermal stresses and shocks, batch operation or usage of rotary machinery at very high temperatures, difficulty replacing products in operation, and heat islands that can destroy porous materials (Roeb et al., 2012; Martinek, 2012). Other water-splitting reactors have been proposed that do not fit into these categories, including

a liquid Cadmium receiver concept based on beam-down optics (Perret et al., 2008) and a perovskite membrane reactor that operates similar to an electrolyzer using differences in oxygen chemical potential to drive reduction (Roeb et al., 2012).

Beyond water-splitting, other reactions have been investigated. Dahl et al. (2002) describe a graphite tube receiver where natural gas is dissociated into H_2 and C(s), forming particles in the 20-40 nm range. Hirsch et al. (2004) describe natural gas dissociation in a vortex-flow, direct particle absorption receiver using μm-sized particles and a quartz window, later improved by radially seeding particles in a cloud (Maag et al., 2009). Meier et al. (2004) describes a horizontal rotary kiln reactor used for lime production.

Solar reactor design requires a synergistic fit between reaction scheme and reactor. While inert receivers must be designed only to maximize the absorbed solar energy and achieve the desired temperature, solar reactors must also maintain optimal species transport through the reacting zone. Because these reactions, especially the oxide reduction step (R. 1-1), are sensitive to O_2 concentrations in the gas phase, it is important to control the environment within the receiver reactor. Any direct-absorption reactor must make use of a windowed aperture in order to maintain an enclosure. Challenges presented in other windowed receiver designs, especially retaining mechanical stability under high pressures, are less pronounced for a solid-particle receiver operating at atmospheric pressure.

Beyond fuel production, a solid-particle reactor can be used to achieve high energy-density storage through thermochemical energy conversion. This is achieved by processes that use reversible endothermic reactions like R. 1-1 that are driven by the solar

input. The thermochemical energy can be released in the reverse reaction to deliver thermal energy to a heat-driven power cycle. While the energy stored is of lower quality (in terms of heating value and density) than in fuel production, the operating temperature range can be much lower with reactions active below even 1200 K. Perovskites are one class of materials investigated for lower-temperature processes (Choi et al, 2011). Perovskites display a similar degree of phase stability as ceria but reduce at much lower temperatures (Zhang et al., 1989). Further, perovskites have the advantage of being very optically-dark in the visible spectrum, making them excellent absorbers for a direct-absorption receiver.

Because of the high capital cost involved in building a concentrator field and receiver structure, even at the prototype scale, it is critical to investigate the design performance of the receiver under a wide range of operating parameters using numerical tools. Integrating reactive species into the receiver introduces many more variables that must be optimized and explored, and requires complex modeling tools that can efficiently evaluate the performance response to a wide range of input conditions.

1.5 Central Receiver Modeling

Modeling solar thermal central receivers presents many challenges, primarily in handling the radiation fluxes and associated heat transfer. Solutions are usually specific to the specific receiver architecture and application being studied. Some relatively simple architectures, such as external tube-based receivers, can be modeled with simple phenomenological models without significant difficulty (Li et al, 2010). However, when the receiver geometry becomes more complicated, it is often necessary to accurately

capture the incoming solar radiation and radiation exchange between many surfaces. There a variety of approaches to achieving these goals that will be reviewed later, and all of them have their strengths and weaknesses. The choice of the proper radiation exchange model depends on the specific application and geometry, and must be consistent with the rest of the physical models employed. Gas flow within a solar receiver can be very important, and can be captured with either simplified, semi-empirical models or full computational fluid dynamics (CFD) simulations depending on the goals of the study. When reactions are incorporated into a numerical model, species balance, thermodynamics, and kinetics must be included, due to coupling with the heat-transfer and fluid-flow models.

The variety of models employed for solar receivers range from first-order design models to detailed CFD models. Many simplified models (Dersch et al., 2006; Maag et al., 2009; Palumbo et al., 2004) use 2D or 3D radiation models coupled to simplified 1-D reaction models, with variations depending on the reactor operational physics. More detailed CFD models are usually developed as the next-step in reactor design and rely on fewer simplifying assumptions at greater computational cost and design difficulty. Abadanes et al. (2011) describe a 2D cylindrical CFD model for ZnO dissociation in a particle-cloud reactor that uses Lagrangian-frame, shrinking-shell, constant-T particles, mass-action heterogeneous-reaction kinetics with Arrhenius-form reaction rate, and the discrete-ordinates method for radiation heat-exchange. Villafán-Vidales et al. (2011) present a CFD simulation on a volumetric-foam ferrite receiver that utilizes the P1 radiation approximation and mass-action kinetics based on an Arrhenius parameter for the reaction rates. Ozalp and JayaKrishna (2010) describe a CFD simulation on the

vortex-flow methane reactor seeded with carbon particles. This model makes use of Mie theory and an equivalent particle diameter to calculate particle absorption properties for use in the discrete-ordinates model for radiation heat transfer, mass action kinetics, and the realizable k-ε turbulence model. Martinek (2012) models an aerosol-seeded acetylene gasification reactor using the finite-volume radiation heat transfer, the two-fluid (Euler-Euler) particle treatment with constant-diameter particles, a simplified global reaction mechanism, and particle radiation in the Rayleigh limit.

1.6 Falling Particle Receivers

The operational principles behind falling-particle receivers are straight-forward. Cold particles are injected at the top of the receiver and fall straight down through the receiver. Incoming solar fluxes (from the solar field) directly irradiate the falling particles, which absorb much of the radiation to achieve a higher temperature by the exit of the receiver. The particles speed up along the fall, which decreases the particle number density as they fall through the directly irradiated zone. For reactive particles, heating along the fall can result in species exchange between the particles and the gas phase. The reaction thermodynamics, kinetics, and gas species concentrations determine how the absorbed solar energy is split between sensible heating and reaction.

In particle receivers, there is complex coupling between the particle dynamics, gas-flow, incoming solar energy, and radiation heat-exchange with the walls. Since particles are not blackbodies, some of the incoming radiation is reflected onto the walls or out of the aperture. Depending on the chosen flow parameters, the particle curtain may permit a

large portion of the solar beam to illuminate the rear wall, causing a strong hot-spot that can damage the material.

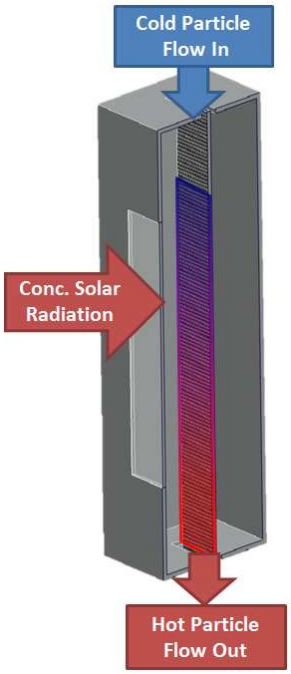

Figure 1-1 – Schematic of falling particle receiver, highlighting the heating of particles under direct solar irradiation.

Falling particle receivers using inert particles have been studied by several groups. Meier (1999) performed 2D CFD simulations of a falling particle receiver to study the particle-gas interaction and evaluate the stability of the flow. Chen et al. (2007) extended these results to 3D in order to aid in the design of a prototype receiver being designed at Sandia National Labs. Siegel et al. (2010) further improved the model of Chen et al. to include an improved treatment of the radiation profile in order to provide additional insight into the experimental results from the prototype receiver. More recently, experiments by Khalsa et al. (2011) have been performed to aid in design and evaluation of the prototype design.

1.7 Objectives and Overview of Current Study

The current study extends the modeling effort and understanding behind the operation of solid particle receivers. Chapter 2 presents the development of a simplified model of inert particle receivers, similar to those already tested. While other studies, (Chen et al., 2007; Siegel et al., 2010; Khalsa et al., 2011) have shown good predictive capability with in-depth CFD models, the simplified model developed represents a valuable design tool to evaluate the impacts of varying physical parameters. This chapter explores the impacts that varying particle sizes, flow rates, temperatures, radiation absorption parameters, and solar flux has on receiver performance in terms of mean outlet temperature, curtain temperature gradient, and receiver efficiency. The specific dynamics of heat-flow within the curtain are investigated in terms of operating temperatures, curtain opacity, and wall interactions. Further, this model will also be applied to design-studies on full-scale commercial receivers, which can be computationally prohibitive for larger codes.

Chapter 3 presents an extension of the inert-particle receiver model to include capability for simulating reactive particle flows. A detailed thermochemical model for ceria captures bulk and surface thermodynamics as well as kinetics based off prior experimental work (Mogensen et al. 2000; Zinkevich et al. 2006; Decaluwe et al., 2010). The thermochemical model integrates with the inert particle receiver to evaluate the impacts that operating parameters have on total performance and in driving reactions. The evolution of the particle curtain is given particular attention to better understand the

key physics affecting performance. The integrated species model is used to evaluate an alternative species composition in the context of full-scale operation to demonstrate the potential that reactive particles have to improve overall solar plant operation.

One of the final objectives of this study is to develop and demonstrate a reactive particle model to be integrated into higher-fidelity CFD simulations with falling-particle geometries. Chapter 4 presents the development of a custom particle model user-defined function that can capture the thermochemical ceria model created in Chapter 3. The results from this simulation are useful in not only validating and improving the simplified design model, but also allowing exploration of key physics related to the gas-flow that cannot be captured in the simplified model. This effort is a significant step forward in the design capability for solar thermal solid particle reactors.

Chapter 2: Modeling Inert Particle Receivers

Design of a solar thermal receiver is a primary challenge for CSP plants due to their complexity and cost. Efficient receiver modeling tools are needed to evaluate the performance and operability of proposed designs before full-scale implementation. For solid-particle receiver designs, complex multi-physics models are needed that include particle-gas flow dynamics, multi-band radiation heat-transfer between the particles and receiver structure, and other modes of heat-transfer for the receiver structure and particles.

In this chapter, prior modeling approaches for the critical physics in solid particle receivers are reviewed. Then, the specific receiver layout used in this study is presented, with the governing equations and specific modeling approach used for that receiver design. Results for a prototype-scale particle receiver reveal design tradeoffs related to receiver operating conditions and design parameters including particle size, mass-flow rate, inlet temperature, and solar concentration. Performance analysis of a larger full-scale particle receiver with grey-body particles provides new insight into the efficacy of selective particle emissivity in improving particle receiver efficiencies. These results and lessons from inert particles play an important role in understanding the modeling efforts of reactive particles presented in later chapters.

2.1 Previous Particle Receiver Modeling efforts

Particle receivers incorporate many physical phenomena, including radiation, conduction, convection, particle flow dynamics, and multi-phase particle-gas flow. Due

to the highly concentrated solar input (around 1 MW m^{-2}) and associated high temperatures, radiation dominates heat transfer within the receiver and heating of particle flows depend on the complex interchange between radiation transmission and reflection through the depth of the particle curtain. The particle heating and motion induce gas flows within the receiver, which can impact the particle flow through drag on and dispersion of the particles. Effective modeling of these complex and coupled physical phenomena require detailed but computationally efficient approaches that capture these effects in a consistent manner.

2.1.1 Receiver Models

Many efforts to accurately model inert falling-particle receivers have been reported in recent years with varying success in capturing the most important physical phenomenon that dominate the performance of the receiver. Early particle receiver models using CFD software and a Monte Carlo radiation model by Meier (1999) were limited to a 2D cavity geometry due to computational limitations. Chen et al. (2007) extended the computational modeling to 3D and implemented a Monte Carlo solar source with a discrete ordinates radiation model for reflected and thermal radiation within the receiver. Chen's model lacked the ability for the solar source to directly interact with the particles, and thus particles were indirectly heated by the walls. More recent work by Siegel et al. (2010) explored direct interaction with the particles by implementing a "solar patch" from a small, obstructed area in the solar aperture, but this approach lost some of the incoming solar source resolution. Khalsa et al. (2011) extended this model to fully resolve the solar source while maintaining particle interaction by implementing a "solar

patch calculator" that breaks the inlet aperture into many smaller pieces and applying the proper direction and intensity in each patch.

Röger et al. (2011) created a semi-empirical receiver model that eschews calculation of the gas flow-field and solves the radiation field using Hottel's zonal method. This method is much less computationally demanding than CFD models and has been chosen as a basis for the work presented in this chapter. The work presented here extends the model of Röger et al. by improving upon the radiative transmission through the particle curtain and including a semi-empirical gas treatment that captures entrainment and curtain spreading.

2.1.2 Multi-band Radiation Models

Because the importance and high computational cost of resolving the radiation field within even a relatively simple geometry, the details of receiver modeling depend heavily on the radiation model employed. The earliest works used a Monte Carlo (MC) ray-tracing approach to resolve the solar field (Meier et al., 1999 and Chen et al., 2007). The MC method works by launching a very large number of ray packets from each release location. These ray packets proceed through many steps, and at each step either transmit, absorb, or scatter with a probability depending on the radiation properties of the interacting medium. Because the MC approach is statistical in nature, many rays (on the order or 10^7-10^8) are required to achieve convergence. While the MC method can approach exact solutions with enough rays, its computation expense makes it prohibitive for implementation in many situations.

Radiation can also be solved using the discrete ordinates (DO) method (Chen et al., 2007; Siegel et al., 2010; and Khalsa et al., 2011). The DO method makes use of the radiative transfer equation (RTE), shown in Eq. 2-1, as a field equation over a set number of angular division is the polar and azimuthal directions.

$$\frac{dI_\lambda(\vec{r},\vec{s})}{ds} = -(a_\lambda + \sigma_s)I_\lambda(\vec{r},\vec{s}) + a_\lambda n^2 I_{b\lambda}(\vec{r}) + \frac{\sigma_s}{4\pi}\int_0^{4\pi} I_\lambda(\vec{r},\vec{s}')\Phi(\vec{s}\cdot\vec{s}')d\Omega' \qquad \text{[Eq. 2-1]}$$

In this equation, $I_\lambda(\vec{r},\vec{s})$ represents the radiation intensity as a function of position ($\vec{r}$) and direction ($\vec{s}$) in any wavelength-bin (λ), a_λ is the spectral absorption coefficient, σ_s is the scattering coefficient, *n* is the refractive index, $I_{b\lambda}$ is the equivalent blackbody emission in the λ-band, Φ is the scattering phase-function, and Ω' is the solid-angle. In simple terms, this equation states that the change in radiation intensity at a point and direction is the sum of the blackbody emission and in-scattered radiation from other directions minus the absorbed and scattered radiation to other directions.

The discrete-ordinates method has been successfully integrated into CFD simulations by solving the radiation transfer on the same spatial grid used for fluid calculations. Despite its strengths, the DO method has drawbacks for many applications due to the directional nature of actual radiation. The DO method is sensitive to grid sizing and angular discretization. For problems with strong specular components, the DO method can introduce errors in the form of numerical diffusion. While less computationally expensive than the MC method, the DO still requires substantial computational memory and calculation times, which can be limiting in many cases.

A simpler method of radiation calculation, applied here in this chapter, is Hottel's zonal method, described in Röger et al. (2011) and Röger et al. (2006), which extends surface-to-surface radiation models to include interacting semi-transparent media. The zonal method calculates view factors between the surfaces of all walls and cells bounding the semi-transparent medium. Radiation is absorbed within the cells containing semi-transparent media, is reflected at the cell surface, and/or is transmitted to the opposite cell face. This method obtains a simultaneous solution for the radiosity from each cell-face. In this implementation, errors are introduced by assuming that reflections are diffuse and transmissions only occurs directly to the opposite cell face. The zonal method has significant computational advantages over DO and MC methods for relatively coarse grids, but becomes less computationally effective for finer grids. A large portion of the computational expense lies in calculation of the cell-face view factors, which is very expensive on finer grids. However, for fixed grids, these calculations are only done once and can be stored between runs to save computational time. The numerical implementation of Hottel's zonal method is discussed in detail below.

2.1.3 Particle-gas Entrainment Models

The flow of gas in highly loaded inert-particle receivers is of secondary importance, but the gas-particle drag interaction impact particle velocities and thus, residence times in the receiver volume. It is important to at least estimate the local gas velocity. Gas-particle interactions can be critical for reactive particles, when local gas-species concentrations near the particle are needed to calculate particle reaction rates. CFD models used to simulate particle receivers inherently resolve the gas-phase in the

entire domain, but at a very large computational expense and with significant uncertainty associated with CFD for particle-laden flows (Hruby et al., 1986; Chen et al, 2007). With these models, drag interactions are calculated using a variety of empirical drag-laws developed for spherical and non-spherical particles (ANSYS, 2011).

When CFD is not used to resolve the entire fluid domain, it is still necessary to somehow obtain information about the local fluid flow around the particles. The model used by Röger et al. (2011) simply uses a set ratio for the local gas velocity to particle velocity within drag calculations. While this approach can be effective, it faces obvious limitations when the particle flow rate or size varies significantly from the fitting location. This approach also tends to under-predict the gas and particle velocities, leading to a terminal particle velocity which is generally not reached by a stream of particles continuously falling.

In order to improve on the set-ratio model used previously, Liu (2003) integrated a particle-gas flow model. This semi-empirical model is based on tests performed by Liu on free-falling dense particle streams, where gas flow rates at different diameters around the particle stream were measured using orifice plates. This study revealed that the gas flow tends to follow a Gaussian profile in the vicinity of the particles. Using this information, Liu was able to describe how gas became entrained in the flow and how the downward velocity developed. The falling particles entrain gas into the downward curtain flow, which eventually exits the receiver along with the particles. The additional gas needed to maintain continuity must be supplied through openings elsewhere in the receiver. This model captures the effects of changing mass flow-rate and particle size and

works for flows over a much larger range of parameters compared to the constant velocity-ratio model.

2.2 Model Geometry

Inert particle receiver studies have been carried out on receivers of two different scales: for a prototype 3 MW_t solar-input and for a full-size 220 MW_t solar-input. Both receivers feature particles falling inside a rectangular cavity with a single aperture to allow solar irradiation as shown in Figure 2-1. The geometries are based on the design found in Siegel et al. (2010). Alternative particle receiver designs have been proposed with tube-based geometries for improved flow control (Martinek et al. 2012, Flamant et al. 2013), but the falling-curtain design provides a simple configuration in which to explore fundamental trade-offs for issues related to direct particle irradiation, particle mass flow rate, particle physical properties, and operating solar concentration.

The prototype-scale falling particle receiver features slight modifications from the receiver in Siegel et al. (2010). These features are implemented to improve performance. The prototype receiver dimensions, documented in the table in Figure 2-1, differ from those of Siegel et al. (2010) by incorporating a smaller entrance region before the directly irradiated zone and a smaller aperture width. A shorter entrance region (1 m) improves particle radiation absorption by exposing the curtain near-entrance region – where particle volume fraction is higher – to the concentrated solar influx. Furthermore, the particles are slowest near their injection point, and reducing the entrance length increases particle residence time in the directly irradiated zone. A smaller window aperture improves receiver performance by decreasing re-radiation losses. Optimal cavity opening

design requires coupled field-receiver modeling, which depends on heliostat field layout and optical performance and is beyond the scope of this study.

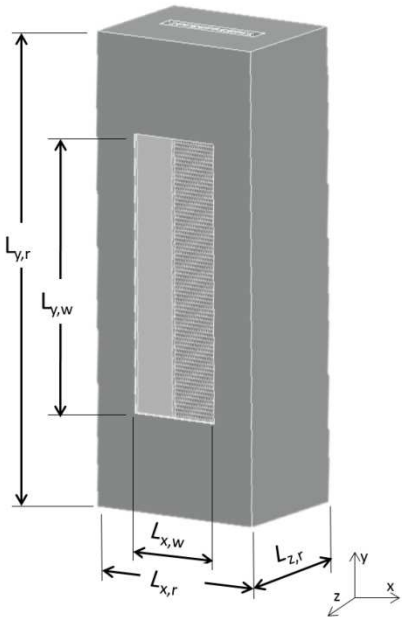

Dimension (m)	Prototype Dimensions	Full-Scale Dimensions
Receiver ($L_{x,r}$, $L_{y,r}$, $L_{z,r}$)	(1.85, 5.0, 1.5)	(12.0, 21.0, 15.0)
Aperture ($L_{x,a}$, $L_{y,a}$, $L_{z,a}$)	(1.0, 3.0, -)	(11.0, 20.0,-)
Curtain ($L_{x,c}$, $L_{y,c}$, $L_{z,c}$)	(1.0, 5.0, 0.01+0.0087·y)	(11.0, 21.0, 0.04+0.0087·y)

Figure 2-1 - Falling particle receiver geometry and sizes for both prototype and full-scale design.

The incident solar flux on the receiver is modeled as a uniform profile pointing horizontally (in the z-direction) to decouple field design impacts and because prior studies have shown that matching total incident flux is sufficient for reliable results (Siegel et al., 2010). Even with these minor modifications to the design from Siegel et al., the receiver configuration in this study is similar enough to compare model results with inert-particles at similar operating conditions to experiments in that previous study.

The full-scale receiver uses dimensions specified by Dr. Clifford Ho (2003) from Sandia National Labs in order to evaluate the expected performance under varying operating conditions for a proposed 100 MWe receiver. This receiver size was used to

study a near-full scale receiver and the effects of varying particle emissivities on receiver performance. In particular particles with selectively high emissivity in the visible range are relatively low emissivity in the mid and far infrared range were studied to see if reducing re-radiation losses could significantly improve particle receiver efficiencies.

2.3 Model Formulation

2.3.1 Solid Phase Dynamics

The falling-particle receiver simulations are performed with a Lagrangian particle model coupled to a 3D heat-transfer model of the radiation transport in the receiver cavity. The Lagrangian model calculates the evolution of the average particle velocity in the y-direction, $\bar{u}_{\mathrm{y,p}}$, and thereby average residence time of particles through momentum balance. The heat transfer to the particles is calculated by coupling the Lagrangian particle model to the 3D radiation heat transfer model, including convection between the particles, gas, and receiver walls.

The average particle velocity $\bar{u}_{\mathrm{y,p}}$ is derived from a *y*-direction force-balance on a single particle, which includes the particle drag force due to the difference between $\bar{u}_{\mathrm{y,p}}$ and the characteristic surrounding gas-phase velocity $\bar{u}_{\mathrm{y,g}}$ and the gravity-driven body force.

$$\frac{d\bar{u}_{\mathrm{y,p}}}{dt} = \frac{3}{4}\frac{\rho_{\mathrm{g}}}{\rho_{\mathrm{p}}} C_{\mathrm{D}} C_{\mathrm{S}} \frac{\left(\bar{u}_{\mathrm{y,p}} - \bar{u}_{\mathrm{y,g}}\right)^2}{d_{\mathrm{p}}} - \frac{\left(\rho_{\mathrm{p}} - \rho_{\mathrm{g}}\right)}{\rho_{\mathrm{p}}} g \qquad \text{[Eq. 2-2]}$$

The stream-coefficient, C_S, adjusts the single-particle drag-coefficient, C_D, to account for the impact of other particles in the curtain according to the model developed by Syamlal and O'Brien (1989) as summarized in Kim et al. (2009). The particle mass density, ρ_p, as used in Eq. 2-2, is a constant for inert particles, as thermal expansion is small for the proposed material.

Integration of the Lagrangian particle momentum equation is converted from a temporal to a spatial (*y*-direction) discretization by recognizing that $\bar{u}_{y,p}$ is the rate of change of particle position.

$$dy = \bar{u}_{y,p} dt \qquad \text{[Eq. 2-3]}$$

Eq. 2-2 is integrated along the length of fall, *y*, with spatial steps small enough that the ode solver held a relative residual tolerance of less than 10^{-6} for each time step. Because the particle temperature (T_p) and gas-cell properties (T_g, $\bar{u}_{y,g}$) are solved on a larger Eulerian mesh to facilitate 3D radiation transport models, their values are linearly interpolated between their cell-center values to provide a basis for calculating the heat transfer between the particles and the surrounding gas-phase flow. Interpolation of the gas-phase solution variables from the Eulerian solver, described below, enables adequate resolution for modeling momentum transfer in the Lagrangian particle model with the coarser Eulerian grid.

2.3.2 Gas Phase Dynamics

The transfer of momentum and heat between the particles and the surrounding gas phase flow provides a basis for modeling gas-phase temperatures (T_g) and characteristic *y*-direction velocities ($\bar{u}_{y,g}$). Because the receiver simulations incorporate computationally expensive 3D radiation transport modeling, the full-enclosure gas-phase fluid dynamics are simplified using the semi-phenomenological model developed by Liu (2003) to capture the gas flow and composition near the falling-particle curtain. Empirical correlations estimate the amount of far-field gas entrained by the falling particles. Combining the entrainment models with the particle-gas momentum and heat exchange models provides a basis for predicting the evolution of T_g surrounding the particles.

The gas-particle entrainment model developed by Liu (2003) for flows of dense particles reduces computational cost for the gas-phase analysis and allows for efficient exploration of design parameter space by removing the demands and uncertainty of solving the full Navier-Stokes equation in a two-phase flow CFD simulation. While this approach is appropriate in this initial study, it does leave questions regarding how a full CFD model might predict gas recirculation within the receiver.

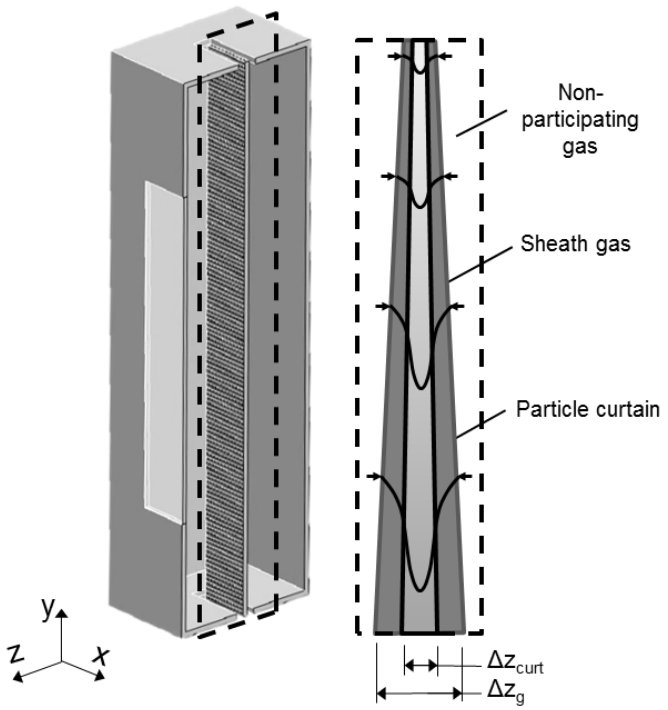

Figure 2-2 – (a) Cross-sectional view inside of the receiver, highlighting the curtain zone, and (b) detailed schematic of curtain flow, showing evolution of gas velocities in the dense curtain, Δz_{curt}, and the sheath gas, Δz_g.

Figure 2-2 illustrates the profile of the downward gas flow entrained in the direct vicinity of the particles. The profile includes a "sheath" of gas flow initiated at the inlet of the reactor and driven by the particle momentum. According to the experiments and model for free-falling, dense particle flows of Liu (2003), the *y*-direction gas velocities $u_{y,g}$ around the curtain can be approximated with a Gaussian velocity profile characterized by a representative velocity, $\overline{u}_{y,g}$ and thickness, Δz_g, which is different from the thickness of the dense-particle core, Δz_c.

$$u_{\mathrm{y,g}} = \bar{u}_{\mathrm{y,g}} \sqrt{2} \exp\left(-\frac{z^2}{\Delta z_{\mathrm{g}}{}^2} \right) \qquad \text{[Eq. 2-4]}$$

Using Eq. 2-4 reduces the complexity of the gas-flow field to calculating $\bar{u}_{\mathrm{y,g}}$ and Δz_{g} with a combination of mass and momentum balance equations in appropriately simplified forms. The mass and vertical-momentum conservation equations can be solved simultaneously to find the *y*-variation in the gas vertical mass and momentum flow rates, $\dot{m}_{y,\mathrm{g}}$ and $\dot{m}_{y,\mathrm{g}} \bar{u}_{y,g}$, respectively. The characteristic gas velocity, $\bar{u}_{\mathrm{y,g}}$, is then found by dividing the momentum by the mass, while the characteristic thickness of the vertical gas flow field, Δz_{g}, is found by integrating Eq. 2-4 to get Eq. 2-5.

$$\dot{m}_{y,g} = \sqrt{\frac{\pi}{2}} \rho \bar{u}_{y,g} \Delta x \Delta z_g \qquad \text{[Eq. 2-5]}$$

The gas mass-flow governing equation is derived from the continuity equation for a semi-infinite plane (due to the large difference is aspect-ratio of the curtain), neglecting *x*-direction variations. The gas density ρ_{g} is calculated from the ideal gas law and thus depends on local temperature and composition. The resulting gas mass flow conservation equation can be written as in Eq. 2-6.

$$\frac{\partial \rho_{\mathrm{g}} \bar{u}_{\mathrm{y,g}}}{\partial y} = -\frac{\partial \rho_{\mathrm{g}} \bar{u}_{\mathrm{z,g}}}{\partial z} \qquad \text{[Eq. 2-6]}$$

Integrating Eq. 2-6 with respect to *z*, and multiplying by the *x*-thickness and *y*-length of a cell yields Eq. 2-7, which shows the change in mass-flow in the *y*-direction equals the influx of mass at the edge.

$$\frac{\partial}{\partial y}\int_0^\infty \left(\Delta x \rho \bar{u}_{\mathrm{y,g}}\right) dz \cdot \Delta y = \int_0^\infty \left(-\rho \Delta x \Delta y \frac{\partial u_{\mathrm{z,g}}}{\partial z} \right) dz = -\rho \Delta x \Delta y \bar{u}_{\mathrm{z,g,edge}} \qquad \text{[Eq. 2-7]}$$

Thus, by simplifying the mass derivative on the Eulerian cells, the continuity equation reduces to a simple mass-flow balance, as in Eq. 2-8.

$$\frac{\partial \dot{m}_{y,\mathrm{g}}}{\partial y}\Delta y = \frac{\Delta \dot{m}_{y,\mathrm{g}}}{\Delta y}\Delta y = \Delta \dot{m}_{y,\mathrm{g}} = -\rho \Delta x \Delta y \bar{u}_{\mathrm{z,g,edge}} \qquad \text{[Eq. 2-8]}$$

In Eq. 2-8, $\bar{u}_{\mathrm{z,g,edge}}$ relies on the model by Liu (2003) for calculating how the falling particles impart downward gas-momentum through drag. The imparted downward gas momentum entrains gas from the surroundings at a velocity $\bar{u}_{\mathrm{z,g,edge}}$ proportional to the downward velocity where the proportionality or entrainment constant, α, varies primarily with particle diameter d_{p} (Liu, 2003). Liu did not fit α for d_{p} and flow regimes relevant to this study, but α is fitted here as a function of d_{p} to the detailed entrainment measurements performed by Kim et al. (2009) using particle size and flow profiles directly applicable. This fitting is sensitive to the particle drag model, and the drag model suggested by Kim et al. (2009) provides the best fit. The resulting fit for $u_{\mathrm{z,g,edge}}$ is shown in Eq. 2-9.

$$u_{z,g,edge} = \alpha \bar{u}_{y,g} \text{ where } \alpha = 5.293(0.99574)^{(10^6 d_p)} \quad \text{[Eq. 2-9]}$$

A comparison of the results found in Kim to the fitting here, as shown in Figure 2-3, shows acceptable agreement over the range of particle sizes and mass flow-rates. The minimum R^2 value is 0.982 for the particle diameter fitting and 0.996 for the mass-flow fittings. This model provides a significant improvement to the constant-ratio model for gas to particle velocities shown in Figure 2-4, with a minimum R^2 of 0.899 for the particle diameter fittings and 0.988 for the mass-flow fittings. Not only does the entrainment model fit the velocities better over a wider range, but it also provides important information about the gas mass flow-rate and profile, which is important for reactive particles. Further, it captures well the variation of the gas flow with changing particle loading. The constant-ratio model predicts identical gas behavior regardless of particle flow. This difference is important for evaluating how changing properties such as mass flow rate impacts performance trends.

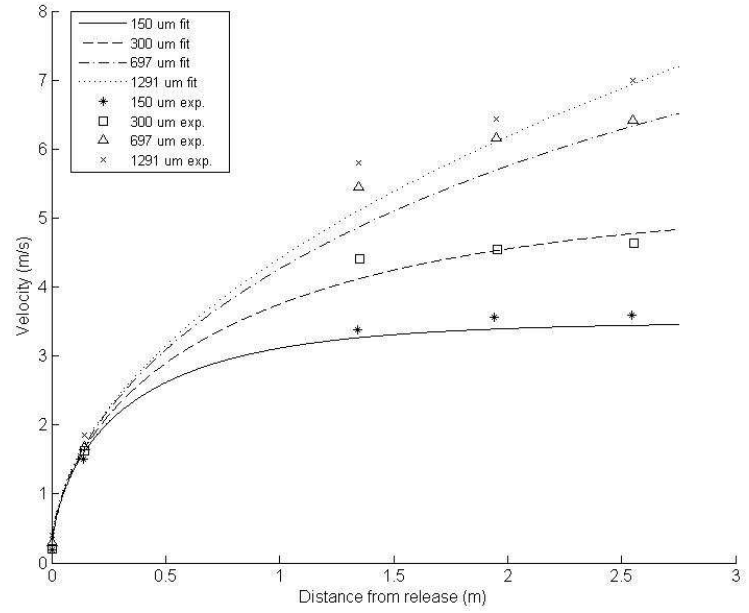

(a)

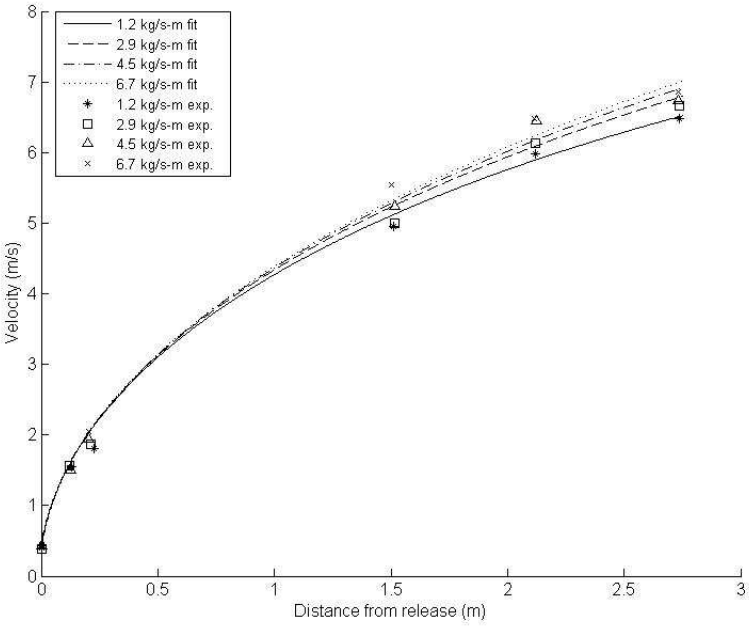

(b)

Figure 2-3 - Particle velocity under isothermal conditions calculated using the Liu model with fit entrainment coefficient (lines) to the experimental data of Kim (symbols): (a) comparison over a range of particle sizes for a particle flow rate of 1.2 kg s^{-1} m^{-1}. (b) comparison over a range of particle flow rates for a particle diameter of 697 μm.

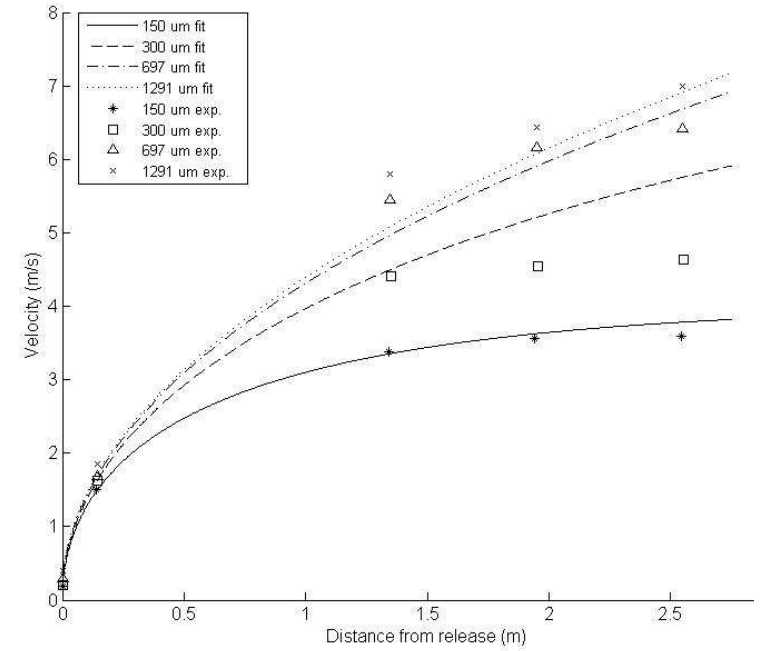

(a)

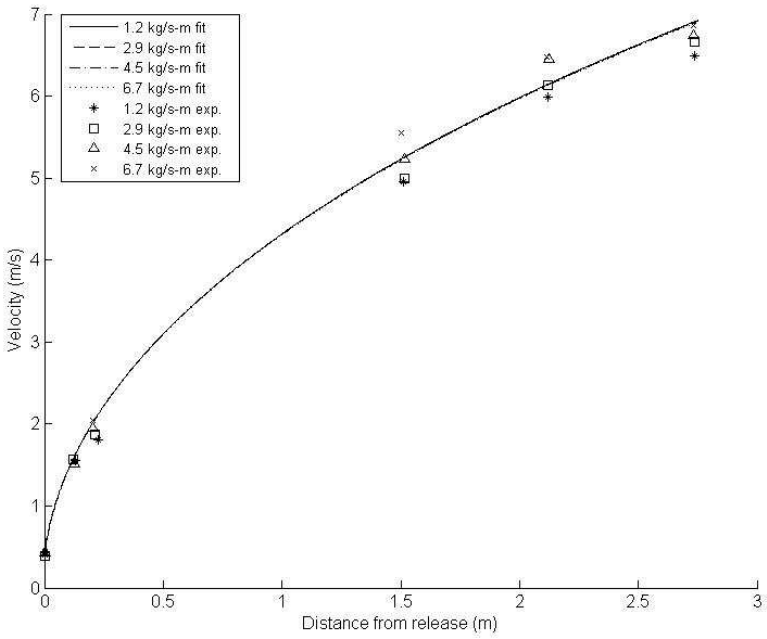

(b)

Figure 2-4 - Particle velocity under isothermal conditions calculated using the constant gas-velocity ratio model fit (lines) to the experimental data of Kim (symbols): (a) comparison over a range of particle sizes for a particle flow rate of 1.2 kg s^{-1} m^{-1}. (b) comparison over a range of particle flow rates for a particle diameter of 697 μm.

The change in gas-momentum is found with a simplified 1D fluid-momentum conservation equation, where the effects of drag within the curtain are assumed to be of much greater magnitude than buoyancy. The drag source-term uses a cell-average particle velocity, which is found by dividing the total particle residence time by the cell fall-distance.

$$\frac{d\left(\dot{m}_{y,g}\bar{u}_{\mathrm{y,g}}\right)}{dy}=\frac{3}{4}\frac{\rho_g\left(\bar{u}_{\mathrm{y,p}}-\bar{u}_{\mathrm{y,g}}\right)^2}{d_{\mathrm{p}}}C_{\mathrm{D}}C_{\mathrm{S}}\left(\frac{\dot{m}_p}{\rho_{\mathrm{p}}\bar{u}_{\mathrm{y,p}}}\right) \qquad \text{[Eq. 2-10]}$$

2.3.3 Heat Transfer Model

The heat-transfer model uses full-cell energy balances to calculate the cell-center particle temperatures, T_{p}, and receiver wall temperatures, T_{w}. To do this, the formulation of Röger et al. (2011) is adopted to capture the dominant radiation heat transfer. Because the energy balance must performed on the Eulerian grid for proper coupling with the radiation solver, linear interpolation must be used within the context of the Lagrangian-phase particle solver. The Eulerian grid temperature calculated from this solver is taken as the cell exit temperature in order to maintain consistency with the particle energy balance.

In the energy balance, the particle temperature-dependence is captured via an enthalpy balance for the constant particle mass flow-rate within a cell, $\dot{m}_p$, in order to capture the changes in particle c_{p} with temperature. The particle convection heat-transfer, $\dot{Q}_{\mathrm{conv}}$, is a source-term that accounts for the convection transfer from the particles to gas-phase, the inter-curtain heat transfer, $\dot{Q}_{\mathrm{curt}}$, accounts for heat exchange between the front and back half of the curtain, the net particle radiation heat-transfer, $\dot{Q}_{\mathrm{rad}}$, accounts for

radiation exchanged within the receiver, and the absorbed solar heat transfer, $\dot{Q}_{\text{sol}}$, is the source-term from the direct solar energy. These terms are captured for the particle-flow in Eq. 2-11.

$$\dot{m}_p\left(h_{\text{p,out}} - h_{\text{p,in}}\right) = \dot{Q}_{\text{conv}} + \dot{Q}_{\text{curt}} + \dot{Q}_{\text{rad}} + \dot{Q}_{\text{sol}} \qquad \text{[Eq. 2-11]}$$

Eq. 2-11 assumes that the particles are isothermal. This assumption is tested by calculating a Biot number, Bi_{rad}, based on the range of equivalent radiative heat transfer coefficients and typical particle conductivities and diameters. Bi_{rad} can be derived by estimating the radiation transfer between a single particle and the solar source, and the conduction heat transfer between the surface and center of the particle.

$$Bi_{rad} = \frac{\left(T_{p,surf} - T_{p,cent}\right)}{\left(T_{sol} - T_{p,surf}\right)} = \frac{\varepsilon_p \sigma r\left(T_{sol}^2 + T_{p,surf}^2\right)\left(T_{sol} + T_{p,surf}\right)}{4k} \qquad \text{[Eq. 2-12]}$$

Calculating Bi_{rad} from Eq. 2-12 gives a sense of the expected temperature difference within the particle compared to the particle and the radiation source temperature. For a radiation load of $\dot{q}''_{sol}$ =1 MW m^{-2}, the effective blackbody source temperature is T_{sol} = 2049.3 K. For T_{p} = 1000 K, ε_{p} = 0.85, d_{p} = 300 μm, and k = 2.0 W m^{-1} K^{-1}, Bi_{rad} = 0.029 << 0.1, which indicates that the temperature drop across the particle is small relative to the "temperature drop" between the solar source and the particles. Conduction heat transfer should be able to keep up with radiation heat transfer and maintain an approximately constant temperature within the particles.

The convection term, shown in Eq. 2-13, is modeled with a Ranz-Marshall correlation to calculate the particle heat-transfer coefficient with the internal gas, as shown in Eq. 2-14.

$$\dot{Q}_{conv} = h_p a_s N_p \left(T_g - T_p\right) \qquad \text{[Eq. 2-13]}$$

where N_p is the number of particles in the given discretized Eulerian cell.

$$Nu = \frac{h_p \cdot d_p}{k_p} = 2 + 0.6\,\mathrm{Re}^{1/2}\,\mathrm{Pr}^{1/3} \qquad \text{[Eq. 2-14]}$$

Since the particle volume fractions are typically below 5% in this study, inter-curtain heat exchange $\dot{Q}_{curt}$ between the front and back half of the curtain, is driven by radiative exchange across differences in temperature between the front and back of the current. The radiation exchange is calculated by assuming the front and back halves of the curtain are two semi-transparent surfaces whose common face have a view-factor of 1. With the multiple diffuse reflections between particle zones and near-uniformity of radiation parameters between the front and back, Eq. 2-15 is derived to quantify the radiation between semi-transparent surfaces, accounting for multiple reflections.

$$\dot{Q}_{curt} = \sum_{m=1}^{M} \frac{\varepsilon_{\lambda_m,i}\varepsilon_{\lambda_m,i'}}{1 - \rho_{\lambda_m,i}\rho_{\lambda_m,i'}} \sigma\left(T_{i'}^4 f_{\lambda_m,i'} - T_i^4 f_{\lambda_m,i}\right)\Delta x_i \Delta y_i \qquad \text{[Eq. 2-15]}$$

In this equation, i represents the current cell for which the heat transfer is being calculated, and i' is the common cell face, corresponding to the opposite side of the particle stream. This approach is a significant improvement over the model proposed by Röger et al. (2010), where inter-curtain exchange was treated by an effective conductivity with an arbitrarily chosen value. The effective conductivity approach does not capture the strong temperature dependence of this exchange. Further, when the value suggested by Röger et al. (2010) is used, the curtain maintains a constant temperature between the front and rear, regardless of particle flow-rate.

The radiation energy source terms in Eq. 2-11 and Eq. 2-16 are solved using Hottel's zonal method within the receiver by modeling the curtain as a semi-transparent medium whose optical properties are dependent on the particle properties (such as diameter and surface emissivity), flow properties (such as volume fraction), and curtain properties (such as curtain thickness). This approach is described in the next section.

The steady-state thermal energy balance for the receiver walls includes convection heat-transfer between the walls and outside air, $\dot{Q}_{\text{wall}}$, the conduction heat transfer between wall cells, $\dot{Q}_{\text{cond}}$, the radiation heat-transfer exchanged within the receiver, $\dot{Q}_{\text{rad}}$, and the direct solar heat source-term, $\dot{Q}_{\text{sol}}$, as shown in Eq. 2-16.

$$0 = \dot{Q}_{\text{wall}} + \dot{Q}_{\text{cond}} + \dot{Q}_{\text{rad}} + \dot{Q}_{\text{sol}} \qquad \text{[Eq. 2-16]}$$

Convective losses from the walls to the atmosphere are calculated with Eq. 2-19 by using material properties of Duraboard HD (Siegel, 2010), and assuming an outside-ambient

temperature of 300 K with a heat transfer coefficient $h_{T,amb}$ = 5 W m^{-2} K^{-1}, as in Röger et al. (2011).

$$\dot{Q}_{wall} = h_{T,amb} A_w \left(T_{amb} - T_w \right) \quad \text{[Eq. 2-17]}$$

2.3.4 Radiation Modeling

Solution of the radiation within the receiver is split between two models: a thermal radiation model and a solar source model. The thermal radiation model is a radiosity balance calculation for the radiation exchanged between cells inside the receiver. The solar source model is used for the incoming solar radiation to calculate the absorbed solar power (kW) in each cell, $\dot{Q}_{sol}$, as well as the reflected solar flux (kW/m^2) at each cell, $\dot{q}''_{sol,refl,i}$, which is assumed to be completely diffuse. The absorbed solar energy is a source term used in Eq. 2-11, while the reflected solar flux is a source term in the thermal radiation model.

2.3.4.1 Thermal Radiation Model

Hottel's zonal method solves the radiation balance between the walls, window, and particles. A multi-bin surface-to-surface model captures radiation exchange between semi-transparent media. To model the semi-transparent media, each interacting zone is split into two cells with independent temperatures but coupled radiation transport– cell i and i'.

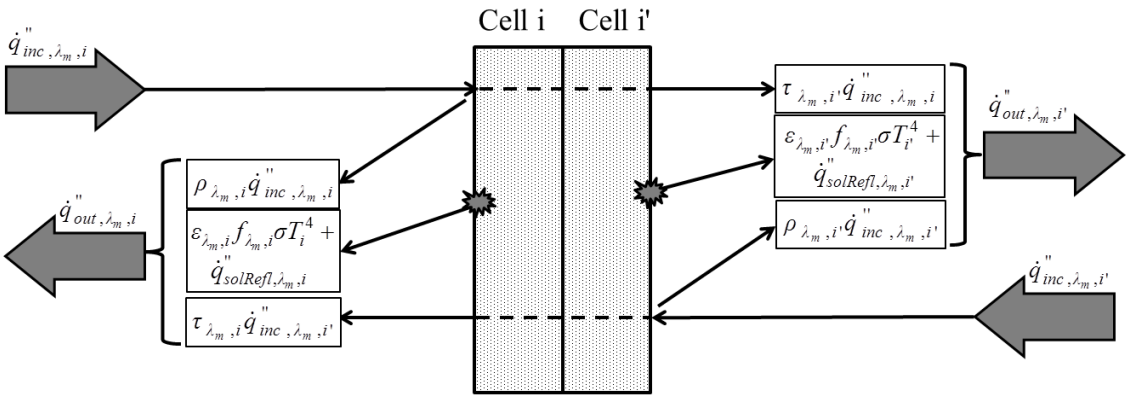

Figure 2-5 – Radiation flux balance for semi-transparent cell pairs using Hottel's zonal method.

$\dot{Q}_{rad,i}$, the net absorbed radiation energy in cell i, is the difference in absorbed and emitted solar energy.

$$\dot{Q}_{rad,i} = A_i \sum_{m=1}^{M} \left(\varepsilon_{\lambda_m,i} \dot{q}''_{inc,\lambda_m,i} - \varepsilon_{\lambda_m,i} f_{\lambda_m,i} \sigma T_i^4 \right) \qquad \text{[Eq. 2-18]}$$

In this equation, Kirchoff's Law for radiation properties is applied to assert $\varepsilon_{\lambda_m,i} = \alpha_{\lambda_m,i}$. As shown in Figure 2-5, the outgoing radiation flux, $\dot{q}''_{out,\lambda_m i}$, from any face to be written in terms of the incoming radiation flux, $\dot{q}''_{inc,\lambda_m i}$, and holds true in each radiation bin, λ_m. This equation is similar to that presented by Röger et al. (2006), with an added source term, $\dot{q}''_{solRefl,\lambda_m,i}$, which represents the incident solar energy within each band that is diffusely reflected. This equation is true for all cells in the domain, even though only the curtain and window (if included) are semi-transparent. For opaque surfaces, there is no companion cell, i', and $\tau_{\lambda_m,i}$ is 0. The value $f_{\lambda_m,i}$ is fraction of energy emitted by a

blackbody in that bin, as shown in Eq. 2-20, where $E_{\lambda,bb}(\lambda,T)$ is the Planck distribution for a blackbody at temperature T.

$$\dot{q}''_{out,\lambda_m,i} = \rho_{\lambda_m,i}\dot{q}''_{inc,\lambda_m,i} + \varepsilon_{\lambda_m,i} f_{\lambda_m,i}\sigma T_i^4 + \dot{q}''_{solRefl,\lambda_m,i} + \tau_{\lambda_m,i}\dot{q}''_{inc,\lambda_m,i'} \quad \text{[Eq. 2-19]}$$

$$f_{\lambda_m,i} = \frac{\int_{\lambda_{m,lower}}^{\lambda_{m,upper}} E_{\lambda,bb}(\lambda,T_i)d\lambda}{\sigma T_i^4} \quad \text{[Eq. 2-20]}$$

The incident radiation on any cell face with area A_i, can be written as a function of outgoing radiation of every other cell, j, and the view-factor between them, $F_{i\text{-}j}$, as in Eq. 2-21. This equation is simplified to Eq. 2-22 by employing the reciprocity relationship, $A_i F_{i-j} = A_j F_{j-i}$.

$$\dot{q}''_{inc,\lambda_m,i} A_i = A_1\dot{q}''_{out,\lambda_m,1}F_{1-i} + \ldots + A_N\dot{q}''_{out,\lambda_m,N}F_{N-i} \quad \text{[Eq. 2-21]}$$

$$\dot{q}''_{inc,\lambda_m,i} = \sum_{j=1}^{N} F_{i-j}\dot{q}''_{out,\lambda_m,j} \quad \text{[Eq. 2-22]}$$

Combining Eq. 2-19 and Eq. 2-22, it is possible to write a linear matrix equation for every cell, as shown in Eq. 2-23. This equation can be solved for $\dot{q}''_{out,\lambda_m i}$ with any linear solver.

$$\sum_{j=1}^{N}\left[\delta_{ij}-\left(\rho_{\lambda_m,i}F_{i-j}+\tau_{\lambda_m,i'}F_{i'-j}\right)\right]\dot{q}''_{out,\lambda_m,i}=\varepsilon_{\lambda_m,i}f_{\lambda_m,i}\sigma T_i^4+\dot{q}''_{solRefl,\lambda_m,i} \qquad \text{[Eq. 2-23]}$$

By substituting in Eq. 2-19 and Eq. 2-22, Eq. 2-18 can be rearranged in terms of the known quantities, $\dot{q}''_{out,\lambda_m i}$, to get Eq. 2-24. This equation uses the relation, $\varepsilon_{\lambda_m}+\rho_{\lambda_m}+\tau_{\lambda_m}=1$, which must be true to conserve energy.

$$\dot{Q}_{rad,i}=-A_i\sum_{m=1}^{M}\left(\dot{q}''_{out,\lambda_m,i}-\left(1-\tau_{\lambda_m,i}\right)\sum_{j=1}^{N}F_{i-j}\dot{q}''_{out,\lambda_m,j}-\tau_{\lambda_m,i'}\sum_{j=1}^{N}F_{i'-j}\dot{q}''_{out,\lambda_m,j}-\dot{q}''_{sol,\lambda_m,i}\right) \qquad \text{[Eq. 2-24]}$$

It is necessary to evaluate radiation properties ($\varepsilon_\lambda,\rho_\lambda,\tau_\lambda$) for all wall and semi-transparent cells, and to choose appropriate radiation bins to accurately capture their spectral variations. For inert particles, three radiation bins and the respective material radiation properties, shown in Table 2-1, are chosen to balance the accuracy of modeling in the window, wall, and particles. For cases with an open aperture, the window values were all set to 0.0 so that all thermal radiation impinging on the aperture from inside the receiver simply escapes.

Table 2-1- Radiation parameters used for inert-particle receivers.

λ range (μm)	$f_{\mathbf{rad}}$ **(%) 5600 K**	$f_{\mathbf{rad}}$ **(%) 1000 K**	$\varepsilon_{\lambda,p}$ [a]	$\varepsilon_{\lambda,\mathbf{wall}}$ [a]	$\varepsilon_{\lambda,\mathbf{wind}}$ [b]	$\rho_{\lambda,\mathbf{wind}}$ [b]
0-1.25	81.0	0.3	0.850	0.200	0.000	0.073
1.25-3.5	18.0	38.0	0.850	0.200	0.046	0.068
3.5-∞	2.0	61.7	0.850	0.800	0.910	0.011

[a]: Siegel et al. (2010)
[b]: Hereaus (2007)

The radiation properties for the semi-transparent particle cells are functions of the particle radiation properties, and must be calculated using an appropriate model. Because of the size of particles, radiation within particle cells can be calculated using geometric optics, which simplifies calculation of the bulk properties. With this assumption, the transmission of solar radiation through a thin "slice" of particles, as shown in Figure 2-6, can be calculated from Eq. 2-25.

$$d\tau = 1 - \frac{A_{part,projected}}{A_{curt,total}} = 1 - \frac{\frac{\pi}{4} d_p^2 N_p}{L_x L_y} \qquad \text{[Eq. 2-25]}$$

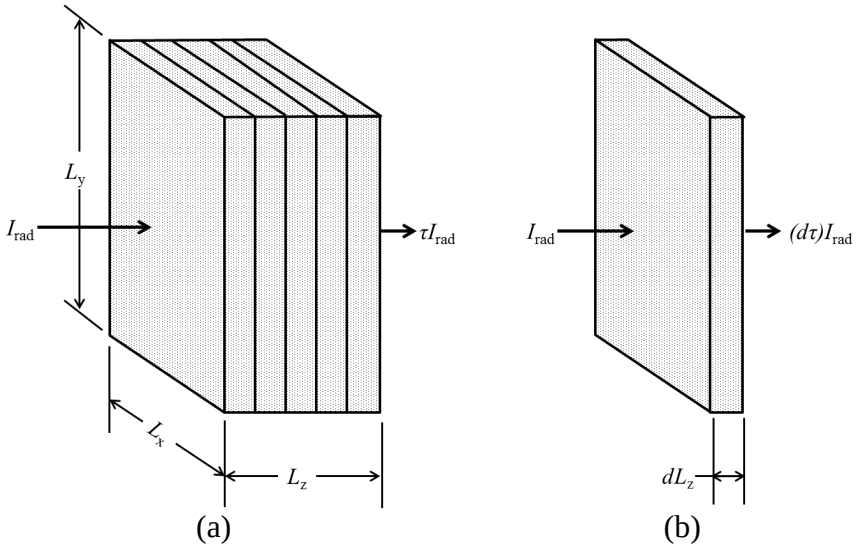

Figure 2-6 - Schematic of radiation transmission through curtain. (a) Transmission through entire curtain, as well as vertical discretization used in derivation of total transmission. (b) Transmission through one single discretization.

Eq. 2-25 can be simplified with the volume fraction, f_v, as defined in Eq. 2-26 in order to obtain Eq. 2-27. In this equation, n_z is the number of *z*-direction discretizations used to

split up the whole curtain, $d\dot{m}_p$ is the mass flow in the *z*-direction discretization. Eq. 2-3 is used here in order to quantify the residence time of particles at a given position.

$$f_v = \frac{\frac{\pi}{6} d_p^3 \left(N_p\right)}{L_x L_y \left(dL_z\right)} = \frac{d\dot{m}'_p L_x}{\rho_p} \frac{L_y}{u_p} \frac{1}{L_x L_y \left(dL_z\right)} = \frac{\dot{m}'_p L_x}{\rho_p n_z} \frac{L_y}{u_p} \frac{1}{L_x L_y \left(dL_z\right)} \qquad \text{[Eq. 2-26]}$$

$$d\tau = 1 - \frac{3 f_v}{2 d_p} \left(dL_z\right) = 1 - \frac{3}{2 d_p} \frac{\dot{m}'_p}{\rho_p n_z} \frac{1}{u_p} \qquad \text{[Eq. 2-27]}$$

The total transmission through the entire length, L_z, is found by multiplying the transmission through each discretization geometrically, as shown in Eq. 2-28. Eq. 2-28 is further simplified by using Eq. 2-27, and letting $x = \frac{3}{2 d_p} \frac{\dot{m}'_p}{\rho_p u_p}$. When taking the limit as n_z approaches inifinity, this becomes the exponential. This approximation works very well for simulations in this study, as the total thickness of the particle curtain is ≥ 0.01 m, while d_p is ≤ 0.0007 m. When n_z is greater than 14 (the minimum number of d_p sized z slices for a 0.01 thickness curtain), the difference between the first form of Eq. 2-28 and the second form is much less than 0.001%.

$$\tau = \left(d\tau\right)^{n_z} = \left(1 - \frac{x}{n_z}\right)^{n_z} \approx \exp\left(-x\right) = \exp\left(-\frac{3}{2 d_p} \frac{\dot{m}'_p}{\rho_p u_p}\right) \qquad \text{[Eq. 2-28]}$$

The final form of spectral curtain transmissivity is found by applying Eq. 2-26 to Eq. 2-28 and recognizing that the path travelled by a ray through the curtain depends on the incident angle θ, so that $L_z = \Delta z_c/\cos(\theta)$, where Δz_c is the curtain thickness. This agrees with the equation presented in Röger et al. (2011). This form is appropriate for spectral sources, such as the incident solar energy, but must be integrated over the full range of θ for diffuse radiation as calculated in Eq. 2-23.

$$\tau_{\lambda_m,i}(\theta) = \exp\left(\frac{-3 f_v \Delta z_c}{2 d_p \cos\theta}\right) \qquad \text{[Eq. 2-29]}$$

τ_{λ_m} found using Eq. 2-29 is compared to the experimental data from Kim et al. (2009) for falling particles under isothermal conditions in Figure 2-7. This comparison was performed for 697 μm particles with a density of 3560 for the ρ'_p shown. The model values were calculated using the Eq. 2-29 and the solid-phase dynamics model described in section 2.3.1. This comparison shows relatively good agreement with the experimental data, although the model over-estimates τ_{λ_m} along the fall, with a maximum difference between the model and experiment of 0.0732 near the end of the measurement window. The experimental data used here uses back-lit images at various points along the fall. As such, this data is subject to errors due to transients and inhomogeneities within the flow (Kim et al., 2009).

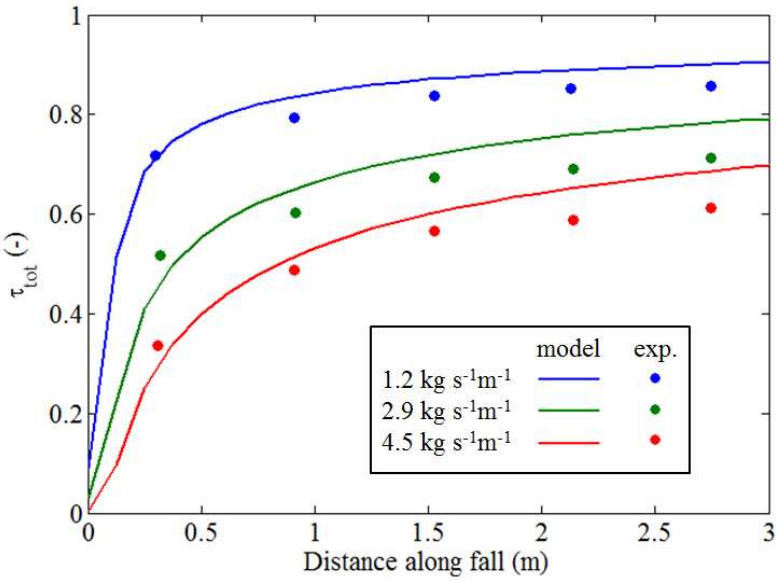

Figure 2-7 – Comparison of curtain τ_{tot} from the particle model and experimental data from Kim et al. (2009) for isothermal particles at the □'$_p$ shown.

To evaluate the particle curtain thickness Δz_c in Eq. 2-29, detailed particle curtain measurements by Kim et al. (2009) under isothermal conditions are used to incorporate particle spreading as the curtain falls. According to their measurements, Δz_c is relatively insensitive to the inlet conditions. Because the simplified model used here does not calculate particle dispersion, a fitting of the data from Kim et al. (2009) in Eq. 2-30 is used.

$$\Delta z_c = 0.01 + 0.0087\, y \qquad \text{[Eq. 2-30]}$$

The curtain reflectance is then found in Eq. 2-31 by multiplying the intensity of the irradiation that intersects the particles, $\left(1-\tau_{\lambda_m,i}\right)$, by the actual material reflectivity, 1-ε_p, which holds true for opaque particles. Spectral absorptance (also spectral emittance by

Kirchoff's law) is found by conserving the energy in the applied radiation, as shown in Eq. 2-32.

$$\rho_{\lambda_m,i} = \left(1-\varepsilon_{p,\lambda}\right)\left(1-\tau_{\lambda_m,i}\right) \quad \text{[Eq. 2-31]}$$

$$\varepsilon_{\lambda_m,i} = 1-\tau_{\lambda_m,i}-\rho_{\lambda_m,i} \quad \text{[Eq. 2-32]}$$

In these equations, $\varepsilon_{p,\lambda}$ is the surface emissivity of the particle material, which is constant for the CarboCeram material used here (Siegel et al., 2010). Eq. 2-31 and Eq. 2-32 are used to find $\rho_{\lambda_m,i}$ and $\varepsilon_{\lambda_m,i}$ for the curtain cells in Eq. 2-18, Eq. 2-19, and Eq. 2-23. It is important to capture the spectral nature of these surface properties as they can vary significantly with λ, which leads to different net absorption properties depending on the source temperature. The spectral binning allows this effect to be captured, as emitted energy shifts between the wavelength bins λ_m, while the surface properties can stay constant within that bin.

2.3.4.2 Solar Source Model

The incoming solar energy follows a uniform specular profile traveling horizontal from the open aperture into the receiver. The solar input is specular and must be calculated separately from the thermal radiation model, which applies for diffuse radiation. To this end, the solar radiation is represented with a large set of rays evenly spread over the aperture, and the incoming solar energy is split into respective radiation spectral bins, as shown in Table 2-1. If the aperture is windowed, these rays pass through

the front half of the window, and energy is either absorbed or reflected out of the receiver. The transmitted portions of the rays then pass through the rear half of the window. If the aperture is open, then there is no interaction with these cells. The rays exiting the window pass through the front-half of the curtain, where diffuse reflection and absorption are calculated. Here, the diffuse reflection out of the front half of the curtain includes all reflected energy going through the whole depth of the curtain, and this calculated flux is added to $\dot{q}''_{solRefl,\lambda_m,i}$, as shown in Eq. 2-33, where $\dot{q}_{ray}$ is the energy of the ray reaching that point. All of the $d\dot{q}''_{solRefl,\lambda_m,i}$ from the rays that pass through cell i are added together to get $\dot{q}''_{solRefl,\lambda_m,i}$.

$$d\dot{q}''_{solRefl,\lambda_m,i} = \rho_{\lambda_m,i}\frac{\dot{q}_{ray}}{A_i} \qquad \text{[Eq. 2-33]}$$

The absorbed solar energy in cell i from a given ray is found with Eq. 2-34, which has this form because $\varepsilon_{\lambda_m,i}$ in the curtain is the absorption through the full length of the curtain, and $\dot{q}_{ray}$ has the reflected portion already removed. As with the reflected solar energy, $\dot{Q}_{sol,i}$ is found by adding all of the absorbed energy from every ray inside each λ_m band, $d\dot{Q}_{sol,\lambda_m,i}$.

$$d\dot{Q}_{sol,\lambda_m,i} = \frac{1-\sqrt{\varepsilon_{\lambda_m,i}}}{1-\rho_{\lambda_m,i}}\dot{q}_{ray} \qquad \text{[Eq. 2-34]}$$

After these calculations, the rays are passed to the back half of the curtain, where the radiative energy is further absorbed. The radiative energy from the rays that is projected through the curtain hits the back wall of the receiver, where the remaining radiation is diffusely reflected.

The split of energy between radiation bands, λ_m, is achieved by finding the fraction of energy within each band according to the ASTM Solar Source (ASTM, 2000) measurements at-sea level, as shown in Figure 2-8. A 5600 K source, scaled to better show the comparative representative energy distribution, is also shown in Figure 2-8 as it is frequently suggested to calculate spectral distributions using a treatment similar to Eq. 2-20. While a 5600 K source provides a reasonable estimation of the actual solar source for many applications, it can introduce errors when spectrally selective surfaces are used.

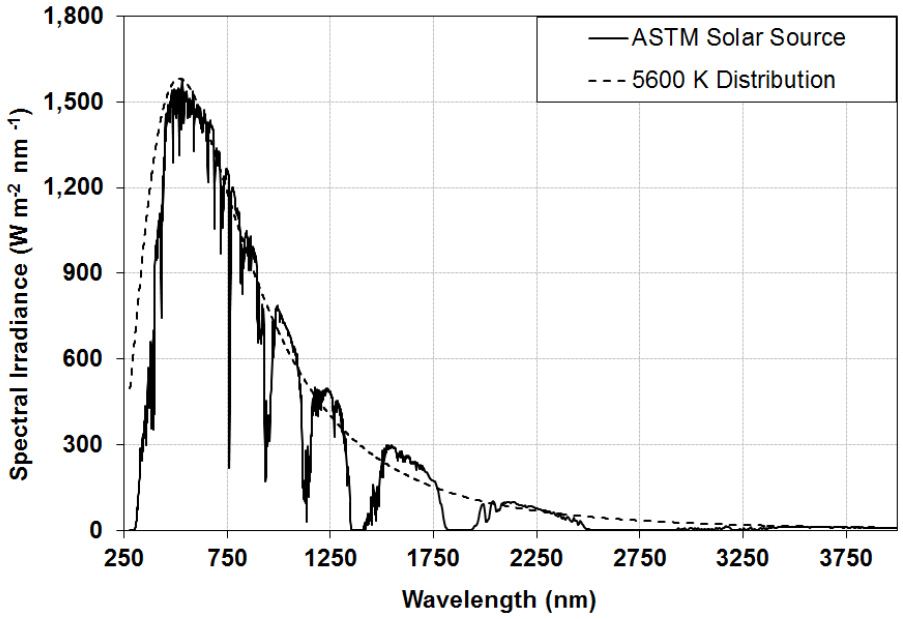

Figure 2-8 - Wavelength distribution of ASTM Solar Source (ASTM, 2000) and a 5600 K blackbody distribution scaled to a solar source.

2.3.4.3 Radiation View-Factors

In order to evaluate the thermal radiosity balance in the receiver presented in Eq. 2-23 and Eq. 2-24, the model must calculate the view factors between all of the computational cells. While there are many methods for performing this calculation, in this study view factors are calculated evaluating the double-area integration shown in Eq. 2-35. In this equation, θ_i and θ_j are the angles between the normals of differential elements dA_i and dA_j and the cell-center distance between these two faces, R, as shown in Figure 2-9. The value OF_k is the added obstruction factor to account for blocking by other faces for any given path-length.

$$F_{i-j} = \frac{1}{A_i} \int_{A_i} \int_{A_j} \frac{\cos(\theta_i)\cos(\theta_j)}{\pi R^2} (OF_k) dA_i dA_j \qquad \text{[Eq. 2-35]}$$

The double-area integration is carried out with the *dblquad* function, which performs a quadrature over both areas, adaptively choosing points to achieve results matching a specified tolerance. While quadrature can have difficulties with such discontinuous functions as shown in Eq. 2-35, using a high enough tolerance is able to circumvent these problems. This implementation was tested by using known test-geometries, as those in Incropera et al. (2006), and a tolerance of 10^{-5} was sufficient to match analytical results within 0.1%.

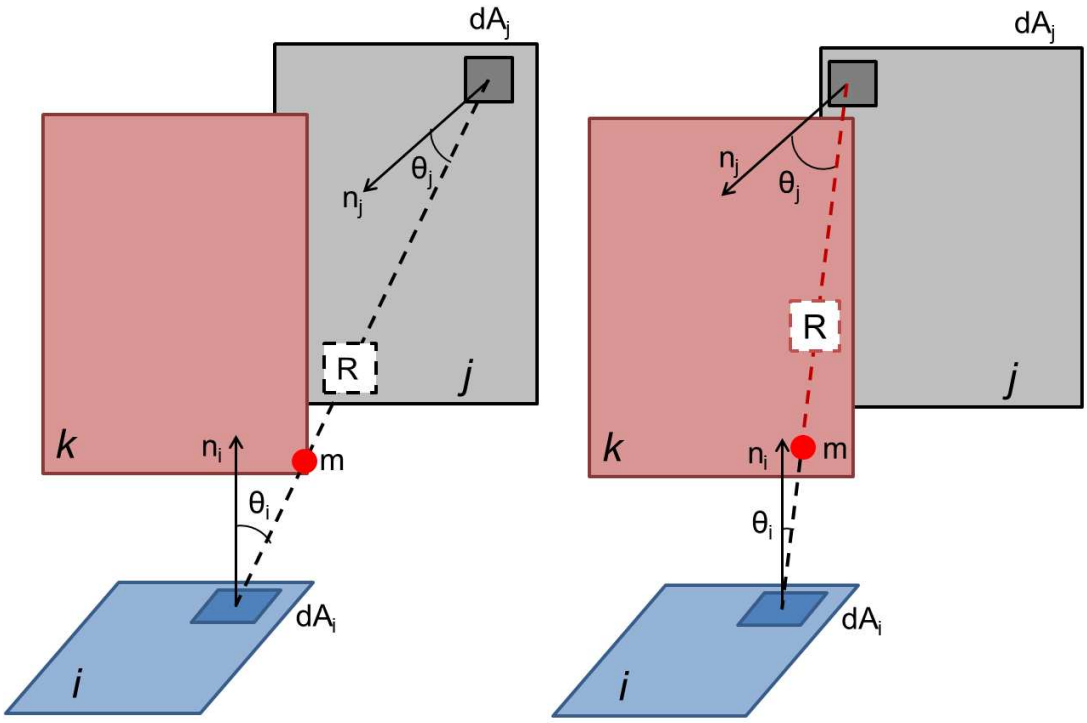

Figure 2-9 - Schematic illustrating the geometry used for calculation of view factors between cells i and j. In this example, two cases are shown: (left) a particular differential path-length is not obstructed and (right) a path obstructed by the presence of another interacting face.

This double integration can be very time-consuming, taking about 1 day for the prototype-scale geometry, but it is completely geometry dependent and only needs to be performed once for any prescribed geometry. Further, using the reciprocity relationship, $A_i F_{i-j} = A_j F_{j-i}$, cuts computational time in half.

After all view factors have been calculated for any geometry, there is a secondary check that $\sum_j F_{i-j} - 1 < e$, where e = 0.95. If the error is greater than 1 – e, the tolerance is increased and the whole-domain view factors are run again until the error is acceptable. Then, each row in the view-factor is normalized to a value of 1 to conserve energy,

accepting that this will create slight errors in the total view factors. The degree of these errors was deemed acceptable enough for the level of this model, as they do not significantly influence any of the captured trends or major physical impacts.

2.3.5 Solution Method

A schematic of the solution method for the entire receiver model is shown in Figure 2-10. The solution starts with a reasonable guess for the temperature fields and gas/particle coupling between the gas and solid phases. The solid particle tracking in the Lagrangian frame Eq. 2-2 uses the ode23tb solver in MATLAB to solve for $\bar{u}_{y,p}$ with a tolerance of 10^{-6}. Next, the gas-phase mass, energy, and momentum balances in the Eulerian frame, Eq. 2-5, Eq. 2-6, and Eq. 2-8, are solved to find T_{gas} and $\bar{u}_{y,g}$ using the updated $\bar{u}_{y,p}$ values from the particle solver. The solid and gas-phase models are iterated until the maximum relative change in the solution variables is less than 10^{-4}. After the velocities and gas temperature have converged, the solid-phase energy balance, Eq. 2-11, is solved to update the wall and particle temperatures using the lsqnonlin solver with a tolerance of 10^{-4}. This solver accounts for the majority of the solution time, most of which is spent on matrix inversions to solve Eq. 2-23. The solver checks for convergence in the particle temperatures, and iterates on the process if the maximum residual is greater than 10^{-3}. Total runtime for a single case is on the order of 1-4 hours for the prototype-scale and 10-30 hours for the full-scale, with less time if a prior solution (and thus better starting-guess) is used at initialization.

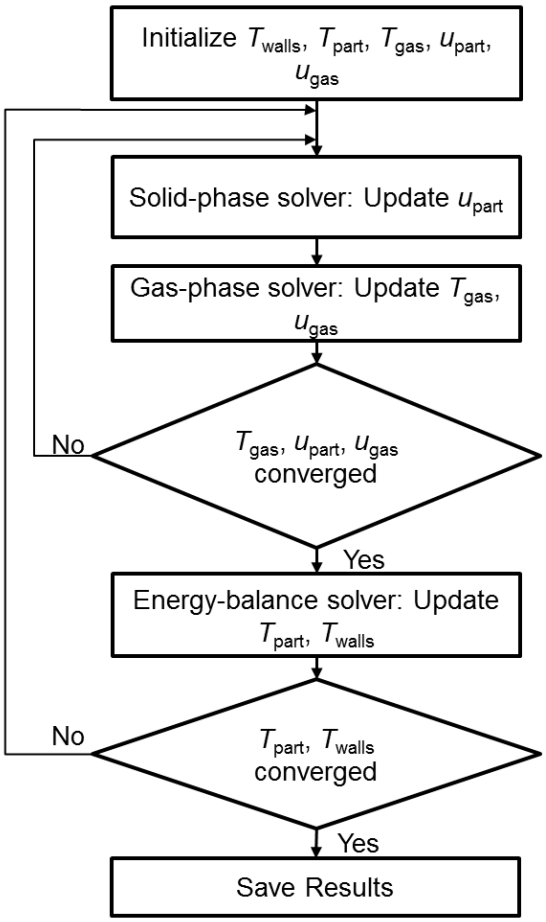

Figure 2-10 - Solution method for inert particle receiver model.

2.4 Model Validation

The model developed here was evaluated under similar conditions to the experimental conditions described by Siegel et al. (2010) in order to provide a benchmark of the performance. The operating conditions for these simulations are shown in Table 2-2. There are a few differences between the experiments of Siegel et al. (2010) and the simulations performed here. The experimental data has a much greater particle entrance region (~3 m) prior to reaching the directly irradiated zone. To mitigate this effect, the

particles were given in inlet velocity, $u_{p,in}$, of 6.0 m/s which closely matches the accumulated particle velocity obtained through the extended the entrance region. The experimental data also obtained a non-uniform radiation profile into the aperture, with a large portion of the incoming energy not directly incident on the particle curtain. To capture the influence of this non-uniform profile, a Gaussian solar profile was applied over the whole aperture as shown in Eq. 2-36, with a variance in the x-direction ($\sigma^2_{rad,x}$) and y-direction ($\sigma^2_{rad,y}$) of 0.6. The Gaussian amplitude was set such that the total inlet energy matched the experimental value reported in Siegel et al. (2010).

$$d\dot{q}''_{\lambda_i,Sol} = C_{rad} \exp\left(\frac{-x^2}{2\sigma^2_{rad,x}} + \frac{-y^2}{2\sigma^2_{rad,y}} \right) \quad \text{[Eq. 2-36]}$$

Table 2-2 – Dimensions and run parameters used for comparison of simulation results with the experimental data from Siegel et al. (2010) for a prototype-scale inert particle receiver.

Property	Value (Baseline)
Receiver Dim. (m) ($L_{x,r}$, $L_{y,r}$, $L_{z,r}$)	(1.85, 5.0,1.5)
Aperture Dim. (m) ($L_{x,a}$, $L_{y,a}$, $L_{z,a}$)	(1.5, 3.0, 0.05)
Curtain Dimensions (m) ($L_{x,c}$, $L_{y,c}$, $L_{z,c}$)	(1.0, 5.0, 0.01+0.0087·y)
d_p (μm)	697
ρ_{part} (kg m^{-3})	3560
ε_p (-)	0.85
$T_{p,in}$ (K)	300
$u_{p,in}$ (m/s)	6.0

The results of this validation study are shown in Figure 2-11, which demonstrates that the simulation model over-predicts the temperature obtained by the experimental data with a maximum difference in ΔT_p of 59.8 K with an average error of 27.0 K. This

occurs due to two primary factors: (1) the simulation model does not include the impact the gas flow, including the cold gas entering the receiver aperture, and (2) a mismatch in the radiation profile due to lack of available information. More detailed CFD simulations performed by Siegel et al. (2010) have demonstrated that gas flow out of the window can lead to an additional ~9% loss, which cannot be captured with this model. Testing various solar-source shapes (by changing $\sigma^2_{rad,x}$ and $\sigma^2_{rad,y}$) showed a difference in performance by as much as 39.5 K by exit of the receiver, with performance differences determined by the portion of energy that directly impacts the curtain. Despite the discrepancies, the simplified model presented here shows a relatively good match of the experimental data, especially for an early-stage design tool.

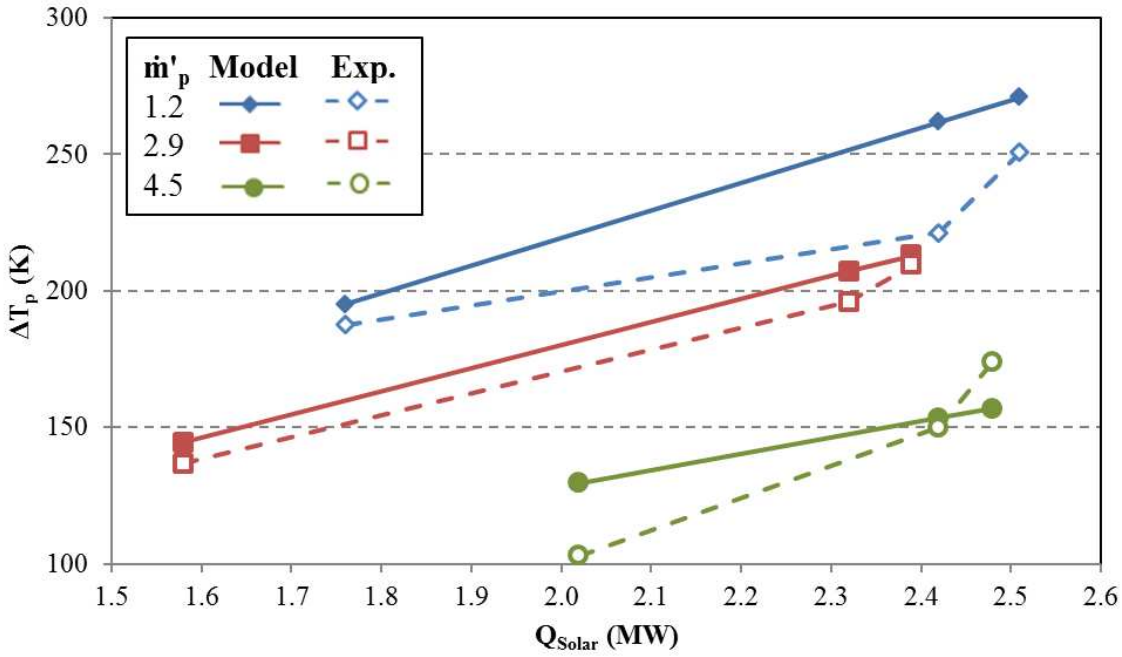

Figure 2-11 – Comparison of $T_{p,out}$ predicted by the model to experimental data for the run conditions ($\dot{Q}_{sol}$ and $\dot{m}'_p$) listed.

2.5 Modeling Results for Prototype-scale Inert-particle Receiver

The prototype–scale solar receiver was run under a variety of conditions relevant to the commercial-scale inert receiver designs being studied by Sandia National Labs. This was done to evaluate the influence of varying operational variables and better understand their operational impacts to aid in that design. The baseline dimensions and operating conditions for these simulations are shown in Table 2-3. All simulations are carried out using these values for all parameters except those varied in any test. The results from these tests are presented, followed by a discussion of these impacts.

Table 2-3 – Baseline dimensions and operating conditions used for prototype-scale inert receiver simulations.

Property	Value (Baseline)
Receiver Dim. (m) ($L_{x,r}$, $L_{y,r}$, $L_{z,r}$)	(1.85, 5.0,1.5)
Aperture Dim. (m) ($L_{x,a}$, $L_{y,a}$, $L_{z,a}$)	(1.0, 3.0, 0.05)
Curtain Dimensions (m) ($L_{x,c}$, $L_{y,c}$, $L_{z,c}$)	(1.0, 5.0, 0.01+0.0087·y)
d_p (μm)	280
$\dot{m}'_p$ (kg s^{-1} m^{-1})	4.0
ρ_{part} (kg m^{-3})	3560
ε_p (-)	0.85
$T_{p,in}$ (K)	600
$\dot{q}''_{solar}$ (kW m^{-2})	1000

2.5.1 Numerical Grid

Eulerian-grid cells were used in the receiver walls and curtain region for both the particle heat transfer and the gas governing equations during the fall through the receiver cavity. This grid used two discretizations for the curtain in the *z*-direction (through the depth of the curtain), as is necessary for the zonal model within the curtain to maintain independent temperatures at the front and back of the curtain. Using two discretizations in the *z*-direction also enabled investigation of variations in temperature into the depth of the curtain. Four discretizations in the *x*-direction capture variation in radiation effects from greater exchange with the walls versus the window without increasing computational cost too significantly. The maximum observed temperature difference between the center and edge curtain temperatures is only 25 K in the irradiated zone, and decreases to less than 2 K by the exit. Thus, four discretizations in the *x*-direction were deemed adequate for the purposes of this study.

The effect of varying *y*-direction (i.e., fall direction) cells was explored to evaluate the grid's influence on the particle temperature and velocity along the length of fall. Within each Eulerian computational cell, the particle dynamics equations were solved over at least 50 steps, with additional steps taken as needed to fulfill the solver's tolerance requirements. These calculations estimated the particle temperatures and gas properties at each point along the fall through linear interpolation with the upstream and downstream cell conditions. This enabled a coarser Eulerian grid for the time-intensive radiation calculations, while still capturing the fall dynamics with greater accuracy. The impact of grid resolutions in the *y*-direction was evaluated for the prototype-scale receiver by twice doubling the number of discretizations (using 20, 40, and 80 cells) to

evaluate the necessary resolution for grid-independence. The change in particle temperatures going from 20 to 40 to 80 cells was less than 3 K (~0.1% change) for each increase. This small variation was due to the particle-air coupling scheme that was employed along the fall. As such, the medium grid (40 discretization) was used as it provided good accuracy with reasonable computational time.

2.5.2 Results

The solid particle receiver model provides full-system temperature profiles as shown in Figure 2-12, Figure 2-11, and Figure 2-14. These profiles give valuable information for understanding receiver operation, selecting materials for survivability, and interpreting trends. These curves show a clear change in the flow of heat within the receiver as particle diameter d_p is increased from 100 to 600 μm. For the 100-μm particles, the hottest T_{wall} is achieved along the front wall of the receiver, caused by reflection of solar energy off of and emission by the curtain. For these smallest particles, the influence of reflection off the curtain accounts for approximately 65% of the radiosity of the front wall, while emission accounts for roughly 35%, depending on position along the fall. As the particle size increases, the hot spot on the front wall remains, but becomes less pronounced as particle emission decreases due to cooler particles and lower curtain density. Going down the walls, there is a clear increase in temperature driven by higher particle radiation emissions. Particle emissions scale with T_p^4, and increase over 7 times between the inlet condition of 600 K and the middle of the curtain at 1000 K. As the particle size increases, a hot-spot develops on the back wall and grows more pronounced because a curtain of larger particles blocks less radiation.

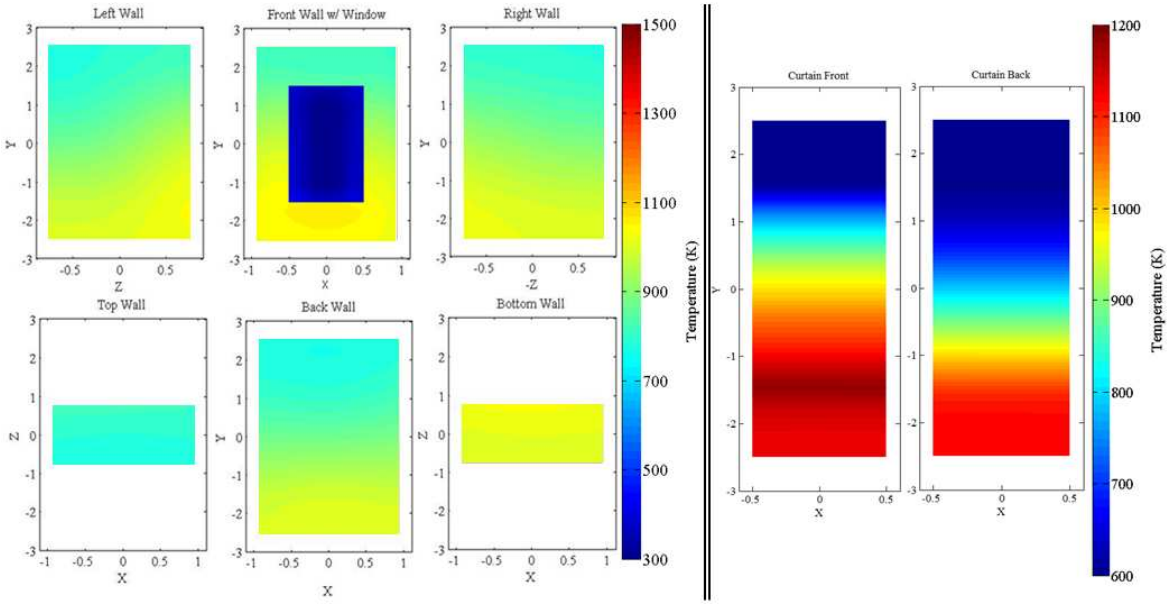

Figure 2-12 - Temperature profiles within an inert, prototype-scale receiver case at the operating conditions shown in Table 2-3 and d_p = 100 μm.

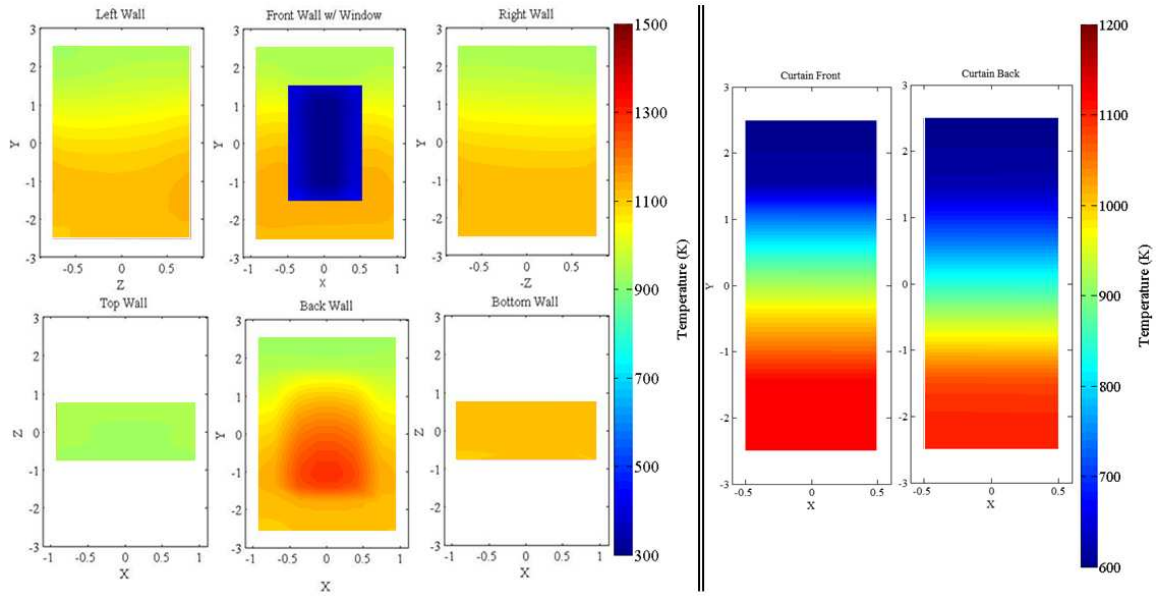

Figure 2-13 - Temperature profiles within an inert, prototype-scale receiver case at the operating conditions shown in Table 2-3 and d_p = 300 μm.

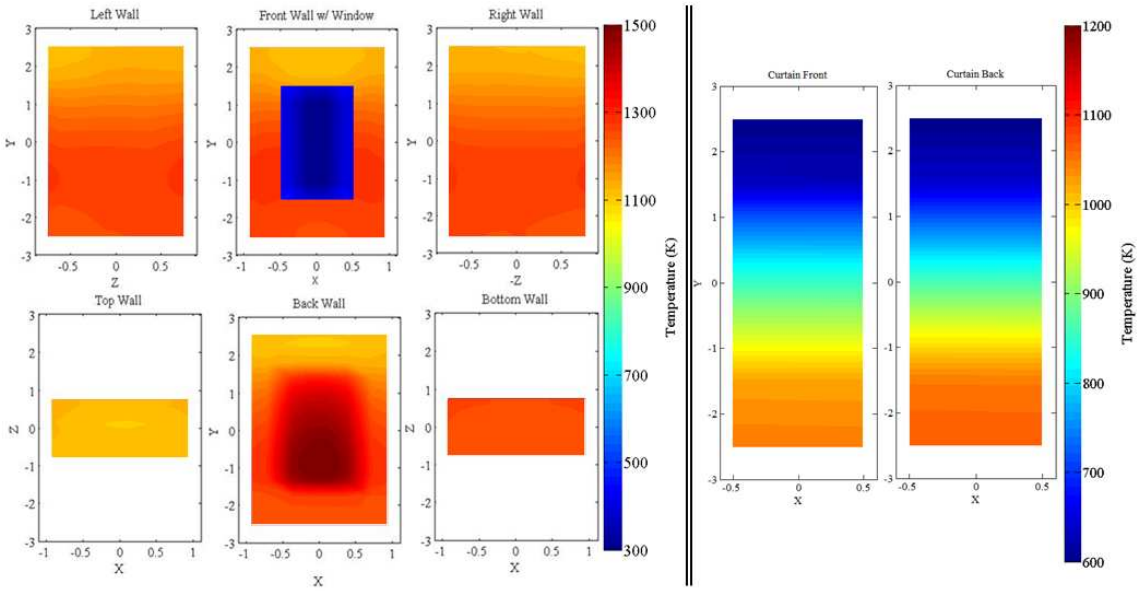

Figure 2-14 - Temperature profiles within an inert, prototype-scale receiver case at the operating conditions shown in Table 2-3 and d_p = 600 μm.

The exchange that greater curtain density creates between absorbed and transmitted energy is apparent by looking at particle outlet temperatures compared to wall temperatures, as shown in Figure 2-15. The largest particles absorb less solar energy and achieve lower temperatures while transmitting a significant amount to the back wall hot-spot. As d_p decreases, less radiation reaches the rear wall, reaching a lower limit at 200 μm, where the maximum wall-temperature is no longer the back wall, but instead the front wall due to reflection off the front of the curtain.

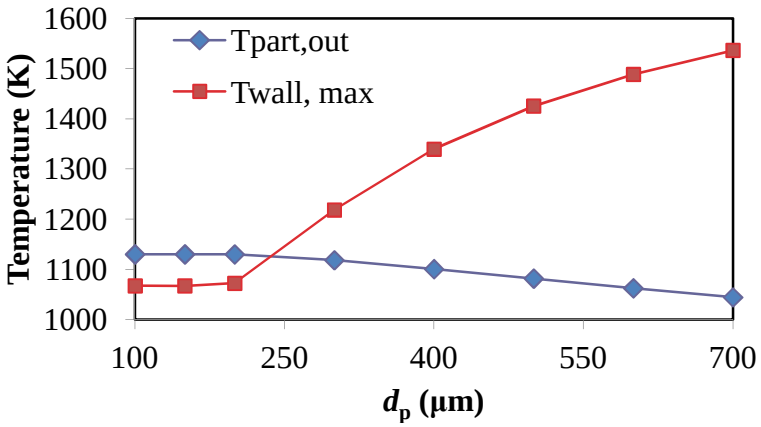

Figure 2-15 – Maximum wall temperature and particle outlet temperature plotted as a function particle diameter (in µm) for prototype-scale inert particle receiver.

The development of the hot spot on the rear of the receiver can be explained in terms of the transmissivity of the curtain plotted in Figure 2-16. The transmissivity gives the fraction of total energy that penetrates over the full thickness of the curtain to reach the back wall. It is clear that, as particles get larger, the curtain quickly gets less opaque more quickly along the fall, causing the hot spots. This explains why the hot spot occurs further along the fall, nearer the end of the directly irradiated zone.

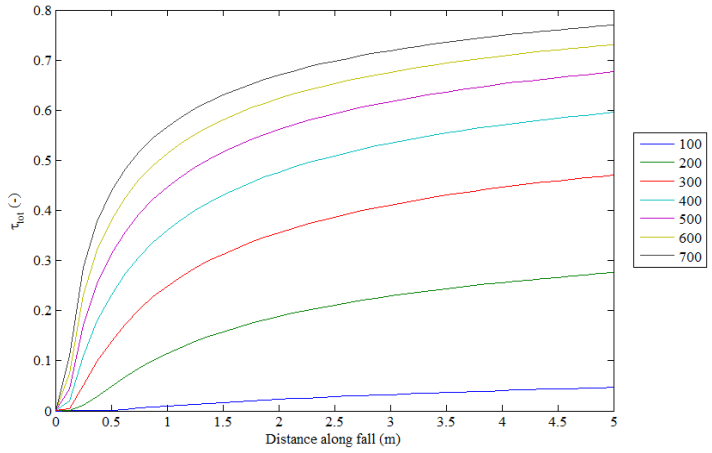

Figure 2-16 – Curtain transmissivity along the length of fall for varying particle diameter (in μm).

The transmissivity changes along the length of fall because the volume fraction f_v decreases rapidly along the length of the fall as shown in Figure 2-15. Eq. 2-29 indicates how transmissivity depends on both f_v and d_p by the exponential $-\frac{f_v \Delta z}{d_p}$. Curtains with larger particles have lower f_v at all points. Although the thickness of the curtain increases slightly with fall distance, the volume fraction reduction dominates the exponential term in Eq. 2-29, and curtain transmissivity increases along the fall. The volume fraction, shown in Eq. 2-26, depends on $\frac{1}{u_p \Delta z}$. As the curtain thickness along the fall is the same for all particle sizes, the volume fraction is higher for smaller particles because they maintain lower velocities, as shown in Figure 2-17.

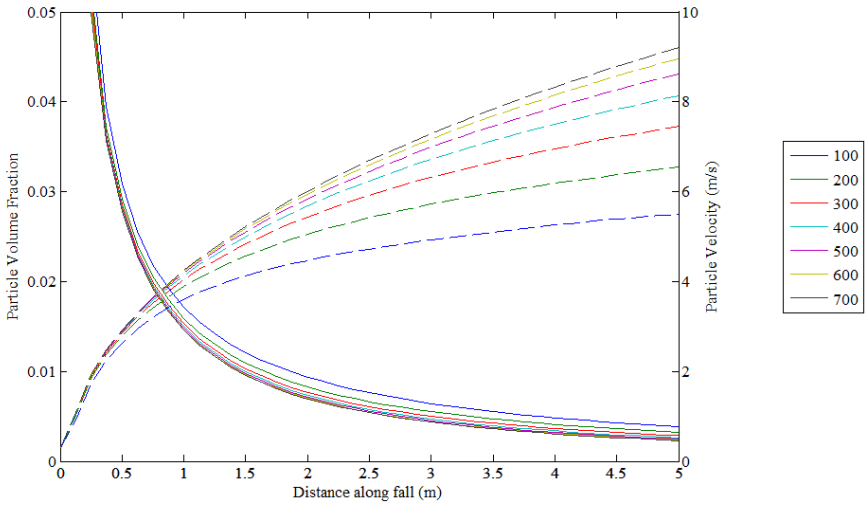

Figure 2-17 – Particle volume fraction (solid lines) and velocity (dashed lines) along the length of fall for varying particle diameters (in μm).

While particle size has a significant impact on radiation transport through the curtain, it also impacts particle heating rates within the curtain as apparent in Figure 2-12, Figure 2-11, and Figure 2-14. The change in particle temperatures for both the front and back curtain is plotted in more detail in Figure 2-18. As the particles are heated by radiation from the hot walls in the entrance zone, larger particles are heated more rapidly because of the hotter walls with larger particles. In the directly irradiated zone, the particles rapidly increase in temperature, and smaller particles absorb more radiation because of lower curtain transmissivities. In addition, smaller particles have lower velocities and longer residence times in the directly irradiated zone.

Three heat flows govern the evolution of particle temperature outside the directly irradiated zone: radiation exchange with the walls, radiation emission out of the front window, and heat exchange within the curtain. Heat exchange from the walls is positive for larger particles with d_p > 250 μm, because wall temperatures are greater than curtain

temperatures as shown in Figure 2-15. For all particles, radiation is lost out of the aperture, and this loss increases for smaller particles that achieve higher maximum temperatures. Figure 2-19 illustrates the importance of heat exchange between the front and rear of the particle curtain. For particles with $d_p \geq 500$ μm, the rear of the curtain is hotter than the front, due to a combination of high solar insolation reaching the rear and radiation from the rear-wall hotspot.

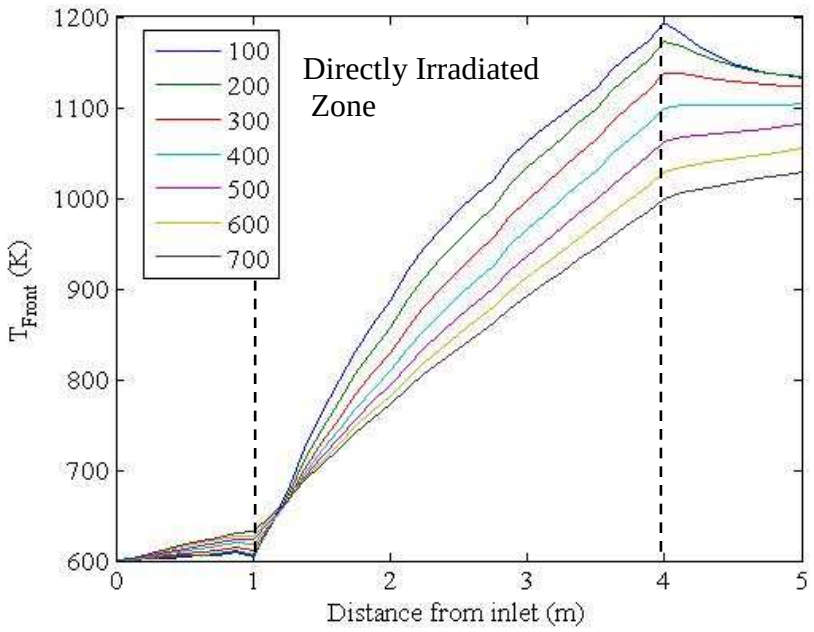

(a)

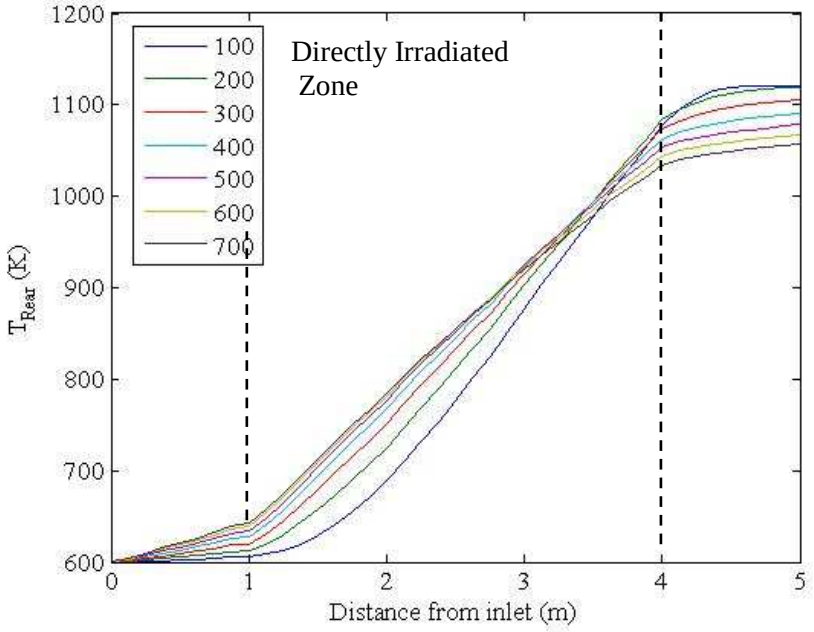

(b)

Figure 2-18 – Particle temperature contours along the fall for the (a) front and (b) rear of the curtain for the varying particle sizes (in μm). The area between the dashed lines is directly irradiated by the incoming solar beam.

The temperature increase of the rear half of the curtain shows a different characteristic to that of the front curtain. In the directly irradiated zone, larger particles initially heat faster than smaller particles, due to the higher wall temperatures that increased transmissivity in the curtain causes. However, as the particle progress through the directly irradiated zone, smaller particles begin to be heated faster than larger particles due to increased inter-curtain heat exchange. In the exit-region, all particles continue to be heated due to inter-curtain exchange for the smallest particles and wall heating for the largest particles. By the exit of the receiver, particles 400 μm and below achieve an approximately uniform temperature thanks to these processes, while the larger particles maintain a temperature gradient across the curtain.

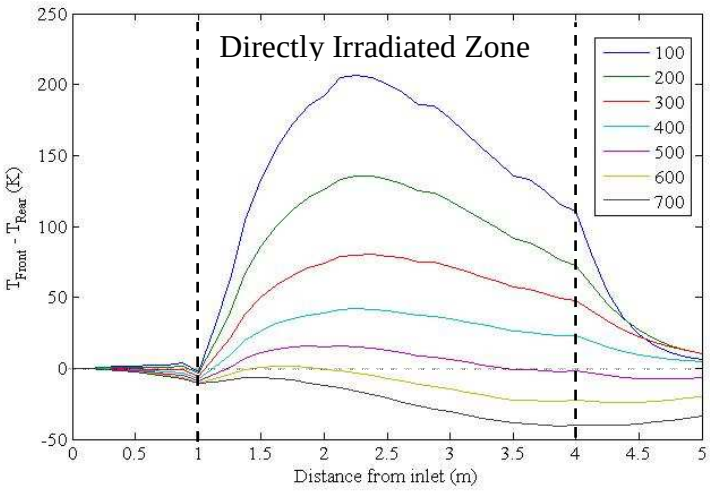

Figure 2-19 – Difference in particle temperature along the fall between the front and rear of the curtain for varying particle sizes (in μm). The area between the dashed lines is directly irradiated by the incoming solar beam.

The solar receiver efficiency η_{solar} is defined in Eq. 2-37 as the fraction of solar flux into the window captured in the particles,

$$\eta_{solar} = \frac{\dot{Q}_{part}}{\dot{Q}_{solar}} = \frac{\dot{m}_p \left(h_{\mathrm{p,in}} - h_{\mathrm{p,out}} \right)}{\dot{Q}_{solar}} \qquad \text{[Eq. 2-37]}$$

Figure 2-20 shows how η_{solar} and change in mean T_p across the receiver vary with d_p. Smaller particles perform better than larger particles with higher η_{solar} and ΔT_p, although there appears to be a limit reached for d_p < 200 μm.

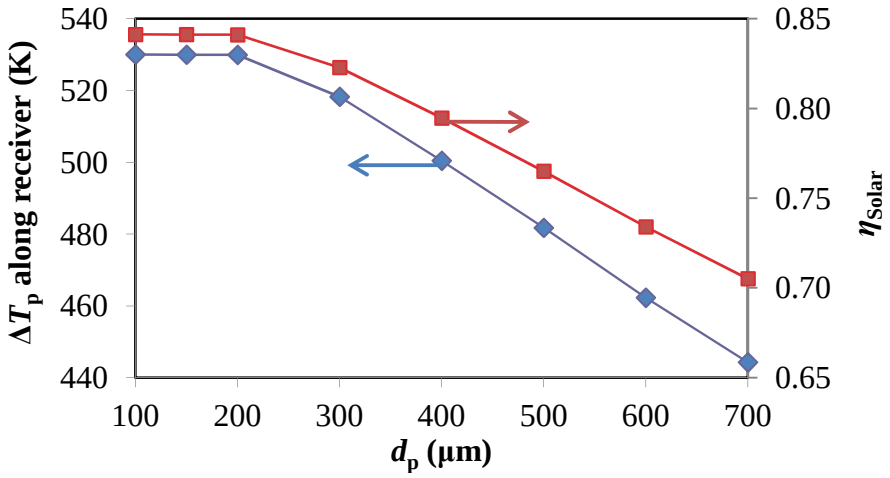

Figure 2-20 - Change in particle temperature from inlet to outlet and efficiency as a function of particle diameter (in μm) of the prototype-scale inert particle receiver.

Besides particle diameter, particle emissivity is an important parameter in receiver operation. η_{solar} and ΔT_p increase with particle emissivity as shown in Figure 2-21. For higher emissivities, wall temperature contours resemble those in Figure 2-13, with a large hot spot on the rear receiver wall. Figure 2-20 shows that as particle emissivity decreases, wall temperatures increase due to reflection of the incoming solar energy off of the particle curtain onto the wall. While the point of maximum temperature is on the rear hot-

spot for emissivities of 0.4 and above, it shifts to the front-wall for emissivities of 0.3 and below.

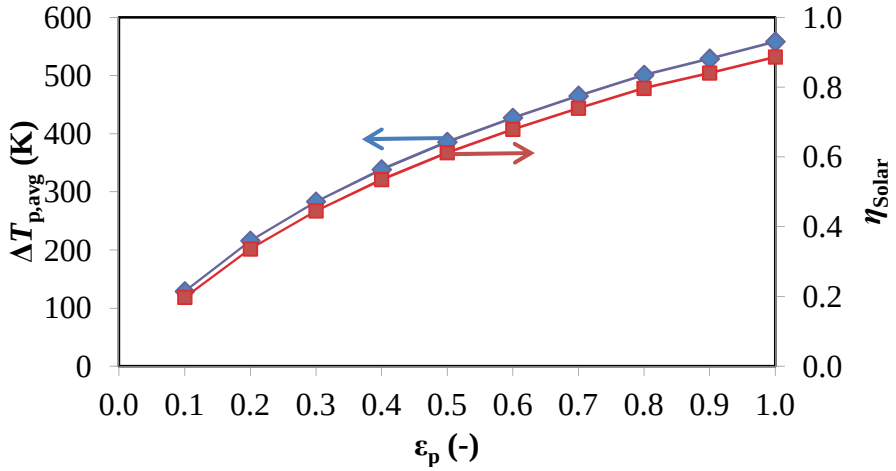

Figure 2-21 - Change in outlet temperature and efficiency with particle emissivity.

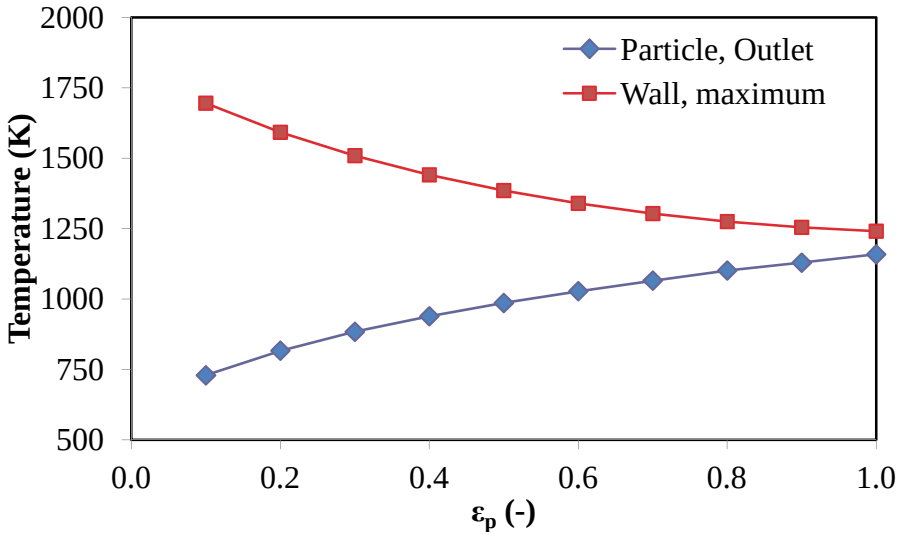

Figure 2-22 – Maximum wall temperature and particle outlet temperature as a function of particle emissivity (and thus absorptivity).

Even if the particles are blackbodies with an emissivity of 1.0, η_{solar} is still limited because of incomplete absorption in the curtain and re-radiation losses. The influence of each major energy loss is displayed in Figure 2-23. As particle emissivity decreases, radiation losses increase from 7.1 to 72.8% due to increased reflection out of the aperture and wall emissions through the aperture. As wall temperatures increase from 1240 K to 1695 K with decreasing emissivity, the convection losses almost double, increasing from 4.1 to 7.9%.

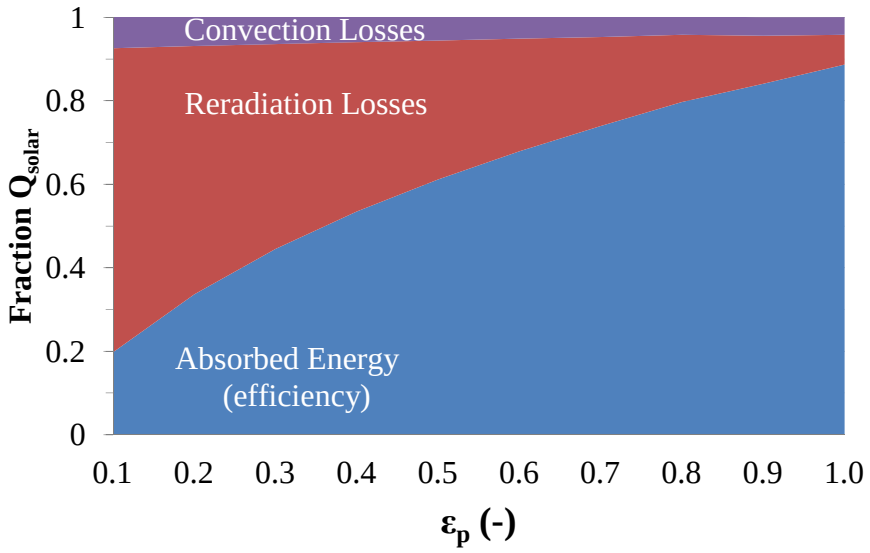

Figure 2-23 – Net energy breakdown, as a fraction of total inlet energy, $\dot{Q}_{Solar}$, for prototype-scale receiver with grey-particle emissivities varying between 0.1 and 0.9.

While changing particle emissivity has very straight-forward impacts on receiver operation, changing particle mass-flow rates results in a design trade-off between efficiency and particle temperature, as shown in Figure 2-24. Above a mass flow rate of 10 kg s^{-1} m^{-1}, the efficiency only increases by a maximum of 1.3%, but there is a decrease

in particle temperature by as much as 167 K. Figure 2-25 shows diminishing returns on efficiency with increasing flow rates. However, there are stiff penalties due to re-radiation losses at lower flow-rates as ΔT_p becomes larger.

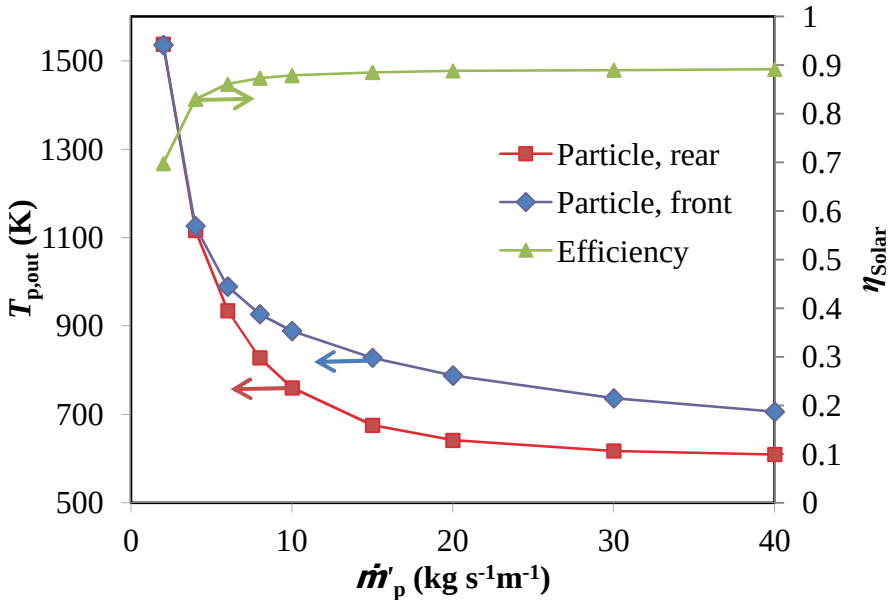

Figure 2-24 - Change in particle temperature for the front and rear of the curtain and efficiency as a function of particle flow rate (in kg s^{-1} m^{-1}).

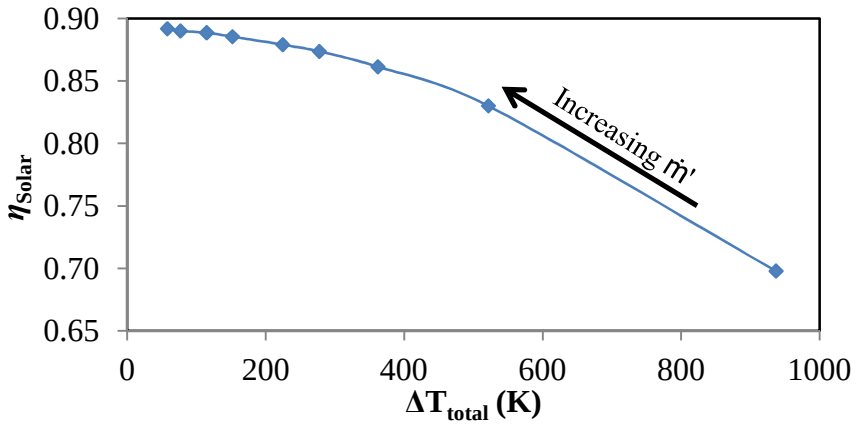

Figure 2-25 – Relationship between total efficiency and mean change in temperature along the fall by varying particle mass flow rate between 2 to 40 kg s^{-1} m^{-1}.

Figure 2-24 shows the temperature disparity between the front and rear of the curtain. Large differences between front and back T_p may be an operational concern depending on how the intended down-stream use of the particle feed. Figure 2-26 shows how varying mass flow rates impacts variation in the front and rear curtain T_p. For the lowest flow-rates, front and rear curtains are both noticeably heated in the entrance region by hotter walls, which occur due to low curtain opacity.

As particle mass-flow rate increases, the difference between the front and rear curtain temperature grows, as shown in Figure 2-27. The shape of these curves can be explained in terms of the transmissivity of the flow, as shown in Figure 2-28, the receiver wall-temperatures, and the inter-curtain heat transport given in Eq. 2-15. At the lowest mass-flow rate, the rear achieves higher temperatures due to greater radiation penetration into the rear as well as high thermal radiation flux from the walls, which achieve a maximum temperature of 1556 K. As the mass flow rate increases, less radiation reaches the rear of the curtain (due to greater opacity from the front half), the wall temperatures decrease due to greater overall absorption, and curtain heat exchange is reduced due to lower overall temperatures. The temperature difference curves also show the strong temperature dependence of inter-curtain heat exchange, as lower $\dot{m}'_p$ cases reach higher T_p to exchange more heat between front and rear. In the exit region, this contributes to the decrease in front curtain temperatures and increase in the rear, as is evident in Figure 2-26. For $\dot{m}'_p$ of 15 kg s^{-1} m^{-1} and above, the difference in temperature grows almost linearly in the directly irradiated zone, as the transmissivity is so low that very little direct radiation even reaches the rear. At even higher flow rates, the rear of the curtain stays almost at the inlet temperature. Heat exchange between the front and rear of the curtain

does reduce the temperature difference outside the directly irradiated zone, but to a lesser extent with increasing $\dot{m}'_p$.

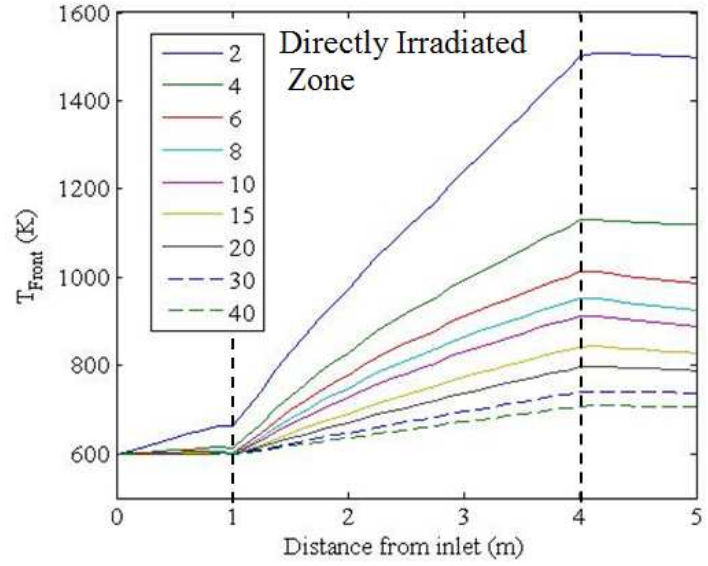

(a)

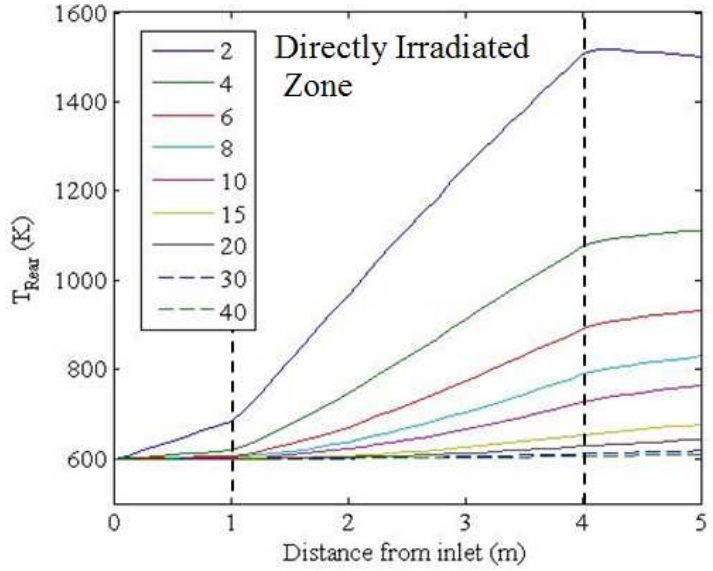

(b)

Figure 2-26 - Particle temperature contours along the fall for the (a) front and (b) rear of the curtain for the specified inlet $\dot{m}'_p$ (in kg $s^{-1}m^{-1}$) shown in the legend.

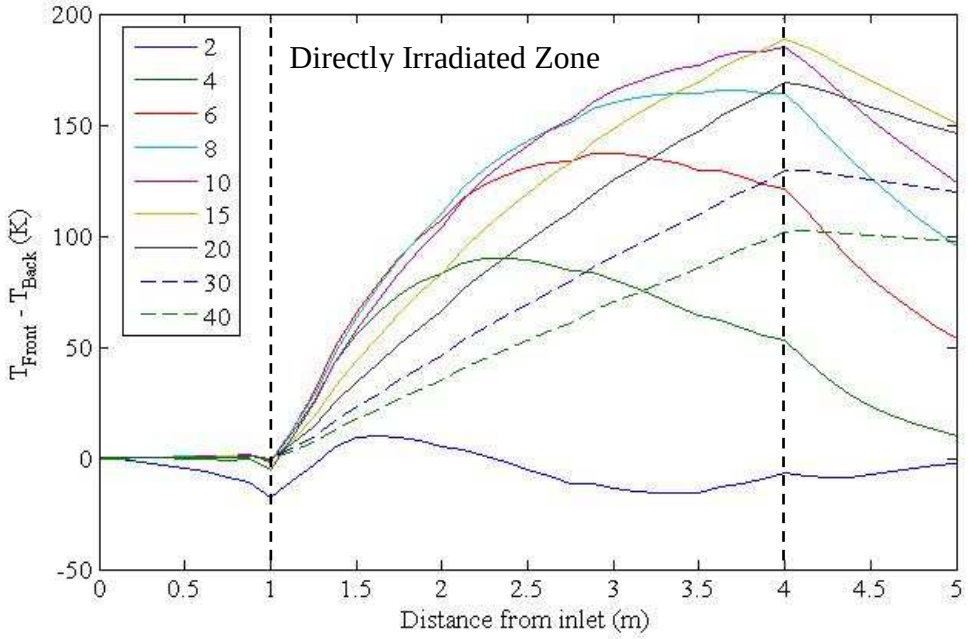

Figure 2-27 - Difference in particle temperature along the fall between the front and rear of the curtain for varying $\dot{m}'_p$ (in kg s^{-1} m^{-1}).

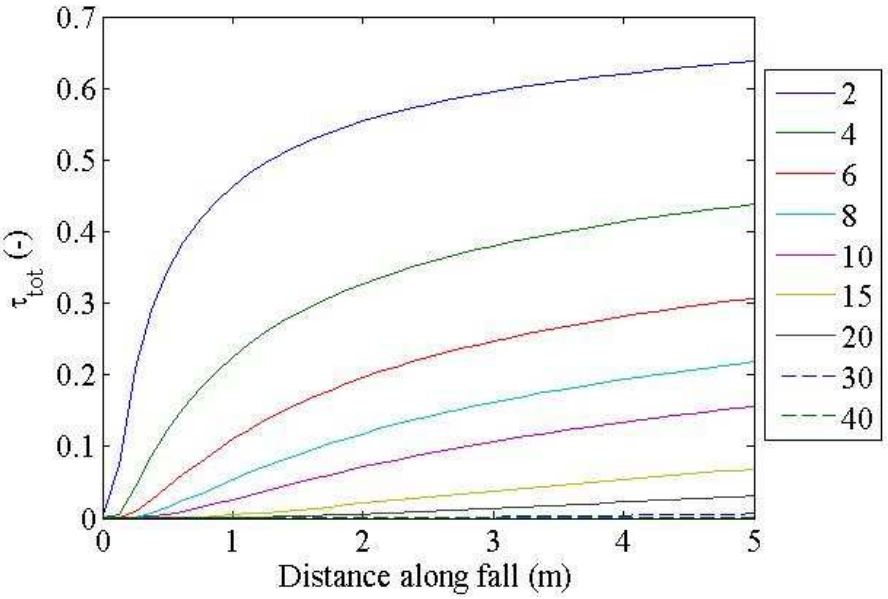

Figure 2-28 - Curtain transmissivity along the length of fall for different particle mass flow-rates (kg s^{-1} m^{-1}).

Variations in solar input impact the optimal design parameters and operating conditions as well as the receiver response to transient conditions. The change in particle temperature, maximum T_{wall}, and overall efficiency are plotted as a function of solar power input (in kW m^{-2}) in Figure 2-29. Wall temperatures and particle temperatures increase monotonically with solar power, although the total efficiency shows a trade-off. As the solar input increases from 300 to 900 kW/m^2, the efficiency increases from 81.2 to 83.4% because, although re-radiation losses increase from 11.9 to 12.6%, the convection losses reduce from 8.0 to 4.5%. Convection losses increase with wall temperatures, which are less than linear. The small increase in re-radiation loss is due to the dominance of reflection losses off of the particles and out the window as opposed to emission. At an outlet temperature of 757 K and 1070 K for the fluxes of 300 and 900 kW m^{-2}, respectively, emission is only 10 and 44%, respectively, of the magnitude of the reflected flux. For solar inputs $\geq$ 1100 kW m^{-2}, η_{solar} falls off as radiation losses grow faster than the convection loss percentages fall.

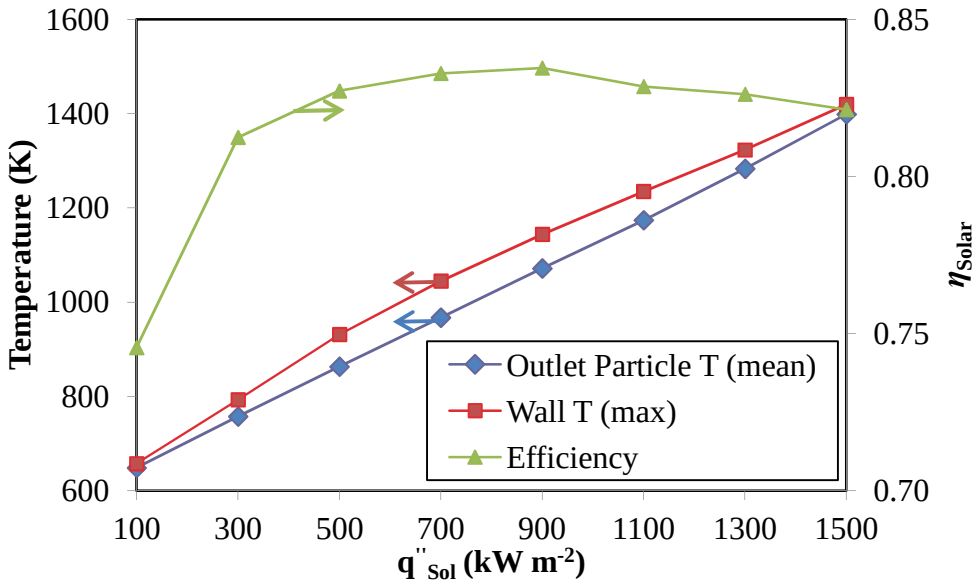

Figure 2-29 – Particle outlet temperature, maximum receiver temperature, and overall efficiency for varying inlet solar flux ($\dot{q}''_{Sol}$).

One final design variable investigated is changing inlet temperature. As expected, both η_{solar} and ΔT_p fall off as inlet temperature increases, as shown in Figure 2-30, due to increased radiation losses. Figure 2-31 shows how the particle and wall temperatures increase with particle inlet temperature. At high enough inlet temperatures, the particle outlet temperature eventually exceeds the maximum wall temperature. This occurs because the degree the impact of particle re-radiation on wall heating relative to direct solar radiation leads to slower increases in wall temperatures than particle temperatures.

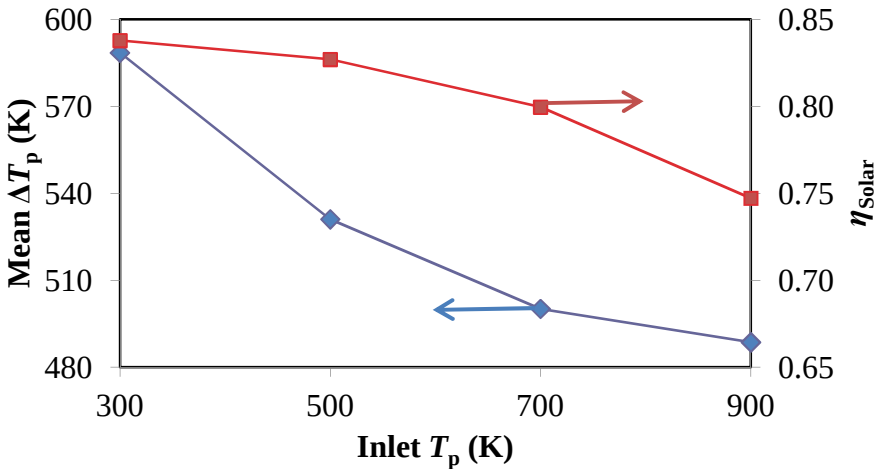

Figure 2-30 – Change in particle temperature between entrance and exit and overall efficiency plotted as a function of varying particle inlet temperature.

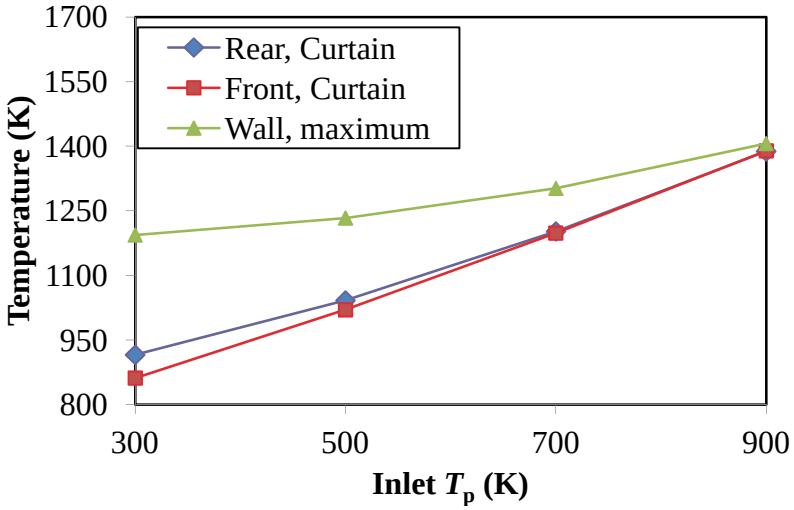

Figure 2-31 – Maximum wall and particle outlet temperature plotted as a function of particle inlet temperature.

2.5.3 Discussion

The primary metrics for evaluating receiver performance are overall receiver efficiency, η_{solar}, and particle outlet temperature, $T_{p,out}$. The total plant energetic efficiency is multiplicative for each individual step, as shown in Eq. 2-38, which includes η_{solar}.

$$\eta_{total} = \eta_{field}\eta_{solar}\eta_{storage}\eta_{power} \quad \text{[Eq. 2-38]}$$

For reference, the US DOE's Sunshot Initiative has set a target for η_{solar} at more than 90% (US DOE, 2014). The CSP power-cycle efficiency η_{power} generally increases with the receiver outlet temperature, but increasing receiver temperature can reduce η_{solar}. The optimal receiver design point for η_{total} can be a complex trade-off between these trends. As such, modeling efforts like the one here can assess receiver performance over a wide operational range to help in optimizing integrated plant performance.

Particle size impacts overall receiver performance for many reasons. The results in Figure 2-12 to Figure 2-20 indicate that smaller particles achieve higher efficiencies and higher temperatures due to a combination of higher curtain opacity and longer residence time. As shown in Eq. 2-29, transmission scales with $\exp\left(-\frac{1}{d_p u_p}\right)$ when $\dot{m}'_p$ and ρ_{p} are kept constant. Thus, not only do smaller particles thus block more radiation due to decreased d_{p}, they also obtain greater opacity by falling slower.

Despite the positives of smaller particle size, they have drawbacks. While this study is unable to capture the effects the internal flow-field on individual particles, the influence that internal gas-flow has on the particles must be taken into account. At the particle size regime used in this study, the Stokes number, which characterizes the independence of the particles flow from the surrounding gas flow, is proportional to d_{p}^2, As Stokes number decreases, the particles are more influenced by individual gas eddies, and the particle curtain becomes less stable with increased likelihood that individual particles recirculate within the receiver. Prior studies such as that done by Meier (1999)

in a 2D domain have shown that particles much smaller than 300 μm are susceptible to flow interruption by wind gusts through an open aperture and recirculation cells that form inside the receiver. Thus, for smaller particles, careful design must be employed to prevent particle loss. The velocity profiles for the falling particles are very different than a typical profile for a single particle. While individual particles quickly reach a terminal velocity, streams of particles do not reach a constant velocity anytime along the flow involved due to entrainment and gas velocity increases due to particle drag.

Particle mass flow-rate is an important operating variable for both steady-state as well as transient operation. Particle mass flow-rate can be changed quickly away from an operating point in response to variations in solar input. For steady-state operation, increasing mass flow-rate is beneficial for the efficiency as curtain opacity grows with particle density. However, higher mass loadings reduce the mean particle outlet temperature and increase the temperature disparity between the front and back. While this trend holds for any set of operating conditions, the results shown here are specific to the operating point shown. For 280 μm particles, an increase in $\dot{m}'_p$ from 10 to 20 kg $s^{-1}m^{-1}$ gains only 0.9% in η_{solar} while decreasing $T_{p,out}$ by 101 K. For 697 μm particles, η_{solar} improves by 2.7% and $T_{p,out}$ decreases by 119 K when increasing $\dot{m}'_p$ from 10 to 20 kg $s^{-1}m^{-1}$. Up to a certain flow rate, increases in mass-flow improve η_{solar} due to increases in curtain opacity. After the curtain is dense enough to absorb almost all of the radiation, further gains in efficiency are primarily tied to lower emission losses. In general, η_{solar} levels off when the curtain transmissivity drops below 30% along the fall, as seen from Figure 2-16 and Figure 2-28. While a considerable amount of solar radiation passes through the curtain at 30% transmissivity, the cavity nature of the receiver and high wall

reflectivity in the solar spectrum ($\rho_{\lambda,m}$ = 0.8 for λ < 4.5 μm) allows the curtain to still absorb a majority of this radiation. This behavior helps to explains how ΔT_{part} varies with efficiency in Figure 2-25, which provides a valuable tool in refining the design space for the receiver.

The importance that curtain transmissivity plays in the accuracy of these results calls into question the empirical fitting used for curtain thickness Δz_c in Eq. 2-30. Because this value appears in the equation for volume fraction, Eq. 2-26, as well as the equation for transmissivity, Eq. 2-29, inaccuracies in Δz_c could affect the results. However, because the volume fraction f_v is inversely proportional to Δz_c, and is multiplied by Δz_c directly in Eq. 2-29, the end result is that the Δz_c has no effect on the transmissivity. Thus, curtain thickness primarily affects the model results through the gas-phase balance equations.

While receiver mean outlet temperature is important, in many cases the uniformity of particle heating has a significant impact upon the usefulness of the particle outlet stream for downstream processes. From the perspective of the receiver, a curtain with hotter particles in the front will be less efficient, as these particles will lose more radiation through the aperture than particles with a uniform distribution. While certain conditions do allow the rear of the curtain to be hotter, these occur under non-ideal conditions where curtain transmissivity is high and significant wall-heating leads to higher losses through the aperture. For inert, sensible heat storage, temperature gradients within the particles may be acceptable as particles will equilibrate their temperatures while in close contact during storage. For reactive particles, however, temperature

gradients can be very harmful as reaction equilibrium and rates are strongly affected by the particle temperature.

A few things can be done to maintain total curtain absorption while mitigating transverse temperature gradients in the particle curtain.. Using smaller particles at lower mass-flow rates can achieve the same total absorption as larger particles with higher flow-rates, but with the benefit of higher mean temperatures and lower temperature differences between front and back. Operating at higher temperatures improves inter-curtain heat-exchange.

Finally, under many operating conditions with higher mean outlet temperatures, the receiver walls reach temperatures that may exceed material survivability limits. The maximum wall temperature observed among inert-receiver tests is 1572 K, well below the 2033 K melting point of the Duraboard material. Despite this, high temperature gradients applied cyclically can lead to eventual material failure. Thus, it is important to maintain high curtain opacities to avoid the highest temperatures and gradients that occur in the rear of the receiver. If curtain opacity curtain is too low, it may be possible to install a heat-exchanger along the rear wall to recover that heat and conduct it away from the back to pre-heat particles and avoid such large temperature gradients.

2.6 Modeling Results for Commercial-scale Receiver with Grey-body Emissions

While results for the prototype-scale are helpful for investigating the physical phenomenon in receiver operation, full-scale receiver simulations are necessary to further actual designs. To this end, simulations of such a receiver with geometric dimensions and operating conditions provided by Sandia National Labs (Ho, 2014), were performed.

These studies used inert particles with a wide range of grey-body emissivities in order to aid in selection of particle operating materials. The geometric dimensions, operation conditions, and critical material properties specified for this study are presented in Table 2-4. Only the particle grey-body emissivities are changed in the model. This design is sized for a 100 MWe solar plant with 220 MWt of solar energy input through the solar receiver aperture. This radiation was prescribed with a uniform profile, which is a reasonable estimation for such a large aperture size.

Table 2-4 – Baseline property values used in full-scale grey-particle calculations.

Property	Value (Baseline)
Receiver Dim. (m) ($L_{x,r}$, $L_{y,r}$, $L_{z,r}$)	(12.0, 21.0, 15.0)
Aperture Dim. (m) ($L_{x,a}$, $L_{y,a}$, $L_{z,a}$)	(11.0, 20.0,-)
Curtain Dimensions (m) ($L_{x,c}$, $L_{y,c}$, $L_{z,c}$)	(11.0, 21.0, 0.04+0.0087·y)
d_p (μm)	280
$\dot{m}'_p$ (kg/s-m)	44.0
ρ_{part} (kg/m^3)	3560
ε_p (-)	0.1-0.9
$T_{p,in}$ (K)	600
$\dot{q}''_{solar}$ (kW/m^2)	1000

2.6.1 Numerical Grid

Based on the results of the prototype-scale receiver, a rather coarse numerical grid for the Eulerian flow solver was employed for the full-scale receiver calculations. The model employed 8 cells in the horizontal direction and 21 cells in the fall direction for the particle curtain. With the 8 cells in the horizontal direction, the temperature difference

between the side and middle due to wall-interaction effects was calculated to be less than 15 K for all cases. Along the length of fall, 21 cells enabled accurate capture of the fall-direction temperature increase via linearization within each cell without increasing computational cost. For the full scale receiver, mass flow rates over 20 kg s^{-1} m^{-1} produced highly opaque particle curtains such that all incoming radiation is either absorbed or reflected in the front-half of the curtain. With the assumption of uniform solar flux through the aperture, the total heat-source received in the directly radiated zone by the particles is relatively constant. Further, simulations were performed by increasing the fall-direction cells to 42 and 84 cells, and the maximum difference in particle outlet temperatures is less only 4.2 K and 2.4 K, respectively. Thus, the 21 cell grid is used for its computational savings.

2.6.2 Results

For this full-scale receiver, temperature profiles for the walls and curtain are shown for three different emissivity values in Figure 2-32 to Figure 2-36. All these figures show a clear divide in temperature profiles between the front and rear half of the receiver, due to difference is radiation interaction with the curtain that falls in the middle. The hottest part of the receiver occurs on the front-lip around the aperture, which receives reflected radiation most directly (with highest view factor) from the particle curtain. The maximum temperature in this area decreases monotonically from 1624 to 1302 K as the emissivity increases from 0.1 to 0.9. Going backwards in the receiver along the left and right wall, the temperature initially drops and then increases again for the lowest emissivity (ε = 0.1) case shown in Figure 2-32. This occurs due to difference in view

factors, as the wall starts to “see” the reflected radiation less going backwards due to an increase in angle away from the curtain normal, followed by another increase as the wall closes its proximity to the side of the curtain and receives that incident radiation. This temperature distribution is still clear at an emissivity of 0.5 in Figure 2-34, but is gone at the highest emissivity ($\varepsilon = 0.9$) shown in Figure 2-36. As emissivity increases, the dense particle curtain absorbs more of the incoming solar radiation, leaving less to be diffusely redirected onto the walls. At the same time, absorbing more radiation in the particles increases their temperature and thus emissive power. Because radiation emission scales with εT^4, the highest emissivity particles ($\varepsilon = 0.9$) with a maximum temperature of 1292 K give off 93 times as much radiation as the lowest emissivity particles that achieve a maximum temperature of 718 K.

After the sharp-divide at the location of the particle curtain, the receiver wall temperatures appear to be approximately uniform. The irradiance curves likewise show nearly uniform profiles in these areas, and with magnitudes that correspond with their temperature which clearly varies between each case. While the back half of the receiver receives no direct solar irradiation, and the rear-half of the curtain provides no source, energy enters this region through two means: radiation from the front-half of the walls that get around the curtain, and conduction along the wall. Energy in the back half gets spread evenly by radiation heat transfer, which obtains 60 and 15 times the heat transfer rate between walls as conduction and convection losses through the walls at 1300 K and 750 K, respectively.

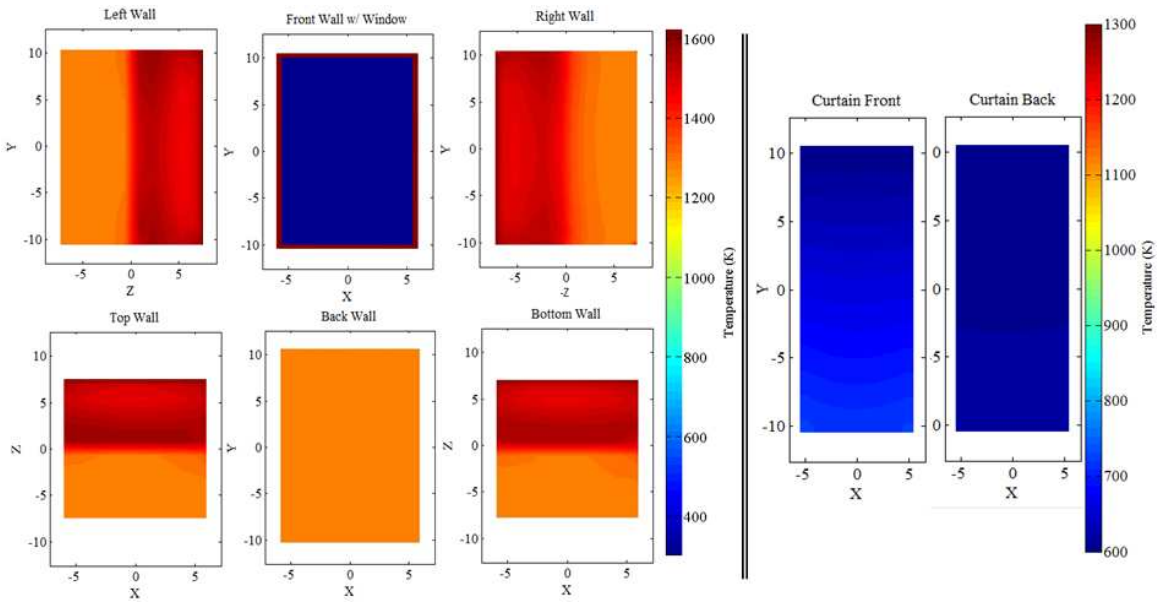

Figure 2-32 – Full-scale receiver wall and curtain temperature profiles using grey particles with operating conditions shown in Table 2-4 and ε_p = 0.10.

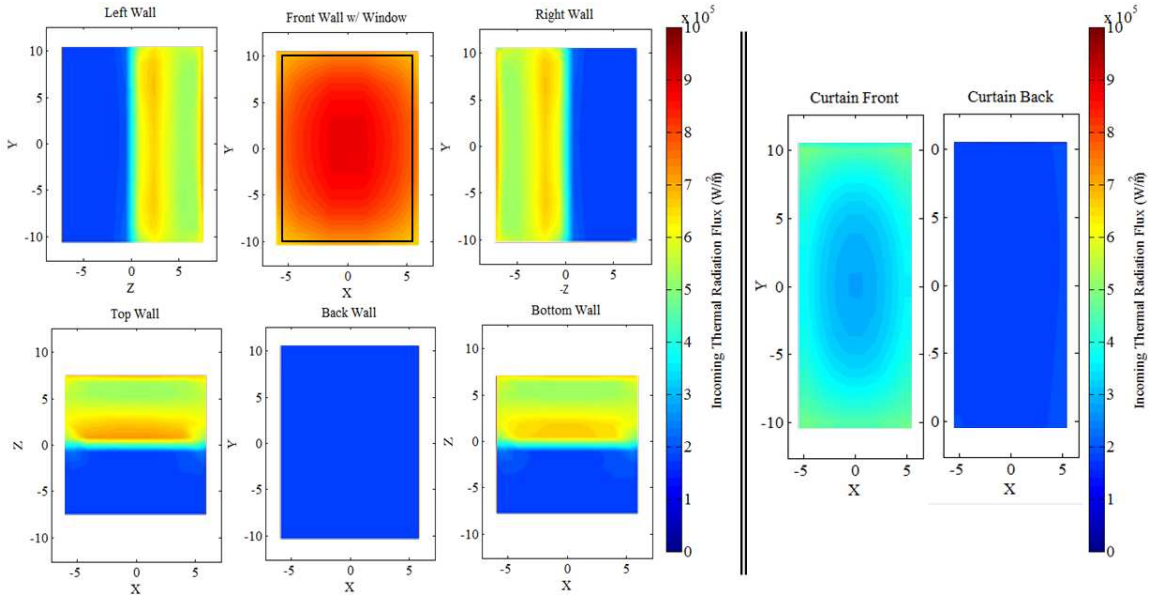

Figure 2-33 - Full-scale receiver wall and curtain incoming thermal radiation flux (W m^{-2}) profiles using grey particles with operating conditions shown in Table 2-4 and ε_p = 0.10 The black box in the front wall panel indicates the aperture area.

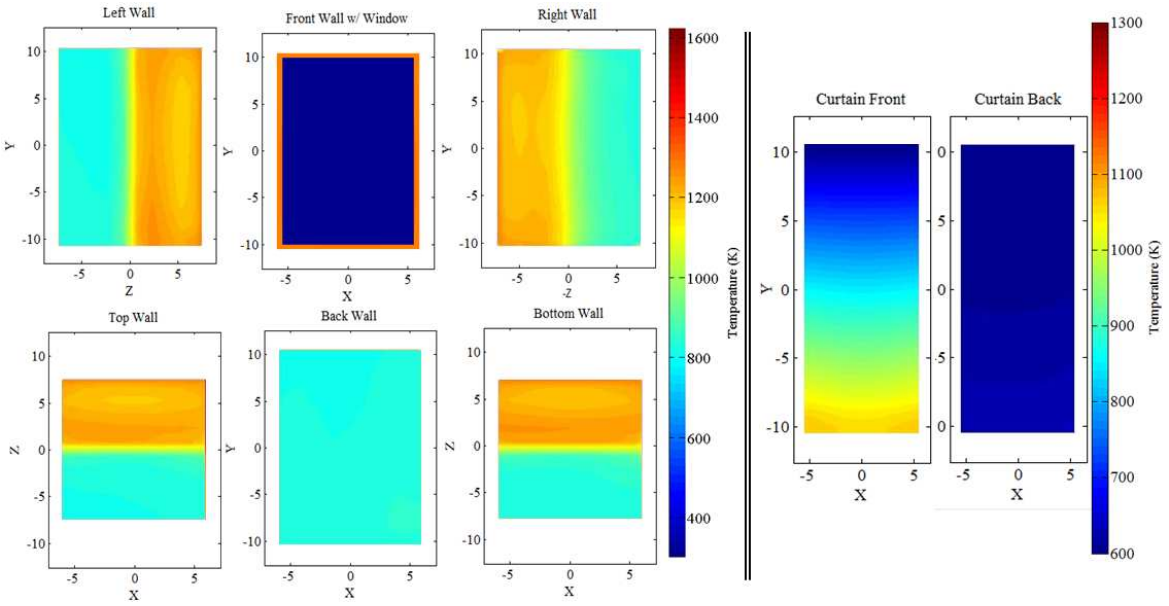

Figure 2-34 - Full-scale receiver wall and curtain temperature profiles using grey particles with operating conditions shown in Table 2-4 and ε_p = 0.50.

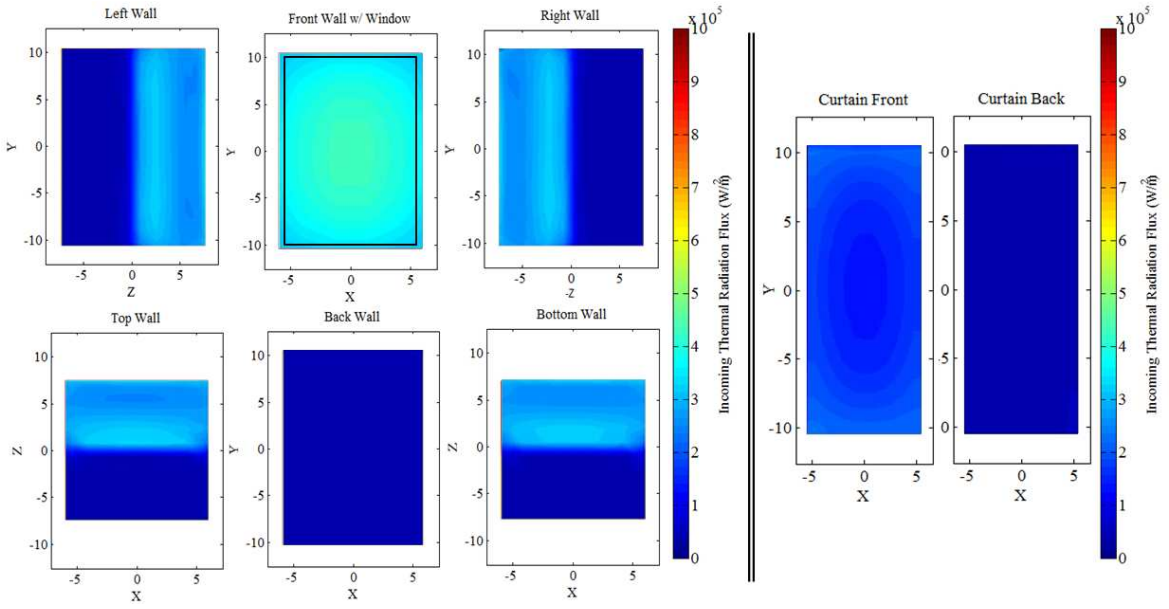

Figure 2-35 - Full-scale receiver wall and curtain incoming thermal radiation flux (W m^{-2}) profiles using grey particles with operating conditions shown in Table 2-4 and ε_p = 0.50. The black box in the front wall panel indicates the aperture area.

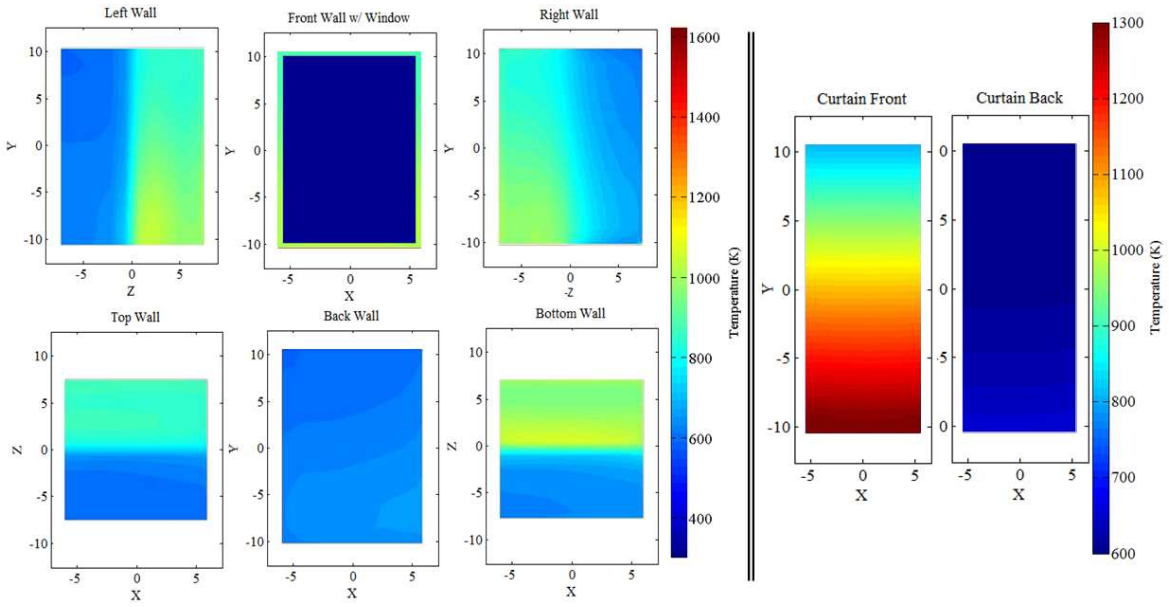

Figure 2-36 - Full-scale receiver wall and curtain temperature profiles using grey particles with operating conditions shown in Table 2-4 and ε_p = 0.90.

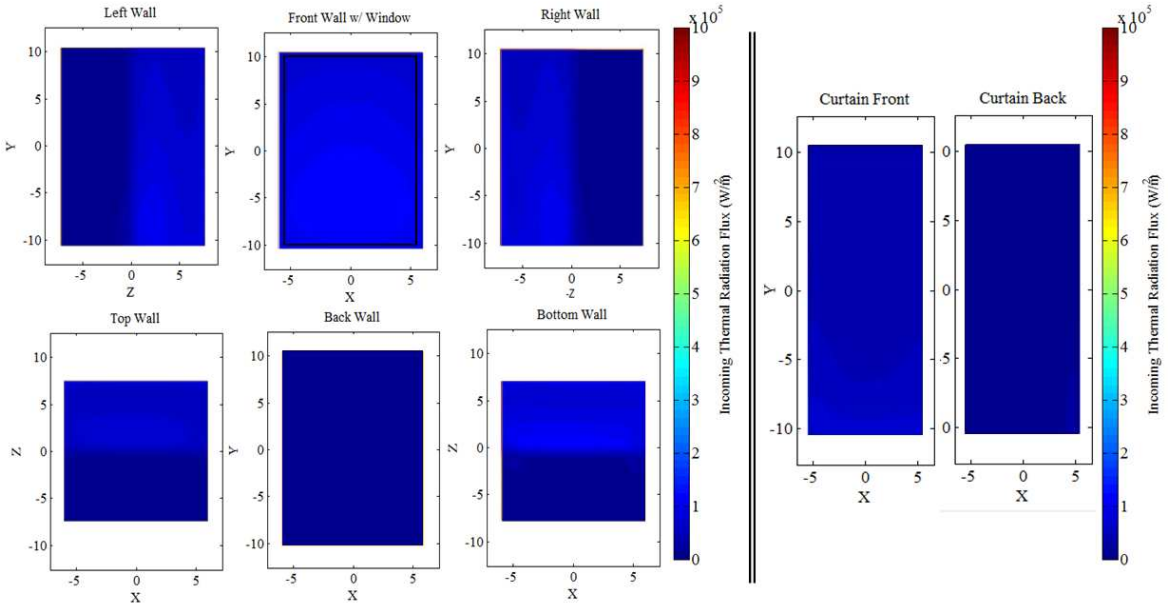

Figure 2-37 - Full-scale receiver wall and curtain incoming thermal radiation flux (W m^{-2}) profiles using grey particles with operating conditions shown in Table 2-4 and ε_p = 0.90. The black box in the front wall panel indicates the aperture area.

Comparing Figure 2-32, Figure 2-34, and Figure 2-36 shows the impact of ε_p on both the particle curtain and wall temperatures. In order to facilitate comparison, the mean temperatures for both the front-half and rear-half of the curtain are plotted in Figure 2-38. For this receiver geometry, the front curtain temperatures increase monotonically even after the directly irradiated zone. This occurs due to two phenomenon, one of them real, and one of them numerical. With lower ε_p, hotter receiver walls (relative to the particles) continue to provide heat to the particles after leaving the directly irradiated zone. For higher ε_p, the walls are colder than the particles, this heating is due entirely to the given cell discretization still having part of its length in the partially irradiated zone. Due to the numerical scheme involved, that heat is spread out between the particles entirely within that cell. Within the directly irradiated zone, the particle temperatures increase almost linearly, due to a constant solar flux. Even for T_p = 1200 K and ε_p = 0.9, the incoming solar flux is 9.5 times the emission from the particles.

The rear curtain temperature profiles in Figure 2-38 shows continued heating after the directly irradiated zone. This heating occurs from wall radiation and internal curtain heat exchange. At these mass flow rates, the incoming solar radiation is either absorbed or reflected by the front half of the curtain, as demonstrated in the prototype-scale results. For lower ε_p, the rear of the curtain is slowly heated almost entirely by radiation from the hotter walls, as indicated most clearly in Figure 2-33. As ε_p increases, the rear walls become cooler and reduce their heating of the particles. At ε_p = 0.5, the rear walls are about 300 K hotter than the rear curtain and provide very little heat. While wall heating is reduced with increasing ε_p, internal curtain exchange between the front and back of the

curtain increases dramatically. This explains the rear temperature profiles for ε_p of 0.7 and 0.9. Those cases show little heating along the first half of the fall when the particle temperatures are still low, but as the particle temperatures increase, the exchange between the front and rear of the curtain increases by a factor of 16 due to T^4 scaling.

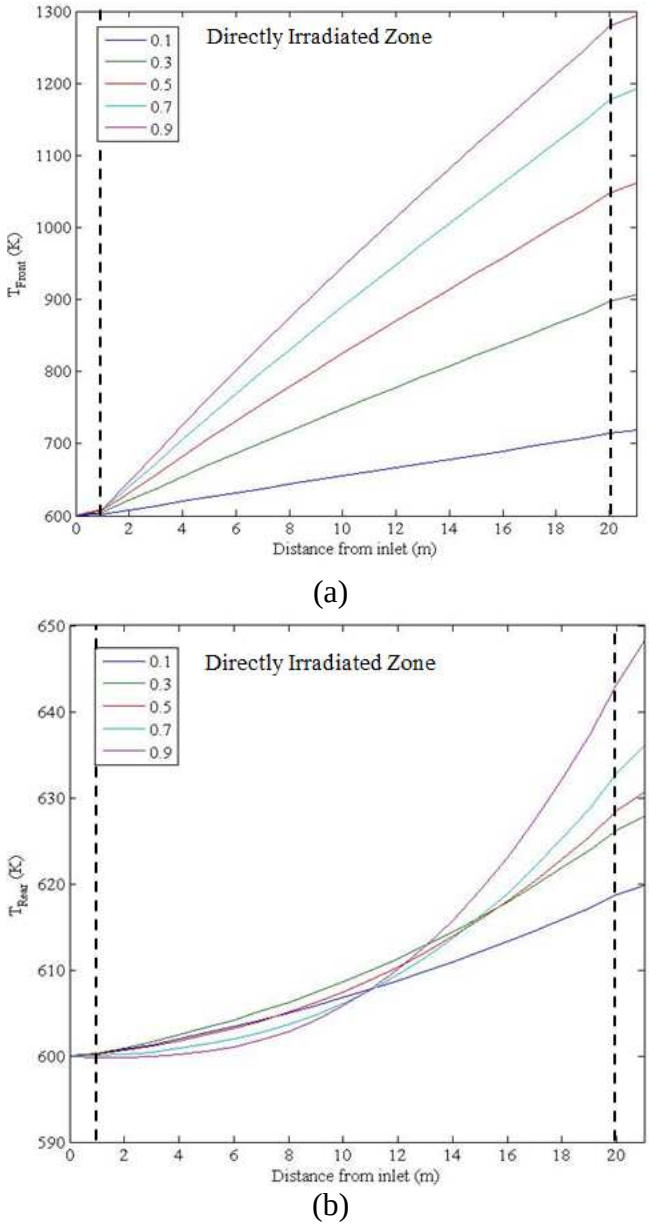

Figure 2-38 – Commercial-scale mean curtain T_p profiles along the length of fall in the (a) front-half and (b) back-half of the curtain, with varying ε_p = 0.1-0.9 as-shown. Note the difference in temperature scales for each plot.

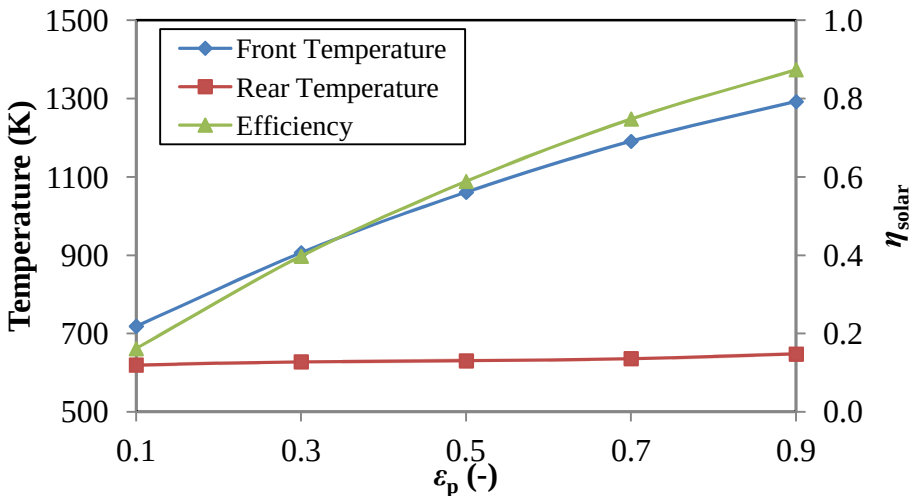

Figure 2-39 - Receiver curtain temperatures and efficiency values for full-scale receiver operating at varying gray-body particle emissivity values.

As with the prototype receiver, the full-scale receiver η_{solar} and $T_{p,out}$, increase monotonically with ε_p, as shown in Figure 2-39. η_{solar} at ε_p = 0.9 approaches the 90% target efficiency for the DOE SunShot Initiative. Despite such high efficiencies, the rear-curtain temperatures remain very low, even for the highest emissivity cases with less than 100 K temperature rise over the fall of the receiver.

2.6.3 Discussion

The results for the grey-body commercial-scale receiver are indicative of the mass-flows with 40 kg s^{-1} m^{-1}. Curtain opacity is high enough at these mass-loadings that almost no direct solar radiation even reaches the rear half of the curtain. This not only dictates the shape of the rear-temperature profiles, but also the wall temperatures. Lower emissivity leads to higher wall temperatures, as fluxes on the walls are dominated by reflections. Because of the high mass loading, when ε_p, is low, very large fractions (as much as 90% near the center of the curtain) of the incoming solar energy are reflected

back out the aperture. As the ε_p increases, the fraction of energy reflected back out the front decreases, but re-radiation losses increases. However, reflective losses are more than an order of magnitude larger than re-radiation, and thus, increasing emissivity always improve efficiency and outlet temperature. Thus, it is important that particles that are as black as possible to maximize solar absorption.

For the mass loadings, the rear curtain in this receives minimal direct solar radiation. Thus, the efficiency could be maintained with higher outlet temperatures at lower mass flow-rates, closer to 10 or 20 kg s^{-1} m^{-1}. Lower mass flow-rates would also improve uniformity of the curtain temperature profile.

A major shortcoming in the high mass-flow receiver is the wasted material usage of the rear-half of the curtain. If it were possible to increase internal curtain heat exchange, it would be possible to increase η_{solar} by at least 2%, as predicted by simulations that enforced such a condition. With the baseline conditions and geometry here, all of the heat is absorbed in the front-half of the curtain, and radiation losses are much higher because the heat is not spread as readily to the rear of the curtain.

2.7 Impacts of Solar Selectivity on Large-scale Receiver Performance

To maximize performance, this study investigated the potential for spectrally selective particle to reduce radiant emission losses. Spectral selectivity implies a material emissivity ε_λ that changes with wavelength, λ. The potential benefit of a selective particle can be illustrated in Figure 2-40, which compares the solar irradiation with spectral emittance of blackbodies at different temperatures characteristic of the receiver particles. Ideally, selective particles would have very high emissivity in the visible spectrum

(around the peak of the solar source irradiance) and low emissivity at higher wavelengths (where the particle emittance exceeds the solar irradiance).

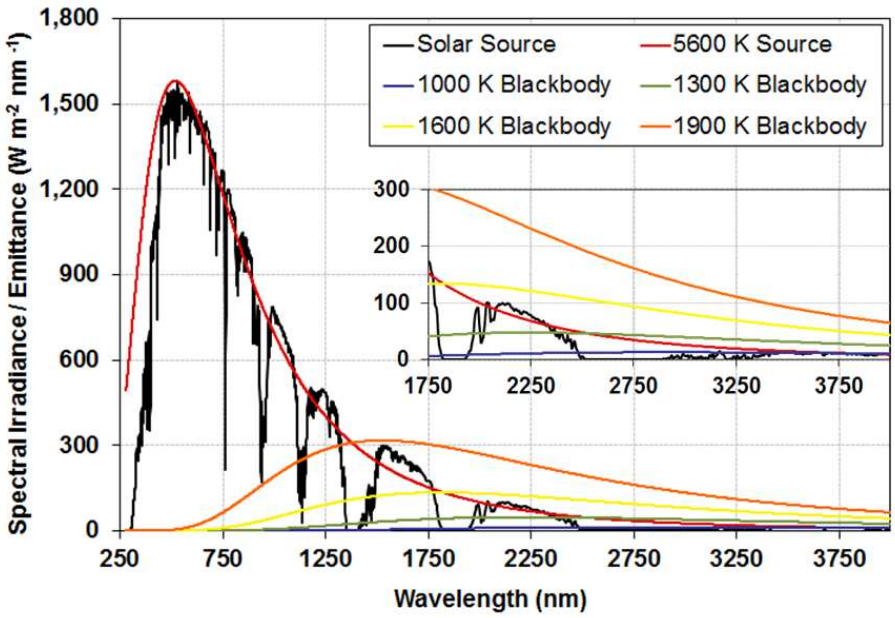

Figure 2-40 – Spectral irradiance as a function of temperature for particles at different operating temperatures compared to incoming solar source (scaled to 1000 suns concentration).

To study the effects of selective ε_p, the same grid, geometry, and operating parameters used for the commercial-scale receiver and displayed in Table 2-4 were employed. However, unlike the grey-particle studies, the emissivity was split spectrally above and below λ = 2.5 μm. For lower λ, the selective emissivity $\varepsilon_{p,\lambda_1}$, associated with the visible and near-infrared radiation, was fixed at 0.9 to capture the maximum solar energy. For λ > 2.5 μm associated with mid- and far-infrared radiation, the selective emissivity $\varepsilon_{p,\lambda_2}$,varied between 0.1 and 0.9.

2.7.1 Results

Wall and particle temperature contours are shown in Figure 2-41 to Figure 2-43. As $\varepsilon_{p,\lambda_2}$,increases, the front and side wall temperatures increase with the front curtain temperatures. The maximum wall temperature, at the bottom wall near the particle exit, increases from 920 to 1091 K as $\varepsilon_{p,\lambda_2}$ increases from 0.1 to 0.9. Particle temperatures reach near 1300 K at the receiver exit and for the high $\varepsilon_{p,\lambda_2}$ particles; particle emissive radiation to the walls at these temperatures competes with the reflected solar energy. For $\varepsilon_{p,\lambda_2}$ = 0.9, particle emittance accounts for nearly 59% of the radiosity leaving the curtain, but decreases to 16% for the most selective particles.

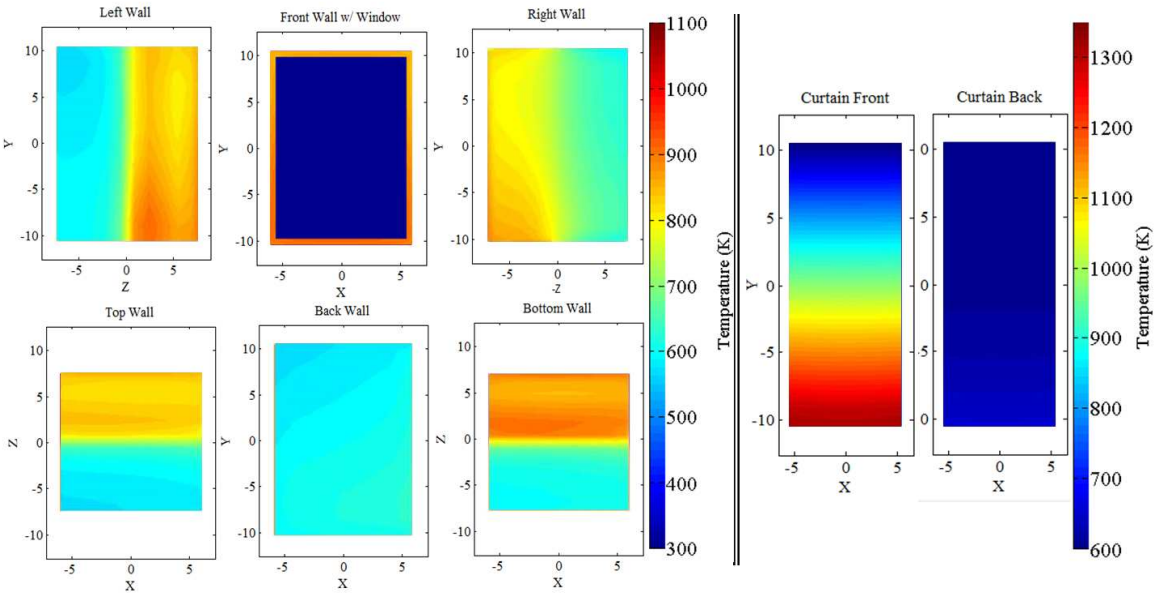

Figure 2-41 - Full-scale, inert-particle receiver wall and curtain temperature profiles using selectively emissive particles with $\varepsilon_{\lambda<2.5\mu m}$ = 0.1. Operating Parameters: T_{in} = 600 K, d_p = 280 μm, $\dot{m}_p$ = 44 kg/s-m, Q_{solar} = 1000 kW/m^2.

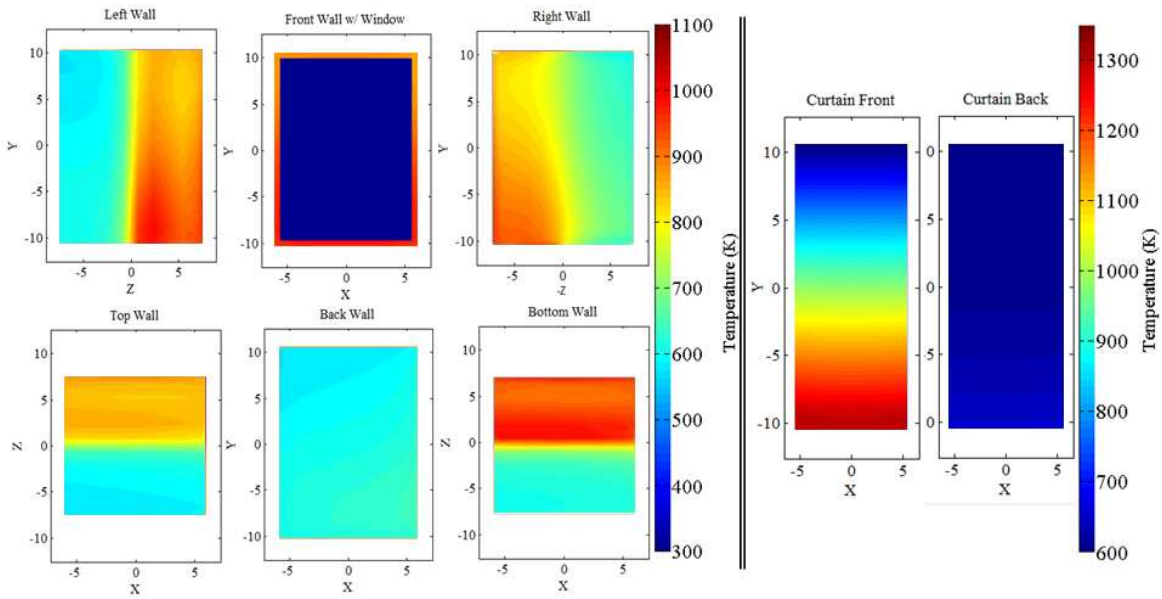

Figure 2-42 - Full-scale, inert-particle receiver wall and curtain temperature profiles using selectively emissive particles with $\varepsilon_{\lambda<2.5\mu m} = 0.5$ and operating parameters shown in Table 2-4.

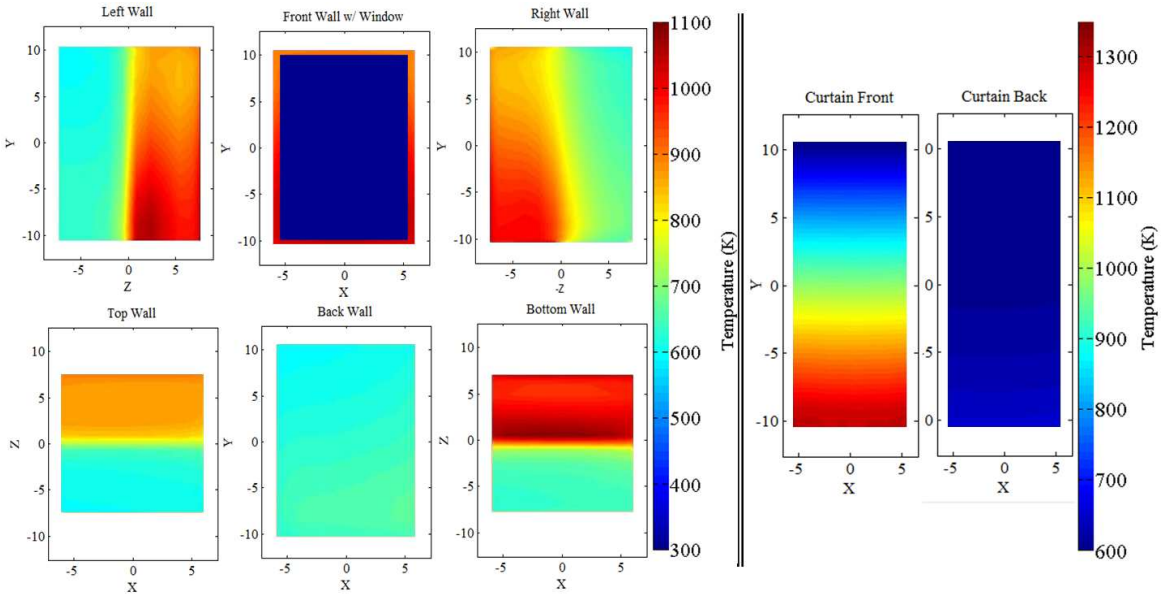

Figure 2-43 - Full-scale, inert-particle receiver wall and curtain temperature profiles using selectively emissive particles with $\varepsilon_{\lambda<2.5\mu m} = 0.9$ and operating parameters shown in Table 2-4.

Despite the large impact that selectivity has on the wall-temperatures for these run conditions, the particle temperature remains relatively constant at the exit. In fact, the front-curtain temperature decreases by only 13 K, corresponding to efficiency decrease of 1.4% between the most-selective particles and the grey particles, as shown by changes in q_{particle} in Table 2-5. Further, the loss in efficiency is entirely attributable to increases in radiation losses. If inter-curtain heat-exchange is increased such that the front and rear maintain an equal temperature throughout the fall, by applying a model proposed by Roger et al. (2011), outlet temperatures reach just over 970 K with less than 0.7% improvement by decrease high-wavelength emissivity from 0.9 to 0.1.

Table 2-5 – Performance comparison for selective particles inside full-scale receiver using the ASTM solar irradiance distribution.

Performance Measure	Units	IR emissivity, $\varepsilon_{p,\lambda 2}$ (λ > 2.5 µm)				
		0.1	0.3	0.5	0.7	0.9
q_{particle}	(-)	0.892	0.888	0.884	0.881	0.878
q_{air}	(-)	0.005	0.005	0.005	0.005	0.005
$q_{\text{loss,radiation}}$	(-)	0.090	0.094	0.098	0.101	0.104
$q_{\text{lost,convection}}$	(-)	0.012	0.012	0.012	0.013	0.013
$T_{\text{particle,out (front)}}$	K	1307	1303	1300	1296	1294
$T_{\text{particle,out (rear)}}$	K	648	648	648	648	648

2.7.2 Impacts in Choosing Solar Source

The results and trends for receiver operation are sensitive to the selection of solar source, to the point that using a 5600 K source can actually give conflicting results on the trends and value of using selective particles depending on the run conditions. For the

operating conditions used for the commercial-scale receiver, the results shown in Table 2-6 indicate that selectivity has no significant change in efficiency or outlet temperature. While the difference in numbers is small, the trend for the data is indicates that adding selectivity is actually harmful to performance when a 5600 K receiver is used. This occurs because emission of radiation for wavelengths longer than 2.5 μm from a particle around 1000 K is only 47.5 kW m^{-2}, while solar radiation flux about 37.1 kW m^{-2} in this band. Because most of the fall-distance is emitting at a temperature lower than 1000 K while absorption of the 37.1 kW m^{-2} is impacted over the whole length of fall, selectivity actually shows a conflicting trend for the 5600 K source compared to the ASTM solar source.

Table 2-6 – Performance comparison for selective particles inside full-scale receiver using a 5600 K distribution for solar energy.

Performance Measure	Units	IR emissivity (λ > 2.5 μm)				
		ε_λ = 0.1	ε_λ = 0.3	ε_λ = 0.5	ε_λ = 0.7	ε_λ = 0.9
$q_{particle}$	(-)	0.874	0.877	0.878	0.878	0.878
q_{air}	(-)	0.005	0.005	0.005	0.005	0.005
$q_{loss,radiation}$	(-)	0.109	0.107	0.106	0.105	0.104
$q_{lost,convection}$	(-)	0.013	0.013	0.013	0.013	0.013
$T_{p,out\ (front)}$	K	1292.5	1294.4	1294.9	1294.9	1294.9
$T_{p,out\ (rear)}$	K	645.7	646.5	647.0	647.3	647.5

2.7.3 Discussion

The most important conclusion that can be drawn from these tests is that solar selectivity is not a worthwhile endeavor to develop for receivers operating in this

temperature regime, unless receiver wall temperatures are unsuitably high. While ideal selectivity does lead to an improvement in efficiency of up to 1.4% and 5 K in mean outlet temperature, there are other methods of improvement that have potential to yield more significant results with less difficulty. For instance, prototype-scale results indicate that improving the emissivity of a grey particle by only 0.03 achieves a similar result. This is especially true given that particle selectivity is sensitive to the cutoff wavelength used in design.

The ideal wavelength-cutoff value is near 2.5 μm for the operating temperatures exhibited in this receiver, as 99.1% of the terrestrial solar energy in the ASTM solar spectrum is contained below 2.5 μm. If the cutoff frequency is reduced to 2.0 μm, total performance decreases as the particles become more selective, with a reduction in efficiency of 0.5% when particle long-wavelength emissivity is decreased from 0.9 to 0.5. This occurs because 3.2% of solar energy is contained between 2.0 and 2.5 μm. If the cutoff wavelength is increased above 2.5 μm, the benefit of selectivity is decreased, although results are not as sensitive to changes as they are for reductions in the cutoff wavelength. Increasing the cutoff wavelength to 3.0 μm covers only 0.05% of the ASTM solar spectrum.

The ideal wavelength cutoff value depends on receiver operating temperature, which for this configuration is driven by front-curtain temperatures as opposed to mean curtain temperatures. This value can be found by using curves such as those in Figure 2-40, where the ideal cutoff wavelength for a desired operating temperature occurs at the point where the emittance curve crosses the ASTM solar irradiance curve. Thus, for an

operating temperature of 1300 K the ideal cutoff frequency is close to 2.4 μm, while the ideal cutoff frequency is 1.8 μm for an operating temperature of 1600 K.

While solar selectivity is probably not worth it for particles that achieve a maximum temperature of only 1300 K, Figure 2-40 shows that the potential for selectivity strongly depends on operating temperature. If the particle inlet temperature is increased to 900 K, front curtain temperatures around 1600 K are achieved. Under these conditions, highly selective particles ($\varepsilon_{\lambda>2.5\ \mu m}$=0.1) can achieve mean temperature increases of over 30 K and efficiency increases of 4.7% versus grey particles, even at a less than ideal cutoff frequency of 2.5 μm for that operating temperature.

Another case in which particle selectivity can become more important is if the degree of solar concentration is reduced (thus shrinking the irradiance curves in Figure 2-40). Under these cases, the potential for selective particles grows, and the ideal cutoff frequency at any temperature shifts. Thus, the importance of selectivity depends on a complex interplay between the strength of the irradiance and the operating temperature of the receiver. This is why solar collectors for sunlight with no concentration benefit from selective surfaces just as much as very high-temperature receivers under high concentration.

The results for a 5600 K source differ, and even show conflicting trends at lower temperatures, because, although the general shape is similar to the ASTM solar source, atmospheric absorption is not captured. This is especially visible - referring to Figure 2-40 - at wavelengths above 2.5 μm, where absorption due to water vapor, CO_2, O_2, O_3, and other components results in almost complete loss of insolation for the ASTM source.

While only 0.87% of total energy occurs above 2.5 μm for the ASTM solar source, 3.71% is contained in these higher bands for the 5600 K source.

2.8 Conclusion

In this study, a simulation model was developed and presented for characterization of primary physical interactions within a falling-particle receiver. This model features a 3D radiation exchange model coupled to one-dimensional falling-particle model with a semi-empirical gas entrainment model. Results obtained demonstrate not only the general state of the receiver during operation, but also the interplay between the key performance metrics of efficiency and mean outlet temperature. Receiver efficiency is closely tied to properties such as curtain transmissivity along the length of fall, which is directly influenced by particle size and mass flow-rate. Particle outlet-temperature is affected by a complex combination of mass flow-rate, curtain transmissivity, solar power-input, particle size, and radiation properties. In most cases, there is a tradeoff between efficiency and particle temperature, not only because of increased radiation emission at higher temperature, but also due to curtain absorption affects.

Prototype receiver results demonstrate that particle size is a key variable, and should be kept as low as possible to both increase curtain absorption and particle residence time to obtain higher temperatures more efficiently. However, while not captured in this study, it is noted that particle-curtain stability is negatively impacted by decreasing particle size, and must be taken into account in any final design.

Particle flow-rate plays a very important role in dictating particle curtain opacity, but, as both prototype and commercial-scale results demonstrated, also affect particle outlet temperature and temperature gradients within the particle curtain. However, results demonstrated that there are diminishing returns on efficiency by increasing particle flow-rate, while particle outlet temperature is significantly reduced and curtain gradients increased. While internal curtain gradients can be accepted in some applications, they have a negative impact in most. Alleviating curtain gradients while maintaining total efficiency requires both optimization and design changes.

Particle grey-emissivity should be maximized to increase particle mean outlet temperature, increase receiver efficiency, and decrease temperature gradients within the curtain. At both the prototype and commercial-scale, increased absorption from the particles decreases wall temperatures because, although emission is increased, reflection onto the front walls decreases the hotspot that develops there. Solar selectivity has the potential to improve receiver performance, but that potential is very dependent on solar flux levels and operating temperature of the receiver. Simple solar irradiance and particle emittance curves can be used to quickly evaluate such potential, with simulations being used for greater clarity.

Overall, inert-particle receivers have great potential to achieve high temperatures and efficiencies during operation, but require careful design in order to perform to ideal standards. The complex interplay between particle-flow properties and performance creates a diverse design space for potential receiver architectures. Future work should consider testing methods to maintain high curtain opacities while reducing temperature gradients in the curtain as an effective way to improve overall receiver performance. This

is especially true for a version of this receiver architecture that may be applied to reacting particles, which are very sensitive to local particle temperatures. A few suggestions have been made in this regard, and hold promise for future improvement. Future chapters of this thesis will look at the performance of reactive particles with the currently proposed architecture.

Chapter 3: Modeling Reactive Particle Receivers

Concentrated solar power (CSP) plants with central tower receivers are an attractive renewable energy system capable of not only making renewable electricity, but also driving high-temperature, endothermic chemical processes, such as splitting H_2O and/or CO_2 for fuel production. Such processes may require temperature inputs > 1000 K in order to achieve adequate kinetic rates for chemical conversion. Many developed receiver designs have lower operating temperatures (< 900 K for commercial plants utilizing molten salt), but solid-particle receivers have been proposed as an approach for efficiently achieving higher temperatures, in excess of 1000 K (Tan and Chen 2010). These higher receiver temperatures can drive endothermic chemical process, such as fuel production or integrated thermochemical storage coupled to a more efficient power-cycle. This paper explores the design of a central tower receiver to capture solar energy in falling cerium oxide ($CeO_{2-\delta}$) particles through both sensible heating and high-temperature oxide reduction. The reduced $CeO_{2-\delta}$ particles can be reoxidized in a separate reactor by splitting CO_2 and/or H_2O as part of a solar fuel production plant as proposed in several previous studies (Chueh and Haile 2010, Lapp et al. 2012, Scheffe and Steinfeld 2012).

Recent research and development on receivers using direct heating of solid particles have demonstrated the effectiveness of sub-mm diameter particles to directly absorb incident solar radiation (Siegel et al. 2010, Tan and Chen 2010). Particle receivers have many advantages for solar energy capture and storage with operating temperatures well above the limits of molten salts and other storage media. Particle receiver designs can mitigate many thermal stress issues associated with fixed storage media if the

particles are transported through a simple, open geometry (Kim et al. 2009, Siegel et al. 2010). Some proposed particle receiver configurations utilize absorption of solar heat in tubular reactors, which encapsulate the particle flow and allow for controlled environments (Maag et al. 2009, Martinek et al. 2012), but these arrangements do not provide as rapid heating as receiver designs with direct particle irradiation. Direct particle irradiation can provide quick response to transients, superior part-load operation, and extended daily hours of operation through faster start-up (Röger et al. 2011). Combining high temperatures and the potential of operation for several hours, directly irradiated particle receivers are an attractive architecture for integration into a fuel-production process involving endothermic reactions such as H_2O or CO_2 splitting to form H_2 or CO respectively (Gokon et al. 2008, Schunk et al. 2008, Chueh & Haile 2010, Lapp et al. 2012, Scheffe and Steinfeld 2012), $CaCO_3$ decomposition (Meier 1999) or CH_4 reforming or carbonaceous material gasification (Dahl et al. 2004, Z'Graggen et al 2006, Martinek and Weimer 2013).

Various reaction schemes based on particle reactors have been investigated for incorporation into CSP plants, including those reviewed by Kodama and Gokon (2009) and Roeb et al. (2012). Many researchers have explored two-step redox cycles involving solar-driven oxide reduction at high-temperatures and a lower-temperature reoxidation of the oxide via H_2O and/or CO_2 splitting. The ceria redox cycle, with lower temperature ceria reoxidation via H_2O splitting to form H_2, is shown here in reactions R. 3-1 and R. 3-2 and represented schematically in Figure 3-1:

$$CeO_2 + \text{heat} \rightarrow CeO_{2-\delta} + \delta/2\ O_2 \qquad \text{[R. 3-1]}$$

$$CeO_{2-\delta} + \delta\ H_2O \rightarrow CeO_2 + H_2 \qquad \text{[R. 3-2]}$$

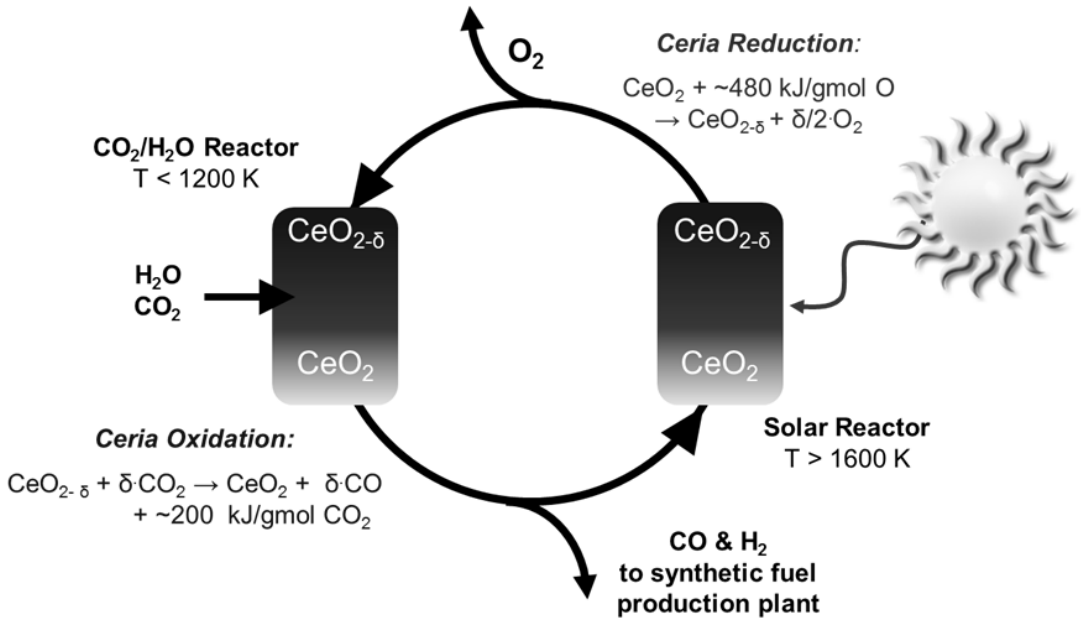

Figure 3-1 – Illustration of the ceria water-splitting cycle. The solar step shows endothermic reduction of ceria at high temperatures and low P_{O2} to evolve oxygen. In a later, lower-temperature step ceria is exothermically re-oxidized to produce CO/H_2.

This redox cycle is attractive because ceria can maintain its cubic fluorite structure through relatively high degrees of reduction (δ): as high as 0.3 (Zinkevich et al 2006). Some ceria cations are reduced from a Ce^{4+} state to a Ce^{3+} state in the high-temperature receiver. By avoiding phase transitions, ceria particles have the potential for reliable performance through large numbers of redox cycles (Chueh and Haile 2010, Scheffe and Steinfeld 2012, Venstrom et al. 2012). On the other hand, the high

temperatures (> 1400 K) associated with ceria reduction have encouraged researchers to explore dopants of the form $Ce_{1-x}M_xO_{2-y}$ (where M is a cation such as Zr) to lower temperatures for the reduction reaction R1 and thereby reduce re-radiation losses and costs associated with such high-temperature receiver operation (LeGal & Abanades 2012, Scheffe & Steinfeld 2012). However, ceria dopants explored to date including Zr (Kaneko et al. 2009, Petkovich et al. 2011, Scheffe et al. 2013, Gibbons et al. 2014), Sc (Lee et al. 2013, Scheffe et al. 2013), Pr (Meng et al. 2012), and Hf (Scheffe et al. 2013) still require temperatures above 1400 K, which presents real challenges on particle receiver designs.

While researchers have explored a variety of material structures for ceria reduction in solar receivers including ordered and disordered porous structures (Chueh et al. 2010, Furler et al. 2012, Rudisill et al. 2013, Gibbons et al. 2014), falling ceria particles provide a unique approach to mitigate structural sintering that plagues fixed structures. However, to date, little work has explored what particle receiver designs might provide an effective means for efficient ceria particle reduction. Development of high-temperature particle reactors requires design and analysis tools that can effectively evaluate performance and accurately capture the close coupling between many complex processes such as multi-phase flow, radiation and convective heat transfer, and heterogeneous chemistry. Modeling challenges are increased because of limited access to accurate physical, chemical, kinetic, and optical data for the relevant materials in the high-temperature regime necessary for reduction.

Several authors have studied particle receivers for inert sensible energy storage and these studies provide a basis for exploring particle receiver designs for ceria

reduction. Chen et al. (2007) studied inert particle receivers and demonstrated tradeoffs between higher outlet temperatures and higher receiver efficiencies in a solid particle receiver by varying particle size and particle flow rate. These results motivated initial designs for further experimentation with inert particle receivers (Siegel et al. 2009). The knowledge from these inert particle receiver studies and the understanding from redox-cycle studies provide a basis for evaluating the feasibility of particle receivers for solar-driven ceria redox cycles. For ceria-based redox cycles, Lapp et al. (2012) highlighted the importance of solid heat recovery in improving redox cycle efficiencies and lowering optimal receiver temperature. Chueh et al. (2010) also showed the importance of minimizing heat loss in ceria-based redox cycles and indicated the possibility of efficiencies of 16-19% without heat recovery by minimizing thermal losses. However, Rager (2012) has disputed these performance values highlighting the necessity to properly account for purge-gas and other parasitic losses, which can be quite substantial.

This study combines insight and understanding gained from inert particle receiver models with knowledge of material properties and requirements for ceria redox cycles. The study presents a model of reacting ceria-particle receiver wherein falling particles are both heated and reduced at adequately high temperatures. The receiver geometry follows closely a design for an inert particle receiver for thermal energy storage (Siegel et al. 2010), but incorporates a window enclosure in order to maintain low O_2 partial pressures for enhanced ceria reduction. In this study, the model is used to investigate the influence of particle size, solar concentration, particle flow-rate, and inlet-temperature on thermochemical energy storage in the reduced ceria particles. The model results provide the basis for identifying underlying principles that can guide future particle-

receiver/reactor development and for assessing the technical feasibility for using CSP plants to drive ceria-based redox cycles for renewable fuel production. In this study, undoped ceria is used for reduction because of its attractive properties and well-understood thermochemical properties. Receiver modeling is carried out by extending significantly the model of Röger et al. (2011) for inert-particle receivers to include the impacts of reaction and more detailed particle-gas coupling.

3.1 Modeling Cerium Dioxide Reduction Thermo-kinetics

Incorporating ceria reactions into the particle receiver model first requires a suitable thermo-kinetic model that captures the particle equilibrium and kinetic evolution over a wide range operating conditions. Ceria reduction depends on local oxygen partial-pressure and temperature, and simulating the reduction process requires a thermodynamic model that can capture these dependencies.

3.1.1 Ceria species

The thermodynamic model implemented for ceria is based on the work of DeCaluwe (2009) for use in solid oxide fuel cells. Partially reduced ceria $CeO_{2-\delta}$ is represented as a mixture of unreduced cerium, Ce_2O_4, and reduced cerium, Ce_2O_3, where the reduction reaction is shown in R. 3-3. Defining the species in this way follows the recommendation of Adler et al. (2007) to represent reacting species as a mixture of charge-neutral states.

$$Ce_2O_4 \rightarrow Ce_2O_3 + 0.5\ O_2 \qquad \text{[R. 3-3]}$$

For surface thermodynamic states, high-temperature Xray photoelectron spectroscopy (XPS) studies of ceria surfaces by DeCaluwe et al. (2010) showed that the thermodynamics of ceria reduction on the surface differed greatly from reduction in the bulk. Species on the surface and near-surface are impacted by non-ideal interactions caused by differences in electronic structure. Atomistic simulations of undoped ceria surfaces by Sayle et al. (1994) have shown that ceria possesses low-energy (111), (110), and (310) surfaces with more facile vacancy formations that extend through 10 Å into the bulk. As such, the ceria on the surface and in the extended sub-surface has different thermodynamic properties for species with increased surface reducibility. Thus, the ceria is modeled in three zones each with unique thermodynamics: (1) a monolayer surface of adsorbed oxygen, O(s), and oxygen vacancies $V_O(s)$; (2) a sub-surface comprised of $Ce_2O_4(sb)$ and $Ce_2O_3(sb)$ species that extends 10 Å away from the surface; and (3) the remaining bulk ceria comprised of $Ce_2O_4(b)$ and $Ce_2O_3(b)$.

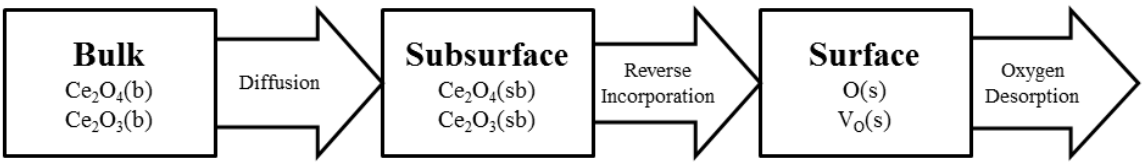

Figure 3-2 – Ceria species and reaction schematic used to represent the evolution of ceria within a particle.

These ceria species reacts as shown in Figure 3-2: oxygen diffuses through the bulk into the subsurface, transforming $Ce_2O_4(b)$ into $Ce_2O_3(b)$ and $Ce_2O_3(sb)$ into $Ce_2O_4(sb)$. From the sub-surface, oxygen undergoes the reverse of the incorporation

reaction, transforming surface vacancies ($V_O(s)$) into surface-adsorbed oxygen (O(s)) and reduce the subsurface $Ce_2O_4(sb)$ to $Ce_2O_3(sb)$ as shown in R. 3-4.

$$Ce_2O_4(sb) + V_O(s) \rightarrow Ce_2O_3(sb) + O(s) \qquad \text{[R. 3-4]}$$

On the surface, two adsorbed oxygen sites interact to form $O_2(g)$ and leave behind oxygen vacancies $V_O(s)$, as shown in R. 3-5.

$$O(s) \rightarrow V_O(s) + 0.5\ O_2(g) \qquad \text{[R. 3-5]}$$

3.1.2 Ceria thermodynamics

As mentioned previously, ceria reduction depends strongly on temperature and O_2 partial pressure. Mogensen et al. (2000) integrated equilibrium ceria reduction from many different researchers over a wide range of experimental conditions to extract the free-energy change of reduction, $\Delta\mu_{red} = \mu_{Ce_2O_3} - \mu_{Ce_2O_4}$, for R. 3-3 by using Eq. 3-1 which is derived from the fact that, at equilibrium, $\Delta\mu_{rxn} = 0$.

$$\Delta\mu_{rxn} = \mu_{Ce_2O_3}(\delta,\mathrm{T}) - \mu_{Ce_2O_4}(\delta,\mathrm{T}) + \frac{1}{2}\left[\mu^0_{O_2}(T) + \overline{R}T\ln\left(\frac{P_{O_2}}{P^0}\right)\right] \qquad \text{[Eq. 3-1]}$$

Once $\Delta\mu_{red}$ is found, it is possible to find both the enthalpy and entropy of reduction, Δh_{red} and Δs_{red} by using $\Delta\mu_{red}(T,\delta) = \Delta h_{red}(T,\delta) - T\Delta s_{red}(T,\delta)$. This is done by using

curves of constant-δ, which are shown in Figure 3-3. In this figure, the slope of the line at any point gives Δs_{red} while the intercept at T = 0 K gives Δh_{red} .

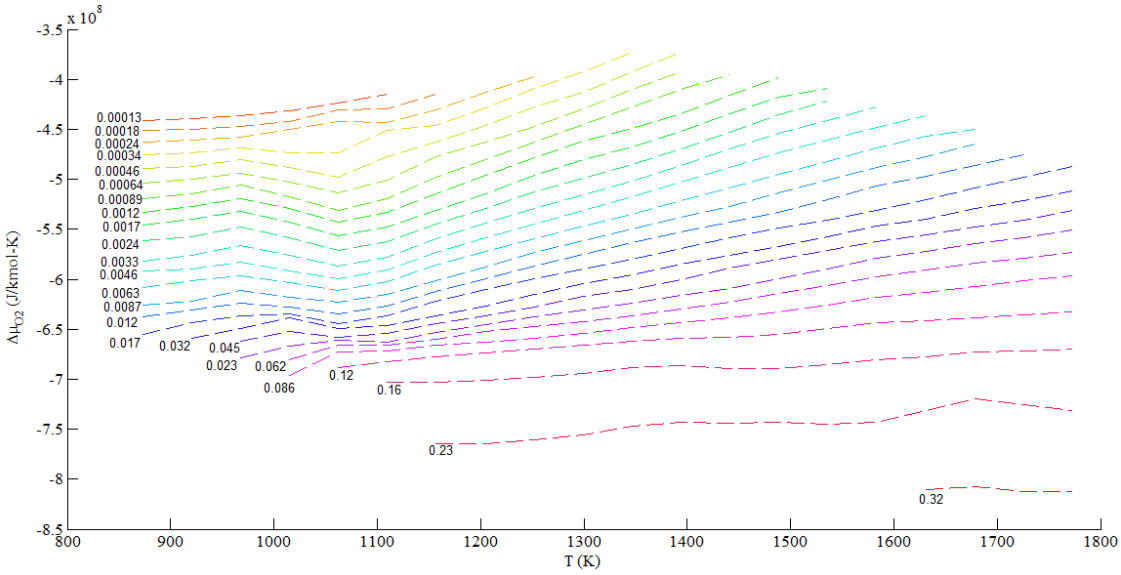

Figure 3-3 - Chemical potential change for reduction for undoped ceria along lines of constant-δ found using the data from Mogensen et al. (2000)

With these basic thermodynamic properties, individual species properties are extracted so that the thermodynamic description can be amenable to kinetics scheme employed (as discussed in more detail later). To do this, it is necessary to split the change in chemical potential of reaction into three components as shown in Eq. 3-2: an ideal component that changes only with temperature, $\Delta\mu_{red}^{0}(T)$; an excess component that accounts for ideal interactions, $\Delta\mu_{red}^{ex,0}(T,\delta)$; and a component that accounts for excess energy due to non-ideal interactions, $\Delta\mu_{red}^{ex}(T,\delta)$.

$$\Delta\mu_{red}(T,\delta) = \Delta\mu^{0}_{red}(T) + \Delta\mu^{ex,0}_{red}(T,\delta) + \Delta\mu^{ex}_{red}(T,\delta) \quad \text{[Eq. 3-2]}$$

In order to obtain the ideal chemical potential change of reduction $\Delta\mu^{0}_{red}(T)$, it is necessary to define ideal-state properties for each species at an appropriate reference state. The reference state is set as fully oxidized Ce_2O_4 at room temperature. For the reference species in the bulk, sub-surface, and surface, specific heat $c_{P,k}$ of the species must be fit as a function of temperature. The remaining thermodynamic properties, those corresponding to the ideal entropy s_k^0 of the species, are fit by choosing a reference temperature where $s_k^0 = 0$. From these reference values, the ideal state of any complementary species derived via reaction, such as Ce_2O_3 for instance, can be calculated by using Δh_{red} and Δs_{red} at the chosen reference temperature and a reference δ value to complete the ideal thermodynamic specification of the materials.

With ideal-state thermodynamics fully specified, the remaining thermodynamic parameters in Eq. 3-2 can be found. To do this, it is necessary to define excess change in chemical potential due to ideal interactions, $\Delta\mu^{ex,0}_{red}(T,\delta)$, and the non-ideal excess, $\Delta\mu^{ex}_{red}(T,\delta)$. The ideal excess potential is defined as the chemical potential-change due to mixing from a dilute solution model, as in Eq. 3-3. This is necessary in order to maintain thermodynamic consistency with the chosen kinetic model. With this specification, the excess free-energy change due to non-ideal interactions can be found using Eq. 3-2.

$$\Delta\mu^{ex,0}_{red}(T,\delta) = RT\ln\left(\frac{X_{Ce_2O_3}}{X_{Ce_2O4}}\right) \quad \text{[Eq. 3-3]}$$

3.1.3 Bulk-ceria thermodynamic fitting

Various thermodynamic models can be used to numerically capture the thermodynamics displayed in Figure 3-3. Because the thermodynamics are closely tied to the kinetics, the chosen model must be able to work over a wide range of temperatures and pressures in a way that is numerically stable. Further, as the specification of the surface reduction, shown later, depends on the reduction state at low temperatures, this fitting must maintain a reasonable degree of accuracy at low temperatures.

The first model suggested by DeCaluwe (2009) assumes that Δh_{red} and Δs_{red} are independent of temperature, and vary only with δ. This assumption is often applicable for many different solid species, as the energy and entropy changes from breaking bonds in a constant structure shows very little variation with temperature. Further, the justification of using this model for ceria can be seen by referring to Figure 3-3, which shows rather straight curves over a large range of parameters, especially at higher temperatures. The results of implementing this model are shown in Figure 3-4, which shows reasonably good performance at temperatures above 1273 K. However, at lower temperatures, this model drastically over-predicts the degree of reduction by many orders of magnitude. This should be expected given the shape of the curves in Figure 3-3 at lower temperatures shows clear non-linearities. Because of the requirement for performance at lower temperatures to allow surface-property fitting, this model was deemed unacceptable.

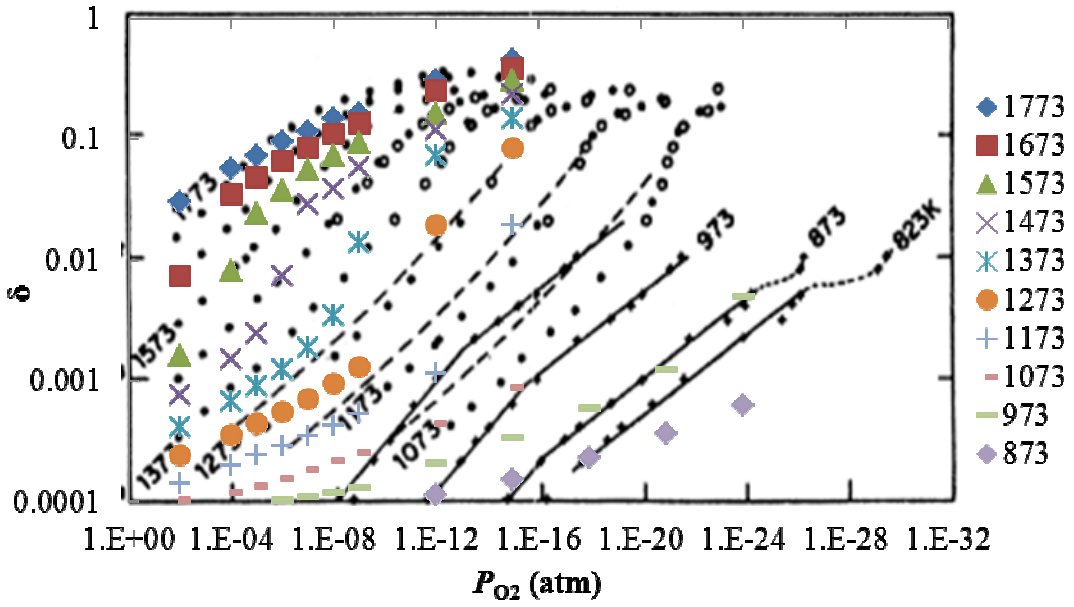

Figure 3-4 – Thermodynamic performance of constant Δh_{red}-Δs_{red} model compared to the results in Mogensen et al. (2000).

The ideal-state ceria thermodynamic properties were calculated by using the data from Reiss et al. (1985) and Morss and Konings (2004) to match the $c_{P,k}$ of Ce_2O_4. This was achieved by using a fitting with the form of NASA polynomial reference values, as shown in Figure 3-5, which has an R^2 of 0.99. Ce_2O_4(b), Ce_2O_4(sb), and O(s) at 25 °C were chosen as the reference state for the other ceria species. The ideal properties for Ce_2O_3(b), Ce_2O_3(sb), and V_O(s) are set based on Δh_{red} and Δs_{red} at δ = 0 and 25 °C, as shown in Table 3-1. The values of Δh_{red} and Δs_{red} at 1500 K and δ = 0 are also provided for reference.

Table 3-1 - Example of ceria thermodynamic values under select conditions.

Property	Units	Value @ 298 K	Value @ 1500 K
Δh_{red} @ $\delta = 0$	kJ/mol-K	460.4	440.1
Δs_{red} @ $\delta = 0$	J/mol-K	112.2	85.7

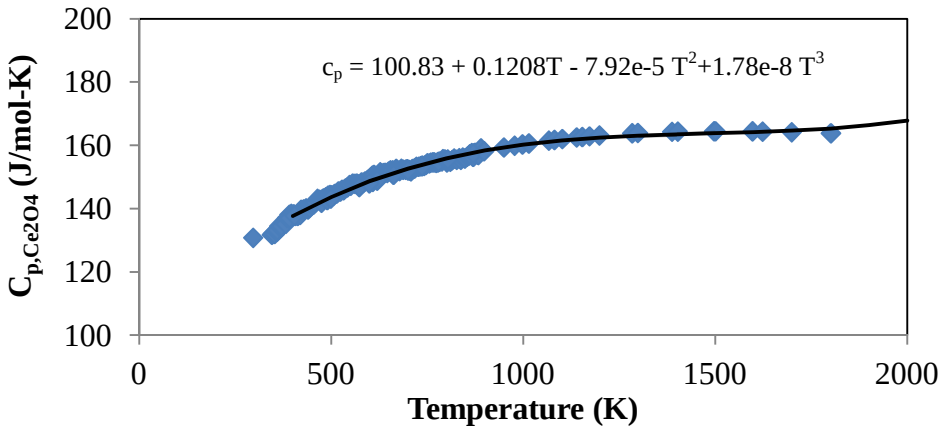

Figure 3-5 – Specific heat constant of Ce_2O_4 with experimental data (symbols) and fitting trend line (line). Experimental data from Reiss et al (1985) and Morss and Konings (2004).

There are more robust thermodynamic models available in the literature, such as those by Lindemer (1986), Hillert et al. (1986), and Zinkevich et al. (2006). Of these models, the one proposed by Zinkevich et al. (2006) is most flexible with reasonable agreement with data to temperatures below 1000 K as well as at higher temperatures. The Zinkevich et al. (2006) model includes a thermodynamic fitting for Ce_2O_4 and Ce_2O_3 species that follow the form of the SGTE Unary Database (Dinsdale, 1991). However, while applying the data by Zinkevich et al. (2006), it was discovered that the model over-predicted the degrees of reduction for ceria by a factor of two, indicating a mistake in their calculations. Further investigation showed that the individual species fittings were

correct, as were the ideal-mixing terms. Therefore, to overcome these errors, the Redlich-Kister terms used to calculate non-ideal interaction effects were refit to the results in Mogensen et al. (2000), as shown in Table 3-2 following the notation used in Zinkevich e al. (2006).

Table 3-2 - Refit thermodynamic interaction parameter used in-conjunction with the Zinkevich et al. (2006) model to capture undoped ceria reduction.

Thermodynamic Interaction Parameter	Re-fit value
${}^{0}L^{F}_{Ce^{3+},Ce^{4+}:O^{2-}}$	$-119172077.425+8141.955T$
${}^{0}L^{F}_{Ce^{4+},Ce^{3+}:Va}$	$190520937.599+457532705T$
${}^{1}L^{F}_{Ce^{3+},Ce^{4+}:O^{2-}}$	$-142153184.881+6421.794T$
${}^{1}L^{F}_{Ce^{4+},Ce^{3+}:Va}$	$207136935.7161-584499.249T$

Having refit these terms, the performance of the model set forth by Zinkevich et al. (2006) in predicting the equilibrium reduction of undoped ceria is evaluated, as shown in Figure 3-6. This model shows excellent agreement with the experimental data above 1000 K, even better than the constant Δh_{red} - Δs_{red} model. Moreover, the performance of the model below 1000 K is reasonable, and, although it under-predicts equilibrium reduction by as much as factor of 5, it does capture the slope of the low-temperature reduction curves. Thus, this model was chosen to provide a full-specification of the bulk undoped ceria thermodynamics.

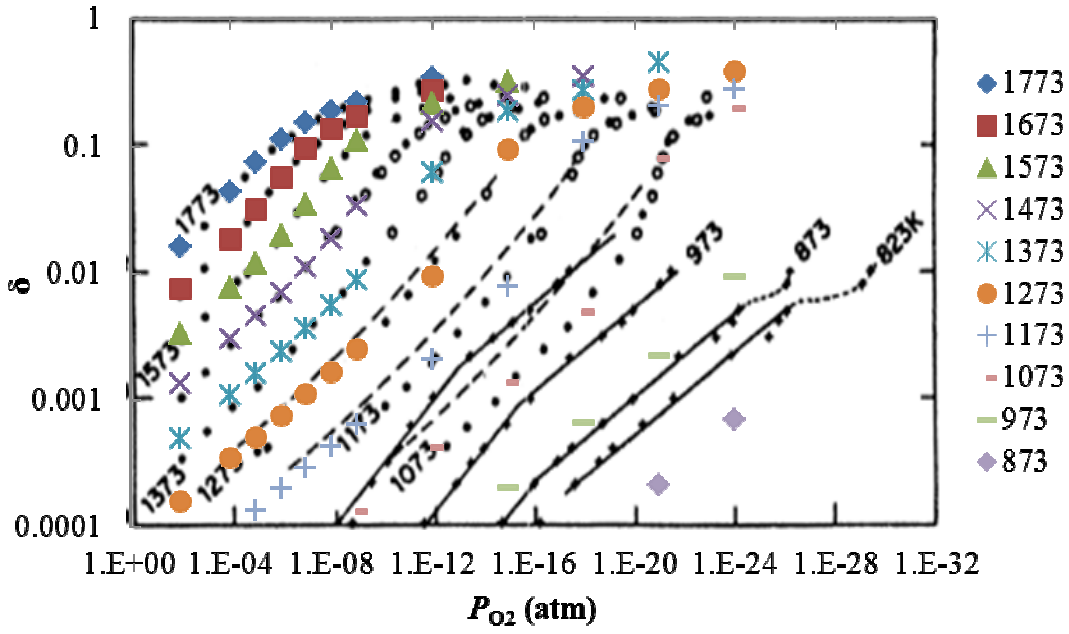

Figure 3-6 – Equilibrium degree of reduction prediction of the Zinkevich et al. (2006) undoped ceria model compared to the experimental results presented by Mogensen et al. (2000).

3.1.4 Surface-ceria fitting

Using the corrected bulk ceria thermodynamic developed by Zinkevich et al. (2006), it was possible now to fit the surface ceria thermodynamics to the data from DeCaluwe et al. (2010), which measures surface reduction at multiple temperatures between 920 K and 1020 K via in-situ XPS. These measurements provide a basis for comparison with bulk ceria reduction measured at the same temperature and P_{O2}, due to the fact that the surface and bulk must be in equilibrium under such conditions, resulting in Eq. 3-4.

$$\Delta\mu_{red,s}(T,\delta_s)-\Delta\mu_{red,b}(T,\delta_b)=0 \qquad \text{[Eq. 3-4]}$$

Interactions due to mixing and non-ideal effects are assumed to be consistent in the bulk and the surface at any given temperature and δ, although higher δ-values on the surface will increase the non-ideal interactions. Eq. 3-4 can be rewritten as Eq. 3-5, where the same functions, $\Delta\mu_{red}^{ex,0}(T,\delta)$ and $\Delta\mu_{red}^{ex}(T,\delta)$, were used for the ideal and non-ideal excess free-energy in the bulk and surface, although evaluated at their respective δ values.

$$\Delta\mu_{red,s}^{0}(T)-\Delta\mu_{red,b}^{0}(T)=\left(\Delta\mu_{red}^{ex,0}(T,\delta_b)+\Delta\mu_{red}^{ex}(T,\delta_b)\right)-\left(\Delta\mu_{red}^{ex,0}(T,\delta_s)+\Delta\mu_{red}^{ex}(T,\delta_s)\right) \qquad \text{[Eq. 3-5]}$$

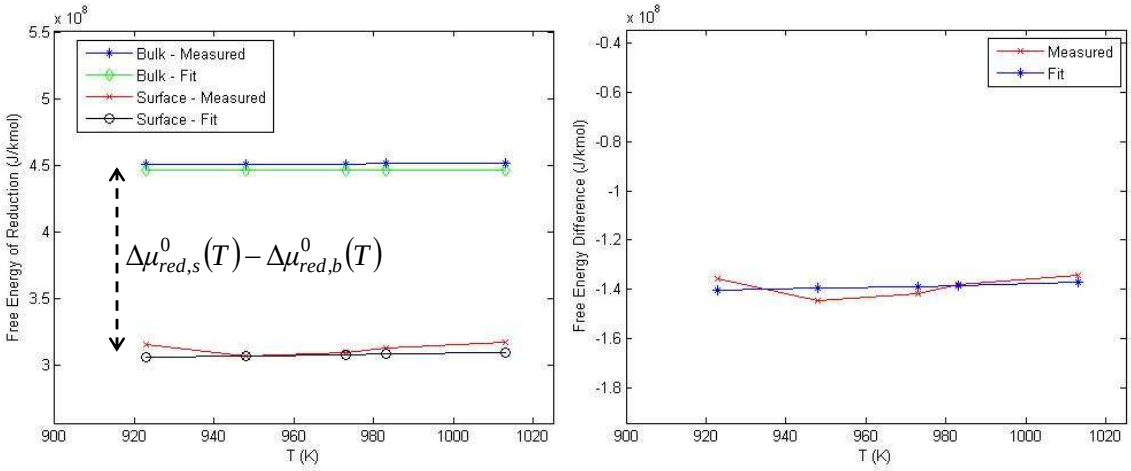

(a) (b)

Figure 3-7 – (a) Ideal chemical potential of reduction, $\Delta\mu_{red}^{0}(T)$, in the bulk and surface from the fitting and measurements (bulk from Mogensen et al., 2000 and surface from DeCaluwe et al.,

2010). (b) Plot of the change in chemical potential shift between the surface and bulk, $\Delta\mu^0_{red,s} - \Delta\mu^0_{red,b}$.

This transformation of the data resulted in Figure 3-7 (a). The shift in chemical reduction potential between the surface and bulk is shown in Figure 3-7(b) and is represented by a constant shift in enthalpy and entropy as shown in Eq. 3-6.

$$\Delta\mu^0_{red,s}(T) - \Delta\mu^0_{red,b}(T) = \left(\Delta h^0_{red,s} - T\Delta s^0_{red,s}\right) - \left(\Delta h^0_{red,b} - T\Delta s^0_{red,b}\right) \quad \text{[Eq. 3-6]}$$

The constant shift occurs because the temperature-dependence is fixed by the specific heat constant. The results from fitting the change in chemical potential to find the shift in enthalpy and entropy are shown in Table 3-3. The sub-surface thermodynamics were found by assuming half of the enthalpy and entropy shift exhibited by the surface.

Table 3-3 – Shift in thermodynamic values between the surface and bulk used to find the ideal surface thermodynamic fitting.

Thermodynamic shift	Value
$\Delta h^0_{red,s} - \Delta h^0_{red,b}$ (kJ/mol)	-173.616
$\Delta s^0_{red,s} - \Delta s^0_{red,b}$ (J/mol-K)	35.775

3.2 Model Description

3.2.1 Receiver Configuration

Simulations were performed on the same prototype-scale receiver in the inert studies reported in chapter 2 but with a high-temperature quartz window (5 cm thick) over the receiver aperture to provide an enclosed environment with a low O_2 partial pressure (P_{O2}) for reducing the ceria particles. By keeping the configuration otherwise identical, the results from inert simulations can be better used to draw insight relevant to reactive particle simulations.

3.2.2 Solid Particle Model

The solid particle model is modified from the inert simulations in order to accommodating particle reactions. The release of O_2 from the particle to the gas phase results in a transfer of mass that impacts gas-composition, momentum, and energy. A reacting particle model must capture the evolution of particle composition during the fall and the impact of the associated O_2 release on the surrounding gas flow. The reactions are strongly coupled to the rate of heat transfer to the particles since the degree of ceria reduction depends strongly on temperature.

The particle reduction is modeled with three steps: 1) diffusion of oxide ions from the bulk of the particle to a near surface region, 2) surface exchange of near surface oxides with surface-site vacancies (sometimes referred to as the reverse incorporation reaction), and 3) associative desorption of surface oxygen to O_2 into the gas phase. The first step is modeled as bulk oxide diffusion through a spherical particle, and the last two steps are modeled as reversible reactions. The diffusion and reaction models adapt ceria thermochemistry and oxide-ion transport from DeCaluwe and Jackson (2011) to calculate the rate of O_2 release from the falling particles in the receiver. The particle model is

coupled to the gas-phase flow model to predict the evolution of gas-phase P_{O2} around the particles as they fall through the receiver.

The particles are divided into three regions – a bulk region (signified by '(b)') consisting of almost all of the mass of the particle, a sub-surface region ('(sb)') consisting of a 5.4 nm shell near the surface (representing about 10 unit cells of the ceria fluorite structure), and a surface layer consisting of occupied and vacant sites for adsorbed oxygen ('O(s)' and 'V_O(s)' respectively). The bulk is modeled by the mole fractions of fully oxidized Ce_2O_4(b) and fully reduced Ce_2O_3(b), i.e., $X_{Ce2O4(b)}$ and $X_{Ce2O3(b)}$. Similarly, the sub-surface phase is modeled by mole fractions, $X_{Ce2O4(sb)}$ and $X_{Ce2O3(sb)}$. Since Ce_2O_4 and Ce_2O_3 are the only solid-phase species considered, the two mole fractions in each region sum to 1, and thus, the degree of reduction is captured by one mole fraction in each region, respectively $X_{Ce2O3(b)}$ and $X_{Ce2O3(sb)}$. Because only O_2 from the gas phase interacts with the ceria surface phase in this study, O(s) and V_O(s) are the only two surface species and the surface state is captured by the fraction of vacant sites $\theta_{Vo(s)}$.

Changes in composition for the bulk, sub-surface, and surface of the particle are tracked by species conservation equations, Eq. 3-7 to Eq. 3-9 below, which incorporate the diffusion flux at the bulk/sub-surface interface (j''_{diff}), the net rate per unit area of oxygen atom exchange between the subsurface and the surface ($\dot{n}''_{R1}$), and the surface desorption rate per unit area ($\dot{n}''_{R2}$).

$$\frac{dX_{Ce_2O_3(b)}}{dt} = \frac{a_b j''_{diff}}{\nu_b \bar{\rho}_b} \qquad \text{[Eq. 3-7]}$$

$$\frac{dX_{Ce_2O_3(sb)}}{dt} = \frac{\left(a_s \dot{n}''_{R1} - a_b j''_{diff}\right)}{v_{sb}\bar{\rho}_{sb}} \qquad \text{[Eq. 3-8]}$$

$$\frac{d\theta_{V_O(s)}}{dt} = \frac{\left(\dot{n}''_{R2} - \dot{n}''_{R1}\right)}{\Gamma_s} \qquad \text{[Eq. 3-9]}$$

The momentum balance for reactive particles is identical to the inert particles, and is repeated here for convenience in Eq. 3-10.

$$\frac{d\bar{u}_{y,p}}{dt} = \frac{3}{4}\frac{\rho_g}{\rho_p} C_D C_S \frac{\left(\bar{u}_{y,p} - \bar{u}_{y,g}\right)^2}{d_p} - \frac{\left(\rho_p - \rho_g\right)}{\rho_p} g \qquad \text{[Eq. 3-10]}$$

The governing equations for $X_{Ce2O3(b)}$, $X_{Ce2O3(sb)}$, and $\theta_{Vo(s)}$ (Eq. 3-7 to Eq. 3-9) and the average particle velocity $\bar{u}_{y,p}$ (Eq. 3-10) along the length of fall are integrated along the fall-direction length, *y*, with spatial steps small enough for the ode solver to hold relative residual tolerance of less than 10^{-6} for each time step. Because the particle temperature (T_p) and gas-cell properties (T_g, $\bar{u}_{y,g}$, Y_{O2}) are solved on a larger Eulerian mesh to facilitate 3D radiation transport models, their values are linearly interpolated between their cell-center values to provide a basis for calculating the transfer of momentum, O_2, and heat between the particles and the surrounding gas-phase flow. Interpolation of the gas-phase solution variables from the Eulerian solver, which is described below, enables adequate resolution of the gas temperature and P_{O2} field to model particle reaction rates and momentum transfer in the more-finely resolved Lagrangian particle model.

3.2.3 Particle Species Thermochemistry

To calculate the surface reaction rates, $\dot{n}''_{R1}$ and $\dot{n}''_{R2}$, and the oxide diffusion rate, j''_{diff}, in Eq. 3-7 to Eq. 3-9 for the particle model, undoped ceria thermochemistry and oxide transport properties as discussed in section 3.1, are used to calculate thermodynamically consistent rates for the reversible surface exchange and O_2 desorption reactions. These rate calculations modify standard mass-action kinetic rate laws by using concepts of transition-state theory and non-equilibrium thermodynamics, as proposed by Adler et al. (2007) and used in DeCaluwe (2009). Under this scheme, the ratio of forward and reverse reaction rate coefficients are determined based on the ideal changes in free energy, commonly called the equilibrium constant, as in Eq. 3-11.

$$k_{rev,R1} = k_{fwd,R1} \exp\left(\frac{\left(\mu^0_{Ce_2O_3(sb)} + \mu^0_{O(s)}\right) - \left(\mu^0_{Ce_2O_4(sb)} + \mu^0_{V_O(s)}\right)}{\bar{R}T} \right) \quad \text{[Eq. 3-11]}$$

The effect of non-ideal excess free energy is added as seen in Eq. 3-12 for the surface-subsurface exchange reaction – where the excess parameter β_{R1} determines how the shift in energetic driving force affects the transition state for the reaction rate energy barrier.

$$\dot{n}''_{R1} = -k_{fwd,R1}\theta_{V_O(s)} X_{Ce_2O_4(sb)} \exp\left(\frac{-\left(1-\beta_{R1}\right)\left[\left(\mu^{ex}_{Ce_2O_3(sb)} + \mu^{ex}_{O(s)}\right) - \left(\mu^{ex}_{Ce_2O_4(sb)} + \mu^{ex}_{V_O(s)}\right)\right]}{\bar{R}T} \right)$$
$$+ k_{rev,R1}\theta_{O(s)} X_{Ce_2O_3(sb)} \exp\left(\frac{\beta_{R1}\left[\left(\mu^{ex}_{Ce_2O_3(sb)} + \mu^{ex}_{O(s)}\right) - \left(\mu^{ex}_{Ce_2O_4(sb)} + \mu^{ex}_{V_O(s)}\right)\right]}{\bar{R}T} \right) \quad \text{[Eq. 3-12]}$$

The gas-surface reaction rate in Eq. 3-13 is calculated from an O_2 sticking coefficient, σ_{O2} and a forward desorption rate constant, $k_{fwd,R2}$, which is calculated in thermodynamically consistent scheme as shown in Eq. 3-14.

$$\dot{n}''_{R2} = 2\left[k_{fwd,R2}\theta^2_{O(s)} \exp\left(\frac{-\left(1-\beta_{R2}\right)\left(\mu^{ex}_{V_O(s)} - \mu^{ex}_{O(s)}\right)}{\bar{R}T} \right) - \sigma_{O_2}\left(\frac{P^0}{\sqrt{2\pi \bar{W}_{O_2} \bar{R}T}} \right) \theta^2_{V_O(s)} \frac{P_{O_2}}{P^0} \exp\left(\frac{\beta_{R2}\left(\mu^{ex}_{V_O(s)} - \mu^{ex}_{O(s)}\right)}{\bar{R}T} \right) \right] \quad \text{[Eq. 3-13]}$$

$$k_{fwd,R2} = \sigma_{O_2}\left(\frac{P^0}{\sqrt{2\pi \bar{W}_{O_2} \bar{R}T}} \right) \exp\left(\frac{-\left(\mu^0_{V_O(s)} + 0.5\mu^0_{O_2} - \mu^0_{O(s)}\right)}{\bar{R}T} \right) \quad \text{[Eq. 3-14]}$$

The rate parameters needed for Eq. 3-11 to 3-14 are specified in Table 3-4.

Table 3-4 - Kinetic data used for ceria reactions. D_O from Giordano et al. (2001), $k_{fwd,R1}$ from Decaluwe (2009), and σ_{O_2} from Leistner et al. (2012).

	Reaction	Kinetic Parameter
Diff:	$Ce_2O_4(b) + Ce_2O_3(sb) \rightarrow Ce_2O_3(b) + Ce_2O_4(sb)$	$D_O = \left(1.0 \cdot 10^{-4}\right)\exp(-40.1/T)$ (m^2/s)
R1:	$Ce_2O_4(sb) + V_O(s) \rightarrow Ce_2O_3(sb) + O(s)$	$k_{fwd,R1} = 3 \cdot 10^6$ (kmol/s), $\beta_{r1} = 0.5$
R2:	$2\ O(s) \rightarrow 2\ V_O(s) + O_2(g)$	$\sigma_{O_2} = 0.75$, $\beta_{r2} = 0.5$

The rate of diffusion through the particle is driven by a chemical potential gradient in mobile O^{2-} ions between the bulk and the sub-surface, as shown in Eq. 3-15. The values used to calculate D_O are shown in Table 3-4.

$$j''_{\text{diff}} = -D_{\text{O}}\bar{\rho}_{\text{p}}^{0}\frac{d\left(\frac{\mu_{\text{O}}}{\bar{R}T}\right)}{dr} \approx f_{\text{D}}\frac{D_{\text{O}}\bar{\rho}_{\text{p}}^{0}}{\bar{R}T}\frac{\left(\mu_{\text{O,sb}}-\mu_{\text{O,b}}\right)}{r_{\text{sb}}} \qquad \text{[Eq. 3-15]}$$

D_{O} is the chemical diffusivity of mobile oxide ions, and $\bar{\rho}_{\text{p}}^{0}$ is the initial molar concentration of oxide ions in the ceria. The gradient in oxide chemical potential μ_{O} was estimated via a linear finite difference between the bulk and subsurface multiplied by a dimensionless factor f_{D} set to 4.0 to account for the shape of the radial profile of concentration near the surface which determines the diffusion flux out of the bulk phase. In Eq. 3-15, $\mu_{\text{O,sb}}$ - $\mu_{\text{O,b}}$, are related by the ceria species chemical potential as shown in Eq. 3-16.

$$\mu_{\text{O,sb}}-\mu_{\text{O,b}} = \left(\mu_{\text{Ce}_2\text{O}_4,\text{sb}}-\mu_{\text{Ce}_2\text{O}_3,\text{sb}}\right)-\left(\mu_{\text{Ce}_2\text{O}_4,\text{b}}-\mu_{\text{Ce}_2\text{O}_3,\text{b}}\right) \qquad \text{[Eq. 3-16]}$$

3.2.4 Gas-flow model

The transfer of momentum, heat, and O_2 between the particles and the surrounding gas phase flow provides a basis for modeling gas-phase O_2 mass fractions $Y_{\text{O2,g}}$, temperatures T_{g}, and characteristic *y*-direction velocities $\bar{u}_{\text{y,g}}$. The gas-phase model for inert-particle curtains is extended to handle multiple gas species, specifically O_2 and N_2. Empirical correlations estimate the amount of far-field gas flow entrained by the falling particles. Combining the entrainment models with the particle-gas momentum,

heat, and O_2 exchange models provides a basis for simulating the evolution of $Y_{O2,g}$ and T_g surrounding the particles.

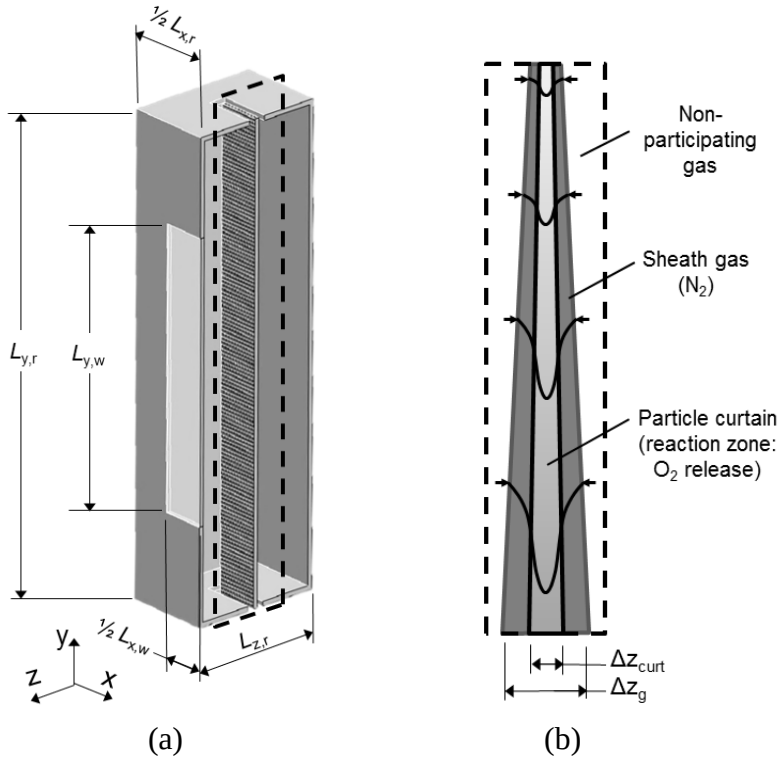

Figure 3-8 - (a) cross-sectional view inside of the receiver, highlighting the curtain zone. (b) detailed schematic of curtain flow, showing evolution of gas through the (inert) sheath and into the dense core, Δz_{curt}, where particle reactions take place.

Figure 3-8(b) illustrates the "sheath" of gas flow around the particles initiated at the inlet of the reactor and driven by the particle momentum. As with the inert flows, the *y*-direction gas flow in the region around the curtain was approximated with a Gaussian velocity profile characterized by a representative velocity, $\bar{u}_{y,g}$ and thickness, Δz_g, which is different from the thickness of the dense-particle core, Δz_c.

$$u_{\mathrm{y,g}} = \bar{u}_{\mathrm{y,g}}\sqrt{2}\exp\left(-\frac{z^2}{\Delta z_{\mathrm{g}}{}^2}\right) \qquad \text{[Eq. 3-17]}$$

Using Eq. 3-17 reduces the complexity of the gas-flow model to calculating $\bar{u}_{\mathrm{y,g}}$ and Δz_{g} with a combination of mass and momentum balance equations in appropriately simplified forms. The mass and momentum equations can be solved simultaneously to find the *y*-variation in the gas vertical mass and momentum flow rates, $\dot{m}_{y,\mathrm{g}}$ and $\dot{m}_{y,\mathrm{g}}\bar{u}_{y,g}$, respectively. The characteristic gas velocity, $\bar{u}_{\mathrm{y,g}}$, is then found by dividing the momentum by the mass, while the characteristic thickness, Δz_{g}, is found by integrating Eq. 3-17 to get Eq. 3-18.

$$\dot{m}_{y,g} = \sqrt{\frac{\pi}{2}}\rho\bar{u}_{y,g}\Delta x\Delta z_g \qquad \text{[Eq. 3-18]}$$

The gas-phase mass conservation for a vertical slice of the curtain is derived for a semi-infinite plane (due to the large difference is aspect-ratio of the curtain), neglecting any *x*-direction variations. The gas density ρ_{g} is calculated from the ideal gas law. The resulting gas mass flow conservation equation can be written as in Eq. 3-19 , where the first term on the right-hand-side is the mass entrained (at the edge of the gas-flow with a velocity of $u_{\mathrm{z,g,edge}}$) and the second term is the mass of gas generated from O_2 release in a cell with a particle density, N_{p}.

$$\frac{\partial\left(\rho_{\mathrm{g}}\bar{u}_{\mathrm{y,g}}\Delta z_g\right)}{\partial y} = 2\rho_{\mathrm{g}}\bar{u}_{\mathrm{z,g,edge}} + a_{\mathrm{s,p}}n''_{\mathrm{r2}}\overline{W}_{\mathrm{O_2}}N_{\mathrm{p}}\Delta z_c \qquad \text{[Eq. 3-19]}$$

Eq. 3-19 is solved for both the front and the rear halves of the current separately.. Downward momentum entrains gas from the surroundings at a velocity $u_{z,g,edge}$ which is set to be proportional to the downward gas velocity with a proportionality or entrainment constant, α. The entrainment constant α varies primarily with particle diameter d_p (Liu 2003). Liu did not fit α for d_p and flow regimes relevant to this study, but α is fitted here as a function of d_p to the detailed entrainment measurements performed by Kim et al. (2009) using particle size and flow profiles directly applicable. This fitting is sensitive to the particle drag model, and the drag model suggested by Kim et al. (2009) provides the best fit. The resulting fit for $u_{z,g,edge}$ is shown in Eq. 3-20.

$$u_{z,g,edge} = \alpha \bar{u}_{y,g} \text{ where } \alpha = 5.293\left(0.99574\right)^{\left(10^6 d_p\right)} \quad \text{[Eq. 3-20]}$$

The change in gas-momentum is found with a simplified 1D fluid-momentum conservation equation, where the effects of drag within the curtain are assumed to be of much greater magnitude than buoyancy. The drag source-term is found using a cell-average particle velocity by dividing the total particle residence time by the cell fall-distance.

$$\frac{d\left(\dot{m}_{y,g}\bar{u}_{y,g}\right)}{dy} = \frac{3}{4}\frac{\rho_g\left(\bar{u}_{y,p}-\bar{u}_{y,g}\right)^2}{d_p}C_D C_S\left(\frac{\dot{m}_p}{\rho_p \bar{u}_{y,p}}\right) + a_{s,p} n''_{r2} \bar{W}_{O_2} N_p \left(\Delta z_c \Delta x \Delta y\right)\bar{u}_{y,p} \quad \text{[Eq. 3-21]}$$

To solve the gas-phase species balance for the gas flow surrounding the particle flow, it is necessary to resolve the nature of the particle-dense curtain core. The particle-core spreading relationship derived from the measurements of by Kim et al. (2009) under

isothermal conditions for inert particles were used for this purpose. This fitting is reproduced in Eq. 3-22.

$$\Delta z_{\mathrm{c}} = 0.01 + 0.0087y \qquad \text{[Eq. 3-22]}$$

With this, the mass-flow in the dense-particle region can be calculated by integrating $\rho u_y dA$ over this region, yielding the core flow-rate at any point in Eq. 3-23.

$$\dot{m}_{\mathrm{g,c}} = \rho \Delta x \sqrt{2}\bar{u}_{y,g} \int_0^{\Delta z_{\mathrm{c}}} \exp\left(-\frac{z^2}{\Delta z_{\mathrm{g}}^2}\right) dz = \dot{m}_{\mathrm{g}} \mathrm{erf}\left(\frac{\Delta z_{\mathrm{c}}}{\Delta z_g}\right) \qquad \text{[Eq. 3-23]}$$

The gas-phase species balance solves for the vertical variation in the average Y_{O2} in the particle-dense core of the curtain using the assumption that the Y_{O2} of the flow entrained from the sheath equals to the inlet flow value.

$$\Delta\left(Y_{O_2}\dot{m}_{\mathrm{g,c}}\right) = Y_{\mathrm{O_2,entrained}}\dot{m}_{g,\mathrm{entrained}} + a_{\mathrm{s,p}} n''_{\mathrm{r2}} \overline{W}_{\mathrm{O_2}} N_{\mathrm{p}} \Delta x \Delta y \Delta z_c \qquad \text{[Eq. 3-24]}$$

In Eq. 3-24, the mass of gas entrained in the core is found by using Eq. 3-23 and recognizing that all of the gas evolved from the particles is done directly into the core, yielding Eq. 3-25.

$$\dot{m}_{\mathrm{g,entrained}} = \Delta\dot{m}_{g,c} - a_{\mathrm{s,p}} n''_{\mathrm{r2}} \overline{W}_{\mathrm{O_2}} N_{\mathrm{p}} \Delta x \Delta y \Delta z_c \qquad \text{[Eq. 3-25]}$$

3.2.5 Heat transfer model

The heat-transfer model for reactive particles follows that of the inert particles, from chapter 2. However, because the particles now exchange mass between reaction zones and with the gas, the full-cell energy balance must be updated to account for the changing species. The mass-flow terms, $\dot{m}_{\mathrm{k}}$, vary between species with the species mass fractions (which are calculated from mole fractions, X_{k}), while the enthalpy terms, h_{k}, are a function of temperature for species k. With these changes, the updated energy balance is shown in Eq. 3-26. All of the terms on the right-hand side of Eq. 3-26 are identical to those in Eq. 2-11.

$$\sum_{k=1}^{k_{tot}} \left(\dot{m}_{\mathrm{in,k}} h_{\mathrm{in,k}} - \dot{m}_{\mathrm{out,k}} h_{\mathrm{out,k}} \right) = \dot{Q}_{\mathrm{conv}} + \dot{Q}_{\mathrm{curt}} + \dot{Q}_{\mathrm{rad}} + \dot{Q}_{\mathrm{sol}} \qquad \text{[Eq. 3-26]}$$

In solving for $\dot{Q}_{rad}$ and $\dot{Q}_{sol}$, four radiation bins, shown in Table 3-5, are chosen to balance the accuracy of modeling in the window and the particles. Because of an irregularly-shaped spectral curve for ceria, bin property values are averaged versus a blackbody at two temperatures: 1600 K for accurate evaluation of thermal radiation, and 5600 K for calculations from the direct solar input. As radiation properties for ceria are only available up through the near-IR range (Ganesan et al, 2013; Marabelli et al., 1987; Niwano et al, 1988), values for the longest-wavelength band of ceria are determined to fit the total weighted emissivity reported in Sully et al. (1952).

Table 3-5 - Optical properties: Ceria surface emissivity ($\varepsilon_{\mathrm{p},\lambda}$) for solar and thermal radiation absorption, quartz window bulk emittance ($\varepsilon_{\mathrm{wind},\lambda}$) and reflectance ($\rho_{\mathrm{wind},\lambda}$), and Duraboard HD bulk emittance ($\varepsilon_{\mathrm{wall},\lambda}$)

λ range (μm)	f_{rad} (%) Solar	$\varepsilon_{p,\lambda}$ [a] Solar	f_{rad} (%) 1600 K	$\varepsilon_{p,\lambda}$ [a] 1600K	$\varepsilon_{wind,\lambda}$ [b]	$\rho_{wind,\lambda}$ [b]	$\varepsilon_{wall,\lambda}$ [c]
0-0.6	31	0.57	0	0.36	0.00	0.073	0.20
0.6-1.25	54	0.26	7	0.17	0.00	0.071	0.20
1.25-3.5	15	0.09	64	0.08	0.046	0.068	0.20
3.5-∞	0	0.51	29	0.34	0.91	0.011	0.80

a: Marabelli & Wachter (1987) in the 0-3.5 range, and Sully et al. (1952) in the 3.5-∞ range
b: Hereaus (2007)
c: Siegel et al. (2010)

3.2.6 Numerical Grid

The reactive-particle receiver model uses the same numerical grid as the inert particle receiver model to save on computational cost in calculating the view factors. This grid uses two discretizations for the curtain in the *z*-direction (through the depth of the curtain) to simulate temperature variations between the front and back of the curtain Four discretizations were used along the *x*-direction of the curtain to explore the effects of variation in radiation effects from greater exchange with the walls versus the window without increasing computational cost too significantly. The maximum observed temperature difference between the center and edge curtain temperatures is 40 K in the irradiated zone, and decreases to less than 2 K by the exit. Thus, four discretizations in the *x*-direction were deemed adequate for the purposes of this study, where the performance along the fall is most-important.

The number of *y*-direction cells was varied to explore the grid influence on the particle species, temperature, and velocity along the length of fall. The impact of grid resolution

in the *y*-direction was evaluated by twice doubling the number of discretizations (using 20, 40, and 80 cells) to evaluate the resolution needed for grid-independence. The change in particle temperatures going from 20 to 40 and 40 to 80 cells was only 3 K and 2.4 K (~0.1% change), while the change in the overall degree of reduction was only 1.4% and 1.1%, respectively, due to the particle-air coupling scheme that was employed along the fall. As such, the coarse grid (20 discretization) was used as it provided sufficient accuracy with less computational time.

3.2.7 Solution Method

A schematic of the solution method for reactive particles is shown in Figure 3-9. The solution starts with a reasonable guess for the temperature fields, solid species concentrations (X_{Ce2O3}), gas species concentration (p_{O2}), and gas/particle coupling between the gas and solid phases. The solid phase is solved in the Lagrangian frame for X_{Ce2O3} and $\bar{u}_{y,p}$ by using the ode23tb solver to solve Eq. 3-7 to Eq. 3-10 with a tolerance of 10^{-6}. Next, the gas-phase is solved in the Eulerian frame to solve Eq. 3-19, Eq. 3-21, Eq. 3-24 and a gas-convection equation to find T_{gas}, $\bar{u}_{y,g}$, and p_{O2}, using an updated O_2 source-term and $\bar{u}_{y,p}$ from the particle solver. The O_2-source term in the gas-equation is updated with an under-relaxation factor of 0.05. The solid and gas-phase models are iterated until the maximum change in the solution variables is less than 10^{-4}. After the species concentrations, velocities, and gas temperature have converged, the solid-phase energy balance, Eq. 3-26, is solved to update the wall and particle temperatures using the lsqnonlin solver with a tolerance of 10^{-4}. This solver accounts for the majority of the solution time, most of which is spent doing matrix inversions to solve for the radiosity

balance. The solver then checks for convergence in the temperature, and iterates on the process if the maximum residual is greater than 10^{-3}. Total runtime for a single-case is on the order of 2-3 hours, with less time if a prior solution (and thus better starting-guess) is used at initialization.

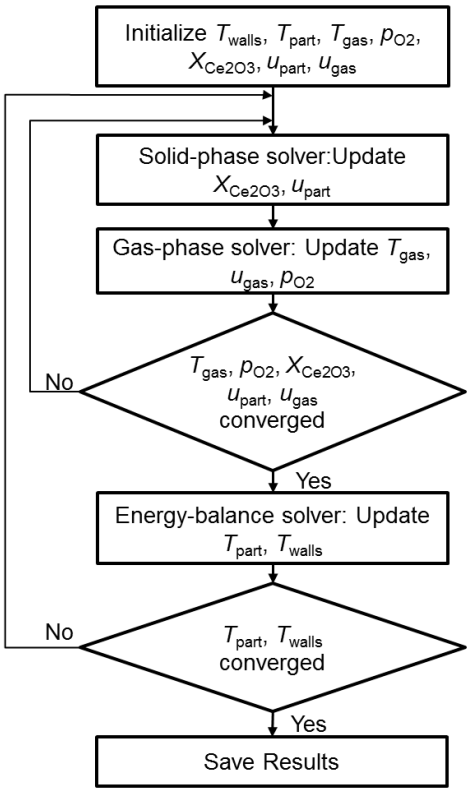

Figure 3-9 – Solution method for the reactive-particle receiver simulation.

3.3 Reactive Ceria Results

3.3.1 Baseline Condition

To provide a general perception of how the receiver performs, a baseline condition for the receiver model, as defined in Table 3-6, was run both with and without the ceria particle reactions included in the simulation. The non-reacting or inert particles provided

an assessment as to how the radiative transfer drives the particle heating independent of the endothermic ceria reduction.

Table 3-6 - Baseline operating conditions for the falling ceria particle receiver model

Property	Value (Baseline)
Receiver Dim. (m) ($L_{x,r}$, $L_{y,r}$, $L_{z,r}$)	(3.0, 5.0, 2.0)
Window Dim. (m) ($L_{x,w}$, $L_{y,w}$, $L_{z,w}$)	(1.0, 3.0,0.05)
Curtain Dimensions (m) ($L_{x,c}$, $L_{y,c}$, $L_{z,c}$)	(1.0, 5.0, 0.01+0.0087·y)
Particle Size (μm)	300
Flow Rate (kg/s-m)	1.0
$T_{part,in}$ (K)	1100
q''_{solar} (kW/m^2)	1000
$P_{O2,in}$ (atm)	$1\cdot(10^{-5})$

The temperature profiles of the walls and curtain for the inert particle case at baseline conditions, shown in Figure 3-10, highlight important performance characteristics of the receiver. At the baseline condition, the relatively low particle flow rate allows heating of the inert particles from 1100 K to an average temperature above 2050 K. For these run conditions, the rear of the curtain is heated faster than the front, with a maximum temperature difference of 63 K half-way down the fall that decreases to a 24 K difference by the particle outlet.

The rear of the curtain achieves higher temperatures because total initial absorptivity of the low-flow rate curtain results in significant solar flux reaching and heating the back wall. The rear of the curtain has the high radiation-exchange with the hotter walls and greater reflection off the back-wall. In the horizontal direction, the curtain temperature is relatively uniform due in large part to the imposed uniform solar radiation flux over the entire receiver window. The temperatures at the sides of the

curtain were about 40-50 K lower than those at the curtain center, due to higher radiative losses to the cooler side walls.

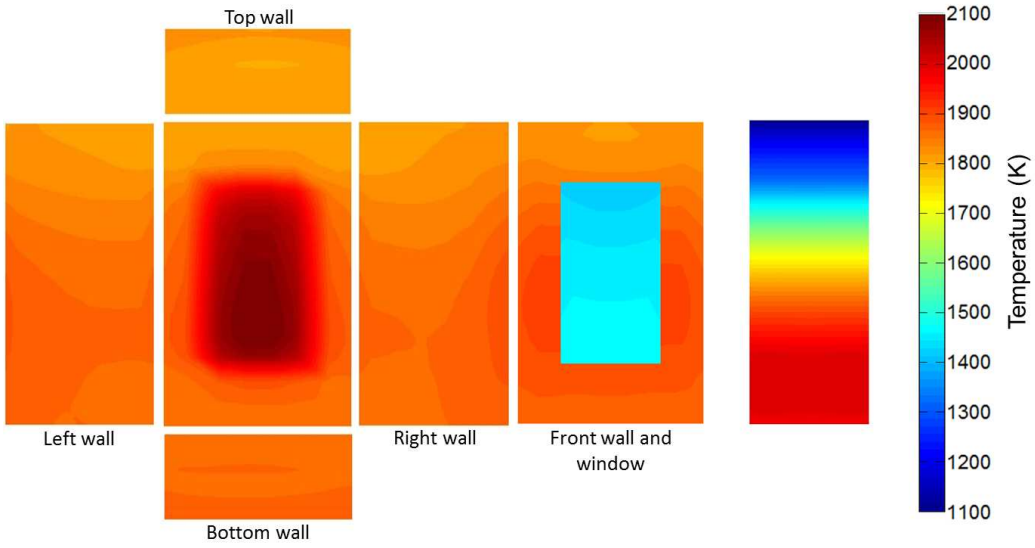

Figure 3-10 - Wall and curtain temperature profiles for inert particles falling with identical properties to the reactive ceria particles with: $\dot{m}_{p,in}$ = 1.0 kg/s-m, d_p = 200 μm, T_{in} = 1100 K, $\dot{q}''_{sol}$ = 1000 kW/m^2.

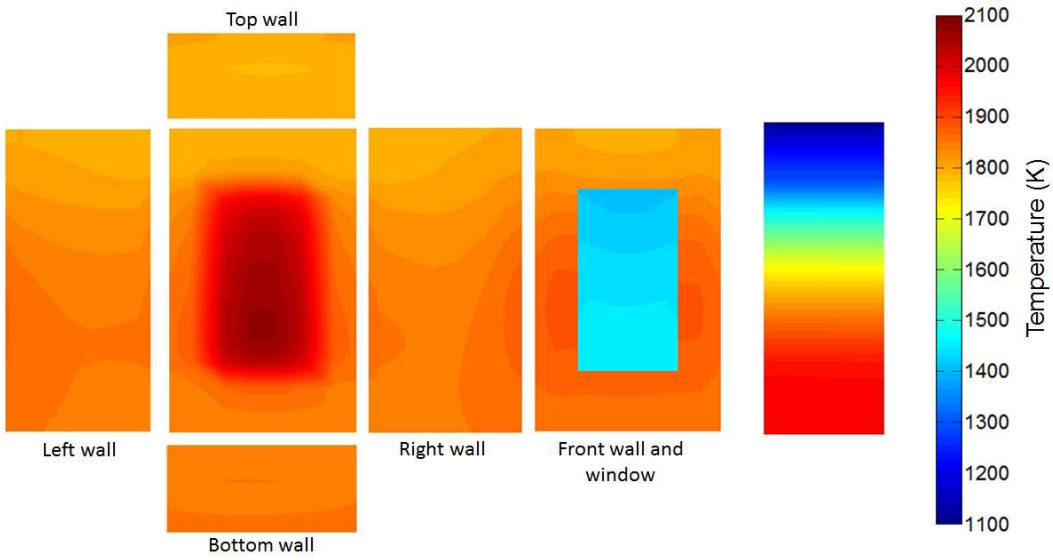

Figure 3-11 - Wall and curtain temperature profiles for reactive ceria particles with: $\dot{m}_{p,in}$ = 1.0 kg/s-m, d_p = 200 μm, T_{in} = 1100 K, $\dot{q}''_{sol}$ = 1000 kW/m^2.

At the relatively low flow-rate of the baseline condition, the curtain volume fraction f_v according to Eq. 2-26 was below 1%. As such, a large amount of the solar radiation from the front aperture passed through the low-density curtain and onto the rear wall, which reached temperatures as high as 2000 K for this case. Transmittance through the curtain increased along the fall as vertical particle velocities $\overline{u}_{y,p}$ increased and f_v accordingly decreased. The volume fraction further dropped due to the spreading of the particle curtain in the *z*-direction (since f_v is proportional to Δz_c^{-1}), but the curtain spreading had no impact on the actual curtain transmittance, because transmittance is proportional to $f_v \Delta z_c$. Further, increased re-radiation of the particles as they were heated along the length of the fall caused the rear-wall temperatures to peak nearer the bottom of the region exposed to the front window through the curtain.

Overall, the radiative emission and reflection off of the particles and the rear wall kept the inner temperatures of all other walls between 1750 and 1850 K for the baseline condition with its small external heat transfer coefficient $h_{T,ext}$ of 5.0 W m^{-2} K^{-1} and low receiver wall conductivity of ~0.5 W m^{-1} K^{-1}. Due to the receiver window's high transmissivity in the solar spectrum, the window stayed considerably cooler than the walls, reaching temperatures of ~1375 K and ~1500 K on the outer and inner face respectively with the low $h_{T,ext}$. Both of these temperatures are above the quartz operating limit of 1300 K, which is necessary to avoid growth of β-cristobalite phases that lead to eventual failure in cyclic operation (Momentive, 2014). The temperatures could be mitigated by a higher $h_{T,ext}$ or lower particle reflectivity and thus reduced radiative loading on the window.

The high temperatures of the particles, walls, and window for the inert-particle case are somewhat mitigated by turning on the endothermic ceria reduction with reacting particles as indicated in Figure 3-11. The reacting particle temperatures do not rise above 2000 K. The hot spot on the rear wall is also close to 2000 K, albeit for a significantly smaller region than for the inert particles. The endothermic reduction of the ceria captured some of the solar energy and lowered the particle temperatures and their radiative loading on the rear and side walls. Nonetheless, because ceria has a relatively low averaged emissivity (i.e. absorptivity) of 0.330 averaged over the solar spectrum shown in Table 3-5, the radiative loading on the side walls is dominated by solar reflection (from the particles or other walls), and thus, other wall temperatures do not drop by more than 15 K with the additional heat sink of the endothermic reaction. This indicated the low energy capture efficiencies (< 5%) of the solar radiation input into

particle chemical energy at these low f_v conditions. A substantially larger fraction (> 16%) of the solar radiation is captured as particle sensible heating. The low fraction of energy stored as chemical energy is due to the high-temperatures required for ceria reduction as illustrated by the thermodynamic equilibrium plots in Figure 3-6. The particle temperatures near 2000 K for the baseline reacting-particle conditions resulted in significant re-radiation losses and thus very low solar capture efficiencies, which would be problematic for an actual cycle. The relatively poor emissivity of undoped ceria and the low f_v necessary to get this level of particle heating caused the poor solar absorbance.

3.3.2 Particle Reduction

The evolution of particle temperature and degree of reduction (at the particle surface δ_s and in the bulk δ_b) along the length of fall are shown in Figure 3-12. For this figure, the operating conditions were varied by increasing the particle T_{in} to 1300 K from the baseline condition of 1100 K. The higher T_{in} increased the particle temperatures along the length of the fall and thus, the ceria degree of reduction (δ_s and δ_b). The actual δ_s and δ_b are compared with their equilibrium values ($\delta_{s,eq}$ and $\delta_{b,eq}$) calculated as a function of T_p and P_{O2} at any point.

In Figure 3-12, δ_s (initially at its equilibrium value at the inlet) decreased at the beginning of the fall because O_2 desorption from the particle surface was the dominant rate-limiting process for reduction according to the kinetic rates in Table 3-4. The slow surface desorption rate caused an initial buildup of O(s) at the particle surface even though the surface, with its lower heat of reduction had a much higher degree of reduction (i.e., $\delta_s > \delta_b$). The rapid increase in temperature over the directly irradiated zone

caused higher O_2 desorption rates. With the rate-limiting surface reaction, the sub-surface (δ_{sb} not shown) and the bulk δ_b remained very close to equilibrium with the surface state.

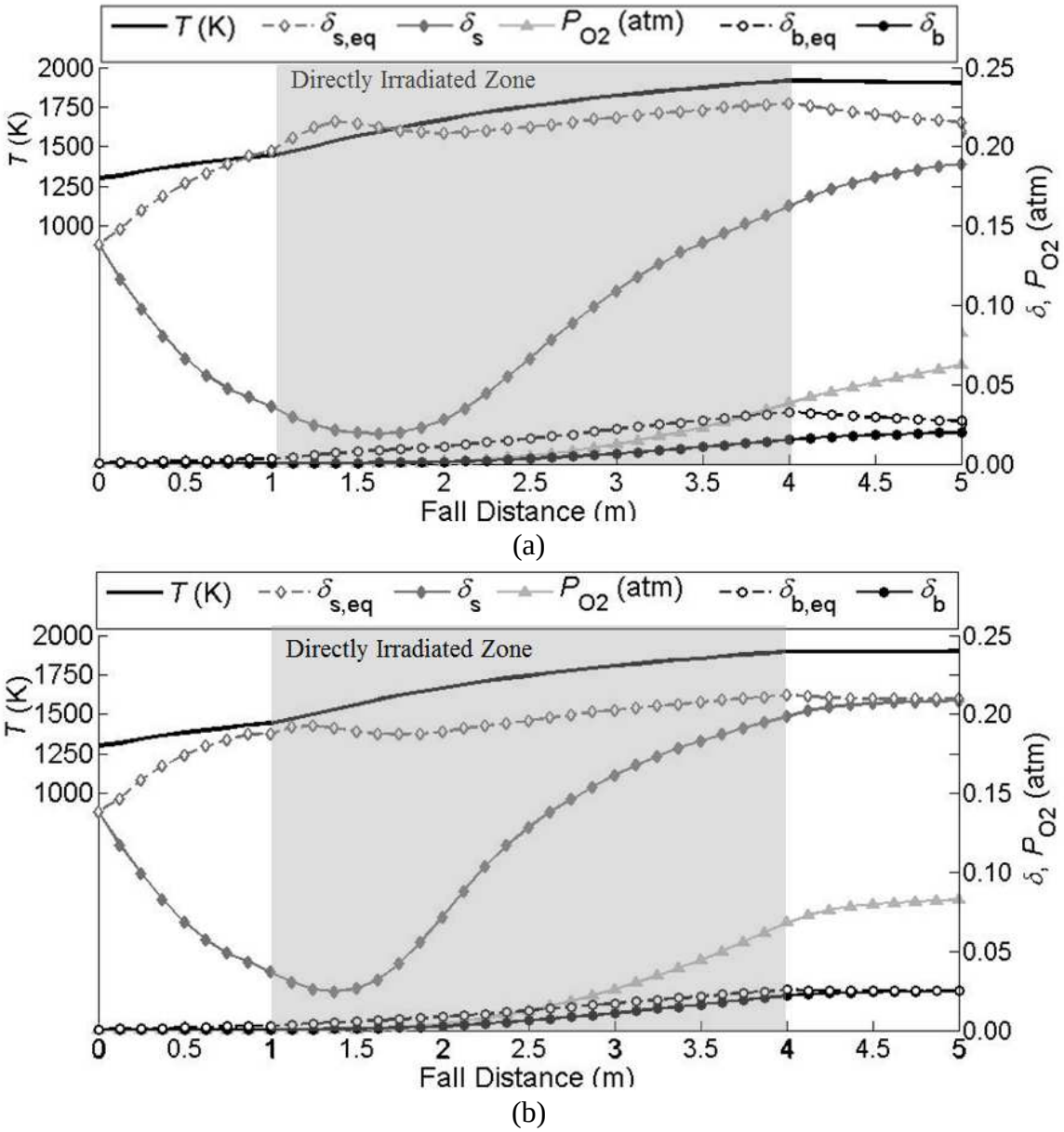

Figure 3-12 - Particle curtain performance, compared to equilibrium values, using the suggested sticking coefficient of (a) 0.75 and (b) 0.10 for the following operating conditions: $\dot{m}_{p,in}$ = 1.0 kg/s-m, d_p = 300 μm, T_{in} = 1300 K, $\dot{q}''_{sol}$ = 1000 kW/m^2.

For the conditions in Figure 3-12(a), the particle surface did not reach equilibrium $\delta_{s,eq}$ over the ~1.5 s residence time of fall in the directly irradiated zone. Thus, even though the particles showed a slight drop in temperature due to re-radiation to the walls after leaving the directly irradiated zone, they continued to react such that some of the sensible energy was converted to chemical energy as the particles reached their near equilibrium state with $\delta_s = 0.21$ and $\delta_b = 0.024$ at the end of the fall. This result indicated that the chemical energy storage rate was slower than the sensible heating rate for the baseline reaction conditions.

Because of uncertainty in the rate-limiting desorption reaction R2 rate at the very high particle temperatures, the reaction rate was changed to assess the sensitivity of the degree of reduction on the rate constant. For Figure 3-12(a), a sticking coefficient $\sigma_{O2} = 0.75$ was adopted from a previous reference (Leistner et al. 2012), and the receiver reached very near equilibrium degrees of reduction near the exit. To assess the sensitivity of the solution to the rate of R. 3-3, σ_{O2} was lowered to 0.10 and the results of that simulation are shown in Figure 3-12(b). With the lower O_2 desorption rate, the particles did not approach equilibrium reduction fractions and were still undergoing significant reduction after leaving the reaction zone by converting some sensible energy into chemical energy. Comparison of Figure 3-12 (a) and Figure 3-12 (b) indicates the sensitivity of the receiver simulations to the uncertain surface kinetics at the high-temperatures and suggests the kinetic parameters might be worth further experimental investigations.

3.3.3 Parametric study results

The baseline simulations shown in Figure 3-12 in no way represent an optimal condition for receiver operation for ceria reduction or solar thermal capture efficiency. To explore how receiver operating conditions might be adjusted to improve critical global performance metrics, parametric studies were performed on the particle inlet temperature, particle flow-rate, solar concentration, and particle size.

In order to aid in evaluation of the reacting flow, two efficiency values are defined: one to account for influence of reaction and another to account for sensible heating. The chemical efficiency, η_{chem}, is defined as the ratio of energy used to drive chemical reaction to total solar input, is defined in Eq. 3-27. The sensible efficiency, η_{sens}, is the ratio of absorbed energy used to heat the particles and the total solar power input, as shown in Eq. 3-28.

$$\eta_{Chem} = \frac{\sum_{i=1}^{n_{cells}} \frac{\dot{m}_{g,react,i}}{W_{O_2}} \Delta h_{reac}\left(T_{p,i}\right)}{\dot{Q}_{Solar}} \qquad \text{[Eq. 3-27]}$$

$$\eta_{Sensible} = \frac{\sum_{k=1}^{k_{tot}} \left(\dot{m}_{\text{in,k}} h_{\text{in,k}} - \dot{m}_{\text{out,k}} h_{\text{out,k}}\right)}{\dot{Q}_{Solar}} - \eta_{Chem} \qquad \text{[Eq. 3-28]}$$

Figure 3-13 shows how increasing particle T_{in} from the baseline value of 1100 K reduces the solar absorption efficiency (based on the sum of the sensible and chemical energy captured in the particles) for a range of flow rates up to four times the baseline flow-rate. However, while the total solar efficiency decreased with higher T_{in}, the actual

amount of energy stored in the chemical reduction of ceria increased with the higher temperatures as indicated by the higher δ with higher T_{in}. The higher temperatures increase the chemical potential driving force for the ceria reduction and thus the energy capture via reduction. However, the higher temperatures increase re-radiation losses which lowers the fraction of total energy capture is lowered. Thus, if the receiver is operated simply to drive a chemical process such as a ceria redox cycle for H_2O or CO_2, increasing T_{in} above 1100 K by using some form of heat recuperation (Lapp et al. 2012) provides advantages. On the other hand, if the goal is to use both sensible and thermal energy for co-generation or some other multifunctional process, increased T_{in} lowers η_{solar}, which may offset the improved ceria reduction.

Related trends with respect to total particle mass flow rates $\dot{m}'_p$ are shown in Figure 3-13. Higher flow rates raise f_v (which scales almost linearly with $\dot{m}'_p$) and thus improve total solar absorption efficiency. However, the increased flow rate lowers the temperatures rise, and the degree of reduction for the ceria drops dramatically with increased $\dot{m}'_{p,in}$. In general doubling $\dot{m}'_{p,in}$ requires more than 200 K increase in T_{in} to achieve a comparable degree of reduction at the increased flow rate. However, the lower temperatures with higher particle flow rates reduces re-radiation losses and thus increases η_{solar}. The denser curtain with its higher absorption lowers the back- and side-wall temperatures dramatically. While the baseline case resulted in a rear-curtain that was appreciably hotter than the front, at the highest flow-rates, the curtain temperature becomes more uniform with a slightly higher temperature in the front. For the most-opaque curtain, when the particle diameter is 200 μm and flow-rate is 4 kg $s^{-1}m^{-1}$, the front half of the curtain is hotter by a maximum of 14 K, with a difference of only 0.3 K

by the exit. In contrast, the least-opaque curtain, with a particle diameter of 700 μm and flow-rate of 1 kg $s^{-1}m^{-1}$ reaches a maximum temperature difference of 110 K, decreasing to 95 K at the exit, with a hotter rear-half of the curtain.

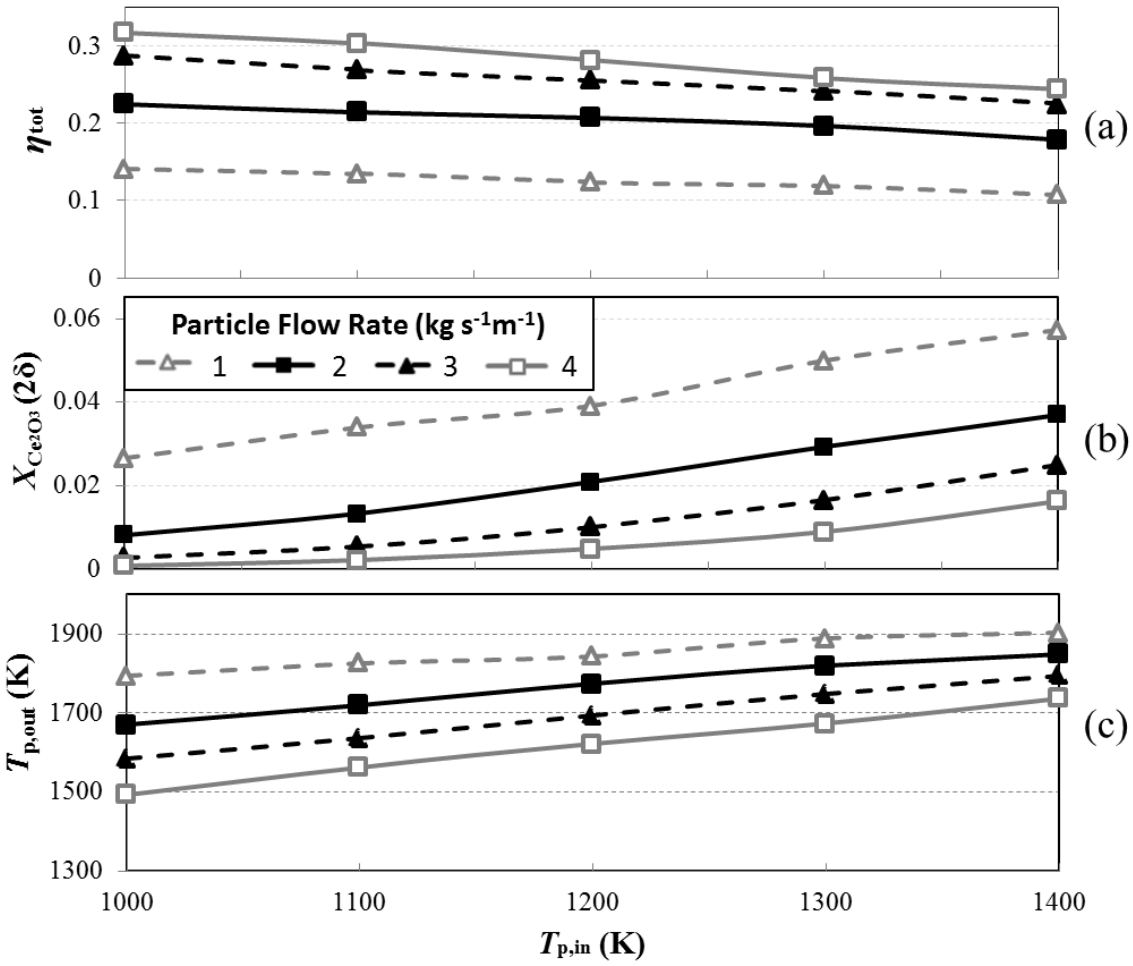

Figure 3-13 – Variation in (a) η_{tot}, (b) X_{Ce2O3}, and (c) Outlet T_p with varying inlet T_p and $\dot{m}'_p$.

Increased particle flow rates can possibly allow for increased solar concentration $\dot{Q}_{solar}$. Thus $\dot{Q}_{solar}$ was varied from 700 to 1400 kW m^{-2} for the range of particle flow rates for the baseline T_{in} of 1100 K. The plot in Figure 3-14(a) indicates that for the most

part the fraction of total solar energy absorbed does not change significantly with $\dot{Q}_{solar}$ for these conditions. Rather, η_{solar} remains relatively constant as $\dot{Q}_{solar}$ increases and drives up outlet temperature and ceria δ. This occurs because re-radiation losses from the particles only increases by ~5% when solar input increases from 700 to 140 kW m^{-2}. The 5% loss is offset by lower convection losses (relative to solar input), which scale with increased wall temperatures but decrease as a percentage of $\dot{Q}_{solar}$ by ~5% over the same range of solar inputs. For the baseline flow-rate of 1.0 kg $s^{-1}m^{-1}$, wall temperatures increase from 1870 to 2300 K as $\dot{Q}_{solar}$ doubles from 700 to 1400 kW m^{-2} (corresponding total input from 2.10 to 4.20 MW), but convection losses $\dot{Q}_{\text{conv}}$ only increase from 0.26 MW to 0.33 MW. The low baseline values for k_{w} and h_{w} limit the $\dot{Q}_{\text{conv}}$ and allow for the increased wall temperatures with increasing $\dot{Q}_{solar}$ not to significantly increases the heat losses through the receiver walls. Thus higher $\dot{Q}_{solar}$ increases the fraction of energy captured by the particles both as chemical energy indicated by outlet X_{Ce2O3}.

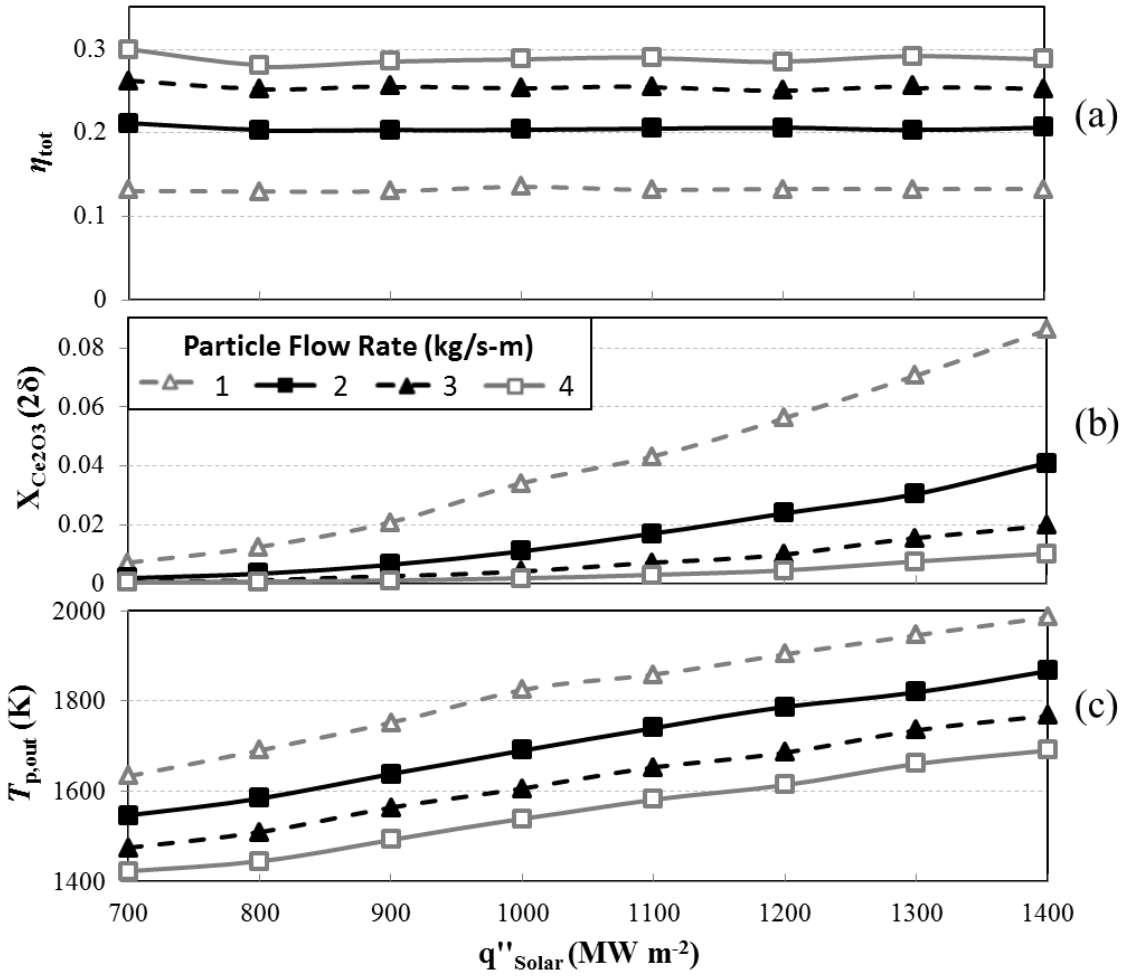

Figure 3-14 - Variation in (a) η_{tot}, (b) X_{Ce2O3}, and (c) Outlet T_p with varying inlet $\dot{q}''_{solar}$ and $\dot{m}'_p$.

For higher particle flow-rates (3.0 and 4.0 kg $s^{-1}m^{-1}$), the particles reach their equilibrium P_{O2} quicker and reduction becomes more constrained by the availability of purge gas, as the volume of O_2 evolved is directly proportional to the mass flow-rate. As $\dot{Q}_{solar}$ increases from 700 to 1400 kW/m^2, outlet P_{O2} increases from 0.014 to 0.132 for the 1 kg s^{-1} m^{-1} flow rate, while it increases from 0.001 to 0.056 for the 4 kg s^{-1} m^{-1} flow rates. As the solar concentration increases, the particle temperature increases by about 50°C per 100 kW m^{-2} additional solar input.

When combined with the increased efficiency from the temperature-dampening effects of the endothermic reduction, reactive particles attain slightly superior performance compared to inert particles that have the same properties. This effect is best observed with smaller particles, as seen in Figure 3-15, which fall slower (due to greater drag), spend more time in the irradiated zone to reach higher temperatures, and undergo more reduction.

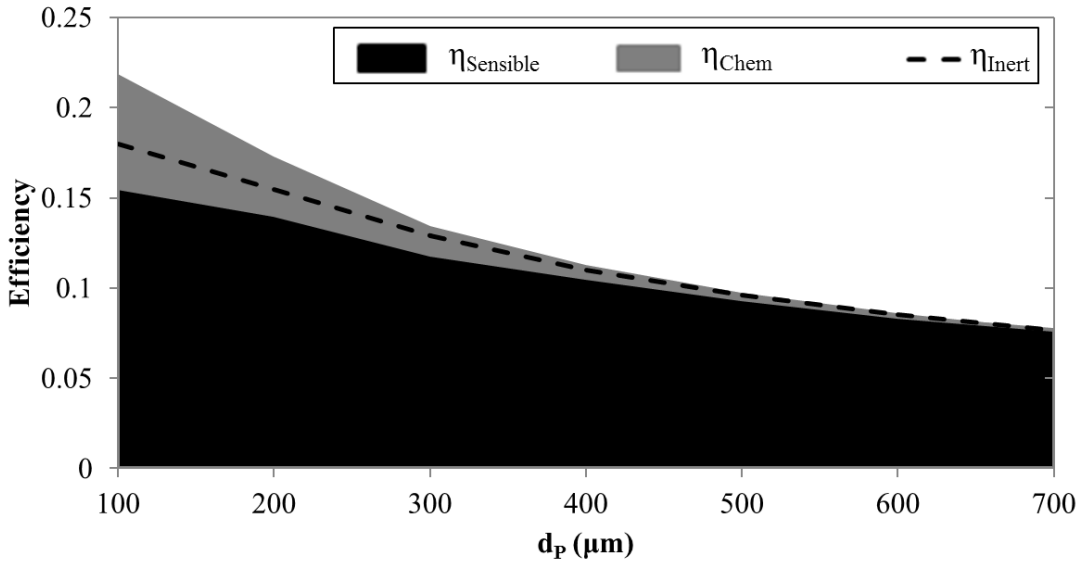

Figure 3-15 – Variation in $\eta_{Sensible}$ and η_{Chem} with d_p compared to η_{Inert} calculated for flows identical to ceria but with no reduction. Run conditions: $\dot{m}'_{p,in}$ = 1.0 kg s^{-1}m^{-1}, T_{in} = 1100 K, $\dot{q}''_{sol}$ = 1000 kW m^{-2}.

For $\dot{m}'_{p,in}$ = 1.0 kg s^{-1} m^{-1} with d_p = 100 µm, the maximum particle velocity $u_{y,p}$ reaches 4.59 m s^{-1} approximately half the maximum velocity for the same conditions when d_p = 700 µm (9.05 m s^{-1}). The lower $u_{y,p}$ for the smaller particles increases not only

particle residence times but also curtain particle volume fraction f_v and thus opacity (since f_v scales with $1/u_p$). Thus, for at an $\dot{m}'_{p,in}$ = 1 kg s^{-1} m^{-1}, 100-μm particles reach an outlet T_p = 2050 K, compared to only 1565 K for 700-μm particles under otherwise identical run conditions. Smaller particles also have greater surface area (total area scales with $1/d_p$ for the same $\dot{m}_p$), which increases the rate of the rate-limiting surface reaction. In fact, for the smaller particles, the gas generation in the dense-particle core of the curtain pushes gas out of this region rather than pulling it in via entrainment.

3.4 Discussion of Ceria Reactor Results

Particle reactors involve complex interplay between variables dominated by different physical principles. It is important to explore the operating space to identify optimal combinations that maximize the receiver's efficiency, outlet temperature, and/or energy storage density.

Particle size has one of the greatest impact on receiver performance. Smaller particles increase efficiency, as seen from studies on inert receivers (Chen et al., 2007; Siegel et al., 2010). Smaller particles form an optically thicker curtain, due to decreased terminal velocities, which also increase residence times and thus outlet temperatures. With their higher surface-to-volume ratios, smaller particles can have higher degrees of reduction when as with ceria, the surface reaction is rate-limiting. Despite the positives with smaller particle diameters, flows using smaller particle can lead to increased particle recirculation in the receiver which can soil the window as suggested in simulations by Meier (1999). As the simplified gas-flow model in these simulations cannot capture the

complexity of recirculating flows, particle diameters were limited to 100 μm since prior simulations suggested that smaller particles will be influenced by recirculation in a closed receiver (Meier, 1999). Particle receiver design could greatly benefit from a more detailed study of the particle-air coupling under high temperature gradients in an enclosed space.

Figure 3-15 highlights the advantage of driving reactions on η_{solar} as the particles undergo greater degrees of reduction. The particle reduction mitigates temperature increases while storing energy in the heat of reaction, which lower particle temperatures and re-radiation loss throughout the receiver, Furthermore, the additional stored chemical increases energy storage density.

Analysis of the reduction process showed that the particle reduction is surface rate limited largely due to the build-up of P_{O2} around the particles and the high surface sticking coefficient of 0.75 for the reverse surface reaction, O_2 re-adsorption. This suggests that the reduction can be sped up and driven to greater degrees by reducing the oxygen concentration in the vicinity of the particles. Whether this is achieved by removing oxygen from reaction zone or sweeping with more inert, the costs to separating oxygen must be fully considered, as suggested by Rager (2012).

A few insights from the reactive-particle receiver modeling suggest some changes to improve performance. The primary driver for high losses is the high reduction temperature and low solar absorptivity of ceria, both of which drive high re-radiation losses and lower η_{solar} . A material with better absorption in the solar spectrum has the potential to the baseline η_{solar} to about 19% (a 50% increase over ceria). Beyond material changes, flow management to increase particle residence times can yield greater

reduction and higher efficiencies. However, there must be an upper point of diminishing returns as the curtain reaches higher temperatures and has more re-radiation losses. The current curtain design results in a hot spot on the rear wall that would require some form of mitigation to prevent overheating of the material and reduce thermal stress by cooling the back wall with some mechanism that preheats the particles before dropping them in the receiver

The results shown in Figure 3-13 and Figure 3-14 show that the receiver flow rate can be varied dynamically to respond to transient radiation conditions and maintain consistent outlet conditions. Outlet temperature and degree of particle reduction can be varied through proper selection of inlet temperature, A downstream fuel-production process, however, requires careful consideration of how the particle chemical and thermal energy will be used downstream. To properly design the receiver, operation must be evaluated in the context of an integrated cycle analysis. The single-component optimum receiver may not optimize the entire plant output. For example, higher receiver outlet temperatures will enable greater efficiencies in the power cycle, which may offset greater re-radiation losses in the receiver. Higher outlet temperatures and greater amounts of reduction increase storage density, reducing the expected capital cost of any storage tank. Ideal solar concentration on the receiver requires evaluation of field arrangement and the trade-off between field costs and receiver performance.

3.5 Modeling Perovskite Reactors

While ceria was shown to not be the ideal material for a direct-absorption solar-thermal receiver due to high required temperatures and poor absorption capabilities, the

numerical experiments with ceria demonstrate the potential of the receiver to work with reactive particles. All reducible oxide materials suitable for H_2O- or CO_2-splitting require high temperature to form the reactive reduced state. However, materials that can provide lower-temperature reduction and reoxidation could improve receiver efficiencies by reducing re-radiation losses and increasing solar energy captured as chemical energy for fuel production. One attractive class of materials – perovskites with the unit crystal stoichiometry of ABO_3 where A and B are metal cations with valence states between +2 and +4 – are particularly attractive because they can undergo very large degrees of reduction while still maintaining a stable crystalline structure. By manipulating the selection of the A-site and B-site cations, perovskites can also be tuned to provide increased reduction at much lower temperatures and higher P_{O2} than ceria. By using multiple cations in either the A- or B-site of the perovskite lattice, reducibility can be further enhanced through creation of extrinsic vacancies. Further, unlike ceria, perovskites are often very dark in color, giving them very high solar-spectrum emissivities for good absorption.

To evaluate perovskites for solar-driven reduction in particle receivers , a candidate composition from the literature was studied within the reactive receiver model. The material chosen for investigation was $La_{0.1}Sr_{0.9}Co_{0.8}Fe_{O.2}O_{3-\delta}$ (LSCF-1982 or here LSCF), which has been shown to be a promising composition of high reducibility and fast reduction kinetics (Choi et al. 2011, Choi et al. 2012). LSCF is not an ideal material for commercial receiver operation due to its relatively high cost, but it has many attractive properties representative of perovskites, including an emissivity of $\varepsilon = 0.90$ (Guar et al. 2013). Further, sufficient thermodynamic and material property data exist for

LSCF to perform reasonable numerical calculations (Choi et al. 2011, Choi et al. 2012). Thus, LSCF was chosen for testing in this numerical model to evaluate the potential of perovskite materials to improve solar thermal receiver performance and storage capabilities.

3.5.1 LSCF thermodynamic and kinetic model parameters

As with ceria, $La_{0.1}Sr_{0.9}Co_{0.8}Fe_{O.2}O_{3-\delta}$ was modeled as a mixture of two-neutral species, $La_{0.1}Sr_{0.9}Co_{0.8}Fe_{O.2}O_3$ ($LSCFO_3$) and $La_{0.1}Sr_{0.9}Co_{0.8}Fe_{O.2}O_2$ ($LSCFO_2$). LSCF was modeled in two zones – the bulk and the surface – in order to separate the impacts of oxide-ion diffusion through the particle and the O2 desorption reaction at the surface. Unlike ceria, the changes in thermodynamics between the surface and the bulk have not been well quantified. Thus, for this study, the thermodynamics are the same in both the surface and the bulk, Thermodynamic data on LSCF reduction from Choi et al. (2012) as shown in Figure 3-16 is used similarly to derive thermodynamic properties including the non-ideal excess free energy terms. In this figure, ΔS_O is equal to $0.5\Delta S_{O2}$ that was used for ceria.

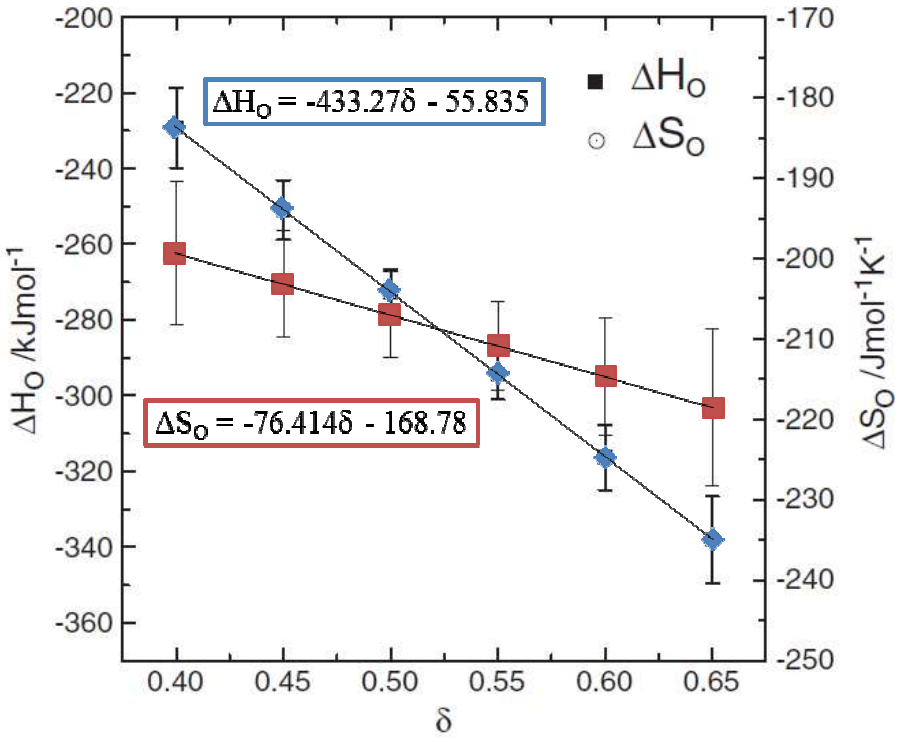

Figure 3-16 – LSCF thermodynamic fitting overlaid on the experimental data from Choi et al. (2012)

From this data, it is possible to find the value of the chemical potential change during reduction for LSCF by using Eq. 3-29 and Eq. 3-30.

$$\Delta\mu_O = \Delta H_O - T\Delta S_O = \frac{1}{2}\bar{R}T\ln\left(\frac{P_{O_2}}{P^0}\right) \qquad \text{[Eq. 3-29]}$$

$$\Delta\mu_{red} = \mu_{LSCFO_2}(\delta,\mathrm{T}) - \mu_{LSCFO_3}(\delta,\mathrm{T}) = \frac{1}{2}\mu^0_{O_2}(T) + \Delta\mu_O \qquad \text{[Eq. 3-30]}$$

As with ceria, Eq. 3-2 applies to define the chemical potential of the individual species. The excess chemical potential change due to ideal interactions is defined in Eq. 3-31,

while the ideal properties are specified by using the specific heat (c_p = 145.0 J $mol^{-1}K^{-1}$) suggested by Beale et al (2011).

$$\Delta\mu_{red}^{ex,0}(T,\delta) = RT\ln\left(\frac{X_{LSCFO_2}}{X_{LSCFO_3}}\right) \quad \text{[Eq. 3-31]}$$

3.5.2 LSCF Model Changes

The particle, gas flow, and heat-transfer equations are identical for LSCF simulations follow the equations used in the ceria modeling. The species equations are very similar, with $LSCFO_3$ and $LSCFO_2$ used in place of Ce_2O_4 and Ce_2O_3, respectively. Because LSCF is modeled without a sub-surface, the bulk diffuses directly to the surface, and thus R. 3-2 is eliminated. Finally, the surface reaction rate takes on a different form, shown in Eq. 3-32, as suggested in Choi et al. (2011). In this equation, δ_{eq} is the equilibrium reduction at the given particle temperature and P_{O2}

$$\dot{n}''_{R2} = k_s\bar{\rho}^0_{O(s)}\left(\delta_{eq}-\delta\right) \quad \text{[Eq. 3-32]}$$

The oxide-ion transport and surface kinetic parameters used for LSCF transport are defined in Table 3-7.

Table 3-7 - Governing transport properties for LSCF from Choi et al. (2011).

Reaction		Kinetic Parameter
Diff:	$LSCFO_3(b)+V_O(s)\rightarrow LSCFO_2(b)+O(s)$	$D_O = \left(1.01\cdot10^{-4}\right)\exp\left(-6730.9/T\right)$ (m^2/s)
R1:	N/A	N/A

R2:	2 O(s) → 2 V_O(s) + O_2(g)	$k_s = (0.109)\exp(-8935.8/T)$ (m/s) $\beta_{r2} = 0.5$

3.6 LSCF Reactor Results

3.6.1 LSCF Prototype-Scale Operating Conditions

Simulations were performed using the prototype-scale receiver in order to investigate how changes in $\dot{m}'_p$, ε_p, and the surface reaction rate constant - k_s impact LSCF-particle receiver performance. Changes in $\dot{m}'_p$ were helpful in establishing a potential operating point for the commercial scale receiver. Variations in ε_p and k_s were performed in order to assess the importance of these properties in design of new perovskite materials. The baseline parameters and operating conditions for the prototype-scale are shown in Table 3-8. The results for prototype-scale receiver are presented, followed by results for a commercial-scale receiver.

Table 3-8 - Baseline operating conditions for the prototype-scale LSCF reactor.

Property	Value (Baseline)
Receiver Dim. (m) ($L_{x,r}$, $L_{y,r}$, $L_{z,r}$)	(1.85, 5.0, 1.5)
Window Dim. (m) ($L_{x,w}$, $L_{y,w}$, $L_{z,w}$)	(1.0, 3.0, 0.05)
Curtain Dimensions (m) ($L_{x,c}$, $L_{y,c}$, $L_{z,c}$)	(1.0, 5.0, 0.01+0.0087y)
d_p (μm)	300
ε_p (-)	0.9
$\dot{m}'_p$ (kg $s^{-1}m^{-1}$)	7.0
$T_{part,in}$ (K)	800
q''_{solar} (kW m^{-2})	1000
$P_{O2,in}$ (atm)	0.001

3.6.2 LSCF Prototype-Scale Results

Prototype-scale LSCF receiver results are strongly dependent on $\dot{m}'_p$ .As seen in Figure 3-17, increasing particle flow-rate from 3 to 7 kg s^{-1} m^{-1} increases receiver efficiency η_{solar} from 61% to 76% due to higher curtain opacity. However, as with inert particles, the average outlet temperature falls from 1402 K to 1209 K due to lower absorption by each individual particle. Even though η_{solar} increases with $\dot{m}'_p$, the chemical storage efficiency η_{chem} decreases from 20% to 9%, due to lower temperatures and less reduction. At an $\dot{m}'_p$ of 3 kg s^{-1} m^{-1}, the outlet $\Delta\delta$ = 0.16 and outlet P_{O2} = 0.62 atm in the dense-particle core. At the highest $\dot{m}'_p$ = 7 kg s^{-1} m^{-1}, the outlet $\Delta\delta$ decreases to 0.03 while the outlet P_{O2} = 0.28 atm in the dense-particle core.

Because LSCF is used as a representative perovskite material, the influence of ε_p, which can vary with perovskite composition, is explored over a range from 0.7-0.95. As shown in Figure 3-18, T_{out}, η_{solar} and η_{chem} all increase with ε_p. T_{out} increases only 44 K from 1170 K to 1214 K as ε_p increases from 0.7 to 0.95, due to the temperature-damping effects of additional chemical storage. η_{solar} increases from 67% to 78%, with 4% of that increase due to additional chemical storage. Over this range, $\Delta\delta$ increases from 0.021 to 0.035 while outlet P_{O2} increases from 0.22 to 0.32 atm in the dense-particle core.

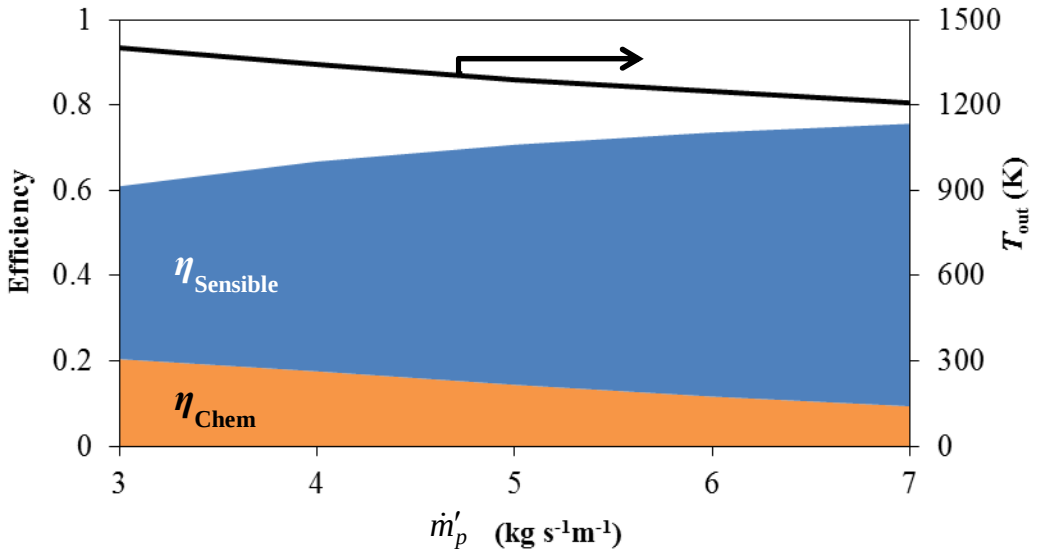

Figure 3-17 – Efficiency and outlet temperature as a function of $\dot{m}'_p$ for the prototype-scale receiver using LSCF particles operating at baseline conditions in Table 3-8.

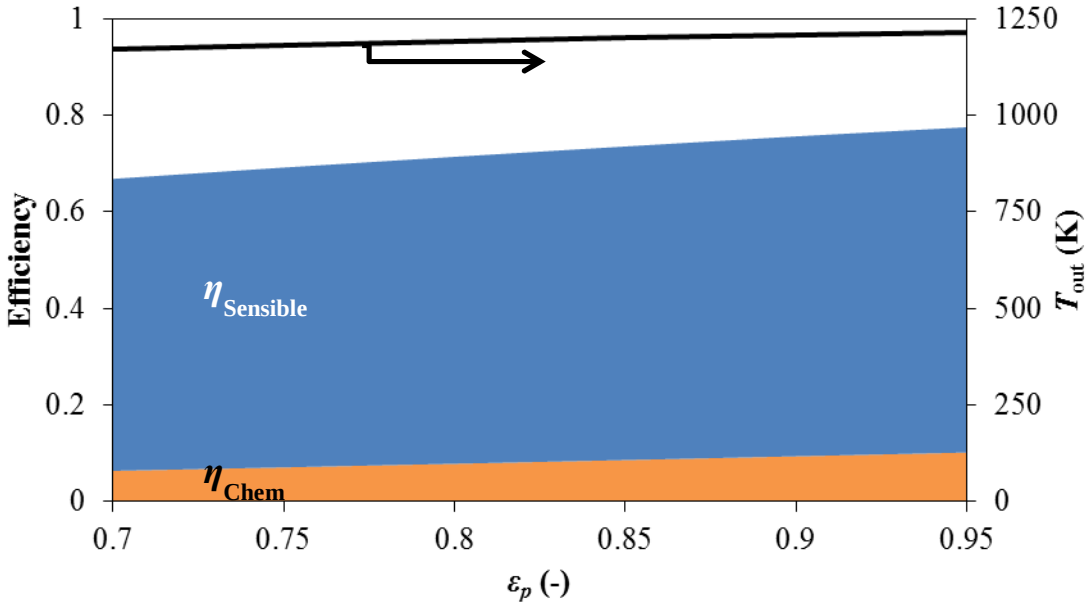

Figure 3-18 – Efficiency and outlet temperature as a function of ε_p for the prototype-scale receiver using LSCF particles operating at baseline conditions in Table 3-8.

The evolutions of the curtain T_p, P_{O2}, δ, and equilibrium δ_{eq} at the baseline inlet conditions are shown in Figure 3-19(a) for the base-case operating conditions. T_p increases from an inlet value of 800 K to 815 K in the entrance region, reaches a maximum temperature of 1226 K by the exit of the directly irradiated zone, and then decreases to 1208 K by the exit due mostly to conversion of sensible energy to chemical energy. The evolution in P_{O2} and δ indicate little O_2 release until about 1 m into the directly irradiated zone.

In Figure 3-19 $\delta_{eq} - \delta$ represents the thermodynamic driving force for the reduction. A strong driving thermodynamic force over the entirety of the directly irradiated zone is offset by slow kinetics until T_p reaches around 970 K in the directly irradiated zone. The relatively large thermodynamic forcing at the exit of the receiver indicates that kinetics limit the performance of the perovskite and suggests that kinetics are a critical performance metric for evaluating alternative oxide compositions. Closer investigation shows that difference between δ_b and δ_s is very small and thus for this range of particle sizes, diffusion of oxide-ions is not rate limiting. Rather, as with ceria, the surface desorption of O2 controls the rate of perovskite reduction.

In order to investigate the potential of similar perovskites that can achieve faster kinetics, a sensitivity analysis was conducted by artificially increasing the surface reaction-rate constant k_s by a factor of 10, as shown in Figure 3-19(b). Doing this greatly increases the outlet P_{O2} and $\Delta\delta$ to 0.56 atm and 0.089, respectively. The increased chemical energy storage decreases the outlet T_p by 90 K compared to the slower reaction case. Even with faster kinetics, reaction is not complete by the exit of the directly irradiated zone, and sensible energy is converted to chemical energy as T_p falls while δ

continues to rise. In fact, the particles have not equilibrated by the exit of the receiver, and would continue this conversion process, although the reaction would be constrained by increasing P_{O2}.

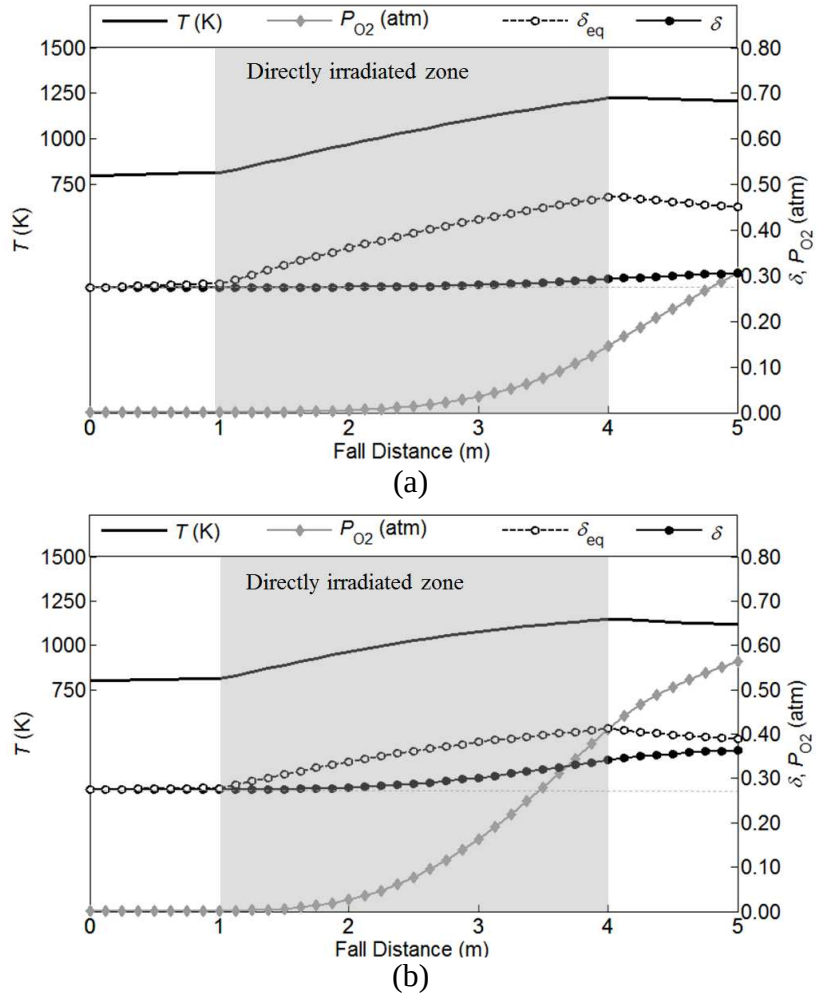

Figure 3-19 – Evolution along the length of fall of average T_p, δ, and P_{O2}, as well as the equilibrium δ at the given T_p and P_{O2} for operating conditions in Table 3-8 and kinetic rate constant (a) k x 1 and (b) k x 10.

Figure 3-20 shows he influence of both reaction rate and d_p on η_{solar}. As with inert receivers, smaller particles perform better than larger particles due to higher curtain

opacity and greater surface area to drive reduction. The impact of increased surface area is more apparent at lower reaction rates, where the increase in chemical storage is greater than linear as d_p decreases.

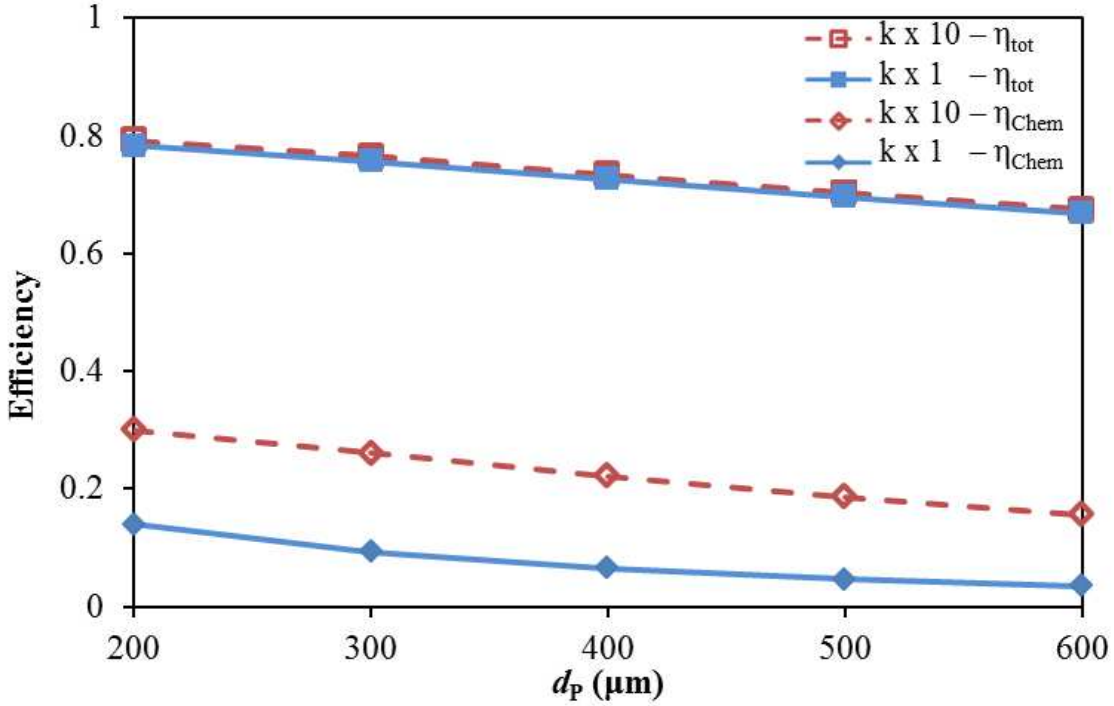

Figure 3-20 – – Prototype-scale receiver efficiency, chemical and total (includes chemical and sensible), for LSCF particles operating with baseline conditions in Table 3-8 and differing d_p and two reaction-rates. The k x 10 cases utilizes a reaction rate constant that a factor of 10 larger.

With faster kinetics, a greater fraction of the absorbed solar energy goes into chemical storage. For the cases in Figure 3-19, , the reactor with faster kinetics stores 26.1% of inlet solar energy as chemical energy and 50.4% as sensible energy, compared to 9.3% chemical storage and 66.5% sensible storage for the slower kinetics. Faster kinetics greatly increase the chemical storage, the η_{solar} by less than 1% in all cases. The small increase in total efficiency is driven by lower radiation losses due to lower particle

temperatures, as shown in Figure 3-21 This occurs because η_{solar} is dominated by the ability of the curtain to absorb incoming radiation, which is unaffected by reaction.

The T_p profiles change significantly with the kinetic rates. When kinetics are slower, the outlet T_p behaves more like an inert particle receiver, with reducing outlet temperature as d_p increases due to inferior absorption. Unlike inert particles, the competing effect of chemical storage actually causes lower T_p at the smallest particle sizes, due to the impact of greater surface area. Decreasing d_p from 600 to 200 μm increases $\Delta\delta$ from 0.012 to 0.048 for slower kinetics. With faster kinetics, the impact of greater surface area dominates the effect of greater absorption, and outlet T_p decreases monotonically with d_p while $\Delta\delta$ increases from 0.053 to 0.102.

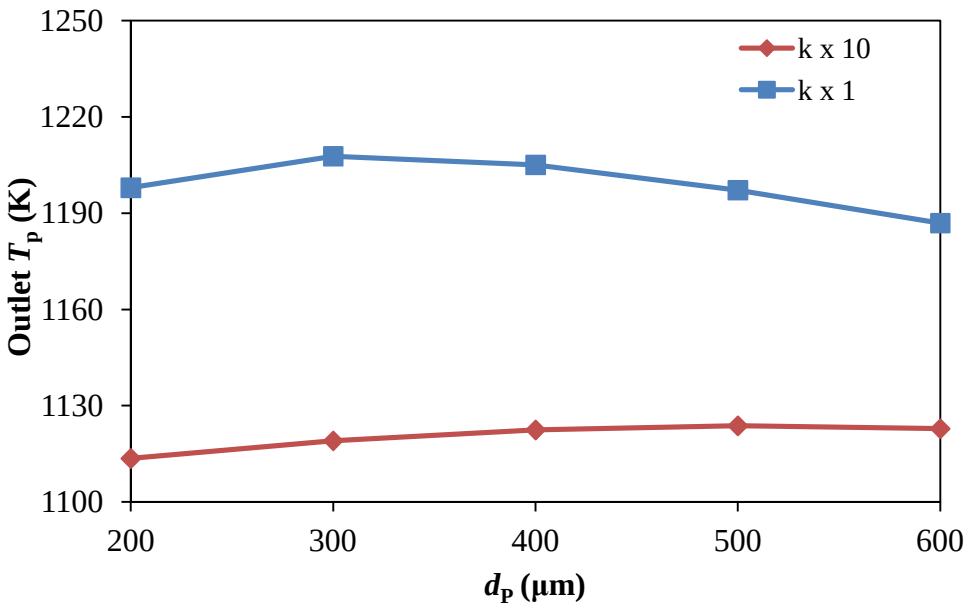

Figure 3-21 - Prototype-scale receiver average outlet temperature for LSCF particles operating with baseline conditions in Table 3-8 and differing d_p for two reaction-rates. The k x 10 cases utilizes a reaction rate constant that is a factor of 10 larger.

3.6.3 LSCF Commercial-Scale Operating Conditions

LSCF was tested in the commercial-scale receiver operating at atmospheric P_{O2} gas inflow. This allowed the receiver to operate with an open aperture. The operating parameters used for these tests are shown in Table 3-9. These tests not only evaluate the potential for a perovskite material in a direct absorption receiver, but also study the impacts of a reactive flow at high mass-flow conditions.

Table 3-9 - Baseline operating conditions for the commercial-scale LSCF reactor.

Property	Value (Baseline)
Receiver Dim. (m) ($L_{x,r}$, $L_{y,r}$, $L_{z,r}$)	(12.0, 21.0, 15.0)
Aperture Dim. (m) ($L_{x,a}$, $L_{y,a}$, $L_{z,a}$)	(11.0, 20.0,-)
Curtain Dimensions (m) ($L_{x,c}$, $L_{y,c}$, $L_{z,c}$)	(11.0, 21.0, 0.04+0.0087·y)
d_p (μm)	280
ε_p (-)	0.9
$\dot{m}_p$ (kg $s^{-1}m^{-1}$)	10.0-80.0
$T_{part,in}$ (K)	800
q''_{solar} (kW m^{-2})	1000
$P_{O2,in}$ (atm)	0.21

3.6.4 Commercial-Scale Results

The prototype-scale receiver results, such as those in Figure 3-19 demonstrated that LSCF particles continued to react even when the local P_{O2} was above atmospheric concentrations (0.21 atm). Thus. LSCF particle reduction were simulated in a commercial-scale reactor-receiver. Temperatures within a commercial-scale receiver at

$\dot{m}'_p$ = 20 kg s^{-1} m^{-1} are shown in Figure 3-22, which shows very different temperature profiles compared to the commercial-scale inert receiver results in Figure 2-36. The rear-wall temperature increases further down the receiver due to direct solar insolation because particle spreading decreases curtain opacity. The side walls are also heated along the length of fall due to re-radiation from the particles and rear-wall. Moving from the rear to the front along the side walls, there is a bump in the temperature on the side-walls due to exposure to the hotter front-half of the curtain than the rear.

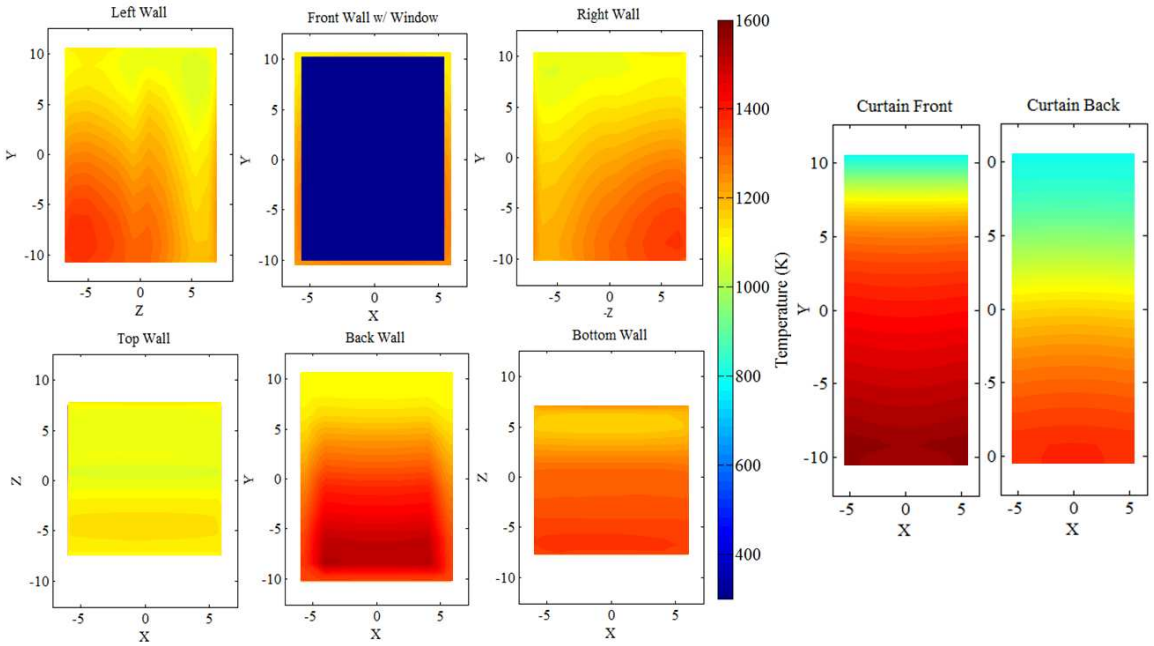

Figure 3-22 - Wall and curtain temperature profiles for reactive ceria particles with operating parameters in Table 3-9 for $\dot{m}'_p$ = 20 kg $s^{-1}m^{-1}$.

The curtain transmissivity for LSCF particles, as shown in Figure 3-23, is higher than for the inert CarboCeram particles at the same particle size and $\dot{m}'_p$. Transmissivity

scales with $\exp\left(-\frac{\dot{m}'_p}{d_p \rho_p u_p}\right)$. Because ρ_p for LSCF is 1.84 times larger than that of CarboCeram and the particle velocity differs LSCF particle curtains with all other parameters equal have a transmissivity that is $\tau_{LSCF} = (\tau_{CarboCeram})^{0.46}$. Physically, this happens because, at the same $\dot{m}'_p$ and d_p, there are more particles in a flow with that has lower ρ_p.

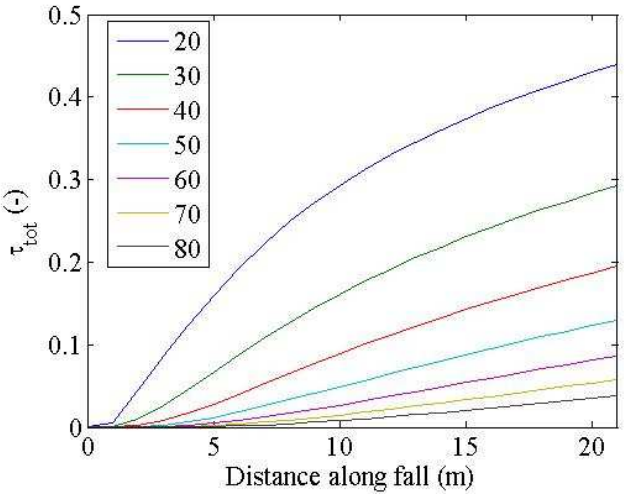

Figure 3-23 – Profiles of curtain τ for varying $\dot{m}'_p$ (kg $s^{-1}m^{-1}$) along the length of fall.

Profiles for T_p, δ_p, and P_{O2} along the length of fall are shown in Figure 3-24 to Figure 3-26. The transition between the lower-temperature region without reactions and the higher-temperature region with reactions starts around a T_p of 970 K. As $\dot{m}'_p$ increases, greater distances along the fall length are required before the reactions become significant. The T_p at the rear of the curtain increases much slower than the front, due to a diminished solar beam penetrating to that depth.

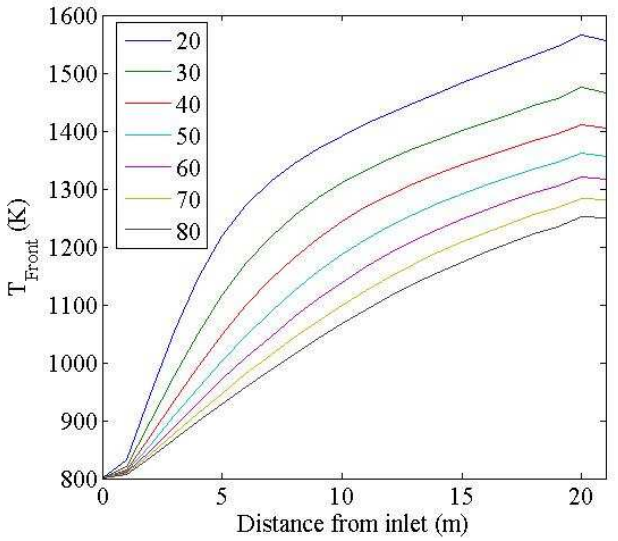

(a)

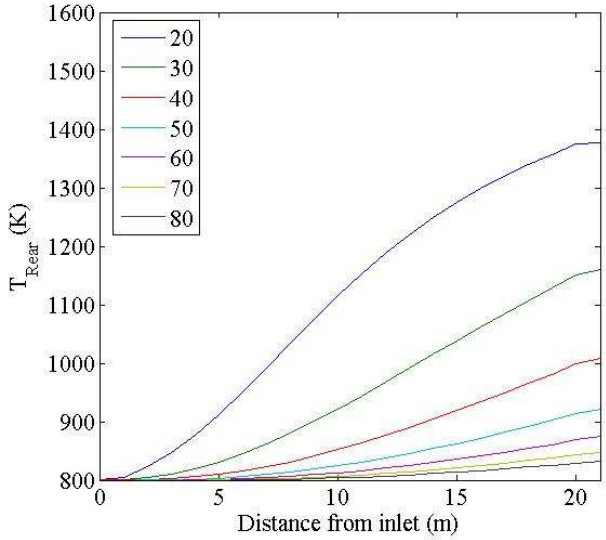

(b)

Figure 3-24 – Profiles of average T_p for varying $\dot{m}'_p$ (kg s^{-1}m^{-1}) in the (a) front-half and (b) rear-half of the curtain along the length of fall.

The higher T_p achieved at lower $\dot{m}'_p$ cases enables significantly greater δ_p, as shown in Figure 3-25. While all mass flow rates obtain a $\Delta\delta_p$ greater than 0.078 in the front of the curtain, only the lowest flow-rates exhibit any in the rear. This demonstrates

that, even more than an inert receiver, reactive receiver performance is strongly influenced by temperature gradients across the depth of the curtain.

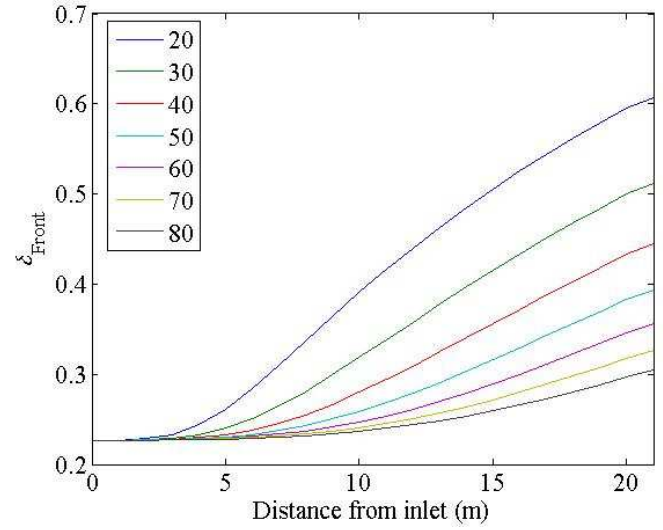

(a)

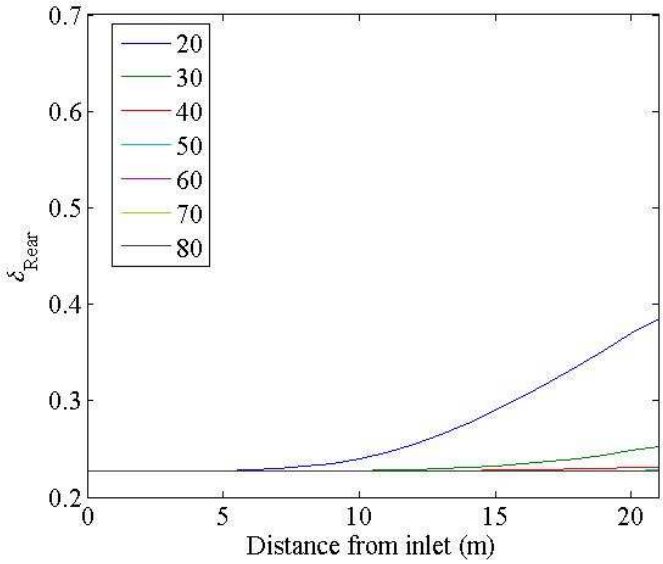

(b)

Figure 3-25 – Profiles of average δ for varying $\dot{m}'_p$ (kg s^{-1}m^{-1}) in the (a) front-half and (b) rear-half of the curtain along the length of fall.

$\delta_{p\ is}$ influenced by P_{O2} as well as T_p. P_{O2} is plotted in Figure 3-26 for a range of $\dot{m}'_p$. The smallest $\dot{m}'_p$ case achieves a $\Delta\delta_p$ that is 2.8 times that of the highest $\dot{m}'_p$ case, but the local P_{O2} only differs by less than 30%. Even though the individual particles do not release as much oxygen at high $\dot{m}'_p$, the higher total loading of particles causes a similar amount of oxygen release. For example at 40 kg s^{-1} m^{-1}, $\Delta\delta_p$ = 0.001 yet the flow has nearly the same outlet P_{O2} as the 30 kg s^{-1} m^{-1} case with a $\Delta\delta_p$ = 0.005.

Increased gas entrainment and lower $\Delta\delta_p$ for higher $\dot{m}'_p$ reduces the impact of higher particle loadings on P_{O2}. The total mass of air over the width of the curtain increases from 0.18 to 0.61 kg s^{-1} m^{-1} as $\dot{m}'_p$ increases from 20 to 80 kg s^{-1} m^{-1}.

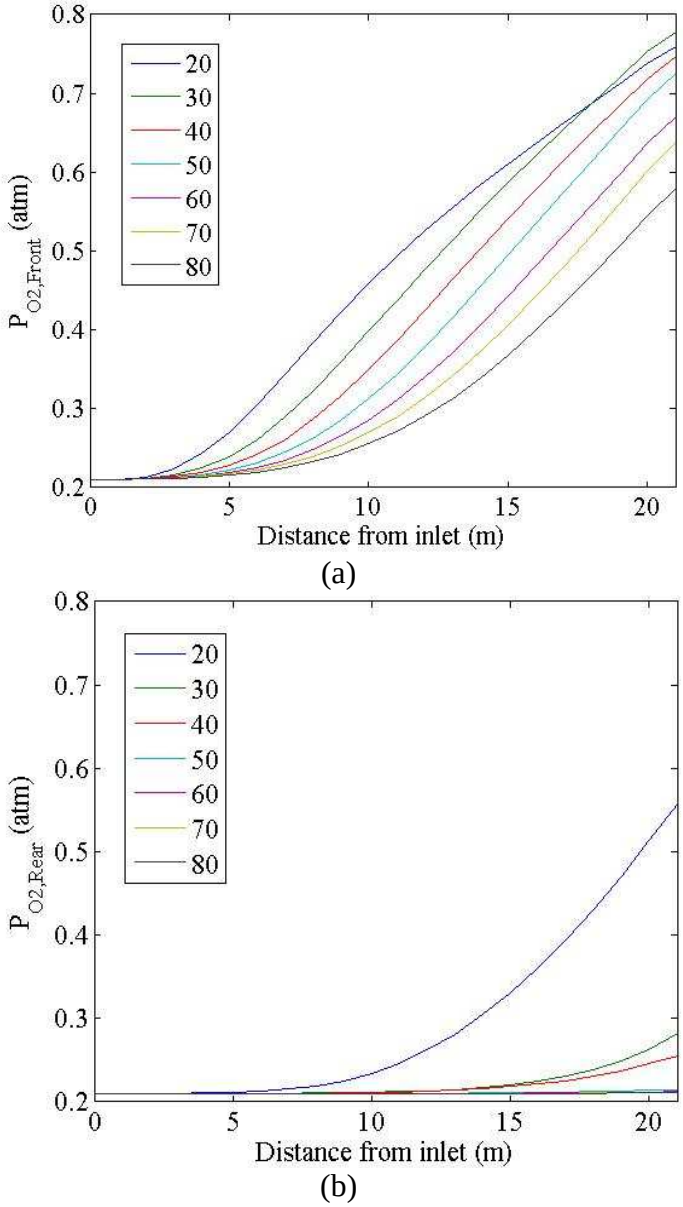

Figure 3-26 - Profiles of average P_{O2} for varying $\dot{m}'_p$ (kg $s^{-1}m^{-1}$) in the (a) front-half and (b) rear-half of the curtain along the length of fall.

Higher $\dot{m}'_p$ results in lower temperatures and chemical storage, but with the advantage of higher η_{solar}, as shown in Figure 3-27. Increasing $\dot{m}'_p$ increases the total absorption of the particle curtain and increases the disparity in T_p between the front and rear of the particle flow. At higher $\dot{m}'_p$, a greater proportion of energy is absorbed as

sensible heating, and the increase in sensible heating is greater than loss of chemical storage. The increased curtain opacity at higher $\dot{m}'_p$ mitigates any hot spots on the rear-wall hot-spot and decreases the average rear-wall temperature. The maximum T_{wall} decreases from 1524.6 K to 1062.7 K as $\dot{m}'_p$ increases from 20 to 80 kg s^{-1} m^{-1} flow.

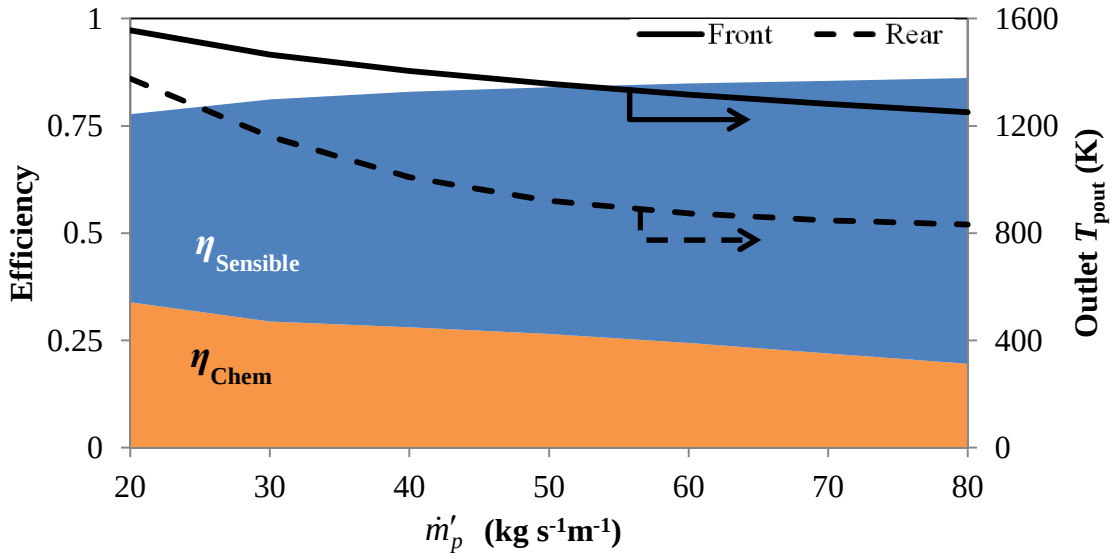

Figure 3-27 - Commercial-scale receiver efficiencies and temperatures using LSCF particles operating with baseline conditions in Table 3-9 and the specified mass flow-rates.

3.7 Discussion of LSCF Performance

The LSCF simulations illustrate the potential of perovskites in a direct-absorption solar reactor. The favorable thermodynamics of LSCF reduction shows the potential to work with relatively high P_{O2}, which mitigates the balance of plant costs of separating O_2 from the flow (Rager, 2012). The driving force for the reduction process, the chemical potential, has a strong temperature dependence due to the large ΔS_O shown in Figure

3-16. Larger ΔS_O values enable the chemical reduction process to be driven to greater $\Delta\delta$ values with lower driving temperatures.

While the thermodynamics of LSCF are very attractive, the model kinetics were not optimal. For both the prototype-scale and commercial-scale, the LSCF reduction along the fall did not keep up with the particle heating, causing a significant thermodynamic driving force to remain at the exit of the receiver. Outside the directly irradiated zone, T_p begins to fall as particles converted sensible energy into chemical storage. This process will eventually equilibrate in storage, at a δ that depends on the choice of storage P_{O2}. This hurts performance as the particles maintain a higher T_p within the receiver, leading to greater re-radiation losses. Further, this reduction in maximum T_p decreases the value of the stored energy for use in down-stream processes. While T_p can be raised at a later time by controlling the P_{O2} to oxidize the materials to a higher temperature, doing so imposes an energy penalty in obtaining a flow at higher P_{O2} and heating that flow.

The tradeoff between higher η_{solar} with a larger $\dot{m}'_p$ and higher, more uniform T_p with greater η_{chem} at lower flow-rates represents an interesting design problem. As with inert receivers, this performance underscores the need to maintain a curtain with high opacity along the fall, in order to maximize solar absorption. The large hot-spot that develops at lower $\dot{m}'_p$ in Figure 3-22 is mirrored by increasing transmissivity in Figure 3-23. As the fall distance increases, particle spreading hurts curtain performance. Higher performance can be immediately obtained by having particles fall in multiple stages, so that their velocity could stopped and reset, without a significant increase in receiver complexity. Higher $\dot{m}'_p$ increases η_{solar} but with significant temperature gradients across the flow. This leads to a similar problem raised by the kinetics: higher re-radiation and

difficulties in storage. While particles will eventually equilibrate, raising the rear-curtain temperature in storage releases significantly more O_2. If particle temperature equilibration is not handled correctly, any benefit of added chemical storage will be mitigated by limited reduction due to the high P_{O2}.

These challenges highlight the necessity of closely matching the reacting particle to the receiver design. Ideal operation occurs when the particles react continuously to stay at their equilibrium value and the curtain is heated evenly along the fall. Thus, if particle kinetics cannot be increased, then particle heating rate should be adjusted so that there is a better match. Decreasing u_p improves residence time and allows the kinetics and inter-curtain heating to respond to the solar heating.

Ideal receiver design must be done within the context of full-cycle analysis. The receiver must be sized so that the desired outlet temperature can be reliably obtained. As mentioned earlier, any kind of perovskite particle requires careful consideration of how the excess O_2 is going to be utilized. Further, the stored chemical energy creates new possibilities, such as purposefully oxidizing the particles to obtain temperatures higher than the storage temperature.

Finally, perovskite materials require additional studies beyond the capabilities of this model. LSCF, as well as other perovskites, have a propensity to sinter at high temperatures (Choi et al., 2012), impacting long term viability of the particles. The interaction of the flowing particles with the gas-phase, especially in terms of particle stability, requires further investigation. The gas entrainment-model itself also requires evaluation as to how well it applies to reacting particles. This is one of the goals of Chapter 4.

3.8 Conclusions

In this study, a reactive-particle model was developed and integrated into a simplified solar receiver model previously developed. This demonstrated the potential for reactive particles within the context of a solar receiver. The results of ceria highlighted the necessity for lower reaction temperatures and higher emissivities to achieve performance that is realistically useful. At the same time, improved efficiencies compared to inert particles showed a promising opportunity for reactive particle integration within a receiver: for improved receiver efficiency and storage densities.

However, these results do raise some important concerns that should be investigated in more detail. The entrainment model used here was developed for isothermal particles in an open environment, where there is a large mass of excess gas, no thermal expansion or buoyancy, and without the gas-flow due to particle reaction. To better understand the impacts of an internal flow and natural convection currents on particle flow and spreading, particle flows should be studied with more in-depth (CFD) models. The results show that chemical thermodynamics and kinetics have a very important impact on the overall performance of the flow, and alternative chemistries should be investigated. Maximum cycle reduction temperature has a significant effect on total efficiency, although lower temperatures result in less reduction. The results from LSCF cases clearly indicate that lower-temperature reduction cycles may improve efficiency significantly.

Particle physical and optical properties, most notably the emissivity, play a very important role in receiver design, and higher absorption is required for an efficient

receiver. Proper receiver design requires looking at the receiver in a full-cycle context in order to understand the full impacts and design tradeoffs available in the receiver. This reactive receiver model is an excellent tool to generate the data needed to perform a full-cycle analysis and optimize operation. Down-stream processes must be properly investigated (heat recovery, conveyance, storage, reactor processing) to close the loop on cycle design. Particle receivers have great potential due to their flexibility, storage density, and simple operation. Reactive particles, if chosen correctly, can supplement any design and further improve their yields.

Chapter 4: Modeling Reactive Particle Receivers with Computational Fluid Dynamics

Solid particle receivers have potential to work with reactive particles to drive endothermic reactions for either high-density thermochemical energy storage or high-temperature H_2O and/or CO_2-splitting reactions. Simplified models presented in the previous chapter have highlighted the interplay between heat transfer to the particles temperatures and particle reaction progress in a solid particle receiver. However, these simple models have relied on semi-empirical gas-phase treatments, and the influence of the gas-phase flows on the reacting particle flow was not explored in adequate detail to fully resolve the impacts of the gas flow-field on the receiver performance metrics.

In this chapter, the performance of reactive ceria particles is evaluated in the context of a computational fluid dynamics (CFD) simulation that fully resolves the gas-flow field. Simulation of the 3-D flow-field incorporates the multi-phase gas/particle flows with inclusion of gas-release from the reacting particles. The CFD simulations provides a higher fidelity assessment of how operating conditions can impact receiver performance. Further, CFD simulations can be used to modify the receiver structure for better control of the gas-flow to improve performance.

To perform these complex reacting multi-phase simulations, custom models must be developed to handle the thermodynamic and kinetic rates of the reacting particles. In this case, for oxide particle reduction, the thermodynamics and kinetics are based on derived from previous measurements of equilibrium particle reduction. The thermochemistry are integrated into the commercial CFD package ANSYS Fluent through a set of user-

defined functions for the particle reactions and inter-phase coupling. Ceria was again chosen as the test species to allow comparisons between models and to take advantage of the wealth of ceria thermodynamic and physical property data. The thermo-kinetic model for ceria described in chapter 3 is adapted to work with the particle models employed by Fluent. Results obtained for a range of particle sizes and flow-rates are analyzed and compared to the simplified model data. These CFD results are then used to consider improvements to the solid particle reactor designs.

4.1 Modeling reactive particle receivers with Fluent

4.1.1 Previous CFD simulations

Many researchers have performed CFD simulations on solar receivers with inert particles and separately on stationary solar reactors. These provide a baseline for development of a CFD model for the reactive particle receiver studied here. As mentioned in previous chapters, multiple studies have looked at inert solid particle receivers in the context of a CFD simulation. Meier (1999) performed the first CFD simulations of a particle receiver in a 2D domain using a Lagrangian framework for particle-tracking. Meier used the Monte Carlo (MC) method for the solar radiation input, and a k-ε turbulence model for the Eulerian simulation gas-phase flow field. Chen et al. (2007) performed calculations in a 3D domain with Lagrangian particle-tracking, MC ray-tracing for the solar loading, and the discrete ordinates (DO) model for thermal radiation, and the realizable k-ε turbulence model for modeling the gas flow field. Siegel et al. (2010) improved on the model of Chen et al. (2007) by implementing a DO model for the incoming solar loading. Khalsa et al. (2011) improved the DO solar model further

to fully capture the incoming solar radiation within the context of the DO model by using a ‘solar patch calculator.’

A variety of CFD solar reactor models have been implemented for alternative geometries with simple reaction models. Villafán-Vidales et al. (2011) modeled $NiFe_2O_4$ reduction inside of a volumetric foam receiver with a 2D axis-symmetric domain, a global one-step reaction model, and P1-approximation of the radiative transfer equation. Multiple researchers have simulated small-particle solar reactors using a Eulerian-Eulerian particle-gas flow model for ZnO reduction (Haussener et al., 2009), methane-cracking with carbon seed-particles (Ozalp et al., 2010), and steam gasification of biomass (Z’Graggen and Steinfeld, 2008; Martinek et al., 2012). These models all implement the DO radiation transfer model and single-step reactions in 2D (Abanades et al, 2007; Z’Graggen and Steinfeld, 2008) and 3D domains (Ozalp et al., 2010; Martinek et al., 2012). Abanades et al. (2007) modelled a ZnO particle solar reactor in a 2D domain with a Eulerian gas flow and Lagrangian particle tracking with a single-step reaction-rate model, and DO radiation transfer.

4.1.2 Model formulation

This study extends the model described in Chen et al. (2007) to include reactive particles. The gas phase is modelled in an Eulerian framework, while particles are tracked in a Lagrangian reference frame. The model includes gas-particle coupling through species, momentum, and heat exchange terms. A Lagrangian treatment of the particles is appropriate for these flows over most of the fall distance, as, past the near-entrance region (less than 0.5 m from the entrance depending on flow rate) particles maintain a

volume fraction below 10% (Kim et al, 2003). Particle flows with volume fractions below 12% are considered dilute enough to have very little inter-particle momentum exchange via collision while falling (Hruby et al., 1986) such that Lagrangian particle tracking methods can be used.

4.1.2.1 Gas Equations

The gas continuity, momentum, species, and energy equations are solved for the mean gas velocity vector $\overline{u}_{g,i}$, pressure P, gas species mass fraction $\overline{Y}_k$, and mean gas temperature $\overline{T}_g$. These equations for mean properties are solved for the turbulent flow via time-averaging in accordance with the k-ε turbulence formulation. The instantaneous properties, φ, are represented as a combination of the time-average quantity, $\overline{\varphi}$, and a fluctuation, φ', around the mean, where φ represents $u_{g,i}$, T_g, and Y_k.

$$\varphi = \overline{\varphi} + \varphi' \qquad \text{[Eq. 4-1]}$$

The continuity equation is shown in Eq. 4-2, where S_m^Y is the mass source term for species, m, due to reactions from the Lagrangian particles. For the ceria particles, oxygen is the only species exchanged between the particles and the gas.

$$\frac{\partial \rho_g \overline{u}_{g,i}}{\partial x_i} = \sum_{m=1}^{n_m} S_m^Y \qquad \text{[Eq. 4-2]}$$

The species equation is shown in Eq. 4-3, where D_m is the diffusivity of species m, μ_t is the turbulent viscosity, and Sc_t is the turbulent Schmidt number. Sc_t is set to 0.7 as

suggested by Yimer et al. (2002) for jet flows, which have similar physics to the entrained-gas flows in this study.

$$\frac{\partial}{\partial x_j}\left(\rho_g \bar{u}_{g,j}\bar{Y}_m\right) = \frac{\partial}{\partial x_j}\left[\left(\rho_g D_m + \frac{\mu_t}{Sc_t}\right)\frac{\partial \bar{Y}_m}{\partial x_j}\right] + S_m^Y \qquad \text{[Eq. 4-3]}$$

The gas momentum equation is shown in Eq. 4-4, where S_i^M is the momentum source term for the gas phase due to particle drag.

$$\frac{\partial}{\partial x_j}\left(\rho_g \bar{u}_{g,i}\bar{u}_{g,j}\right) = -\frac{\partial P}{\partial x_i} + \frac{\partial}{\partial x_j}\left[\mu\left(\frac{\partial \bar{u}_{g,i}}{\partial x_j} + \frac{\partial \bar{u}_{g,j}}{\partial x_i}\right) - \rho_g \overline{u'_{g,i}u'_{g,j}}\right] + S_i^M - \rho_g g_i \qquad \text{[Eq. 4-4]}$$

The Reynold's stress term, $\rho_g \overline{u'_{g,i}u'_{g,j}}$, due to turbulent interactions is determined by Eq. 4-5, to be consistent with the Boussinesq hypothesis (Hinze, 1975).

$$\rho_g \overline{u'_{g,i}u'_{g,j}} = \mu_t\left(\frac{\partial \bar{u}_{g,i}}{\partial x_j} + \frac{\partial \bar{u}_{g,j}}{\partial x_i}\right) - \frac{2}{3}\rho_g \delta_{ij} k \qquad \text{[Eq. 4-5]}$$

In Eq. 4-5, k is the turbulent kinetic energy associated with the flow according the turbulence model employed, μ_t is the turbulent viscosity, and δ_{ij} is the Kronecker delta function. The turbulent viscosity is determined by Eq. 4-6, where ε is the turbulence dissipation, and C_μ is a variable that changes with the mean flow and turbulence as described by ANSYS (2011).

$$\mu_t = \frac{\rho_g C_\mu k^2}{\varepsilon} \qquad \text{[Eq. 4-6]}$$

The gas phase energy equation is shown in Eq. 4-7, S^T is the heat source term due to convection from the particles to the gas. Pr_t is the turbulent Prandtl number, set to 0.90 as suggested by Chen et al (2007).

$$\frac{\partial}{\partial x_j}\left(\rho_g \bar{u}_{g,j} c_{p,g} \bar{T}_g\right) = \frac{\partial}{\partial x_j}\left[\left(\alpha_g + \frac{\mu_t}{\mathrm{Pr}_t}\right)\frac{\partial \bar{T}_g}{\partial x_j}\right] + S^T \qquad \text{[Eq. 4-7]}$$

The gas density is determined from the ideal gas law, as shown in Eq. 4-8, where R is the ideal gas constant and P_{OP} is the baseline operating pressure.

$$\rho_g = \frac{P_{OP} + P}{R\bar{T}_g \sum_{m=1}^{n_m} \frac{\bar{Y}_m}{W_m}} \qquad \text{[Eq. 4-8]}$$

Turbulence in the gas flow is handled with the realizable *k-ε*, as suggested by Chen et al. (2007), which is a modification of the standard *k-ε* model to satisfy mathematical constraints that prevent non-physical Reynolds stresses from developing. The realizable *k-ε* model has shown to have superior accuracy for flows with rotation, boundary layers with adverse pressure gradients, separation, recirculation (ANSYS, 2011).

The equation for the transport of turbulent kinetic energy is shown in Eq. 4-9. In this equation, σ_k, the turbulent Prandtl number for k, is set 1.0; G_k is turbulent energy production due to gradients in the mean velocity; and G_b is turbulent energy production due to buoyancy effects, as described in (ANSYS, 2011).

$$\frac{\partial}{\partial x_j}\left(\rho_g \bar{u}_{g,j} k\right) = \frac{\partial}{\partial x_j}\left[\left(\mu + \frac{\mu_t}{\sigma_k}\right)\frac{\partial k}{\partial x_j}\right] + G_k + G_b - \rho_g \varepsilon \qquad \text{[Eq. 4-9]}$$

The transport of turbulence dissipation is described by Eq. 4-10, which relates ε to the mean rate of strain S.

$$\frac{\partial}{\partial x_j}\left(\rho_g \bar{u}_{g,j} \varepsilon\right) = \frac{\partial}{\partial x_j}\left[\left(\mu + \frac{\mu_t}{\sigma_\varepsilon}\right)\frac{\partial \varepsilon}{\partial x_j}\right] + \rho_g C_1 S - \rho_g C_2 \frac{\varepsilon^2}{k + \sqrt{v}} + C_{1\varepsilon} C_{3\varepsilon} \frac{\varepsilon}{k} G_b \qquad \text{[Eq. 4-10]}$$

In Eq. 4-10, the nomenclature include constants σ_ε = 1.0, C_2=1.9, and $C_{1\varepsilon}$ = 1.44, and variables as indicate in Eq. 4-11 to Eq. 4-14.

$$S = \sqrt{2 S_{ij} S_{ij}} \qquad \text{[Eq. 4-11]}$$

$$\eta = S \frac{k}{\varepsilon} \qquad \text{[Eq. 4-12]}$$

$$C_1 = \max\left[0.43, \frac{\eta}{\eta + 5}\right] \qquad \text{[Eq. 4-13]}$$

$$C_{3\varepsilon} = \tanh\left|\frac{\bar{u}_z}{\sqrt{\bar{u}_x^2 + \bar{u}_y^2}}\right| \qquad \text{[Eq. 4-14]}$$

Wall and inlet effects play a very important role in determining the evolution of the flow field. In order to avoid using a large number of discretization in the near-wall region to resolve the strong shear, the standard wall functions are used. This approach imposes a set wall profile to calculate the flow properties in cells adjacent to the wall, while still accurately capturing the wall-effects (Launder and Spalding, 1974). The turbulent inlet conditions are specified according to the intensity, I_t, and hydraulic diameter of the particle inlet slit, D_h.

4.1.3 Particle Equations

The particles are represented by a set of Lagrangian-frame equations that are integrated along the fall direction. The particles are treated as uniform-sized spheres of the chosen diameter. The total mass flow-rate of particles is split evenly among a large number of injection points, from which a representative particle is released. While the Lagrangian governing equations are solved for an individual particle, each trajectory actually represents many particles, $\dot{N}_p$, as shown in Eq. 4-15, where $\dot{m}_p$ represents the particle mass flow-rate associated with that injection.

$$\dot{N}_p = \frac{\dot{m}_p}{\rho_p\left(\frac{\pi}{6}d_p^3\right)} \qquad \text{[Eq. 4-15]}$$

In order to include the impacts of turbulent particle dispersion, stochastic particle tracking is used in conjunction with the discrete random walk (DRW) model for the instantaneous gas velocity at each point. With this formulation, each individual particle injection is repeated n_{drops} times. For each drop, the instantaneous local gas velocity, $u_{g,i}$, is a combination of the time-averaged gas velocity, $\bar{u}_{g,i}$, and an instantaneous random fluctuation, $u'_{g,i}$ as shown in Eq. 4-16. The gas velocity fluctuation, determined by Eq. 4-17, is different for each drop and each particle step through ς, whichis a randomly distributed number to determine the local strength according the DRW model.

$$u_{g,i} = \bar{u}_{g,i} + u'_{g,i} \qquad \text{[Eq. 4-16]}$$

$$u'_g = \varsigma\sqrt{\overline{u'^2}} = \sqrt{\frac{2k}{3}} \qquad \text{[Eq. 4-17]}$$

The momentum equation shown in Eq. 4-18 equates the change in particle momentum with the drag from the gas and gravitational acceleration. The particle Reynolds number Re_p calculated in Eq. 4-19 is based on the difference between the particle velocity and instantaneous gas velocity. The particle drag coefficient, C_D, is shown in Eq. 4-20, and is applicable to smooth particles over a wide range of Re_p (Morsi and Alexander, 1972).

$$\frac{du_{p,i}}{dt} = \frac{18\mu}{\rho_p d_p^2}\frac{C_D \operatorname{Re}_p}{24}\left(u_{g,i} - u_{p,i}\right) + \frac{g_i\left(\rho_p - \rho_g\right)}{\rho_p} \qquad \text{[Eq. 4-18]}$$

$$\operatorname{Re}_p = \frac{\rho_g d_p \left|u_p - u_g\right|}{\mu_g} \qquad \text{[Eq. 4-19]}$$

$$C_D = a_1 + \frac{a_2}{\mathrm{Re}_p} + \frac{a_3}{\mathrm{Re}_p^2} \qquad \text{[Eq. 4-20]}$$

The particle energy equation, Eq. 4-21, balances the increase in sensible energy with convection, heat of reaction, and radiation balance. The convection heat-transfer coefficient, h_p, is determined by a Ranz-Marshall correlation, Eq. 4-22. The reaction molar species transfer rate, $\dot{n}_{reac}$, and corresponding molar heat of reaction, Δh_{reac}, are determined by the reaction model described below.

$$\sum_{m=1}^{N_m} m_{p,m} c_{p,m} \frac{dT_p}{dt} = a_p h_p \left(T_g - T_p\right) + \dot{n}_{reac} \Delta h_{reac} + a_p \varepsilon_p \sigma \left(T_R^4 - T_p^4\right) \qquad \text{[Eq. 4-21]}$$

$$Nu = \frac{h_p d_p}{k_g} = 2.0 + 0.6\,\mathrm{Re}_p^{1/2}\,\mathrm{Pr}^{1/3} \qquad \text{[Eq. 4-22]}$$

The effective radiation temperature, T_R, represents the total local radiation intensity, and is determined from Eq. 4-23 and Eq. 4-20.

$$T_R = \left(\frac{G}{4\sigma}\right)^{1/4} \qquad \text{[Eq. 4-23]}$$

$$G = \sum_{i=1}^{N_\lambda} \int_{\Omega=4\pi} I_\lambda \, d\Omega \qquad \text{[Eq. 4-20]}$$

As the particle falls, at each time-step the individual source terms contributions for particle-gas coupling in the current cell are calculated according to Eq. 4-21 to Eq. 4-23.

$$dS_m^Y = \frac{\dot{N}_p}{n_{drops}} \dot{n}_m W_m \left(\frac{\Delta t}{V_{cell}} \right) \qquad \text{[Eq. 4-21]}$$

$$dS_i^M = \frac{\dot{N}_p}{n_{drops}} \left[\frac{18\mu}{\rho_p d_p^2} \frac{C_D \operatorname{Re}_p}{24} \left(u_{g,i} - u_{p,i} \right) m_p + \dot{n}_m W_m u_{p,i} \right] \left(\frac{\Delta t}{V_{cell}} \right) \qquad \text{[Eq. 4-22]}$$

$$dS^T = \frac{\dot{N}_p}{n_{drops}} \left[a_p h_p \left(T_p - T_g \right) + \dot{n}_m \left(h_m^0 \left(T_p \right) - h_m^0 \left(T_{ref} \right) \right) \right] \left(\frac{\Delta t}{V_{cell}} \right) \qquad \text{[Eq. 4-23]}$$

Time steps are chosen so that there are multiple steps within each cell, and that the last step within a cell ends on the boundary. Thus, the total source terms - S_m^Y, S_i^M, and S^T - are the sum of all the individual contributions over all the particle trajectories and averaged over every stochastic drop.

The differential species source-term is defined in Eq. 4-21, where $\dot{n}_m$ production of species m due to particle reactions. For ceria, the only species exchanged between the gas and solid phase is O_2. The momentum source term in Eq. 4-22 accounts for drag interactions, while the energy source term in Eq. 4-23 accounts for convective exchange. These equations are reduced by n_{drops} as a means of averaging the source terms due to the random turbulent effects of the stochastic process.

4.1.4 Radiation Equations

Radiation is modelled with the DO model, which solves the radiative transfer equation, for spectral radiation intensity, I_λ, at every location, $\vec{r}$, and direction, $\vec{s}$. A finite number of discrete solid angles are defined at specific directions by setting the number of polar and azimuthal discretizations, N_θ and N_φ respectively. In this implementation, the polar angle is measured from the positive-z direction, while the azimuthal angle is measured from the positive-y direction. Each octant of the Cartesian grid is discretized with $N_\theta N_\varphi$ solid angles, creating $8N_\theta N_\varphi$ for each wavelength band. Cell faces often do not align with the defined solid angles, causing portions of the energy contain in certain directions to be leaving from the cell volume while the rest is incoming. In order to account for this discrepancy, discrete control angles can be pixelated into sub-angles by defining the number of polar and azimuthal pixels, N_{θ_p} and N_{φ_p}. With pixelation, the portion of the solid angle that is outgoing and incoming within each sub-angle can be estimated, as illustrated by ANSYS (2011). While increasing pixelation does increase computational cost, it is significantly less expensive than increasing the number of directions (Siegel et al., 2010).

The radiative transfer equation is shown in Eq. 4-24, and balances the change in radiation intensity along any direction $\vec{s}$, with the radiation lost due to absorption and out-scattering, the radiation increase from gas and particle emission, and the direction increase due to in-scattering from other directions. In this equation, a_λ is the gas spectral absorption coefficient, a_p is the equivalent particle absorption coefficient, σ_p is the equivalent particle scattering coefficient, n is the gas refractive index, $I_{b\lambda}(\vec{r})$ is the gas

spectral blackbody radiation emission intensity, $S^{I}_{\lambda,p}$ is the cell spectral radiation source due to particle emission, $\vec{s}'$ is the scattering direction vector, Ω is the solid angle, and Φ is the scattering phase-function.

$$\nabla \cdot \left[I_\lambda(\vec{r},\vec{s})\vec{s} \right] = -\left(a_\lambda + a_p + \sigma_p\right) I_\lambda(\vec{r},\vec{s}) + a_\lambda n^2 I_{b\lambda}(\vec{r}) + S^{I}_{\lambda,p} + \frac{\sigma_p}{4\pi} \int_0^{4\pi} I_\lambda(\vec{r},\vec{s}')\Phi(\vec{s}\cdot\vec{s}')d\Omega' \qquad \text{[Eq. 4-24]}$$

The DO implementation in ANSYS Fluent is unable to include spectral variations in a_p and σ_p, and cannot capture anisotropic scattering in due to particulate effects. The particle absorption coefficient, scattering coefficient, and cell spectral emission source-term are calculated summing of all the individual contributions of each particle trajectory and averaging over every stochastic drop for each trajectory. The absorption coefficient is calculated by Eq. 4-25, where ε_p is the particle surface emissivity and V_{cell} is the Eulerian cell that the particle is passing through. The scattering coefficient is calculated by Eq. 4-30, where f_σ is the scattering fraction defined the particle material. The cell spectral radiation source in Eq. 4-31 represents the radiation intensity due to particle radiation emission within the cell.

$$da_p = \frac{\dot{N}_p}{n_{drops}} \left(\frac{\pi}{4} d_p^2 \right) \varepsilon_p \left(\frac{\Delta t}{V_{cell}} \right) \qquad \text{[Eq. 4-25]}$$

$$d\sigma_p = \frac{\dot{N}_p}{n_{drops}}\left(\frac{\pi}{4}d_p^2\right)(1-f_\sigma)(1-\varepsilon_p)\left(\frac{\Delta t}{V_{cell}}\right) \quad \text{[Eq. 4-30]}$$

$$dS_{\lambda,p}^{I} = \frac{\dot{N}_p}{n_{drops}} f_{\lambda_m} a_p \varepsilon_p T_p^4 \left(\frac{\Delta t}{V_{cell}}\right) \quad \text{[Eq. 4-31]}$$

In Eq. 4-31, f_{λ_m} is the fraction of energy contained in spectral band $\Delta\lambda_m$ for blackbody radiation at the given temperature, as shown in [Eq. 2-20]. $E_{\lambda,bb}(\lambda,T)$ is the Planck distribution for a blackbody at temperature *T*, and σ is the Stefan-Boltzmann constant.

$$f_{\lambda_m} = \frac{\int_{\Delta\lambda_m} E_{\lambda,bb}(\lambda,T)d\lambda}{\sigma T^4} \quad \text{[Eq. 4-32]}$$

$I_{b\lambda}(\vec{r})$ is the gas spectral blackbody radiation emission intensity as defined in Eq. 4-33.

$$I_{b\lambda}(\vec{r}) = f_{\lambda_m}\sigma\left[\overline{T}_g(\vec{r})\right]^4 \quad \text{[Eq. 4-33]}$$

4.1.5 Heat transfer user-defined function

In order the capture the evolution δ, T_p, and the gas-phase source terms in Eq. 4-21 and Eq. 4-23 utilizing the custom thermodynamics and kinetics developed in Chapter 3, a custom-made UDF particle model was developed. The particle heat-transfer is described here

Numerical integration of Eq. 4-21 over a time-step of Δt is given in Eq. 4-26, where α_{T_p} and β_{T_p} are defined in Eq. 4-27 and Eq. 4-28.

$$T_p = \alpha_{T_p} + \left(T_p^0 - \alpha_{T_p}\right)\exp\left(-\beta_{T_p}\Delta t\right) \quad \text{[Eq. 4-26]}$$

$$\alpha_{T_p} = \frac{h_p T_g - \dot{n}''_{O_2}\Delta h_{reac} + \varepsilon_p \sigma T_R^4}{h_p + \varepsilon_p \sigma \left(T_p^0\right)^3} \quad \text{[Eq. 4-27]}$$

$$\beta_{T_p} = \frac{a_p h_p + a_p \varepsilon_p \sigma \left(T_p^0\right)^3}{m_p c_p} \quad \text{[Eq. 4-28]}$$

The integration assumes that $c_{p,i}$, $m_{p,i}$, h_p, $\dot{n}''_{O_2}$, and T_p^0 do not change during a time step, Δt. As Δt is very on the order of 10^{-4}, this assumption is quite accurate. In Eq. 4-26, T_p^0 is the particle temperature at the start of the time step.

In Eq. 4-27, $\dot{n}''_{O_2}$ is the molar reaction rate of O_2 from the particle surface as defined in section 4.1.6. Δh_{reac} is the heat of reaction for ceria reduction as shown in Eq. 4-29, and is a function of only T_p.

$$\Delta h_{reac} = h^0_{O_2} + 2h^0_{Ce_2O_3} - 2h^0_{Ce_2O_4} \quad \text{[Eq. 4-29]}$$

4.1.6 Modified oxide reduction kinetics

The Fluent Lagrangian particle model uses forward Euler direct integration. As this is an explicit method, it can face significant stability issues for noisy equations. The

kinetic scheme for ceria reduction in chapter 3 causes such stability issues due to a very small surface mass. Individual particles have a surface mass of less than 10^{-12} kg compared to a bulk mass exceeding 10^{-7} kg. The surface kinetic scheme can be used with the integration scheme if Δt is kept very less than 10^{-7} s, but such small time steps is prohibitively expensive computationally.

An implicit scheme could be implemented for integration of the particle model, but the complexity of implementing the scheme into Fluent incurs a large penalty in computational time. As shown in chapter 3, ceria reduction is kinetically controlled by the surface reaction rate. As shown in Figure 4-1, the surface is not in equilibrium with the gas-phase, but closely follows the equilibrium with the bulk.

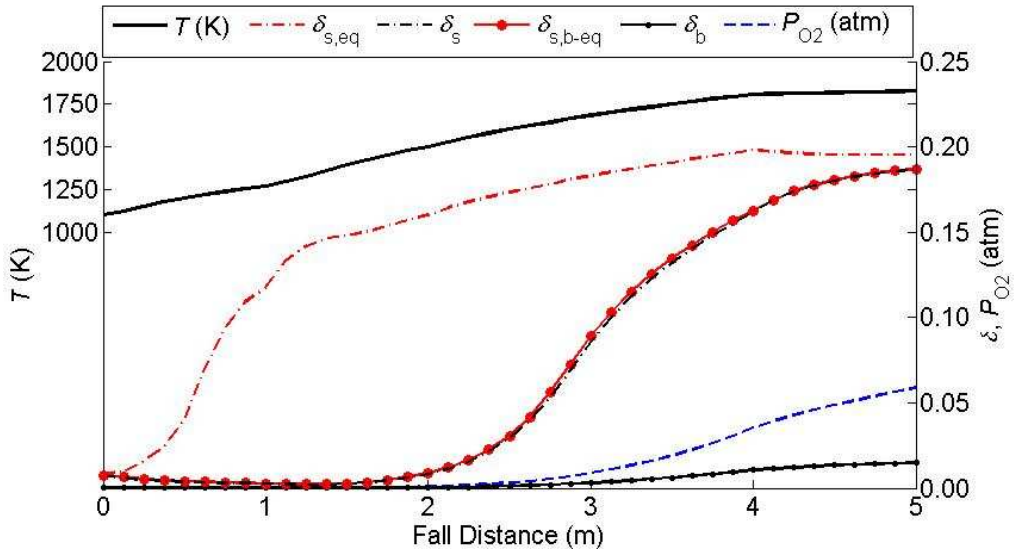

Figure 4-1 – Curves of δ for the bulk and surface within the receiver. $\delta_{s,eq}$ is the equilibrium surface δ with respect to T, P_{O2}. $\delta_{s,b\text{-}eq}$ is the equilibrium surface δ with respect to δ_b.

Thus, reaction rate at the particle surface depends on δ_s which can be approximated to be in equilibrium with δ_b. At equilibrium, $\Delta\mu_{b\text{-}s}$ in Eq. 3-4 is zero. This

problem has no simple analytical solution with the complex non-linear ceria thermodynamics employed. Thus, to calculate δ_s using this equation, an iterative method must be employed.

$$\Delta\mu_{b-s} = \Delta\mu_{red,b}\left(T_p, \delta_b\right) - \Delta\mu_{red,s}\left(T_p, \delta_s\right) \qquad \text{[Eq. 4-30]}$$

The bisection method is used to calculate δ_s from Eq. 4-30, as outlined in Figure 4-2. Bisection is used because of its unconditional stability for these flows, whereas other faster methods tested had convergence issues. Further, as radiation takes up such a large portion of the computational time, this method does not significantly increase the solution time. Because δ varies significantly over the conditions within the receiver, from 10^{-7} up to 0.5, the range was represented logarithmically. Bisection allows exact control over the error by specifying n_{max}, maximum number of iterations. With 20 iterations, the maximum error in $\log_{10}(\delta) = 6.296(10^{-6})$, leading to an error of $\sim 10^{-5}$.

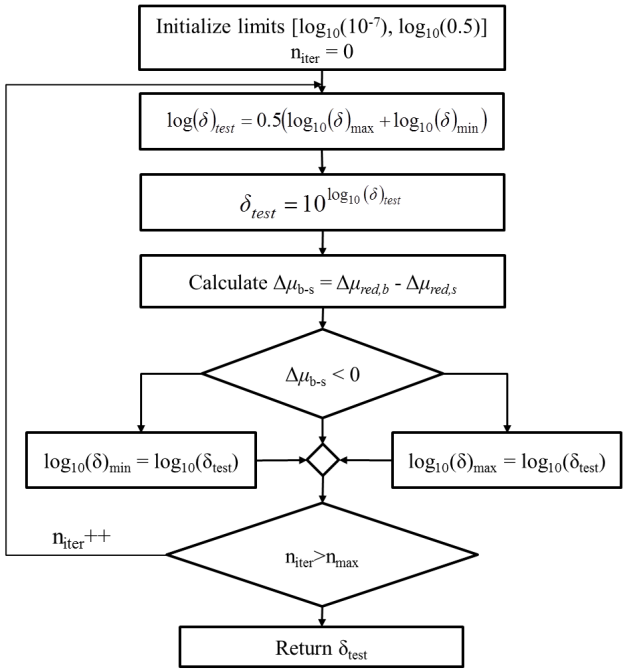

Figure 4-2 – Solution method for δ_s in equilibrium with the bulk.

The bisection method specifies a range over which $\log(\delta_s)$ can fall, in this case [-7, -0.301]. δ_{test} is set to the midpoint of the range. The difference in the reduction chemical potential between the bulk and surface, $\Delta\mu_{b\text{-}s}$, is calculated. Based off the sign of $\Delta\mu_{b\text{-}s}$ the range for δ_s is cut in half, and the iteration is repeated.

After δ_s is calculated to the desired tolerance, the reduction kinetics could be calculated using Eq. 3-13 to find the molar surface rate of reaction for oxygen from the surface. This rate calculation is a modification of the standard mass-action kinetic rate laws using concepts of transition-state theory and non-equilibrium thermodynamics, as proposed by Adler et al. (2007) and used in DeCaluwe (2009).

$$\dot{n}''_{O_2} = 2\left[k_{fwd,R2}\theta^2_{O(s)} \exp\left(\frac{-(1-\beta_{R2})\left(\mu^{ex}_{V_O(s)} - \mu^{ex}_{O(s)}\right)}{\overline{R}T} \right) - \sigma_{O_2}\left(\frac{P^0}{\sqrt{2\pi \overline{W}_{O_2} \overline{R}T}} \right) \theta^2_{V_O(s)} \frac{P_{O_2}}{P^0} \exp\left(\frac{\beta_{R2}\left(\mu^{ex}_{V_O(s)} - \mu^{ex}_{O(s)}\right)}{\overline{R}T} \right) \right] \quad \text{[Eq. 4-31]}$$

In this equation, the gas-surface absorption rate is calculated from an O_2 sticking coefficient, σ_{O2}. The ratio of forward and reverse reaction rate coefficients are determined as suggested by Adler et al. (2008), based on the ideal changes in free energy, commonly called the equilibrium constant as shown in Eq. 3-14.

$$k_{fwd} = \sigma_{O_2}\left(\frac{P^0}{\sqrt{2\pi \overline{W}_{O_2} \overline{R}T}} \right) \exp\left(\frac{-\left(\mu^0_{V_O(s)} + 0.5\mu^0_{O_2} - \mu^0_{O(s)}\right)}{\overline{R}T} \right) \quad \text{[Eq. 4-40]}$$

4.1.7 Model domain and boundary conditions.

Simulations were performed on the closed, widowed geometry shown in Figure 2-1, which is identical to the closed reactor in Chapter 3. Walls are all 0.05 m thick opaque surfaces that use shell-conduction for exchange between wall cells. The wall heat-exchange and spectral-radiation properties listed in Table 4-1 match those suggested by Siegel et al. (2010). The window is a 0.02 m thick semi-transparent surface, and uses heat-exchange suggested by Röger et al. (2006). The window radiation properties were selected to closely match the thermal radiation properties (λ > 4.5 μm) of Hereaus (2010).

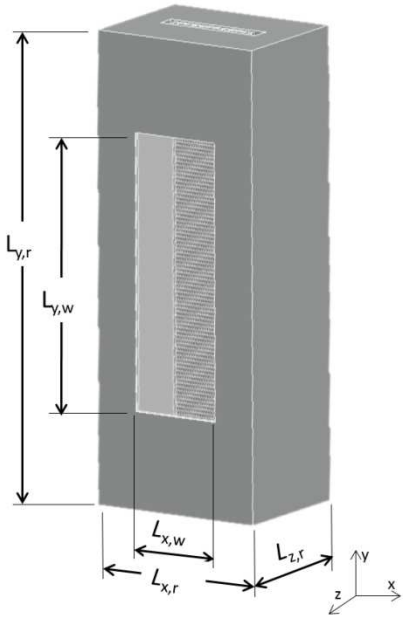

Dimension (m)	Prototype Dimensions
Receiver ($L_{x,r}$, $L_{y,r}$, $L_{z,r}$)	(1.85, 5.0, 1.5)
Window ($L_{x,w}$, $L_{y,w}$, $L_{z,w}$)	(1.0, 3.0, 0.02)

Figure 4-3 - Falling particle receiver geometry and sizes for both prototype and full-scale design.

Table 4-1 – Receiver wall and window thermal and radiation properties.

Property	Value
k_{wall} (W m^{-1}K^{-1})	-0.0129+0.0001858·T_p
h_{wall} (W m^{-2}K^{-1})	5
$\varepsilon_{wall,\Delta\lambda_1}$ (-)	0.2
$\varepsilon_{wall,\Delta\lambda_2}$ (-)	0.8
k_{wind} (W m^{-1}K^{-1})	1.2+0.00156·T_p
h_{wind} (W m^{-2}K^{-1})	4
a_{wind} (m^{-1})	1.14
n_{wind}	1.725

The particles are modelled with a constant-diameter using the properties listed in Table 4-2. The density of Ce_2O_3 was set to 6879.8 kg m^{-3} in to be consistent with the constant-d_p model as the particle reacts. Because particle radiation properties must be constant with λ, the value of ε_p is the solar-weighted value using the ceria absorption properties found in Chapter 3. The particle scattering factor, f_σ is set to 0, meaning that all

of the radiation that is incident on the particles is either absorbed or scattered, as is consistent with the geometric particle optics used in Chapter 3.

Table 4-2 – Particle physical and radiation properties.

Property	Value
$\rho_{Ce_2O_4}$ (kg m^{-3})	7215.0
$\rho_{Ce_2O_3}$ (kg m^{-3})	6879.8
ε_p (-)	0.335
f_σ (-)	0.0

The solar radiation boundary condition uses a uniform solar flux inlet through the window as shown in Table 4-3. q''_{solar} is reduced from 1000 kW m^{-2} to account for the effects of front-surface reflection and window absorption before the radiation beam enters the domain. The beam direction is consistent with the horizontal inlet condition used in Chapter 3. The beam width and diffuse fraction are consistent with a collimated beam.

Table 4-3 – Solar radiation boundary condition parameters.

Property	Value
q''_{solar} (kW m^{-2})	929.4
Beam Direction	[0, 0, -1]
Beam Width – $\Delta\theta$ x $\Delta\varphi$ (deg)	0.001 x 0.001
Diffuse Fraction	0.0

Particle injection points (315 in all) are spread evenly over an inlet slit 0.01 m thick and 1.0 m wide as shown in Figure 4-4. This distribution gives an even particle density and blockage along the fall. Multiple injection strategies were tested, and the staggered distribution displayed showed superior performance. If the particles are

insufficiently staggered with too few injection points, locations of lines of low-particle density form along the fall and cause artificial hot-spots to form on the rear-wall. Injections with a total of 150, 315, 450, and 630 points, with mass-loading split evenly between each point, were tested. Results showed no noticeable change in the receiver for injections with a total of 315 points and above. These findings are consistent with the results reported in Siegel et al. (2010).

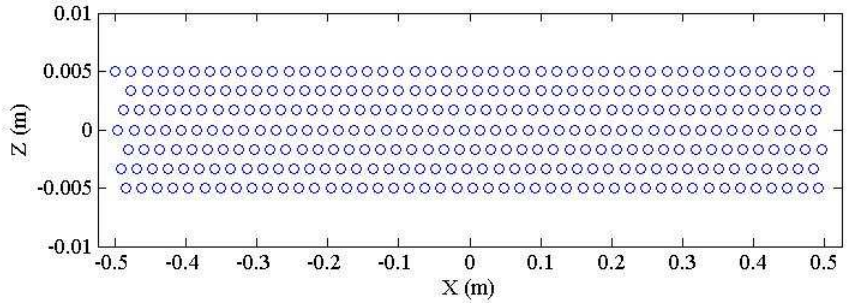

Figure 4-4 – Particle injection locations specified at the inlet.

Stochastic particle testing was used in order to capture the impacts of two-way turbulence coupling and particle curtain spreading. The final results are consistent for cases where n_{drops} is greater than 10, although 20 stochastic drops were used in order to smooth the effects of random variation. Further, a particle source under-relaxation factor of 0.05 was used to maintain stability and ensure convergence.

Gas was injected into the receiver in the direct vicinity of the particles with a velocity of 0.3 m s^{-1}, as suggested by Röger et al (2011) and Chen et al. (2007). The gas turbulence was specified at the inlet with a turbulence intensity, I_t, of 2% and D_h of 0.02 m as suggested by Chen et al. (2007). Because the receiver was closed, additional gas (air in this case) was injected to maintain continuity with curtain gas entrainment and minimize gas back-flow. Two air-vents 0.1 m thick were defined on either side of the

particle to satisfy entrainment and provide the "gas sheath" described in Chapter 3. This gas was inlet with $\bar{u}_g$ of 1.0 m/s,- I_t of 2%, and D_h of 0.2 m.

Despite the additional air injection around the particles, there was still gas backflow from of the particle outlet due to the strong buoyant flow. This backflow was assumed to be at $T_{p,in}$.

4.1.8 Receiver Grid

Solutions were found on unstructured grids of 169,742 and 383,976 tetrahedral elements to assess need for grid resolution modeling a receiver operating at the base-line run conditions and d_p of 200 μm. The smallest particles were used because they show the greatest sensitivity to local flow conditions. The results of these two grids show very close agreement with one another. The maximum receiver wall temperature was 2080.8 K for the smaller grid and only 0.02 K higher for the larger grid. The mean particle temperature along the fall is shown in Figure 4-5, which shows very little change between the two cases. The maximum temperature difference at the exit is 17.8 K

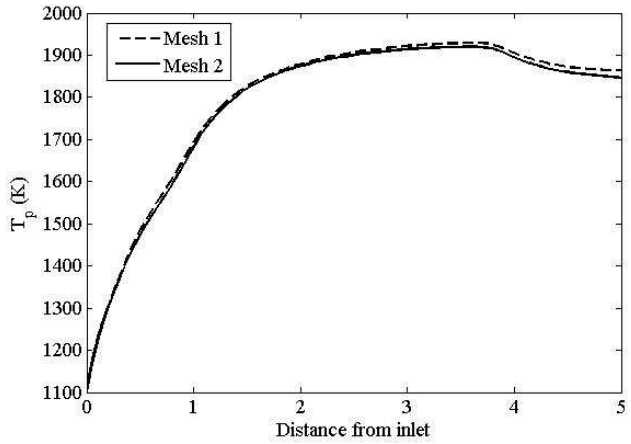

Figure 4-5 –Particle mean temperature along the fall.

Likewise the mean gas-phase temperature in the vicinity of the falling particles is shown in Figure 4-6. Just as with the particles, the gas-phase temperatures are very close to one another, and vary by a maximum of only 24.7 K. Because these differences are negligible, the smaller grid is used for reactive studies in order to minimize computational time.

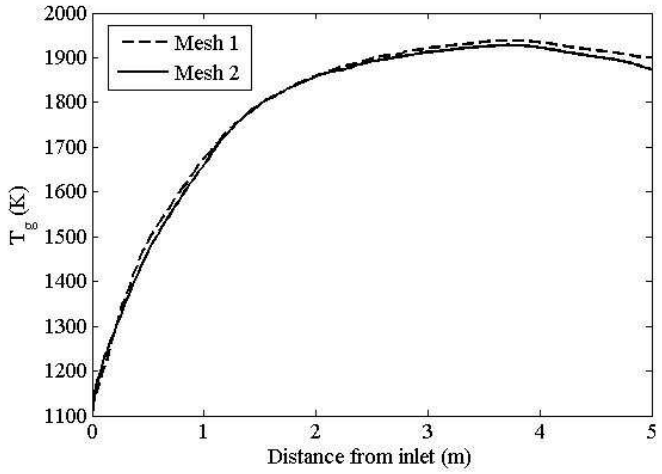

Figure 4-6 – Gas mean temperature in the vicinity of the particles.

The numerical grid not only impacts the gas and particle-phase convergence, but also the radiation balance, which is solved on the same grid. Beyond the spatial mesh used, the solution to the radiation equation relies on the angular discretizations N_θ and N_φ respectively. Because $8N_\theta N_\varphi$ equations must be solved for the radiation scheme, increasing the angular discretizations is very expensive. However, due to the specular nature of the inlet solar beam, the solution is very sensitive to the degree of discretization. In order to maintain the secularity, the solver picks the closest directional bin to the defined solar propagation direction and puts all of the energy into that bin. Tests showed that N_φ = 5 was sufficient to resolve the polar direction sufficiently, with little change

seen for higher values. The vertical propagation of the solar beam continues to approach the horizontal, but shows noticeable change even at N_θ = 11. Despite this, the final particle temperature does not change much past N_θ = 9, changing only 5.2 K when N_θ is increased to 11.

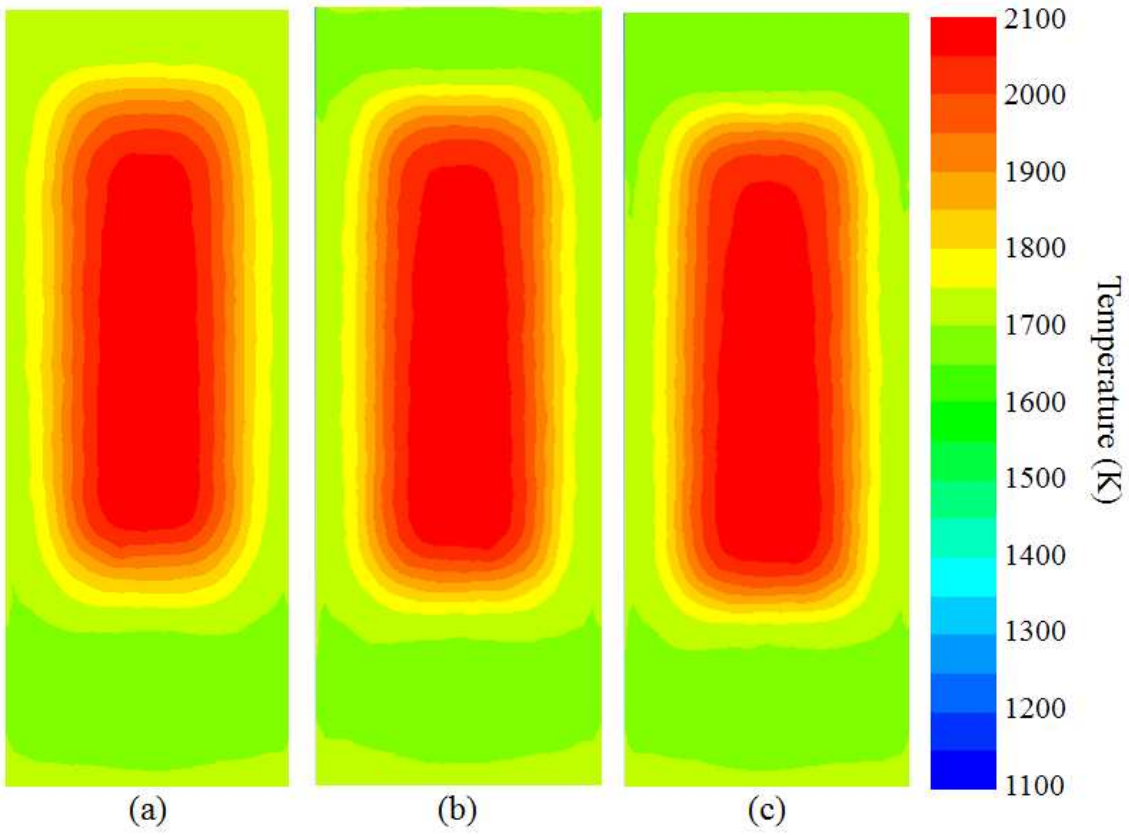

Figure 4-7 – Rear wall temperatures showing the location of the solar hot-spot for DO angular discretizations N_θ x N_φ of (a) 5 x 5, (b) 9 x 5, and (c) 11 x 5.

While the impact is less dramatic than angular discretization, the angular pixelation does influence the solution of radiation equations. Tests showed that any further increase beyond 7 x 7 did not change the solution. Although the wavelength-dependent properties of the particles could not be captured, the spectral dependence of

the walls had a significant impact on the wall and gas temperatures. As such, two spectral bins were employed as shown in Table 4-4 to accurately capture the exchange between the walls and the particles.

Table 4-4 – Radiation model and discretization parameters.

Property	Value
N_θ x N_φ	9 x 5
N_{θ_p} **x** N_{φ_p} **.**	7 x 7
$\Delta\lambda_1$ (μm)	[0, 4.5]
$\Delta\lambda_2$ (μm)	[4.5, 100]

4.2 Results

The reactive particle model was run for a few cases around the base case described in Table 4-5, varying d_p and $\dot{m}'_p$**,** as theses have been identified as very important variables in the research in Chapter 3. δ_{in} is the equilibrium δ value at the specified $T_{p,in}$ and $P_{O2,in}$.

Table 4-5 - Baseline operating conditions for the falling ceria particle receiver model

Property	Value (Baseline)
d_p (μm)	300
$\dot{m}'_p$ (kg $s^{-1}m^{-1}$)	2.0
$T_{p,in}$ (K)	1100
δ_{in} (-)	$4.5\cdot(10^{-5})$
$P_{O2,in}$ (atm)	$1.0\cdot(10^{-5})$
P_{OP} (atm)	1.0

4.2.1 Baseline case results

Results for the baseline case are shown in Figure 4-8 to Figure 4-13. Receiver wall temperature contours are shown in Figure 4-8, and show similar behavior to that

observed with the simplified MATLAB model in Chapter 3. Noticeable hot-spots on the rear of the receiver and on either-side of the front window are predicted by the CFD model, The CFD model predicts a maximum rear-wall temperature that is 18 K higher than the simplified model, because the CFD model predicts higher direct solar flux due to the implementation of isotropic particle scattering, causing forward scattering rather than pure reflection. For the particle diameters in this study, the isotropic scattering is not a good assumption and there should be some consideration as to how to implement directional scattering as a function of particle size into ANSYS Fluent. The maximum side-wall temperatures are cooler by 100 to 120 K than those of the simplified model. The cooler hot spots are due to the internal convection from the internal air flows over the walls.

Figure 4-9 shows gas temperature profiles along central *y-z* and *x-y* planes in the receiver. The gas temperatures are influenced by particle convection, wall heating, and gas recirculation caused by the vacuum created due to entrainment by the falling particle curtain. The effects of convection from the walls and the particles are evident in Figure 4-9(b) as the gas is heated to a maximum in the same vicinity of the solar spot. After reaching a peak along the fall, the gas is cooled by the particles, which give off a significant amount of radiation. Further, there is a small but noticeable impact of gas backflow around the edges of the particle outlet in Figure 4-9(b).

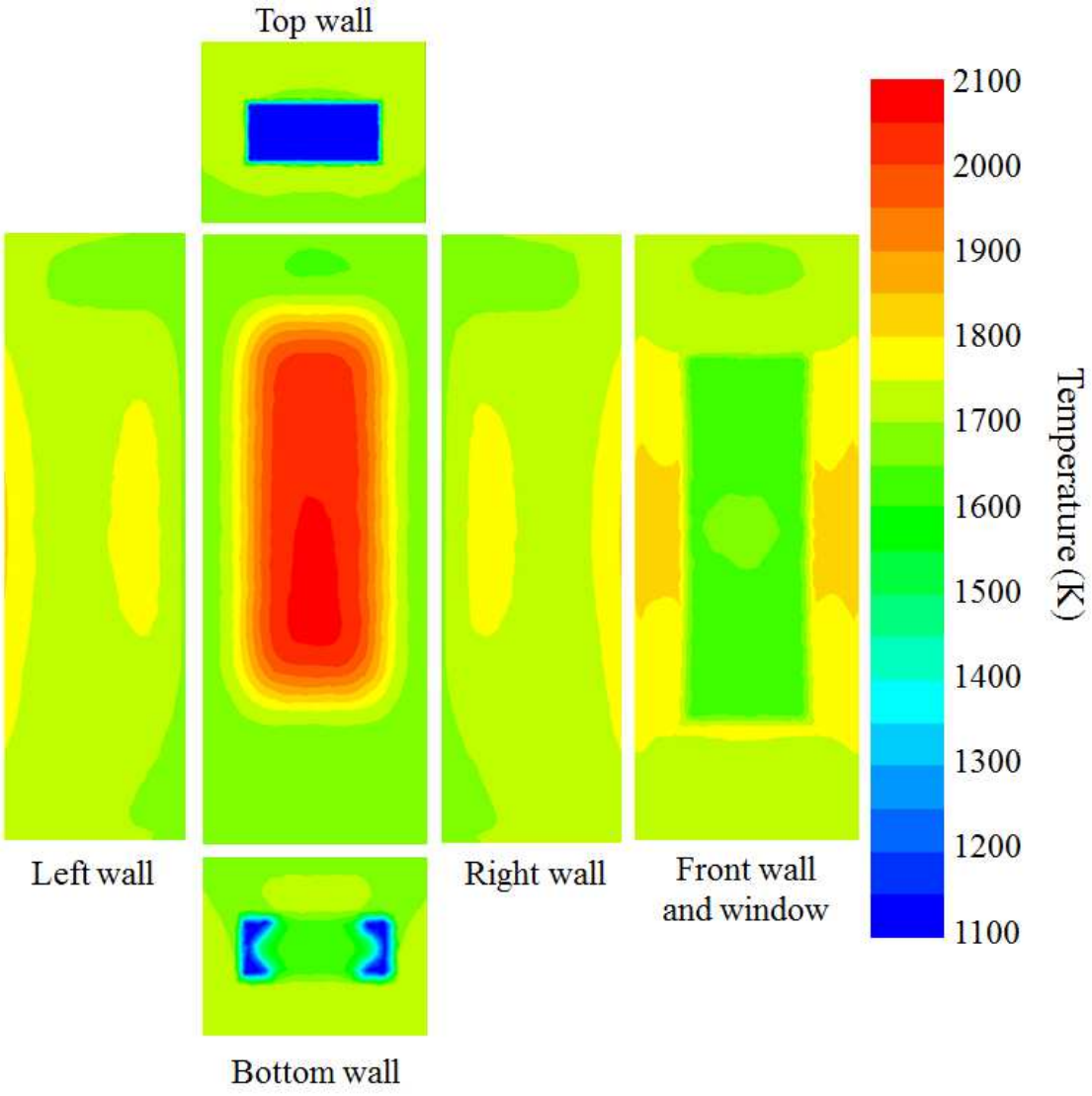

Figure 4-8 – Receiver inner wall temperature contours (K) predicted by the CFD model at the baseline conditions shown in Table 1-5.

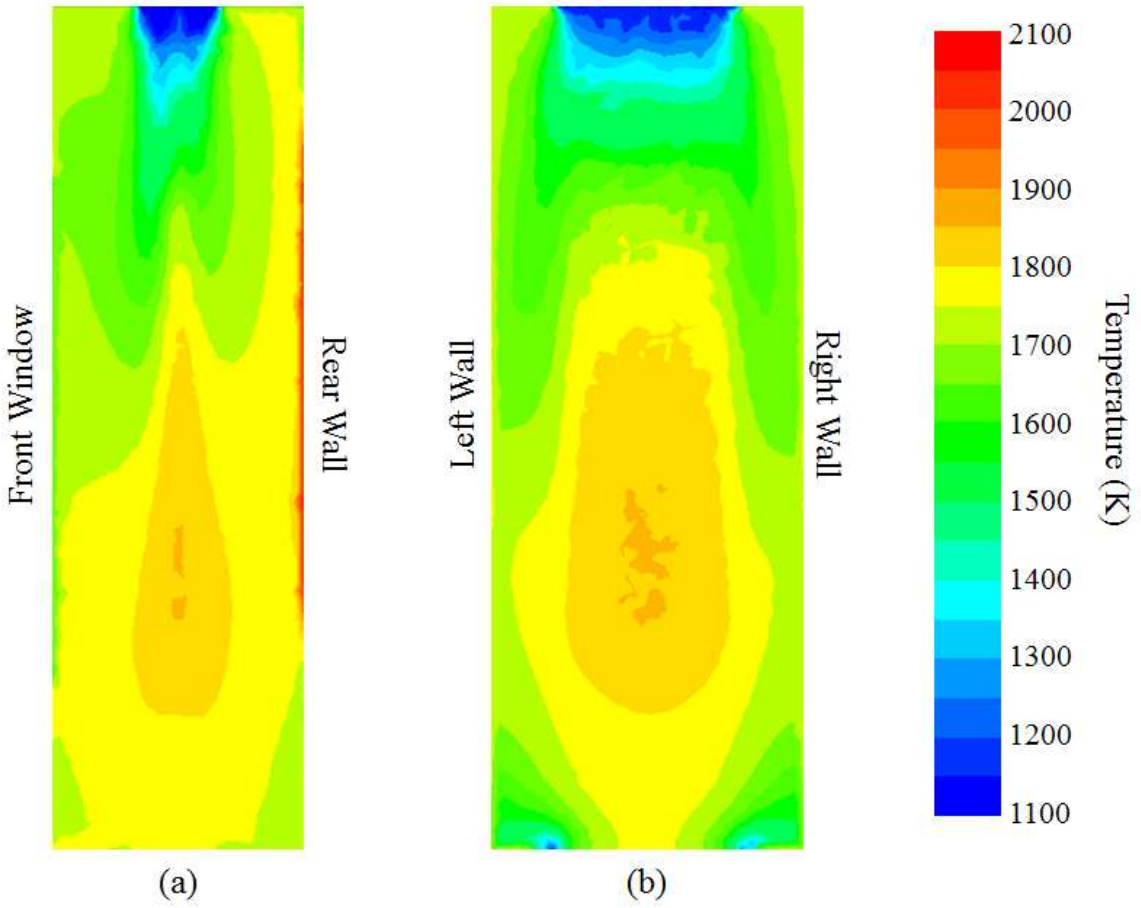

Figure 4-9 – Predicted gas temperature contours within the receiver operating at the baseline conditions in Table 1-5: (a) along the central *y*-*z* plane of the receiver, and (b) along the central *x*-*y* plane through the middle of the particle curtain.

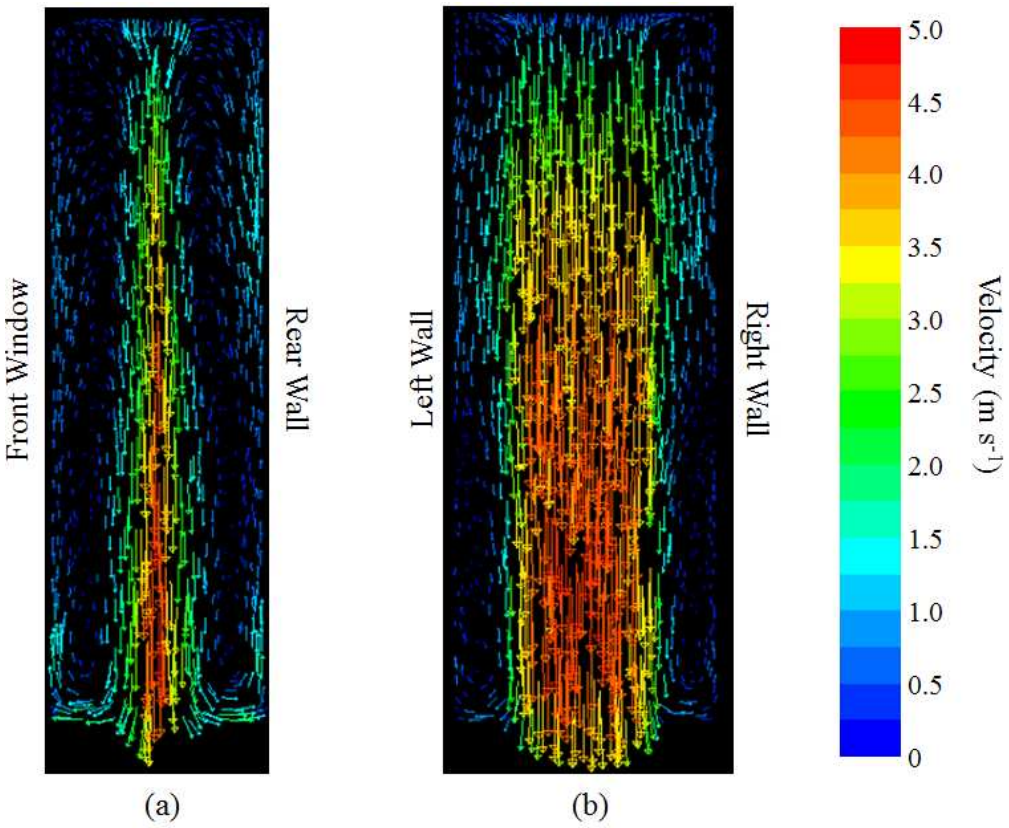

Figure 4-10 – Predicted gas velocity vectors (colored by magnitude) within the receiver operating at the baseline conditions in Table 1-5: (a) along the central *y-z* plane of the receiver, and (b) along the central *x-y* plane through the middle of the particle curtain.

The predicted gas-velocity vectors in Figure 4-10 show how the gas flow is dominated by the entrainment by the particle curtain. The resulting vacuum away from the curtain results in gas convection cells that form in front and behind the curtain, The recirculation behind the curtain is stronger because of the additional buoyant driving force created from the heating of the rear wall. In the vicinity of the particles, the gas reaches a velocity of 5.0 m s^{-1} by the exit, which is slower than the particles, which reach 9.6 m s^{-1} at the exit. Figure 4-10(b) illustrates that the gas is slowed down by the side walls near the edge of the particle flow. A similar impact can be seen for the particles. The development of this flow profile is due to the added drag on the edges of the curtain.

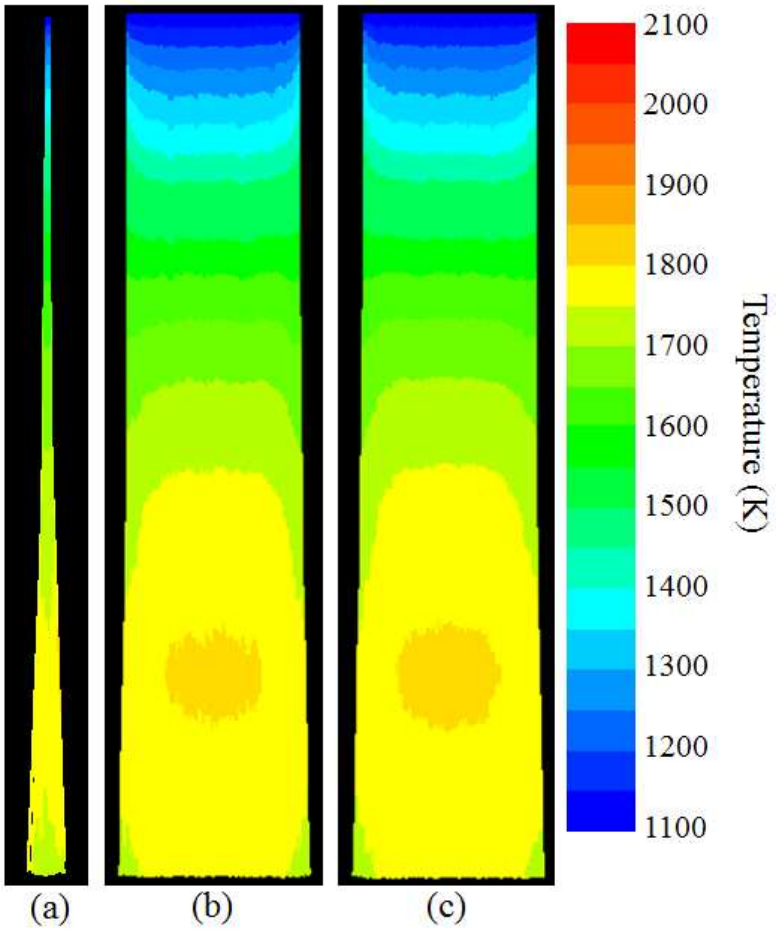

Figure 4-11 – Particle temperature contours (K) viewed from the (a) side, (b) front, and (c) rear of the curtain as predicted by the CFD model at the baseline conditions shown in Table 1-5.

Curtain temperatures are shown in Figure 4-13. As with the simplified model results, the curtain temperature profile evolution follows closely the incoming solar irradiation profile. A unique difference in the particle temperature profiles from the simplified model profiles. In Figure 11, the front temperature of the curtain is very comparable to the rear as opposed to in the simplified model which predicts as much as 40 K lower temperature in the front. The forced constraint of isotropic particle scattering in the CFD modeling artificially increases heat exchange between the front and back of

the curtain and likely causes the increased uniformity between the front and back temperature profiles here.

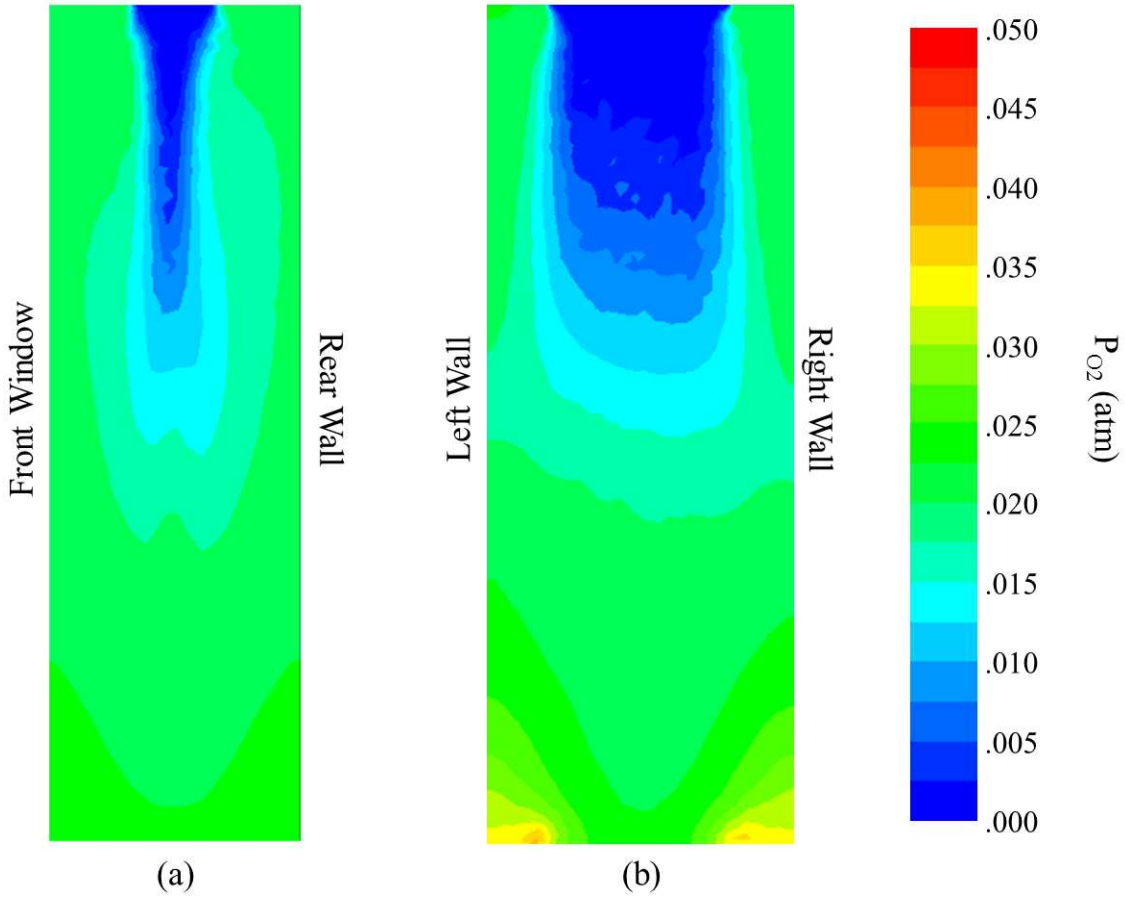

Figure 4-12 – Predicted contours of P_{O2} for a receiver operating at the baseline conditions in Table 1-5: (a) along the central *y-z* plane of the receiver, and (b) along the central *x-y* plane through the middle of the particle curtain.

P_{O2} of the gas flow, as shown in the profiles of Figure 4-12 grows monotonically around the particles as they fall due to the O_2 release from the particle reduction. In addition to the gas release from the reactions, the recirculation cells return gas with a higher P_{O2} to the top of the receiver such that the P_{O2} of the entrained gas flow is higher

than estimated in the simplified model. This happens due to a combination of entrainment and turbulent mixing along the flow. Thus, the P_{O2} grows due to a combination of both reduction and mixing. These results suggest that the fidelity of the simplified flow model could be improved by incorporating a variable P_{O2} in the entrained gas-flow based on the expected dynamics of the recirculating flow.

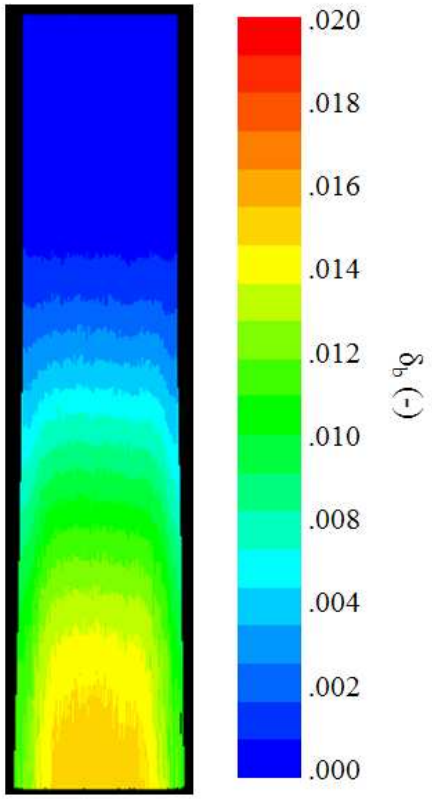

Figure 4-13 - Contours the curtain of ceria oxygen non-stoichiometry δ at the front of the particle curtain as predicted by the CFD model at the baseline conditions shown in Table 1-5.

The evolution of the curtain along the length of fall is shown in Figure 4-13. Figure 4-13 shows that δ grows continuously along the fall-direction. However, δ grows faster in the middle of the curtain due to higher temperatures and lower P_{O2}. The mean outlet-δ predicted by this CFD model is 0.0133, which is more than double the predicted

value of 0.006 from the simplified model. This discrepancy occurs for two reasons: (1) the CFD model predicts a temperature that is 51 K higher, and (2) the CFD model predicts a P_{O2} of 0.025 atm compared to the value of 0.062 atm from the simplified model. This indicates that the simplified model needs to account more for the turbulent mixing of gas between the particle-dense core and the entrained sheath-gas. While the obtained δ is small, it is close to the δ_{eq} of 0.0151 for the outlet P_{O2} and T_p.

4.2.2 Variations of particle size

Beyond the baseline case, the receiver was tested for a range of d_p between 200 and 500 μm. Increasing particle size significant lowers the mean T_p along the length of the fall as shown in Figure 4-14 and also observed in the simplified model in Chapter 3. Smaller particles have more surface area for absorption and fall slower, making them more effective for absorbing heat. This is consistent with the findings from the simplified model, although the effect is less dramatic in this case. Whereas the simplified model predicts that the mean T_p will decrease by 230 K, the Fluent model predicts a reduction in T_p of only 80 K. This is due to the differences in radiation schema, which allows more radiation to penetrate into the receiver due to isometric scattering.

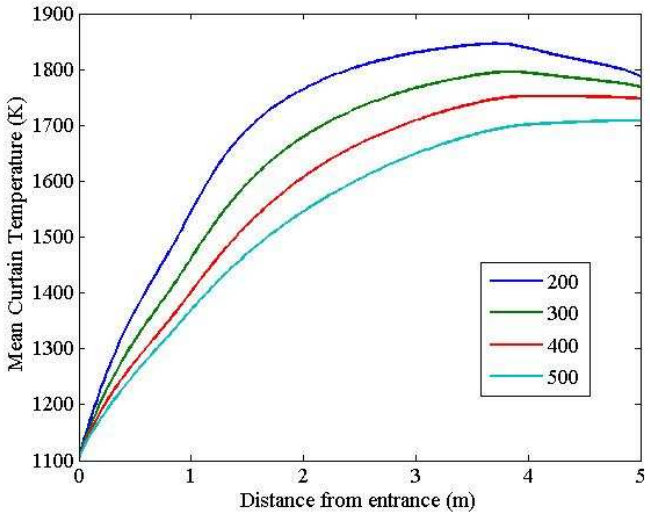

Figure 4-14 – Mean T_p along the fall for various d_p at constant particle flow rates of $\dot{m}'_p$ = 2.0 kg $s^{-1}m^{-1}$, inlet temperatures of 1100 K, and $P_{O2,in} = 10^{-5}$ atm.

Further, the temperature profiles in Figure 4-14 show a faster increase in temperature in the entrance region of the curtain. This is due to the positive effect of gas-recirculation within the receiver, which helps to pre-heat the particles before entering the directly-irradiated zone. However, these gas flows can influence the particles and may cause recirculation in particles that are too small. While particles even as small as 200 μm did not face any issues with recirculation due to buoyant gas-flows, an analysis of the particle curtain-spreading showed that smaller particles were more effected by turbulent dispersion. There is little change in the amount of dispersion for particles with d_p > 300 μm, all of which reach a curtain thickness of about 0.12 m by the exit. When d_p is decreased to 200 μm, the particles spread much further, reaching a thickness of 0.22 m by the exit. These values are consistent with the isothermal measurement data from Kim et al. (2008) and the curtain-spreading model used in the simplified model.

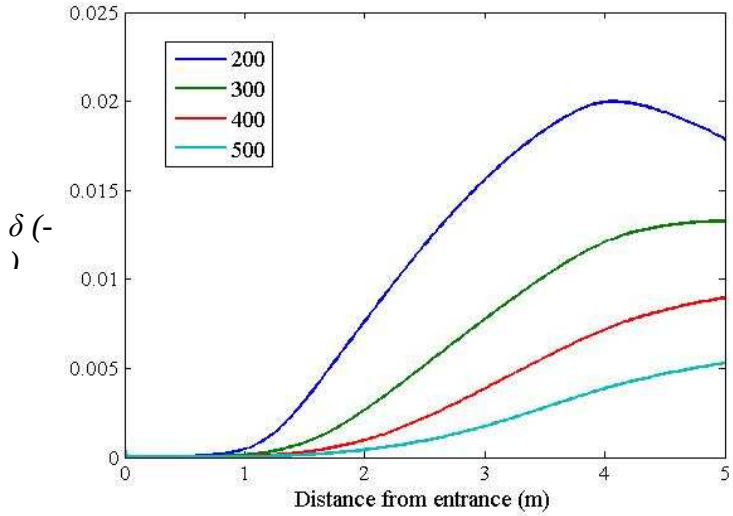

Figure 4-15 – Mean particle δ along the length of fall for various d_p at constant particle flow rate of $\dot{m}'_p$ = 2.0 kg $s^{-1}m^{-1}$, inlet temperatures of 1100 K, and $P_{O2,in} = 10^{-5}$ atm.

Curves for δ along the length of fall in Figure 4-15 show that smaller particles react further and faster, due to greater reacting surface-area and higher temperatures. When d_p = 200 μm, the particles approach equilibrium within the receiver and start to re-absorb oxygen along the fall as they cool. This can be seen clearly in Figure 4-16(a). This case also provides a good benchmark for comparison to the simplified model, as they both reach similar outlet temperatures of 1796 K for the CFD model and 1801 K for the simplified model. The outlet δ in both cases is also close at 0.013 for the simplified model and 0.017 for the CFD model. It is clear that, for this size particle the kinetics are fast enough to catch up with the thermodynamics rather quickly. Thus, the CFD model δ is expected to drop to ~0.014 just outside the receiver.

Despite the similarities, this comparison also highlights the differences between the models. The CFD model has more even heating over the domain due, as mentioned earlier, gas heating, as well as more wall reflection due to the radiation scheme. The CFD

model has a lower PO_2 by the exit to the domain due to higher gas-loading in the receiver. The simple entrainment model did not consider the additional make-up gas that would have to either be supplied or be pulled out via back-flow. The sheath-gas mass provided in the CFD simulations is 0.14 kg s^{-1}, much higher than the core entrainment of only 0.01 from the simplified model.

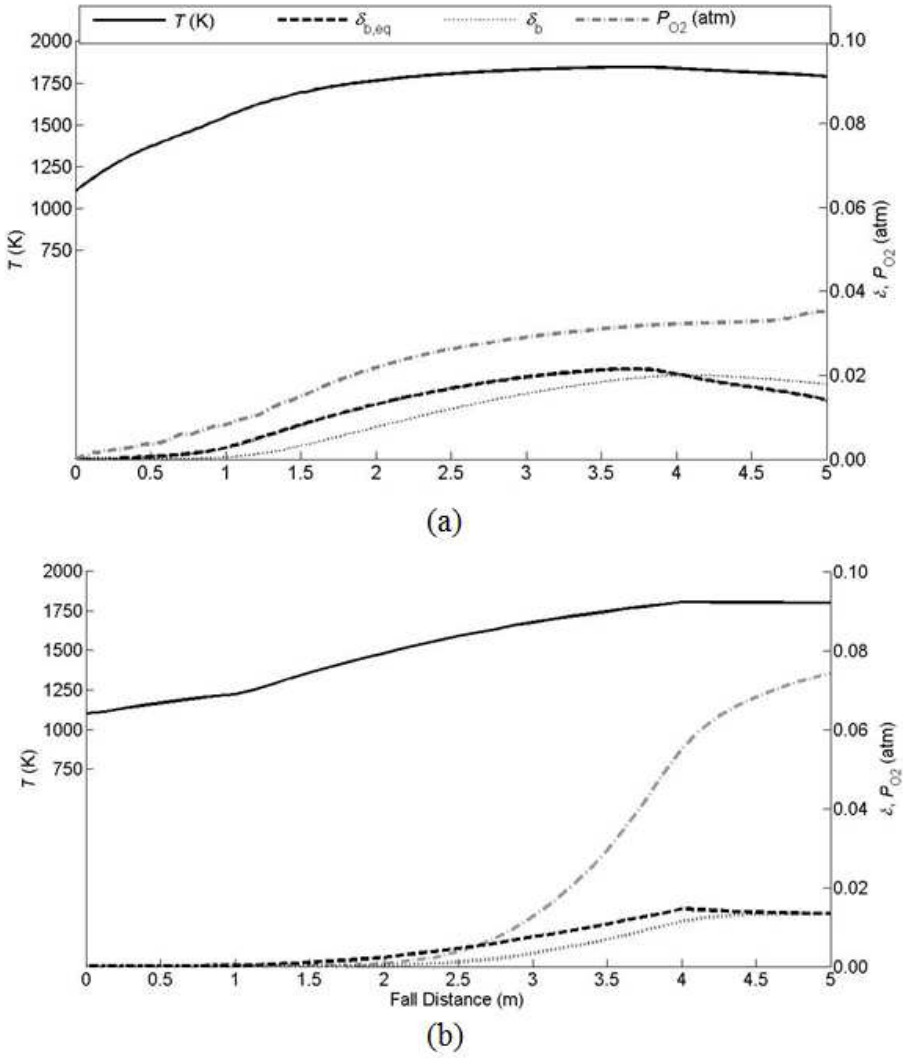

Figure 4-16 – Curves of T_p, P_{O2}, δ, and δ_{eq} for d_p = 200 μm case at $\dot{m}'_p$ = 2.0 kg $s^{-1}m^{-1}$, inlet temperatures of 1100 K, and $P_{O2,in} = 10^{-5}$ atm as (a) modeled with Fluent. and (b) modeled with the simplified model in Chapter 3.

The effect of changing particle size can be seen by examining the total energy breakdown for the receiver, as shown in Figure 4-17. Reflection losses through the front quartz window and convection losses through the walls do not change significantly with . d_p. On the other hand, radiation losses increase with d_p, despite lower maximum particle temperatures due to lower curtain opacity. Energy for heating gases increase with particle size, as greater momentum at the exit causes more back-flow into the receiver. The sensible and chemical storage is higher for smaller particles due to better absorption and higher surface areas for reaction.

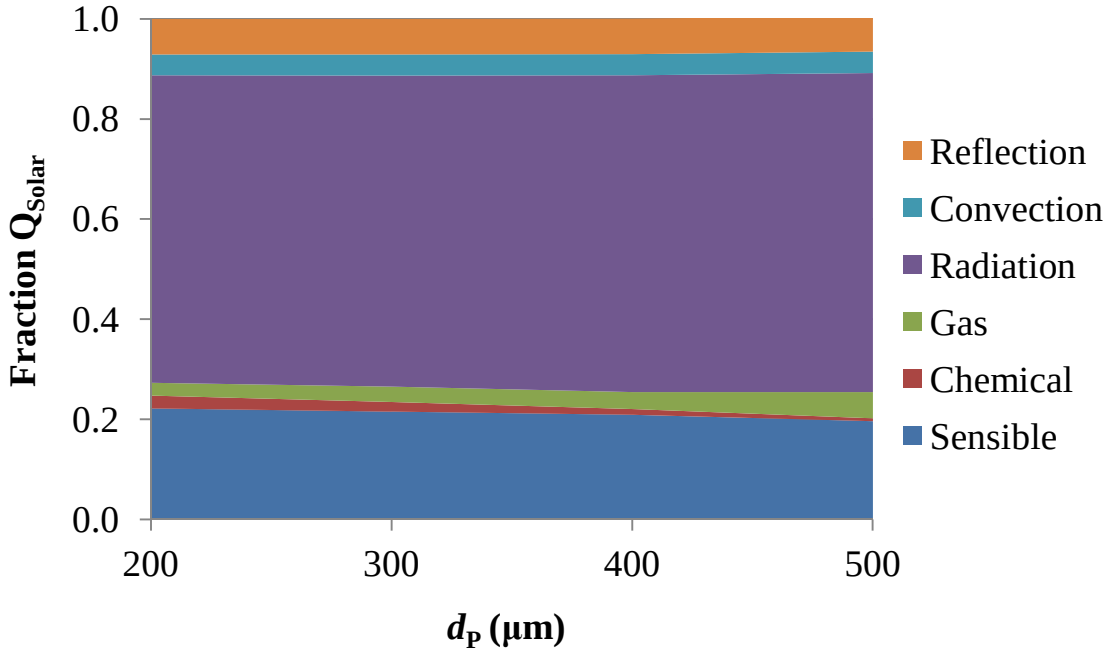

Figure 4-17 – Distribution of $\dot{Q}_{Solar}$ to storage and losses in the receiver as a function of d_p at constant $\dot{m}'_p$ = 2.0 kg $s^{-1}m^{-1}$, inlet temperatures of 1100 K, and $P_{O2,in} = 10^{-5}$ atm.

4.2.3 Variations of particle flow-rate

The CFD receiver model was run for a range of $\dot{m}'_p$ from 2 to 4 kg $s^{-1}m^{-1}$ at a constant d_p = 300 μm. Figure 18 compares mean δ with δ_{eq} (based on the local P_{O2} and T_p) The evolution of δ clearly levels off near the outlet, due to slightly declining T_p past ~3.8 m along with rising P_{O2}.

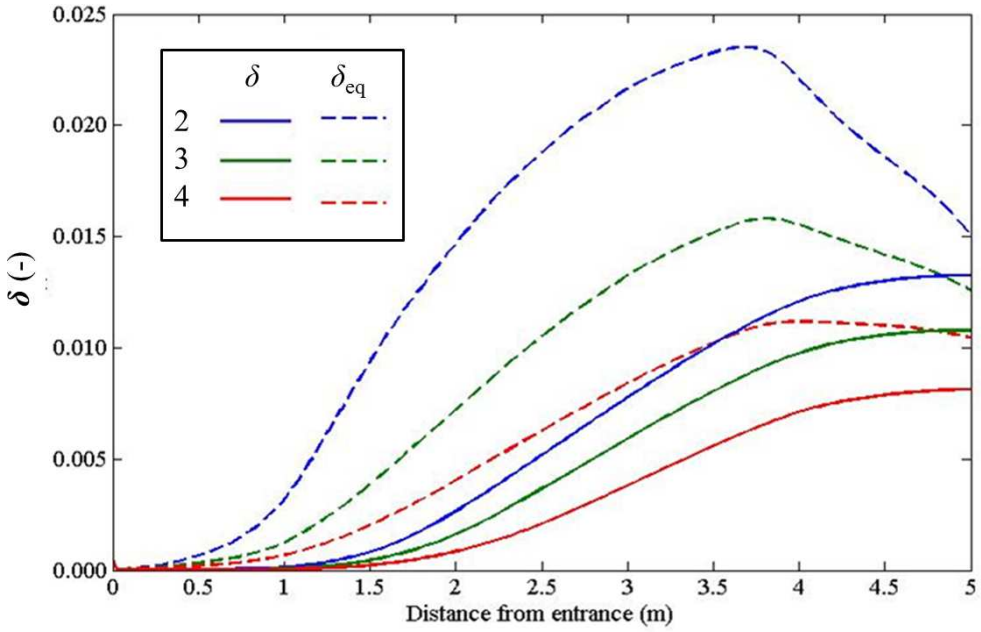

Figure 4-18 – Mean δ along the length of fall, compared to δ_{eq} at the mean local P_{O2} and T_p as a function of $\dot{m}'_p$ for constant d_p = 300 μm, inlet temperatures of 1100 K, and $P_{O2,in} = 10^{-5}$ atm.

Figure 1-19 plots the continued increase in P_{O2} as the particles fall down the receiver. The increase occurs because of the gas release inside the core and the entrainment from the high-P_{O2} recirculated gas from outside the core of the curtain. The combined reduction in T_p and increase in P_{O2} significantly decreases the thermodynamic driving force δ_{eq} in the final meter of the curtain. Higher $\dot{m}'_p$ flows achieve lower δ due to lower T_p and greater O_2 release to the gas-phase for the same $\Delta\delta$. Even though the 4 kg

s^{-1} m^{-1} flow only reaches δ of 0.008 by the exit of the flow, the released mass of oxygen is 0.003 kg s^{-1}, 20% higher than the 2 kg s^{-1} m^{-1} flow. Even though the 3 kg s^{-1} m^{-1} releases 0.00293 kg s-1 of oxygen - virtually the same total mass as the 4 kg $s^{-1}m^{-1}$ flow, the P_{O2} is higher for the 4 kg s^{-1} m^{-1} flow due to the increased recirculation of the gases with the higher entrainment flow rates.

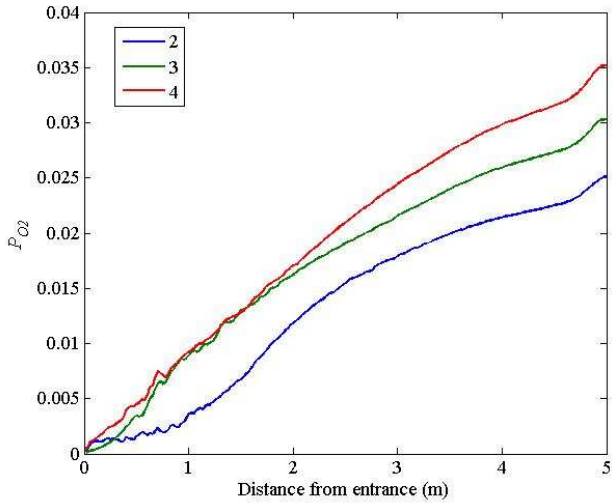

Figure 4-19 – Mean P_{O2} along fall direction for the given $\dot{m}'_p$ for constant d_p = 300 μm, inlet temperatures of 1100 K, and $P_{O2,in} = 10^{-5}$ atm.

As expected, the higher $\dot{m}'_p$ decreases T_p within the receiver, as shown in Figure 4-20. However, the change in outlet T_p between the 2 kg s^{-1} m^{-1} case and the 4 kg s^{-1} m^{-1} case is only 50 K, significantly less than the 151 K drop seen in the simplified model of Chapter 3. This significant difference in the two models stems from implementing isotropic scattering in the CFD model when the particle is large enough to be primarily reflective. With the simplified model, as curtain opacity increases, incident solar radiation on the particle curtain is reflected back out the window. With isotropic scattering, a large

fraction (approximately half) of the energy that should be reflected backwards is instead propagated in the forward direction, artificially increasing the efficiency.

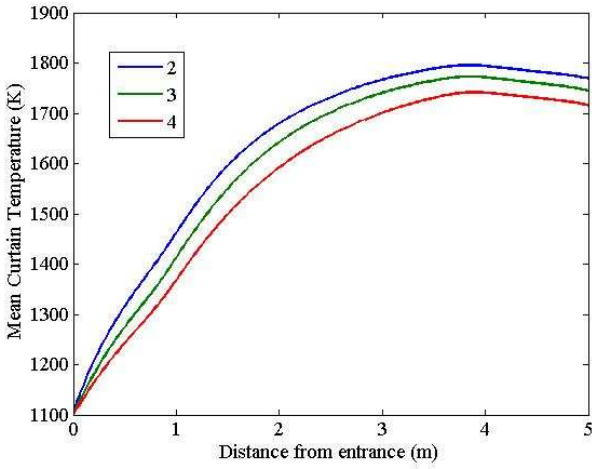

Figure 4-20 – Mean T_p along the fall direction for the given $\dot{m}'_p$ for constant d_p = 300 μm, inlet temperatures of 1100 K, and $P_{O2,in} = 10^{-5}$ atm.

In fact, this gain in efficiency can be seen in Figure 4-21. With the CFD model, radiation losses are reduced from 62.1% to 45.2% when $\dot{m}'_p$ is increased from 2 to 4 kg s^{-1} m^{-1}. For comparison, the same reduction in $\dot{m}'_p$ for the simplified model reduces the radiation losses from 62.8% to 54.6%. Most of additional absorbed energy in the curtain goes to sensible energy. These results agree with the observations of Gobereit et al. (2012), who compared a similar simplified model to CFD simulations with the DO method for inert particle receivers. Their CFD simulations predicted lower radiation losses from the particles due to reduced emissions and reflection from the particles. The reflection from the particles is even more prevalent for ceria particles with the low emissivity of ε_p = 0.335 in this implementation.

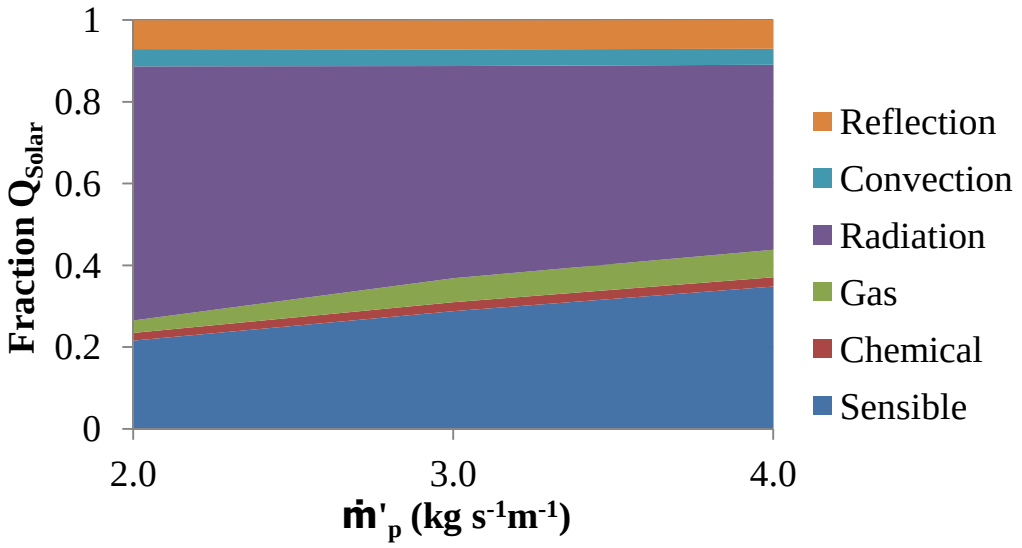

Figure 4-21 - Distribution of $\dot{Q}_{Solar}$ to storage and losses in the receiver as a function of $\dot{m}'_p$ at constant d_p = 300 μm, inlet temperatures of 1100 K, and $P_{O2,in} = 10^{-5}$ atm.

4.3 Discussion

The CFD model results demonstrate some important physics missing in the simpler simulations of the closed receiver in earlier chapters. For one, the gas-flow plays a more important role within the receiver than originally thought. Unlike open-aperture receivers which are free to entrain air through the front, closed-receivers require additional gas input to prevent major back-flow through the particle outlet. The entrained-gas flow combined with the buoyant convection cells actually cool the walls, and the heat extracted internally to the recirculated gas provides additional heat to the particles before they enter the directly irradiated zone. Despite the positives, this flow field does recirculate released O_2 into the gas entrained around the particles and the resulting increase in P_{O2} around the particle curtain can reduce the chemical reduction of the ceria.

For this reason alternative gas injection strategies are investigated. One of the most promising options is low-P_{O2} gas injection on the bottom of the receiver near the walls, so that the injected mass pass upward along the walls to preheat before being pulled into the particle stream. This increases the gas temperature in the vicinity of the particles, and may provide more control of the gas P_{O2} as well. Further, controlling the velocity inlets at the bottom helps to reduce the mass of gas that flows back from the particle outlet.

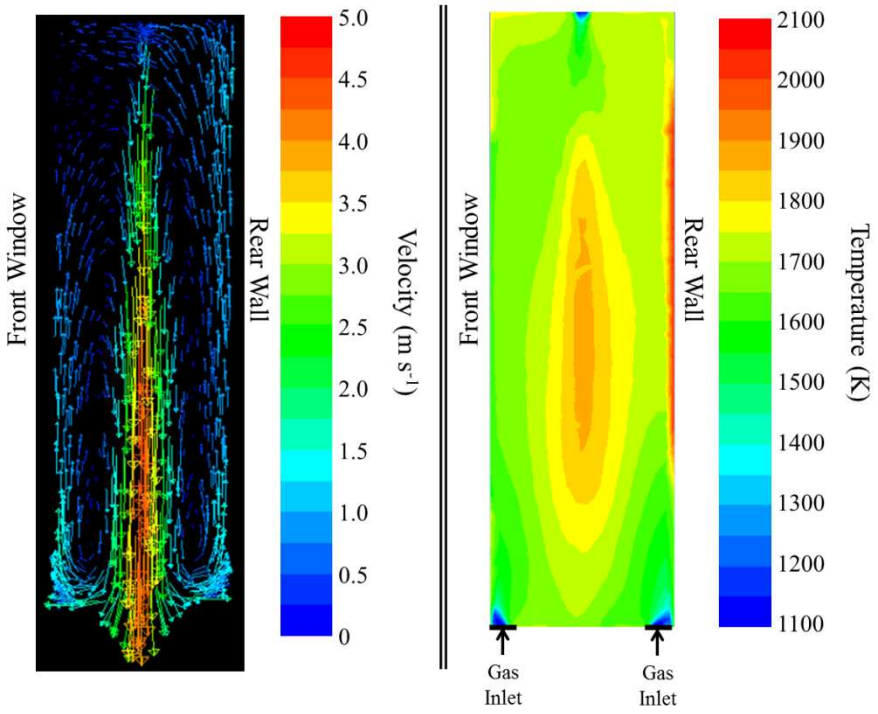

Figure 4-22 – (a)Velocity vectors and (b) gas temperature contours at the mid-point through the receiver using the baseline flow-conditions specified in Table 4-5.

The gas-flow results from the CFD model indicate the potential to improve receiver performance with gas flow management and also provide ideas of how to incorporate such effects through improved entrainment sub-models in the simplified

receiver simulations. The monotonic evolution of P_{O2} going down the receiver indicates that a more simple plug-flow model may be justified. The turbulent spread of the gas-phase thermal energy and species was not modelled, and shows that the domain over which the gas-phase interacts with the particles should be increased. The local P_{O2} for the particles is shared with some of the entrained air outside of the dense-particle core.

The performance comparisons between the simplified model and CFD model similarly exposes weaknesses in the treatment of the radiation within the receiver. As mentioned earlier, isotropic scattering enforced in the current radiation model for Fluent is an incorrect assumption for the few-hundred μm particles studied here. This assumption can lead to significant errors when the particles are not highly absorptive. There errors are amplified by the low ε_p of ceria, where a larger portion of the energy should end up back-scattered. The lack of spectral selectivity for the particles also influences the performance of the particles. In practice, ceria has higher absorption in the near-IR range than the UV-Vis. spectrum. Given that the temperature of the surrounding walls is greater than ceria over most of the receiver, the ceria material ends up absorbing more energy than it should. Depending on the temperature, this can improve the absorption by ceria by as much as double.

4.4 Conclusions

This chapter demonstrates a method to implement a custom reactive-particle model within the framework of the Fluent CFD package. This model calculates the particle thermal balance, the reaction thermo-kinetics, and inter-phase exchange terms. This model was applied to the closed, reacting ceria receiver tested in Chapter 3, in order to

provide a basis for comparison about the strengths and weaknesses of each model. The results of this model demonstrated the importance of capturing the gas-phase to properly describe the action within the receiver. Further, it was demonstrated that alternative gas-injection strategies can improve the performance of the receiver so that it operates under more ideal conditions.

Comparisons between the simplified model and the CFD model developed in this chapter demonstrated methods by which both can be improved. The particle-radiation interaction using the DO-model has important limitations that need further development to be overcome. The gas-phase treatment within the simplified model can be improved utilizing the results from the CFD model.

Particle diameter d_p was once again shown to be an important operating parameter, and, by specifying the whole flow-field, it was possible to assess the stability of particle curtains for d_p down to 200 μm in an enclosed reactor. The particle flow rate is also important in determining the overall performance, with a tradeoff between η_{Sol} and the outlet values for T_{p}, and total reacted mass. These results, along with the simulation strategies discussed in this chapter, provide valuable information to aid in the both the design and modelling of a solid-particle reactor.

Chapter 5:Conclusions and Outlook

This work has examined the physics behind solid particle receivers with direct solar-irradiation of dense-particle falling curtains. Solid particle receivers have the potential to achieve high temperatures and solar absorption efficiencies. This study developed computational models for the design and assessment of operating conditions for a relatively simple falling-curtain receiver for both inert and reactive particles. This was split into three major tasks:

- development of a model for inert falling particle receivers to aid in the design of both the prototype and commercial-scale (Chapter 2);
- creation of a flexible reactive-particle model that can extend the inert model to study how reactions are coupled to the particle-flows (Chapter 3);
- implementation of the detailed particle-model into a CFD environment to evaluate the gas flow-field and be used as a benchmark for previous models (Chapter 4).

Completing these tasks has revealed a great deal about the physics behind both inert and reactive falling-particle flows. Nonetheless, many design aspects that still require further study, but the tools from this study provide a framework in which to tackle further efforts in designing and analyzing falling-particle receivers for storage and/or chemical reactions in concentrated solar plants. The major conclusions from each major task of this study are presented below, along with a brief discussion of the improvement opportunities that remain.

5.1 Modeling of Inert Particle Receivers

5.1.1 Summary of results

Chapter 2 focuses on the development of an inert particle receiver model to evaluate important flow-parameters for both prototype and commercial-scale receivers. The developed model was driven by a modified multi-bin, surface-to-surface radiation model using Hottel's zonal method to simulate the particle curtain as a semi-transparent media. To simplify the complex gas flows for more computationally efficient receiver modeling, an entrainment sub-model by Liu (2003) was adopted and fit to experimental data from Kim (2009) to capture entrainment of the gas around the particles. This gas phase was described in the Eulerian frame, while a Lagrangian falling-particle model was employed for calculation of the particle properties along the fall. A method incorporating radiation exchange between the particles across the thickness of the curtain was developed to capture temperature gradients that can impact energy storage differences between the front and back of the curtain.

The simulations performed with the inert particle receiver demonstrated how curtain opacity impacts the solar absorption efficiency within the receiver. A more opaque curtain is able to capture more of the total solar energy, by as much as 28 %, but in doing so can cause undesirable temperature gradients as large as 600 K between the front and back of the curtain. Curtain opacity can be increased by reducing particle size or by increasing total particle mass flow. Smaller particles fall more slowly and have greater frontal area for absorbing direct solar irradiation across the curtain. As such, the advantages of smaller particles can provide improve performance in terms of energy storage density and solar efficiency, but the stability of falling particle curtains as

diameters are reduced well below 500 μm must be evaluated with higher fidelity multi-dimensional gas-phase models as performed in the CFD modeling later in this work.

Increasing particle mass flow can also increase solar absorption efficiency. However, higher mass flow-rates without increased solar irradiation results in lower particle temperatures that could be detrimental to driving more efficient power cycles. In addition, the temperature gradients across the thickness of the curtain can become significant, which presents additional inefficiencies for an integrated solar plant. In general, direct particle receivers have a primary tradeoff between increasing maximum operating temperature and decreasing efficiency due to higher re-radiation losses. This tradeoff can be best mitigated by having particle material radiative properties such as emissivity to maximize solar absorption and minimize re-radiation losses.

The influence of particle radiation effects was explored in greater detail, especially in the context of commercial-scale receivers. This study showed that is important to maximize the grey-body emissivity to achieve performance as high as 91%. Further delving into the radiation parameters by studying the impacts of selectively-absorbing particles, this study demonstrated that particle selectivity is of little value – less than 1% efficiency and 5 K increase in outlet T_p – for the proposed operating conditions for a commercial-scale power. However, if the operating temperature is increased or solar concentration decreased, then selectivity can quickly become important for improving solar absorption efficiencies. When the operating temperature is increased by 300 K, selectivity can yield an improvement in efficiency as high as 4.7% and T_p by more than 30 K.

5.1.2 Proposed future work

This demonstrated trade-offs between solar efficiency and particle outlet temperature distribution could be explored further by looking at alternative receiver geometries and particle-flow management. This study provides some guidance for further development. Further studies may explore the possible advantages of multiply stacked curtains in the receiver depth, or multiple apertures with shorter fall distances seek to maintain high curtain opacities without developing large temperature gradients within the curtain.

The model developed in this work raises some questions about the validity of individual modeling components. The internal curtain heat-exchange term, $\dot{Q}_{curt}$, accounts for radiation exchanged between the front and rear halves of the curtain, but do not account for particle exchange between these zones. This mixing occurs due to particle dispersion driven by turbulent interactions. In order to explore the impact of mixing, experiments can be performed with different colored particles to measure the mixing by different heights and loadings. Further, while this model shows the importance of absorption into the depth of the curtain, it should be extended to include more discretization in the curtain depth and better capture the temperature profile at higher τ'_p.

While the model demonstrated here is an excellent design tool for early-stage development, it does have its limitations due to the simplified treatment of the gas-phase. After narrowing down the design range, a more comprehensive design-tool should be employed that can capture the impacts of the gas-phase within the receiver and through the front aperture as well as the actual radiation-field as opposed to the uniform field employed, as illustrated by in the CFD simulations performed by Khalsa et al., (2011).

5.2 Modeling Reactive Particle Receivers

5.2.1 Summary of results

In Chapter 3, the inert particle receiver model from Chapter 2 was extended to include reacting oxide particles. This required implementing species-exchange and thermochemistry of selected oxides. Undoped ceria was selected as a development material, due to the interest for solar water-splitting cycles and the wealth of data available from use in other applications. As such, complex ceria thermochemical model was adapted from Zinkevich et al. (2006), to model the equilibrium degrees of bulk ceria reduction as a function of P_{O2} and particle temperature. With this bulk description, the shifts in the thermodynamics of the ceria surface were adopted from DeCaluwe et al. (2010). Thermodynamically consistent bulk transport and reaction kinetics for the ceria particles were employed that included oxide-ion diffusion through the bulk, reverse incorporation to the surface, and desorption into the gas-phase. To close the species-transport model, the gas-phase entrainment model was updated to solve the species conservation in the gas phase to capture the evolution of P_{O2} around with the particles as they fall through the receiver.

The performance of a prototype-scale reactor-solar receiver for ceria reduction was simulated with the reactive particle model under a variety of operating conditions. These results highlighted the interplay between key performance metrics – particle outlet temperature, solar efficiency, and total degree of ceria reduction. Higher outlet temperatures increase the total degree of reduction by as much as double, but decrease the total receiver efficiency because the very high temperatures (> 1500 K) required to drive ceria reduction result in large re-radiation losses. These losses are exacerbated by

the relatively low emissivity (ε_p < 0.35) for ceria over the spectral region for the solar irradiation.

As with inert particles, higher ceria mass flow-rates lead to lower temperatures, and this also lowers the degree of reduction which decreases the potential for the partially reduced ceria to drive the desired downstream process for H_2O or CO_2 splitting. Profiles of degree of reduction along the fall clearly demonstrate that undoped ceria reduction process was rate-controlled by the surface reaction, and in all cases with particle outlet temperatures below 1800 K did not reach equilibrium by the end of the fall. The slow surface kinetics increases the value of smaller particles even further, which not only absorb radiation better, but also have greater surface areas for reaction.

To further explore the potential of more favorable oxides for reduction, , the perovskite $La_{0.1}Sr_{0.9}Co_{0.8}Fe_{0.2}O_{3-\delta}$ (LSCF) was tested within the receiver-reactor model. LSCF is prohibitively expensive for the large masses required for thermochemical energy storage, but it might have applicable for H_2O and/or CO_2 splitting. The properties of this particular composition of LSCF are sufficiently well studied (Choi et al. 2011, Choi et al. 201) and provide an example of a highly reducible perovskite that might be used for either thermochemical energy storage or solar-driven fuel production. Results from prototype-scale LSCF simulations indicated that the reduction of LSCF was also surface rate limited. However, these results also demonstrated that the added chemical storage increased total storage density, which could account for over 44 percent of the storage, while slightly improving solar receiver efficiency. Because LSCF has a very large entropy of reduction, it can undergo reduction above atmospheric P_{O2} at temperatures below 1300 K. Such high reducibility makes LSCF a suitable material for a commercial-

scale receiver. Simulations of the commercial-scale receiver at high mass-flow rates reinforced the importance of mass-flow rate of receiver performance. The higher mass flow rates still show the tradeoff between efficiency and particle outlet temperature, but the higher curtain temperatures greatly increase LSCF reduction which increases energy stored per unit mass that can be used for subsequent heat release for power or for H_2O and/or CO_2 splitting. The endothermic reduction improved overall receiver solar efficiency by reducing the particle temperatures and thus radiation losses required for a particular amount of energy storage.

5.2.2 Proposed future work

The results of the reactive particle model identified some important areas where future development could further improve the potential of particle receivers. The ceria results demonstrated a very low efficiency due to a combination of poor optical properties and high operating temperatures. While undoped ceria is not a viable material for this kind of receiver, the physics underlying its performance can be applied to many different reaction chemistries. Alternative water-splitting materials with lower operating temperatures and superior optical properties should be researched for implementation in such a receiver.

The ceria reaction model here combines many physical processes in order to evaluate the controlling kinetics. While this model is able to identify the importance of the surface reaction, there are uncertainties remaining in the rates used. In order to improve the value of this model, experimental data is required for high-temperature ceria reduction kinetics. Prior experience attempting to extract kinetic data from temperature-

programmed reduction experiments in a solar simulator has shown that ceria kinetics outpaced the heating rate when very-high surface area ceria fibers are used. Further, the surface-rate sensitivity study performed in this work demonstrated the importance of the surface reaction and, thus, the species surface area. Therefore, ceria kinetic studies should be performed for varying sample specific surface areas. The kinetic rates can be determined by fitting the model constants to experimental temperature programmed reduction experiments with varying the sample surface-areas. This work will serve to provide both a measurement of the error inherent in the reaction model as well as further validation of the kinetics.

Another major question raised about the results found in these studies relates to qualification and quantization of the errors inherent in the calculations. While errors can be difficult to quantify, it is important to address the uncertainty provided by the model results and provide greater context to their interpretation. To perform these modeling error estimations, a full sensitivity study should be performed on the influence of chosen parameters for each model. The results of this study can then be evaluated via a least-squares fitting to provide error limits. Not only does this improve the value of the results by highlighting the importance of relative differences, it also improves the value of the validation studies performed.

The model results with LSCF demonstrated that more reducible oxide materials have potential to improve the receiver performance and storage capabilities. Because of the relative high costs of LSCF, alternative cost-effective perovskite compositions should be sought that improve upon many of the promising properties of LSCF:

- structural stability over large changes in δ,

- high emissivity in the visible range to maximize absorption efficiency,
- high reduction entropies to work at high P_{O2},
- high specific heat and reduction enthalpy to maximize storage capability.

This work only focused on the receiver performance, but the receiver performance must be examined in the context of the full concentrated solar plant (for power generation and/or fuel production). Further studies should explore how variations in particle temperatures and degrees of reduction might impact designs of storage facility and other downstream components such as reoxidation reactors. Reoxidation reactors either with O_2 or H_2O/CO_2 require further research to assess what materials have favorable thermodynamics and kinetics to work in a full concentrated solar plant

In future work, performance metrics of a full plant simulation can be included into larger process-design calculations in order to inform optimal receiver designs. For example, full plant simulations could explore process-design strategies that can maximize the value of the energy from the receiver. For water-splitting cycles, strategies such as heat recovery, combined energy and fuel generation, or utilizing the excess sensible heat to drive another process should be explored.

As with the inert receiver, alternative architectures should also be investigated for the reactive particle receiver. Further, while gas flow is less important for inert particles, it is critical for describing the operation of the reactive particles which depend on P_{O2}. While the validity of the gas-flow model is investigated in this work, alternative gas-injection strategies should be further explored in order to maintain a more favorable atmosphere in the vicinity of the particles.

5.3 CFD Modeling of Reactive Particle Receivers

5.3.1 Summary of results

Chapter 4 of this work focused on the development of a particle reaction model that could be integrated into a 3D CFD model using ANSYS Fluent. The undoped ceria thermodynamic model in Chapter 3 was simplified by assuming bulk-surface equilibrium in the ceria, and with this reasonable simplification, the chemistry was imported into the framework with ANSYS Fluent's reacting particle model. Results from these simulations using Lagrangian particle-tracking demonstrate how the flow-field develops around the particles within the receiver, including large recirculation zones around the curtain. The development of the P_{O2} field within the receiver showed the importance of gas recirculation within the receiver that carried some of the higher P_{O2} flow from the exit towards the inlet.

Analysis of the receiver using different size particles confirmed the superior thermal performance of smaller particles, although the impact was much less drastic than seen in the simplified models. However, the flow stability of smaller particles was demonstrated through larger spreading by smaller particles in the flow. An exploration of the effects of mass-flow rate on the receiver showed a strong influence on the receiver efficiency. In comparison to the simplified model, the CFD model predicted higher efficiencies and particle temperatures at higher flow-rates. These effects were attributed to a combination of the influence of the gas and the different radiation schemes employed. A brief analysis of varying the gas-injection strategy in the receiver was able to improve the flow-control around the particles.

5.3.2 Proposed future work

The results of this study identified opportunities to improve the performance of the receiver. As mentioned in previous sections, alternative chemistries should be further investigated in the context of this receiver. While one demonstrated alternative gas injection strategies showed promise, alternative strategies should be further explored.

All of the studies performed in this work looked at averaged, steady-state performance of the receiver, ignoring transient effects. However, transient impacts such as time-varying solar insolation and particle-flow inhomogeneity should be looked at in more detail. The ability to respond quickly to changing solar conditions is important to maintain a consistent output temperature, and requires varying the particle mass flow-rate with q''_{solar} to maintain a consistent outlet temperature. However, the speed at which this can be varied depends upon the controlling feed mechanism. Further, these changes will impact the instantaneous η_{sol} due to variations in $\square'_p$. Particle flow inhomogeneity, or clumping of particles as they fall into areas of higher-density and lower density, has been observed in experiments such as Kim et al. (2009). The impact of this are greater at lower d_p due to the lower Stokes number, which makes particles more impacted by local disturbances in the flow. At low $\square'_p$ this will lead to areas of varying T_p, while also increasing rear-wall q''_{solar}. While it is expected that the influences of inhomogeneities should be small on high $\square'_p$ flows, it does warrant further testing in laboratory-scale experiments over a range of $\square'_p$ and d_p.

Finally, this study leaves as future work an exploration of the methods to improve both the simplified and CFD models demonstrated through the performed comparisons. The flow-field and P_{O2} analysis of the CFD model suggested that, while the entrainment model captured the general description of the flow-field, it needed to be improved to

include the influence of the gas-flow over a wider range around the particles. Analysis of the gas-phase temperatures in the CFD model revealed the importance of the recirculation in heating the particles, which could be included into the entrainment model via solution of a simple counter-flow along the walls. Analysis of the particle and wall temperatures revealed the need for improvement in the particle-treatment within the DO-irradiation model to account for the impacts of anisotropic scattering and radiation selectivity. The improvements to the simplified model increases its value further as a design tool for the solar thermal field, while improvements to the particle-coupling within the DO model increases the value of this method for a diverse range of high-temperature particle flows.

Glossary of Symbols Used

a	area per particle, m^2
a_λ	DO absorption coefficient m^{-1}
A	Area, m^2
C_D	single particle drag coefficient
C_S	stream coefficient
d	diameter, m
D	diffusivity, $m^{2}\cdot s^{-1}$
f_D	diffusion correction factor
f_v	volume fraction
f_{λ_m}	fraction of radiant energy in m^{th} λ-bin
$F_{i\text{-}j}$	View factor of cell j for cell i
g	acceleration due to gravity, $m^{2}\cdot s^{-1}$
h	specific enthalpy, $J\cdot kg^{-1}$
h_p	convection coefficient, $W\ m^{-2}K^{-1}$
I_λ	radiation intensity
j''_{diff}	diffusion flux, $kmol\cdot m^{-2}\cdot s^{-1}$
k	reaction rate-constant
k	conductivity, $W\cdot m\text{-}\cdot K^{-1}$
L	length, m
$\dot{m}$	mass flow rate, $kg\cdot s^{-1}$
$\dot{m}'_p$	mass flow rate per unit curtain length, $kg\cdot s^{-1}m^{-1}$

$\dot{n}''$	species flux, $kmol \cdot m^{-2} \cdot s^{-1}$
n_s	number of species
N_p	number of particles per m^3
Nu	Nusselt number
P	partial pressure, bar
Pr	Prandtl number
$\dot{q}''$	heat flux, $W \cdot m^{-2}$
$\dot{Q}$	heat transfer rate, W
r	radius, m
$\vec{r}$	location, m
$\vec{s}$	DO direction vector
S	Source term
$\bar{R}$	universal gas constant, $J \cdot mol^{-1} \cdot K^{-1}$
Re	Reynolds number
t	time, s
T	temperature, K
$\vec{u}$	velocity, $m \cdot s^{-1}$
v	volume per particle, m^3
$\overline{W}$	molar mass, $kg \cdot kmol^{-1}$
X	species mole fraction
x, y, z	coordinates
Y	species mass fraction

Greek symbols

α	entrainment constant
β	excess parameter
δ	degree of reduction
ε	material surface emittance
ε_λ	bulk emittance
θ	site density
θ	DO polar angle
λ	wavelength (μm)
μ	chemical potential, J mol^{-1}
η	efficiency
ρ	density, $kg \cdot m^{-3}$
ρ_λ	bulk reflectance
$\bar{\rho}$	molar density, $kmol \cdot m^{-3}$
σ	Boltzmann's constant, $W \cdot m^{-2} \cdot K^{-4}$
σ	sticking probability for adsorption
σ_s	scattering coefficient m^{-1}
φ	DO azimuthal angle
τ_λ	bulk transmittance
Γ	site density per unit area, $kmol \cdot m^{-2}$
Φ	Scattering phase function
Ω	DO solid angle

Subscripts

c	curtain
eq	equilibrium
g	gas
G	Gaussian
i	cell index
k	species index
m	radiation bin index, species index
p	particle
R1, R2	reaction 1,2
th	top-hat
w	window
(b)	bulk
(s)	surface
(sb)	sub-surface

Superscripts

ex	excess properties
0	ideal-state, reference-state
I	radiation intensity
M	momentum
T	temperature
Y	species

Bibliography

Abanades, S., Villafán -Vidales, H., 2011. CO2 and H2O conversion to solar fuels via two-step solar thermochemical looping using iron oxide redox pair. Che. Eng. J., 175, 368-375.

Adler, S., Chen, X., Wilson, J., 2007. Mechanisms and rate laws for oxygen exchange on mixed-conducting oxide surfaces. Journal of Catalysis, 245, 91-109.

Agrafiotis C., Roeb, M., Konstandopoulos, A., Nalbandian, L., Zaspalis, Z., Sattler, C., Stobbe, P., Steele, A., 2005. Solar water splitting for hydrogen production with monolithic reactors. Sol. Energy, 79, 409-421.

Amsbeck, L., Buck, R., Heller, P., Jedamski, J., Uhlig, R., 2008. Development of a tube receiver for a solar-hybrid microturbine system. 14th Biennial CSP SolarPACES Symposium.

ANSYS, Inc., 2011. ANSYS FLUENT theory guide. Canonsburg.

ASTM, 2000. Solar Spectra: Standard Air Mass Zero. Accessed via: http://rredc.nrel.gov/solar/spectra/am0/ASTM2000.html

Ávila-Marín, A., 2011. Volumetric receivers in solar thermal power plants with central receiver system technology: a review. Solar Energy, 85, 891-910.

Beale, S., Le, A.D., Roth, H., Pharoah, J., Choi, H.W. De Haart, L.G.J., Froning, D., 2011. Numerical and experimental analysis of a solid oxide fuel cell stack. ECS Transactions, 35 (1), 1107-1114.

Charvin, P., Abanades, S., Lemort, F., Flamant, G., 2008. Analysis of solar chemical processes for hydrogen production from water splitting thermochemical cycles. Energy Convers. and Management, 49, 1547-1556.

Chen, H., Chen, Y., Hsieh, H.T., Kolb, G. Siegel, N., 2007. Numerical investigation on optimal design of solid particle solar receiver. Proceedings of ASME Energy Sustainability 2007, Paper #ES2007-36134, 971-979.

Choi, M.B., Jeon, S.Y., Park, J.Y., Yang, H.S., Song, S.J., 2011. High-temperature transport properties of $La_{0.1}Sr_{0.9}Co_{0.8}Fe_{0.2}O_{3-\delta}$. Solid State Ionics, 192, 269-274.

Choi, M.B., Lim, D.K., Wachsman, E.D., Song, S.J., 2012. Oxygen nonstoichiometry and chemical expansion of mixed conducting $La_{0.1}Sr_{0.9}Co_{0.8}Fe_{0.2}O_{3-\delta}$. Solid State Ionics, 221, 22-27.

Chueh, W.C., Falter, C., Abbott, M., Scipio, D., Furler, P. Haile, S.M., 2010. High-flux solar-drive thermochemical dissociation of CO2 & H2O using nonstoichiometric ceria. Science, 330, 1797-1801.

Chueh, W.C., Haile, S.M., 2010. A thermochemical study of ceria: exploiting an old material for new modes of energy conversion and CO_2 mitigation. Philosophical Transactions of the Royal Society A: Mathematical, Physical, and Engineering Sciences. 368, 3269-3294.

Dahl, J., Buechler, K., Finley, R., Stanislaus, T., Weimer, A., Lewandowski, A., Bingham, C., Smeets, A., Schneider, A., 2002. Rapid solar-thermal dissociation of natural gas in an aerosol flow reactor. Proc.2002 U.S. DOE Hydrogen Program Review.

Decaluwe, S.C., 2009. Quantifying the role of cerium oxide as a catalyst in solid oxide fuel cell anodes. UMI/ProQuest, Michigan.

DeCaluwe, S.C., Grass, M.E., Zhang, C., El Gabaly, F., Bluhm, H., Liu Z., Jackson, G.S., McDaniel, A.H., McCarty, K.F., Farrow, R.L., Linne, M.A., Hussain, Z., Eichhorn, B.W., 2010. In situ characterization of ceria oxidation states in high-temperature electrochemical cells with ambient pressure XPS, Journal of Physical Chemistry C, 114, 19853-19861.

DeCaluwe, S.C., Jackson, G.S., 2011. Experimentally validated simulations of undoped ceria electrodes for H_2 oxidation and H_2O electrolysis in solid oxide electrochemical cells. ECS Transactions, 35(1), 2883-2895.

Dersch, J., Mathijssen, A., Roeb, M., Sattler, C., 2006. Modelling of a solar thermal reactor for hydrogen generation. Modelica, 441-448.

Dinsdale, A.T., 1991. SGTE data for pure elements. CALPHAD, 15(4), 317-425.

Felderhoff, M., Bogdanović, B., 2009. High temperature metal hydrides as heat storage materials for solar and related applications. Intl. J. Of Mol. Sci., 10, 325-344.

Flamant, G., Gauthier, D., Benoit, H., Sans, J.-L., Garcia, R. Boissiere, B., Ansart, R., Hemati, M., 2013, Dense suspension of solid particles as a new heat transfer fluid for concentrated solar thermal plants: on-sun proof of concept. 102, 567-576.

Ganesan, K., Dombrovsky, L.A., Lipinski, W., 2013. Visible and near-infrared optical properties of ceria ceramics. Infrared Physics & Technology, 57, 101-109.

Ghandehariun, S., Naterer, G.F., Dincer, I., Rosen, M.A., 2010. Solar thermochemical plant analysis for hydrogen production with the copper-chlorine cycle. Intl. J. of Hydrog., 35 (16), 8511-8520.

Gibbons, W.T., Venstrom, L.J., DeSmith, R.M., Davidson, J.H., Jackson G.S., 2014. Ceria-based Electrospun Fibers for Renewable Fuel Production via Two-Step Thermal Redox Cycles for Carbon Dioxide Splitting. Physical Chemistry Chemical Physics, DOI:10.1039/C4CP01974A.

González-Aguillar, R., Ignacio, B., Zarza, E., Schiel, W., Pitz-Paal, R., Tamme, R., Laing, D., Heller, P., Möller, S., Sugarmen, C., Olalade, G., Flamant, G., Konstandopoulos, A., 2007. Concentrating solar power - from research to implementation. European Communities, Luxembourg.

Guar, A., Montinaro, D., Sglavo, V., 2013. Electric field assisted sintering of LSCF and LSCF/GDC composities. European fuel cell conference presentation, Rome.

Haussener, S., Hirsch, D., Perkins, C., Weimer, A., Lewandowski, A., Steinfeld, A., 2009. Modeling of a multi-tube high-temperature solar thermochemical reactor for hydrogen production. J. of Sol. Energy. Eng., 131, 024503.

Hereaus, (2010). Quartz Glass for Optics: Data and Properties.

Hinze, J.O., 1975. Turbulence. McGraw-Hill Publishing Co., New York, 1975.

Hirsch, D., Steinfeld, A., 2004. Solar hydrogen production by thermal decomposition of natural gas using a vortex- flow reactor. Intl. J. of Hydrogen Energy, 29, 47-55.

Ho, C., 2013. Private e-mail communication with A.S.Oles.

Hruby, J., Steeper, R., Evans, G., Crowe, C., 1986. An experimental and numerical study of flow and convective heat transfer in a freely falling curtain of particles. J. Fluids Eng, 110 (2), 172-181.

Kaneko, H., Taku, S., and Tamaura Y., 2011. Reduction reactivity of CeO_2-ZrO_2 oxide under high O2 partial pressure in two-step water splitting process. Solar Energy, 2011, 85, 2321-2330.

Khalsa, S. S., Christian, J. M., Kolb, G.J., Röger, M., Amsbeck, L., Ho, C. K., Siegel, N.P., Moya, A.C., 2011. CFD Simulation and Performance Analsys of Alternative Designs for High-Temperature Solid Particle Receivers. Proceedings of ASME 2011 5th Intl. Conf. on Energy Sustainability 2011. Paper #ES2011-54430, 687-693.

Kim, K., Siegel, N., Kolb, G., Rangaswamy, V., Moujaes, S., 2009. A study of solid particle flow characterization in solar particle receiver. Solar Energy, 83, 1784-1793.

Kodama, T. and Gokon, N., 2007. Thermochemical cycles for high-temperature solar hydrogen production, Chem. Review, 107, 4048-4077.

Kolb, G., Ho, C., Mancini, F., Gary, J., 2011. Power tower technology roadmap and cost reduction plan, Sandia Natl. Lab.

Lapp, J., Davidson, J.H., and Lipinski, W., 2012. Efficiency of two-step solar thermochemical non-stoichiometric redox cycles with heat recovery. Energy, 37(1), 591-600.

Launder, B.E. and Spalding, D.B., 1974. The numerical computation of turbulent flows. Computer Methods in Applied Mechanics and Engineering, 3, 269-289.

Le Gal A., Abanades S., 2012. Journal Physical Chemistry C, 116, 13516-13523.

Lee, C.I., Meng, Q.L., Kaneko, H., Tamaura, Y., 2013. Solar hydrogen productivity of ceria-scandia solid solution using two-step water-splitting cycle. J. Sol. Energy Eng., 135, 011002.

Leistner, K., Nicolle, A., Da Costa, P., 2012. Modelling the kinetics of NO oxidation and NOx storage over platinum, ceria, and ceria zirconia. Applied Catalysis B: Environmental, 111-112, 415-423.

Liu, Z.Q., 2003. Air entrainment in free falling bulk materials, University of Wollongong Thesis Collections.

Lovegrove, K., Luzzi, A., Soldiani, I., Kreetz, H., 2004. Developing ammonia based thermochemical energy storage for dish power plants. Sol. Energy, 76, 331-337.

Maag, G., Zanganeh, G., Steinfeld, A., 2009. Solar thermal cracking of methane in a particle-flow reactor for the co-production of hydrogen and carbon. Int. J. of Hydrogen Energy, 34, 7676-7685.

Magrab, E., Azarm, S., Balachandran, B., Duncan, J., Herold, K., Walsh, G., 2010. An Engineer's Guide to MATLAB, 3rd ed. Prentice Hall, New York.

Marabelli, F., Wacther, P., 1987. Covalent insulator CeO_2: optical reflectivity measurements. Physical Reviews B, 36-2, 1238-1243.

Martinek, J., Bingham, C., Weimer, A.W., 2012. Computational modeling and on-sun model validation for a multiple tube solar reactor with specularly reflective cavity walls. Part 1: Heat transfer model. Chemical Engineering Science, 81, 298-310.

Martinek, J., 2012. Computational modeling and optimization of a mutliple tube aerosol flow reactor for high temperature solar-thermal processes. Univ. of Col. Boulder Thesis.

Martinek, J., Weimer, A.W., 2013. Evaluation of finite volume solutions for radiative heat transfer in a closed cavity solar receiver for high temperature solar thermal processes. International Journal of Heat and Mass Transfer, 58(1-2), 585-596.

Medrano, M., Gil, A., Martorell, I., Potau, X., Cabeza, L., 2010. State of the art on high-temperature thermal energy storage for power generation. Part 2 – Case studies. Renewable and Sustainable Energy Reviews, 14, 56-72.

Meier, A., 1999, A predictive CFD model for a falling particle receiver/reactor exposed to concentrated sunlight. Chemical Engineering Science, 54, 2899-2905.

Meng, Q.L., Lee, C.I. Kaneko, H., Tamaura, Y., 2012. Solar thermochemical process for hydrogen production via two-step water splitting cycle based on $Ce_{1-x}Pr_xO_{2-\delta}$ redox reaction. Thermochimica Acta, 532, 134-138.

Miller, J., Allendorf, M., Diver, R., Evans, L., Siegel, N., Stuecker, J., 2008. Metal oxide composites and structures for ultra-high temperature solar thermochemical cycles. J. Mater. Sci, 43, 4714-4728.

Mogensen, M., Sammes, N., Tompsett, G., 2000. Physical, chemical, and electrochemical properties of pure and doped ceria. Solid State Ionics, 129, 63-94.

Morsi, S.A., Alexander, A.J., 1972. An investigation of particle trajectories in two-phase flow systems. J. Fluid Mech, 55 (2), 193-208.

Niwano, M., Sato, S., Koide, T., Shidara, T., Fujimori, A., Fukutani, H., Shin, S., Ishigame, M., 1988. Optical properties of CeO2 crystal in photon energy range of 2.5-40 eV. Journal of Physics Society Of Japan, 57-4, 1489-1496.

Ozalp, N., JayaKrishna, D., 2010. CFD analysis on the influence of helical carving in a vortex flow solar reactor. Int. J. of Hydrogen Energy, 35, 6248-6260.

Palumbo, R., Meunecke, M., Möller, S., Steinfeld, A., 2004. Reflections on the design of solar thermal chemical reactors: thoughts in transformation. Energy, 29, 727-744.

Perret, R., Chen, Y., Besenbruch, G., Diver, R., Weimer, A., Lewandowski, A., Miller, E., 2005. High-temperature thermochemical. DOE Hydrogen Program.

Perret, R., Weimer, A., Wong, B., Brown, L., Diver, R., Siegel, N., Lewis, M., Chen, Y., 2008. Development of solar-powered thermochemical production of hydrogen from water. DOE Hydrogen Program.

Petkovich, N.D., Rudisill, S.G., Venstrom, L.J., Boman, D.B., Davidson, J.H., Stein, A, 2011. Control of Heterogeneity in Nanostructured $Ce_{1-x}Zr_xO_2$ Binary Oxides for Enhanced Thermal Stability and Water Splitting Activity, Journal of Physical Chemistry C**,** 115, 21022-21033.

Rager,T. 2012. Re-evaluation of the efficiency of a ceria-based thermochemical cycle for solar fuel generation. Chemical Communications, 48, 10520-10522.

Roeb, M., Neises, M., Monnerie, N., Call, F., Simon, H., Sattler, C., Schmücker, M., Pitz-Paal, R., 2012. Materials-related aspects of thermochemical water and carbon dioxide splitting: a review. Materials, 5, 2015-2054.

Röger, M., Pfänder, M., Buck, R., 2006. Multiple air-jet window cooling for high-temperature pressurized volumetric receivers: testing, evaluation, and modeling. Journal of Solar Energy Engineering, 128, 265-274.

Röger, M., Amsbeck, L., Gorbereit, B., Buck, R., 2011. Face-down solid particle receiver using recirculation. Journal of Solar Energy Engineering, 133, 31009.

Scheffe, J.R., Steinfeld, A., 2012. Thermodynamic Analysis of Cerium-Based Oxides for Solar Thermochemical Fuel Production, Energy & Fuels, 26(3), 1928-1936.

Scheffe, J.R., Jacot, R., Patzke, G.R., Steinfeld, A., 2013. Synthesis, Characterization, and Thermochemical Redox Performance of Hf^{4+}, Zr^{4+}, and Sc^{3+} Doped Ceria for Splitting CO_2. Journal Physical Chemistry C, 2013, 117, 24104-24114.

Siegel, N.P.,Ho, C.K., Khalsa, S.S., Kolb, G.J., 2010. Development and evaluation of a prototype solid particle receiver: on-sun testing and model validation. Journal of Solar Energy Engineering, 132, 021008.

Singh, A., Al-Raqom, F., Klausner, J., Petrasch, J., 2011. Hydrogen production via the Iron/Iron Oxide looping cycle. Proc. ASME 2011 5th Intl. Conf. on Energy Sust., ES2011, ES2011-54499.

Steinfeld, A., 2005. Solar thermochemical production of hydrogen—a review. Sol. Energy, 78, 603-615.

Sully, A., Brandes, E., Waterhouse, R., 1952. Some measurements of the total emissivity of metals and pure refractory oxides and the variation of emissivity with temperature. Journal of Applied Physics, 3, 97-101.

Syamlal, M., O'Brien, T.J., 1989. Computer simulations of bubbles in a fluidized bed. A.I.Ch.E. Symposium Series, 85: 2-31.

Tan, T., Chen, Y., 2010. Review of study on solid particle solar receivers. Renewable and Sustainable Energy Reviews, 14, 265-276.

Tester, J.W., Drake, E. M., Driscoll, M.J., Golay, M.W., Peters, W.A., 2012. Sustainable energy: choosing among options. MIT Press, 2nd ed.

Tu, N., Wei, J., Fang, J., 2014. Numerical study on the thermal performance of a solar cavity receiver with different depths. Applied Therm. Eng., 72(1), 20-28.

US DOE. Sunshot concentrating solar power program. Energy.gov. Retrieved: 8 September 2014. http://energy.gov/sites/prod/files/2014/02/f7/sunshot_csp_poster.pdf

Villafán-Vidales, H., Abanades, S., Caliot, C., Romero-Paredes, H., 2011. Heat transfer simulation in a thermochemical solar reactor based on a volumetric porous receiver. Appl. Therm. Eng., 31, 3377-3386.

Wang, F., Tan, J., Shuai, Y., Gong, L., Tan, H., 2014. Numerical analysis of hydrogen production via methane steam reforming in porous media solar thermochemical reactor using concentrated solar irradiation as heat source. Energy Conversion and Management, 87, 956-964.

Yimer, I., Campbell, I., Jiang. L.Y., 2002. Estimation of the turbulent Schmidt number from experimental profiles of axial velocity and concentration for high-Reynolds-number flows. Canadian Aeronautics and Space Journal, 48 (3), 195-200.

Z'Graggen, A., Steinfeld, A., 2008. A two-phase reactor model for the steam-gasification of carbonaceous materials under concentrated thermal radiation. Chem. Eng. And Proc., 47, 655-662.

Zhang, H.M., Yamazoe, N., Teraoka, Y., 1989. Effects of B-site partial substitutions of perovskite-type $La_{0.6}Sr_{0.4}CoO_3$ on oxygen desorption. J. of Materials Science Letters, 8, 995-996.

Zinkevich, M., Djurovic, D., Aldinger, F., 2006. Thermodynamic modelling of the cerium-oxygen system. Solid State Ionics, 177, 989-1001.